FINAL REPORT

ACTIVE DEFORMATION CONTROL OF BRIDGES PRESTRESSED WITH ARAMID FIBER REINFORCED PLASTIC (AFRP) CABLES

Principal Investigator:

DR. M. AROCKIASAMY Research Assistant: KRISHNA SANDEPUDI

Submitted to:
Florida Department of Transportation

Under:

WPI No. 05 10614, State Job No. 99500-7571-119
Contract No. C - 4131
Monitored by: Structural Research Center
Florida Department of Transportation
2007 E. Paul Dirac Drive
Tallahassee, FL 32304

Center for Infrastructure and Constructed Facilities
Department of Ocean Engineering
FLORIDA ATLANTIC UNIVERSITY
Boca Raton, Florida -33431

JANUARY 1995

TECHNICAL REPORT STANDARD TITLE PAGE

1. Report No.	2. Government Accession No.	3. Receipient's Calalog No.
4. Title and Subtitle Active Deformation Control of Bridges Prestressed with Aramid Fiber Reinforced Plastic (AFRP) Cables		5. Report Data January 1995 6. Performing Organization Cods
7. Authors M. Arockiasamy and K.S. Sandepudi		S.Performing Organization Report No.
9. Performing Organization Name and Address Florida Atlantic University Center for Infrastructure and Constructed Facilities Department of Ocean Engineering Boca Raton, Florida 33431		10. Work Unit No. 11. Contract or Grant No. WPI 0510614, C- 4131
12. Sponsoring Agency Name and Address Florida Department of Transportation 605 Suwannee Street Tallahassee. Florida 32399-0466		13. Type of Report an Period Covered Final Report 14. Sponsoring Agency Code 99500-7571-119

15. Supplementary Notes
Prepared in cooperation with the Federal Highway Administration

16. Abstract

Fiber reinforced plastics (FRPs) can successfully be used in concrete structures, in lieu of steel, as reinforcing and / or prestressing elements, owing to high tensile strength, immunity towards low Young's modulus, light weight and high fatigue resistance. Very little experimental results and performance data are available regarding the properties of FRP composites and their application in concrete structures.

This investigation was conducted to establish the feasibility of using Aramid FRP (AFRP) cables reinforcing / prestressing elements in concrete bridge structures. Besides investigating durability of AFRP cables in adverse environments (alkali and seawater), static and ultimate load tests were performed on single Double-Tee beam, together with static, fatigue and ultimate load tests on a half scale model Double-Tee beam bridge system prestressed with AFRP. Large deformations at ultimate load conditions and good fatigue resistance were observed in the experimental studies. A computer code was developed to perform flexural analysis of beams prestressed / reinforced / strengthened by FRP elements. Analytical results showed good correlation with experimental findings. An active deformation / vibration control model is suggested, which can be incorporated in prototype bridges safety and performance data evaluation. Feasibility of application of AFRP tendons in bridge structures is assessed based on the experimental and analytical parameters such as deflections, strains, crack distributions, crack widths, and energy considerations.

17. Key Words	18. Distribution Statement
Active control, Double-Tee beam, Advanced Composite Materials, Fiber Reinforced Plastics, Durability studies, Aramid FRP, ARAPREE, Static test, Fatigue resistance, Ultimate load test.	No restrictions. This document is available to the public through the National Technical Information Service, Springfield, Virginia 22161

19. Security Classif. (of this report)	20. Security Classif. (of this page)	21. No. of Pages	22. Price
Unclassified	Unclassified	276	

Form DOT F 1700.7 (8-89)

DISCLAIMER

The opinions, findings and conclusions expressed in this publication are those of the authors who are responsible for the facts and accuracy of the data presented herein. The contents do not necessarily reflect the views or policies of the Florida Department of Transportation or the Federal Highway Administration. This report does not constitute a standard, specification or regulation.

The report is prepared in cooperation with the Florida Department of Transportation and the Federal Highway Administration.

SUMMARY

One of the major problems the construction industry faces today is low corrosion resistance of reinforcing and prestressing steel, which significantly affects the durability of concrete structures. Theoretically fiber reinforced plastics (FRPs) can successfully be used in concrete structures, in lieu of steel, as reinforcing and / or prestressing elements, owing to high tensile strength, immunity towards corrosion, low Young's modulus, light weight and high fatigue resistance. Very little experimental results. and performance data are available regarding the properties of FRP composites and their application in concrete structures. Thus, to ensure safety of the structures, accurate assessment and continuous performance monitoring of the FRPs together with the structure have to be made with an option of active and / or passive structural control.

This investigation was conducted to establish the feasibility of using Aramid FRP (AFRP) cables as reinforcing / prestressing elements in concrete bridge structures. Besides investigating durability of AFRP cables in adverse environments (alkali and seawater), static and ultimate load tests were performed on single Double-Tee beam, together with static, fatigue and ultimate load tests on a half scale model Double-Tee beam bridge system prestressed with AFRP. Large deformations at ultimate load conditions and good fatigue resistance were observed in the experimental studies. A computer code was developed to perform flexural analysis of beams prestressed / reinforced / strengthened by FRP elements. Analytical results showed good correlation with experimental findings. An active deformation / vibration control model is suggested, which can be incorporated in prototype bridges for safety and performance data evaluation. Feasibility of application of AFRP tendons in bridge structures is assessed based on the experimental and analytical parameters such as deflections, strains, crack distributions, crack widths, and energy considerations.

ACKNOWLEDGMENTS

The authors wish to express their sincere thanks to Dr. Mohsen A. Shahawy, Chief Structures Analyst, Dr. Moussa Issa, Structural Analyst and Mr. Thomas E. Bietelman, Research Engineer of Florida Department of Transportation for their excellent suggestions, discussions and constructive criticisms throughout the project. Special thanks are also due to Mr. Adnan El Saad Research Engineer, and Mr. Tony, Mr. Frank and Mr. Alex of Florida Department of Transportation for assistance in the experimental part of the project. They wish to express their appreciation to Dr. S. E. Dunn, Professor and Chairman, Department of Ocean Engineering, and Dr. C. S. Hartley, Dean, College of Engineering, Florida Atlantic University for their continued interest and encouragement.

Grateful acknowledgements are due to Sireg S.p.A, Italy and AKZO, Germany for supplying the ARAPREE tendons and the anchorages used in this study. Special thanks are also due to ing. Arie Gerritse for his technical suggestions which were very helpful in planning the project. Grateful acknowledgements are due to Dr. Hamid Garmestani, Professor, Department of Mechanical Engineering, FAMU / FSU College of Engineering, for assistance in carrying out SEM analyses.

The valuable assistance in the experimental studies from Mr. Ming Zhuang and Mr. Sowrirajan Raghavachary, Graduate Students, Florida Atlantic University, is gratefully acknowledged. The valuable assistance in the casting and testing of the Double-Tee bridge system from Mr. Srikanth Kanneganti and Mr. Rong Qu, and assistance in durability studies provided by Mr. Subia Kokkalera, Graduate Students, Florida Atlantic University, is gratefully acknowledged. Sincere thanks are also due to Mr. Sattanathan Ponnuswamy and Mr. Arulseelan Thiruppathi for their excellent support provided in the theoretical studies.

TABLE OF CONTENTS

LIST OF FIGURES

LIST OF TABLES

CHAPTER 1

INTRODUCTION

1.1 BACKGROUND

An enormous financial investment is involved in the construction, maintenance and operation of buildings, bridges, dams and other public domain structures. One of the major problems the construction industry faces today is low corrosion resistance of reinforcing and prestressing steel, which significantly affects the durability of concrete structures. Recently a large scale research effort has been directed towards the Advanced Composite Materials (ACM), also referred to as Fiber Reinforced Plastics (FRP) and Continuous Fiber Reinforced Materials (CFRM), as reinforcing and prestressing elements in concrete structures.

Theoretically ACM or FRPs can successfully be used in concrete structures, in lieu of steel, as reinforcing and prestressing elements, owing to high tensile strength, immunity towards corrosion, low Young's modulus, light weight and high fatigue resistance. This concept, before implementation in the construction industry, needs to be substantiated with more comprehensive performance data and experimental results.

A safe structural design should involve complete knowledge regarding loads that would be applied to the structure, and behavior and strength of the materials. Though structures are often designed for the worst expected loading conditions, there is always a possibility for an unexpected loading condition which might override the design loads. Also, very little information is available regarding the properties of FRP composites and their application in concrete structures. Thus, to ensure a safe structure, accurate assessment and continuous monitoring of performance of the ACM together with the structure have to be made with an option of active and / or passive structural control.

Japanese Society of Civil Engineers (JSCE), research sub-committee on CFRM, insist and encourage the researchers and designers to experimentally verify all the properties of CFRM, carry out a thorough structural analysis and use material and member safety factors when designing concrete structures using CFRM. Also, JSCE suggests carrying out a detailed thermal stress analysis whenever aramid or carbon based CFRM is being used.

The task of establishing FRPs as a safe, durable and an economic replacement to steel in concrete structures can be accomplished by making the structure "intelligent". An "intelligent" structure will contain its own sensors, actuators and computational / control capabilities and / or hardware [Measures, 1992]. The function of sensors is to measure / record or "sense" the structural response (say deformation) continuously, and convey the measureand to computational unit where the decision is made, if the measureand is within specified limits. If the measureand (deformation) exceeds the specified limits, the actuators present are activated according to a prespecified algorithm to nullify the excessive deformation, and this concept is termed as structural control. The deformation after control is again measured by the sensors and conveyed to the computational unit to recheck whether the controlled deformation is within the limits, and this is termed as feedback. It might be necessary to incorporate this type of control mechanism in structures constructed using ACM owing to the lack of performance data. The performance or experimental data collected simultaneously would be necessary for development of design guidelines for structures reinforced / prestressed with ACM.

This investigation is an attempt to establish the feasibility of using Aramid FRP (AFRP) cables as reinforcing / prestressing elements in concrete bridge structures. Besides investigating durability of AFRP cables in adverse environments (alkali and seawater), static, fatigue and ultimate load tests will be performed on half scale model Double-Tee beam bridge system. An active deformation / vibration control model is suggested, which can be incorporated in the prototype bridges for safety and performance data evaluation. It is expected that this study would provide a significant amount of performance and experimental data of concrete bridges prestressed

with Aramid fiber reinforced plastic (AFRP) and contribute to the formation of more comprehensive design guidelines for better and more economical design of bridges.

1.2 OBJECTIVE OF THE STUDY

The scope of the investigation will comprise of the following major tasks:

i) Durability studies on AFRP tendons exposed to seawater and alkali solution,
ii) Design and casting of Double-Tee beams,
iii) Theoretical analysis of Double-Tee beams prestressed with AFRP,
iv) Investigation of static, fatigue and ultimate behavior of the Double-Tee beams and bridge system, and
v) Development of methodology for active deformation control of structural elements prestressed with FRPs.

CHAPTER 2

LITERATURE REVIEW

2.1 INTRODUCTION

Owing to the dramatic differences in the properties of steel and FRPs, comprehensive parametric studies have been carried out evaluating different facets of structural analysis, design, and construction of concrete structures prestressed and / or reinforced with FRPs. This chapter summarizes certain selective investigations carried out on the feasibility of application of FRPs in concrete structures.

2.2 TENSILE STRENGTH AND LOSSES UNDER SUSTAINED STRESS

Only limited studies have been carried out to verify the tensile strength and relaxation properties of FRPs. Mukae et al. [19931 conducted tension, creep and fatigue tests on AFRP rods. A bond type anchoring method was used in the tests which proved to be significantly effective for the type of rods used in the investigation. The tensile strength of the AFRP rods showed a normal distribution with values equal to or greater than those of steel reinforcing bars. The results of fatigue tests upto two million cycles revealed the adequate fatigue strength of the material for practical use.

Uomoto and Hodhod [19931 have reported findings on the mechanical behavior and tensile strength of carbon, aramid and S-glass based FRP rods. For each material, three different fiber volume fractions (0.45, 0.55, 0.66) were tested in axial tension. The stress-strain relationships and

strength distribution were obtained based on experiments as well as analyses. The strength distributions showed a shift proportional to the rods' fiber content.

Iyer [1991, 1992] studied the mechanical properties on fiberglass (S-2) and graphite cables (AS-4 and AS-2) under short and long term sustained static loading and the results compared with those of steel cables. For static tension test, the specimens were subjected to short term sustained tension of 1366 MPa for 24 hours and long term sustained tensile stress level of 1000 MPa for six months. The long term sustained tension on graphite cables did not show any significant creep. Rostasy [1991, 1992] proposed use of FRPs as post-tensioning tendons. He presented the basic material properties of FRPs, including stress-strain relations, creep rupture, strength retention and fatigue strength. Kobayashi and Tanaka [1992] conducted impact tensile tests on carbon fiber composite cable (CFCC 1x7, 05) for prestressed concrete and obtained the stress-strain relationships. The results presented include the strain rate dependence of breaking strength, elongation, elastic modulus and absorbed energy. The evaluation of FRPs as effective prestressing elements in concrete structures was based on the ratio of impact value to the static value.

2.3 BOND AND TRANSFER LENGTH CHARACTERISTICS

Several researchers investigated. bond characteristics of FRP tendons with concrete. Makitani [1993] carried out experiments on flexural bond characteristics using beam specimens reinforced with FRP bars. It was observed that bond failure did not take place for the bars with sand coated surfaces and bond length more than 40 times diameter of the bar. Considering the above test results for the CFRP bars, the lap splice joints were tested by arranging an anchor positioned in the center of a truss type concrete specimen. It was recognized that the unit bond strength increased with the increase in length of the lap splice joint, but that it decreased for lap splice length between 40 and 60 times the diameter.

Three series of tests were performed by Kanakubo et al. [1993] in order to investigate the bond performance of concrete members reinforced with CFRP and AFRP bars. At first, a pull out

test was performed to evaluate the bond splitting strength of FRP reinforced concrete without lateral reinforcement. Test results show that the bond splitting strength can be estimated using the ratio of lug height to diameter of FRP bars (h/d) and is given by

$$\tau_{max} / \sqrt{\sigma_B} = 0.67(h/d)^{22} \quad \text{.....(2.1)}$$

where

τ_{max}= bond splitting strength (MPa)

σ_B = compressive strength of concrete (MPa)

h/d = ratio of lug height to average diameter of FRP bars (%)

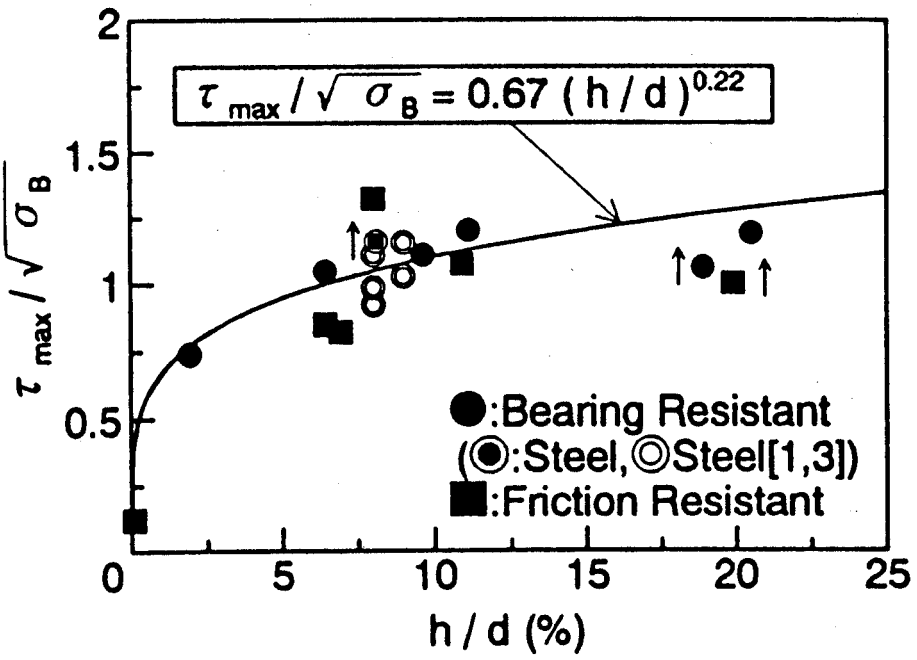

Fig. 2.1 Bond splitting strength vs. h/d

In the second test, a bond splitting test was conducted on cantilever type specimens. These tests were designed to simulate stress conditions in a real structure. Results of these tests showed that bond splitting strength without lateral reinforcement is equal to that obtained by the first pull out test. The percentage increase in the strength caused by lateral reinforcement can be evaluated in terms of elastic modulus. Finally, unsymmetrical loading for actual beams reinforced with FRP bars was carried out. The bond performance of the longitudinal bars show a good correlation with the results obtained from the former two tests.

Depending on the type of resin matrix, aramid tendons may have radial thermal expansion coefficients upto 50x10 and significantly high Poisson's ratio [Gerritse, 1992]. Hence, an increase in temperature in a concrete member bonded to aramid fiber cables would cause complex stress states such as high radial splitting stresses in the prestress transfer zone together with interfacial stresses between concrete and tendon.

Studies performed by Mashima and Iwamoto [1993] reveal that the bond strength of certain FRPs in concrete is affected by freezing and thawing cycles. Also, in pretensioned members, this incompatible thermal expansion coefficients can aggravate the splitting stresses in the prestress transfer zone caused by the Hoyer effect (de Sitter and Vonk, 1993).

Iyer et al. [1991 and 1992] tested the bond strength of graphite cables. . Studies were conducted to investigate transfer length of unbonded graphite cables, development length of sanded graphite cables and the results compared with those of steel strand. Comparison showed that transfer length of unsanded graphite cables was 95 times the diameter, which is higher than the ACI 318-89 recommended value. Sanded graphite cables showed lesser values than the ACI recommended value. Bond strength of graphite cables was doubled by surface preparation, but unsanded graphite cables slipped during transfer of prestress, showing poor bond strength with concrete. On the basis of results, it was stated that the transfer and development lengths for graphite cables are comparable with steel cables. Sen (1992] found that the transfer length of fiberglass rods was about 27 times the strand diameter or 10 in. This is 23% smaller than that of the same size steel strands stressed to the same level.

2.4 DURABILITY OF FRP AS PRESTRESSED TENDON

The resistance to corrosion is one of the major reasons that FRP material is being considered as prestressing / reinforcing elements in lieu of steel. A brief review of investigations evaluating the durability of composite materials for use in prestressed concrete members is presented herein.

Sen et al. [1991, 1993] reported experimental results of durability studies on fiberglass for pretensioned beams. The effect of simulated tidal cycles on the ductility and ultimate capacity of identical steel and fiberglass pretensioned specimens was determined and the relative durability of cracked and uncracked specimens evaluated. Based on the experimental data, the following conclusions were made:

- The durability of the fiberglass specimens exposed to wet and dry cycles is much worse than that of steel. No commensurate reductions were observed in the control specimens kept in air.
- The failure mode of exposure specimens changed from a compression mode to a new mode termed "corrosion mode". In this mode, beams failed without warning immediately following initial cracking.
- There were no visual signs of deterioration of the fiberglass pretensioned beams. This makes them potentially more dangerous in structural applications compared to steel where concrete cracking provides a warning.
- In the durability studies, tests indicated a complete loss of effectiveness of the fiberglass strands after an average of 6 months for the pre-cracked specimens and 15 months for the uncracked specimens. No comparable loss was detected in identical steel specimens.
- The fiberglass strands used are unsuitable for pretensioning applications in a marine environment.

Gerritse [1992] found that FRPs behave generally satisfactorily in carbonated concrete. However, some (with emphasis on glass fiber based FRP) will deteriorate in an alkaline environment. So durability (or residual strength) of any fiber in alkaline environments would define its practical applicability in concrete elements, if in direct contact with the cementitious matrix.

Katawaki et al. [1992] reported a two stage durability experiment that they have performed under actual marine environment condition. In the first stage, they tested specimens of carbon fiber and aramid fiber after exposure under a tensile load of 5 tons. The deterioration of materials was surveyed after exposure for 1.5 years. Results showed that the reduction of tension during exposure represents a relaxation of more than 10% for the aramid and 10-20% for the carbon fiber composite. Cracks developed only in some of the aramid fiber composite and the results indicated 2-5

the change in ultimate tensile strength and elastic modulus. In the second stage, eight beams prestressed with different types of CFRP, AFRP, GFRP, VFRP (vinylon) and steel strands were examined periodically under sea water condition. The results of survey show that carbon fiber composite material and aramid fiber composite material have strength characteristics comparable to steel and exhibit much better anti-corrosion properties desirable for maritime structures.

2.5 BEHAVIOR OF CONCRETE BEAMS PRESTRESSED AND / OR REINFORCED WITH FIBER REINFORCED PLASTIC TENDONS

Besides offering the advantage of being a non-corrosive reinforcement, aramid and carbon fiber based FRPs have higher ultimate tensile strength and lower modulus of elasticity compared to steel. Only limited research has been carried out on the feasibility of using aramid fiber reinforced plastics as prestressing tendons in lieu of steel.

2.5.1 Flexural and Shear Behavior

Sen, [1992] presented the details of a comprehensive research on feasibility of fiberglass pretensioned piles in a marine environment. In the static beam tests, the elastic response of the under-reinforced fiberglass pretensioned beams was identical to that of its steel pretensioned counterpart. However, the post-elastic response of the fiberglass pretensioned beams was more flexible. All failures were tension failures with secondary crushing of concrete in the compression zone. The failure modes were ductile and in every test the ultimate deflection of the fiberglass beams was larger than the comparable steel specimen.

Mckay [1992] found that the use of present design approach for steel pretensioned beams could provide an adequate method for predicting AFRP pretensioned beam behavior, including cracking behavior, development length, transfer length and ultimate moment. Post-cracking deflection calculations may be excessively conservative due to the wide crack spacing that results in significant tension stiffening.

Kato and Hayashida [1993] reported on the flexural behavior of prestressed concrete beams with carbon fiber reinforced plastic tendons. The first crack load of a member with unbonded CFRP tendons is governed by prestressing force similar to bonded specimens and those with conventional PC steel strands. The first crack and ultimate loads in flexure can be roughly estimated by the conventional method. Factors such as effective prestressing force, quantity and type of tensile reinforcement influence deformation at the ultimate stage of PC beams using CFRP tendons.

Naaman [1993] presented a preliminary test evaluation of carbon fiber composite cable for partially prestressed beams. Two T-beams with targeted global reinforcing index of 0.11 with steel strands and partial prestressing ratio of 0.28 with CFCC were prepared and tested under third-point load. CFCC tendons were pretensioned upto 191 ksi, which is approximately 63% of ultimate tensile strength. A few tendons lost pretension due to bond failure between diecast sleeve and the tendon. The flexural behavior including beam curvature, load-deflection characteristics, crack pattern, strain in non-prestressed reinforcement at the critical section, ultimate strength and slip of the strands were investigated in detail. The test results are compared with analytical predictions using a nonlinear analysis procedure and experimental results from previously tested beams that have similar reinforcing index of steel prestressed strands. The test results showed that

i) the load-deflection response of beams prestressed with FRP tendons is essentially trilinear with decreasing slope, and
ii) the load-deflection response of beams prestressed or partially prestressed with FRP tendons can be predicted with reasonable accuracy using conventional methods of equilibrium, strain compatibility and material stress-strain relationships.

Sueoka [1993] tested the mechanical properties of reinforced concrete beams with FRP. Static flexure and shear tests were conducted in this study. The flexural capacity agreed well with values calculated by the conventional method. The shear capacity was computed and found to be 20-30% on the safe side by using the Niwa equation.

Yonkura et al. [1993] have investigated the flexural strength, flexural failure modes and shear strength of post-tensioned PC beams using CFRP and AFRP as prestressing tendons. They reported the following:

- The ultimate strength in flexure of PC beams using FRP rods can be evaluated by conventional calculations. The shear strength of PC beams using FRP rods and FRP web reinforcement is smaller than that using prestressing steel bars when the same shear strength is provided by shear reinforcement.
- Since moduli of elasticity of AFRP and CFRP are about 1/4 and 2/3 of that of prestressing steel bars respectively, the deflection of PC beams using FRP rods are larger than those using prestressing steel bars.
- The ultimate flexural and shear strength of PC beam using FRP rods can be improved by increasing prestressing force.
- PC beams using FRP rods may be designed for either flexural compression failure or tension failure.

Tottori and Wakui [1993] studied the shear behavior and found that shear capacity of RC beams without shear reinforcement can be predicted to some degree by taking into account the tension stiffness of FRP reinforcement. The contribution of prestress to shear capacity can be predicted from decompression moment. Contribution of FRP shear reinforcement to shear capacity is smaller than the value calculated by truss analogy.

An experimental investigation was conducted to study the shear performance of concrete beams with FRP reinforcement [Nagasaka 1993]. Thirty-five half scale beams were subjected to monotonically increasing shear force upto the ultimate capacity. The principal variables were the reinforcement type, shear stirrup reinforcement ratio -and the concrete strength. The beams with FRP stirrups failed due to either breaking of the curved sections of stirrups or crushing of a diagonal concrete strut. The former failure mode was excessively brittle and more undesirable than the latter mode. The ultimate shear capacity increased with increasing amount of FRP stirrup, although the FRP stirrups without yielding did not effectively carry the shear force as conventional steel stirrups. With the same amount of shear reinforcement, the shear capacity of the beams

reinforced with FRP bars was smaller than that of the beams with steel bars. Further, it has been presented that the ultimate shear capacity of beams with FRP stirrups can be fairly well estimated by substituting the tensile strength of curved sections of stirrup for the yield strength in Arakawa's formula.

2.5.2 Fatigue Behavior

Sen [19921 reported fatigue tests performed on two fiberglass pretensioned beams subjected to 2 million cycles at 3 Hz. The applied load varied between 40% and 60% of the measured ultimate static capacity. The results of these tests compared favorably with those recorded in similar stressed steel beams reported in the literature. Material and structural creep studies showed that under a load corresponding to 20% and 30% of the ultimate concrete strength, the prestress losses in the steel specimens were between 16 to 34% greater than that in the comparable fiberglass specimens. The study indicated that fiberglass had the properties required for prestressing and displayed ductility and resistance to impact forces. The response of the fiberglass pretensioned specimens is very similar to that of steel pretensioned ones and differences were attributable to differences in material properties.

Iwamoto et al. [1993] carried out flexural fatigue experiments on prestressed concrete beams using AFRP tendons. The results show that the beams with AFRP behaved well in fatigue compared to that of the beams with prestressing steel wires. The fatigue strength at two million cycles of loading was more than 65% of the static ultimate strength of beam. The effect of initial tension in tendon on the fatigue life of the beam was not observed.

Iyer et. al. [1992] carried out research on evaluation of CFRP for prestressing concrete. The structural behavior was studied based on static flexural tests and cyclic flexure tests. Cyclic loading for two million cycles did not significantly affect the ultimate strength of the beam prestressed with sanded graphite cables.

Kato and Hayashida [1993] also reported research on fatigue characteristics of prestressed concrete beams with carbon fiber reinforced plastic tendons. Bonded and unbonded CFRP tendons and steel strands were used for comparison. After repetitive flexural loading in excess of one million cycles, the maximum flexural strength, load-displacement curve and variation in equivalent rigidity of a PC beam are found to be roughly the same as those under static flexural loading. The effect of repetitive loading is not recognizable and it was concluded that fatigue properties are good.

2.5.3 Ductile Behavior and Serviceability

An experimental investigation was carried out in order to study and evaluate the flexural performance of concrete beams reinforced with continuous fiber bars (Nakano 1993]. Two series of flexural tests were conducted. The primary variables were the fiber material, tensile reinforcement ratio, concrete compressive strength and the bond in prestressing tendon. The flexural performance of concrete beams reinforced with continuous fiber bars can be evaluated by means of conventional methods used in concrete beams reinforced with steel bars.

The ductility of reinforced concrete beams can be controlled by the compressive failure of concrete, while ductility of prestressed concrete beams can be controlled by changing unbonded length of prestressing tendon. The initial cracking load and width of cracks can be controlled by prestressing force. The stiffness after initial cracking can be evaluated in terms of the product of the tensile reinforcement ratio and the tensile modulus of continuous fiber bars. It can be controlled in the same manner as concrete beams reinforced with steel bars.

A research program to improve the ductility of PC members reinforced with FRP tendons was carried out by Taniguchi [1993]. The compressive strength of concrete confined with FRP as transverse reinforcement was investigated. Major improvement could be achieved in the stress-strain relationship of concrete laterally reinforced with FRP and the ductility characteristics of concrete with FRP. Several PC members reinforced with FRP as tendons and transverse

reinforcements were investigated. It was found that marked improvements could be made in the ductility of the PC members with FRP tendons by ensuring flexural compression failure. Kakizawa et al. [1993] carried out a research program of load tests on 16 concrete beams reinforced with carbon FRP bars and cables to study both serviceability and ultimate limit states. The test specimens included the RC, PC and PPC members. The cracking behavior, failure properties and the energy absorption of FRP reinforced concrete have been investigated experimentally, considering the prestress force and bonding properties of the FRP reinforcement as the experimental factors. The experimental results show that cracking and deformation behavior vary with the prestress force and bond property of FRP bars and that the reasonable serviceability condition would be achieved by controlling these factors. Although the failure mode was also affected by these factors and the reinforcing systems these specimens have almost same reinforcement ratio. In relation to the failure mode, the energy absorption, defined as the area enclosed by load-deflection curve, was measured to determine the toughness and ductility for the ultimate limit state. They recommended that the design should take into account the toughness based on the energy absorbed before the maximum load.

2.5.4 Analysis and Design

Analysis of experimental results obtained from tests on forty-five concrete specimens reinforced with fiber reinforced plastic rebars is outlined by Faza and Gangarao [1993]. Theoretical correlation with experimental results is made in terms of elastic and ultimate bending moment, crack width, bond and development length. Equations for design loads and bending resistance, bond and development lengths and crack widths are developed in a simplified form for practical design applications. Similarities and parallels of the proposed design equations with current ACI 318-89 standards are maintained whenever possible. The shear capacity of RC and PC members has not been clearly established.

2.6 ACTIVE DEFORMATION CONTROL OF STRUCTURES

Actively controlled structures are the structures which are integrated with sensors, decision making system and actuators. Sensors which sense either the excitation or response of the structure could be of any type from a simple strain gage to a complex fiber optic sensor. The decision making system is basically an algorithm which decides, based on the "sensed" response, whether or not to apply any control force on the structure. The actuators are also designed in many forms from a hydraulic jack to a shape memory alloy. Considerable research has already been carried out on active control of structures and its application in disciplines such as aerospace engineering, etc. For civil engineering structures, active control is a new concept which is recently drawing attention of the researchers. This section briefly summarizes the research on active control of civil engineering structures till date.

2.6.1 Fiber Optic Sensors for Civil Engineering Applications

"The sensor technology, for monitoring of structures, is only in the beginning of its development. The application of composite materials facilitates a bigger range of applications of sensor technology" [Miesseler, 1992]. Glass fiber composite cables integrated with Optical Fiber (OF) and Copper Wire sensors were used as post-tensioning tendons in Schiessbergstrasse bridge. The bridge was also instrumented with chemical (the so-called corrosion cells) and crack monitoring OF sensors on top and bottom of the bridge deck. The measured values were processed with a specially developed software. " This permanent observation allows at any time to recognize changes in structures and start an early stage countermeasures".

Smart structures and materials will require development of methods for measuring rapidly changing strains simultaneously at many points throughout a structure [Handerek et al., 1992]. The sensors themselves should be simple to construct and the complexity of the signal processing arrangements must be minimized. Optical fiber technology provides a basis for gathering data from many points with negligible cross talk of interference and potentially a very wide bandwidth. While fully-distributed systems potentially offer very attractive features, it may be more cost 2-12

effective in some practical applications to adopt a compromise in the form of quasi-distributed or multiplexed sensing strategies. These schemes employ fixed, pre-positioned, discrete optical sensors sharing a common fiber link.

Sirkis et al., [1992] presented forward and inverse phase-strain-temperature relations, difference between fiber and structure measureands, and the uniqueness and stability of inferred structural data is emphasized. The scalar signal produced by an embedded optical fiber sensor has contributions from a minimum of four quantities (three principal stresses and temperature). Interferometric fiber optic sensors, therefore, do not measure "strain" or "temperature", rather the optical phase shifts from which the strain and temperature states are inferred, which correspond to the location of the optical fiber (actually core) not in the host. Therefore, the relation between the strain and temperature state in the core of the optical fiber and the host should be established. Since the optical fiber is an elastic inclusion, the local strain state in the host is inevitably altered by the presence of the optical fiber. The interferometric sensors (including Bragg grating sensors) are the most prominent sensors in the smart structures arena. It was argued that calibration approaches for determining the individual components of the characteristic matrix of the inverse phase-straintemperature relation is generally unsuitable for structurally embedded optical fiber sensors. Instead, the optical properties in the forward relation should be determined as a function of temperature and wavelength and the forward relation should then be inverted, thus requiring more extensive knowledge of intrinsic optical properties.

A dual Fabry-Perot fiber optic strain sensor system was developed for fast and accurate measurements of strains in a "Smarttmss" [Mason et al., 1992]. SM800 optical fiber with a *phase - strain sensitivity* S= 1.02 deg. $\mu\varepsilon^{-1}$ mm^{-1} at 819 mm. was used to make the Fabry-Perot strain sensor. These optical fiber strain gages have a strain measurement performance comparable to electrical strain gages; phase demodulation of the optical signal is required due to the sinusoidal nature of the low finesse Fabry-Perot fiber optic strain sensor *response function.* The response function is given by:

$$R(t) = \frac{\left[1 + V\cos\left\{\Phi + \Delta\Phi(t)\right\}\right]}{2} \qquad \text{.....(2.2)}$$

where

R(t) = normalized signal,

V = the visibility factor, and

$\Delta\Phi(t)$ = the strain induced phase change.

The multivalued nature of this response function also makes the new sensors vulnerable to interrupt ambiguity (i.e., if the phase-demodulation electronics are interrupted, the new value of the phase becomes non-unique and must be reinitialized). A pseudo-heterodyne phase demodulation system was developed for the Fabry-Perot sensors. This system sinusoidally modulates the wavelength of the laser diode and then samples the backreflected intensity, and thereby the interferometer phase, for three different wavelengths, each corresponding to a $\pi/2$ phase shift for the interferometer. These three phases are used to uniquely determine the phase of the interferometer within one fringe. This system is able to track strain changes on the order of $10^6\mu\varepsilon$ / sec with 1 cm gage length with a drift error of less than $10\mu\varepsilon$ / hour and has a resolution of $10\mu\varepsilon$ with 9mm gage length.

The advantages of optical fiber techniques for applications in civil engineering structures include [Kruschwitz et al, 1992] the immunity of most optical fiber sensor system designs to instrumentation ground loops, the general robustness of optical fiber and cable materials under harsh environmental conditions, and general geometry of fiber sensor systems which allow multiple sensor locations to be placed along a single liner fiber bus of extended length. Extrinsic Fizeau Fiber Interferometric (EFFI) sensors were used to measure strain and temperature over short gage lengths and were spatially multiplexed along a linear sensor data bus. The output signal intensity at the optical detector is proportional to a sinusoidal function difference in phase between the fields reflected at the two fiber end faces. Since the material within the cavity is air, this phase difference is proportional to the relative separation between the two end faces. The EFFI sensors were embedded in concrete specimens and attached to bottom of an existing bridge to measure strain and temperature within a marginal error of 5%.

Experimental studies are presented for members under pure compression and three point bending tests for five years using Fiber Optic Interferometric Sensors (FOIS) [Escobar et al., 1992].

Effect of aging was emphasized to confirm the feasibility of using FOIS for long term monitoring of strains in concrete specimens.

The advantages and feasibility of using Fiber Optic Polorimetric and Interferometric sensors for strain / stress measurement in concrete cylindrical specimens were investigated [A. Nanni et al., 1991]. It was shown that the fiber optic sensors offer the desirable sensitivity, versatility, economy, and durability over the life span of the structure. Besides, the experimental setup for measuring stress- strain relation was established between the half-length to the core radius of the fiber optic sensors. Also, relationships between strain in core and core of the sensor were established taking into account the modular ratio of the core glass and polymer coating materials of the sensors.

. Theoretical concepts together with the technicalities. involved in the applications and durability of the optical fiber sensors embedded in concrete structures are discussed [Mendez et al., 1989]. It is stated that the optical fiber sensor technology offers the possibility of nondestructive, in-situ measurement of strain, stress and deformation of reinforced concrete structures. Also, techniques were proposed for safe embedment of the optical fiber sensors in concrete structures. An analysis is presented on the use of embedded optical fiber sensors in concrete elements and structures for measurement of stress and strain as well as the assessment of structural integrity [Mendez et al., 1992]. The fundamental materials and micro-mechanical aspects of fiber-matrix interaction is discussed in conjunction with mechanical and chemical durability of the glass fibers, interfacial bonding, fiber orientation and coating characteristics.

2.6.2 Active Structural Control

The early concept of actively controlled structure was proposed by Zuk [19681 and some other researchers by the end of 1960s. A rigorous control-theory based concept of structural control was laid down by Yao [1972]. Later on, considerable research efforts have been concentrated in this area [Leipholz 1985, Chong and Liu 1990, Soong 1989]. The idea of active control itself is not only attractive, but potentially revolutionary. One can envisage future structures having two types

of load resisting members. The traditional passive members that are designed to support basic design loads and active members whose function is to augment the structure's capability in resisting extraordinary loads.

The feasibility of applying the optimal control theory to control the vibration of civil engineering structures under stochastic dynamic loading, such as earthquakes and wind loads has been studied [Yang 1975]. When the performance index is the weighted sum of covariance of both the responses and control forces, the optimal control is a linear feedback closed-loop control. The random loading is assumed to be either a stationary or non-stationary Gaussian white noise with zero mean. The optimal control forces are obtained by solving a matrix Ricatti equation. The same optimal control also holds when the excitation is a shock of short duration. Moreover, the feasibility of implementing the optimal control by means of active dampers and servomechanisms is considered.

An instantaneous optimal control is proposed for earthquake-excited structures [Yang 1987] and nonlinear structures [Yang 1988]. The optimal forces are determined analytically by minimizing a time-dependent quadratic performance index. The nonlinear equations of motion are solved using the Wilson-9 numerical procedure. These optimal algorithms are computationally efficient and suitable for on-line implementation of active control systems to realistic nonlinear structures. The combined use of passive / active control systems can be very beneficial. A refined version of the instantaneous optimal control algorithms is presented [Yang 1992] for nonlinear or hysteretic structure system. The main advantage of the proposed algorithm is that the control vector is determined directly from tracking a time dependent system matrix.

Martin and Soong used model control algorithm to deal with multistory structure control problem [1976]. The concept of model control is to affect direct changes of specific dynamic modes and stiffness of the system. Computationally the procedure is straightforward and involves the solution of only linear equations and the calculation of appropriate eigen values and eigen vectors.

A full-scale implementation of active control for tall buildings was carved out [Soong 1991 and Reinhorn 1991]. Similar in concept to the modal control method, a pole assignment method was presented [Abdel-Rohman 1978] for active control algorithm. The pole assignment method proved to be straightforward and provided a design complying with the required performance of the system compared to modal control method. Pole assignment method has the flexibility to change any number of modes and in any desired form. In the same paper, a complete description of a control system for a simple span bridge was given.

Vibration of the bridge decays very fast and the force response can be reduced as desired by introducing active stiffness and damping to the structure. Lee [1987] proposed a bounded state control for linear structure. Lyapunov function concepts are used. This approach follows the pole assignment concept to achieve bounded state control.

A pulse control method was proposed [Masri and Miller et al. 1981, 1982, 1987, 1988] for linear and nonlinear flexible structures. The major difficulties encountered in the application of modern control techniques to building structure systems are the following:

i) Active control requires the ability to generate and apply large controlled forces to the structure. ii) Modern control theory often leads to feedback control laws, thus requiring on-line measurement (or estimation) of all the system state variables.

iii) On-line control requires that both measurement and control be performed in real time.

The pulse control algorithm is designed to overcome the limitations of the existing controller. It destroys the gradual rhythmic build-up of the structural response in the case of resonance by means of short-interval high energy pulses. A continuous monitoring of the system state variables is required. To conserve energy, an open-loop control is activated only when some prespecified threshold has been exceeded. These pulse control procedures are relatively simple to implement. They require less on-line computational efforts compared with other modern control techniques. They also have advantages of possible savings of control energy required. In using active pulse control, the following variables should be determined from the control algorithm:

i) the time at which pulse should be applied,

ii) the magnitude of each pulse, and

iii) the shape and duration of pulse.

Generally, the pulse shape and duration are given because of limitation of control devices. Pulses usually are triggered when the response reaches certain levels. Controller's activation time is determined by the degree of system oscillation near each controller. Pulse magnitude is chosen to be proportional to some power of the response velocity, whereas the proportional constant is selected empirically. The stability condition for the response of the controlled nonlinear system was examined by the direct method of Lyapunov.

A US panel on structural control research has been formed under the auspices of United States National Science Foundation [Housner et al., 1992]. The panel is charged with the responsibilities of (i) facilitating the transmission of information concerning state-of-the-art developments in the field, (ii) identifying and prioritizing needed research and development, (iii) developing preliminary plans for analytical and experimental advancement in the field and (iv) developing plans for performance of full-scale testing and demonstration. Advantages of active systems over passive systems are emphasized together with the conceptual discussions on various control systems and their experimental as well as full scale implementations.

Complete design methodology including modeling, optimal control action and actuator placement was presented [Austin et al., 1992]. Active elements in both differential equation and state-space forms were utilized to model active civil structures. The optimization techniques were extended to give a means of making a quantitative relative assessment between .positions for the active element.

Control design for structures with spatially distributed discrete sensor arrangements was addressed [Reza Katebi, 1992]. An **increase in the damping of the structure is achieved by the optimal controllers. An ideal Euler-Bemouli beam was modeled with the technique and it was**

found that considerable damping can be achieved for a large band width by repeatedly adding sensors to the system.

Several continuous-time approaches have been proposed in recent years to formulate active control algorithms to reduce the response of civil engineering structures under dynamic excitations [Jose Rodellar, 1987]. A general formulation of a new discrete-time control methodology was presented and applied to structural control. A closed loop digital control scheme was considered to solve an n degrees-of-freedom model structure subjected to a dynamic load. Using the formulation, a building structure was modeled as a lumped mass system and analyzed for seismic excitations. The uncontrolled displacement response was compared to that corresponding to optimal and predictive control and advantages of predictive control over optimal control were discussed.

Active control of dynamic response of structures is emerging as a possible design alternative for reducing the vibrations of highly flexible structures [Dhillon et al., 1992]. The practical use of structural control is hindered by various design complications of which time delay of an active control loop execution is one.

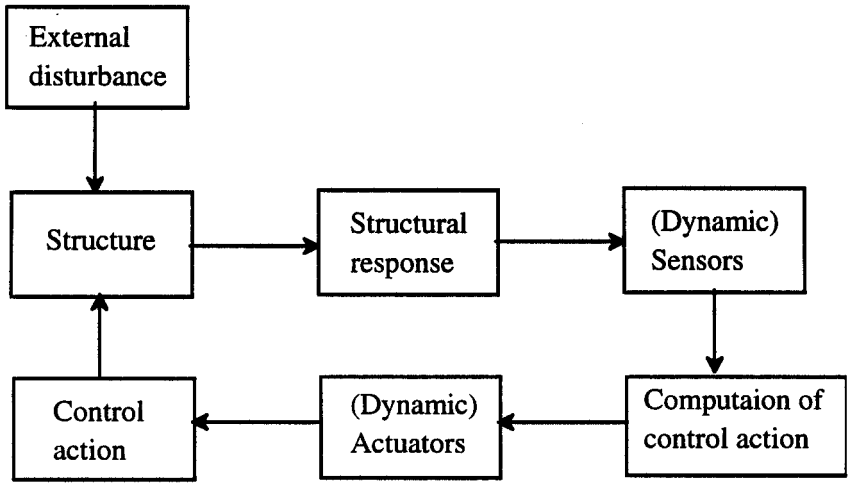

Fig. 2.2 Active control algorithm

Time delay is associated with the stages of active control algorithm (Fig. 2.2). Time delay can only be reduced, not eliminated altogether. A general expression was obtained that allows the designer to , take into account the effect of time delay by modifying the feedback gain. From the results of dynamic response analysis of a closed loop system, it was concluded that the presence of time delay not only degrades the closed-loop system, but also can render it unstable.

CHAPTER 3

ENVIRONMENTAL STUDIES ON NAKED ARAMID FRP CABLES 3.1 INTRODUCTION

Reinforcing or prestressing of concrete is usually carried out by using steel elements. However for some applications, e.g. concrete structures in highly aggressive environment, a combination of concrete with alternative reinforcement materials will prove advantageous. In these alternatives, epoxy coated, galvanized or stainless steel bars or non-metallic fibers such as asbestos, glass, polypropylene, aramid, carbon, etc. can be advantageously utilized. The following discussions would focus mainly on continuous fibers. A range of-, developments in bars and tendons consisting of continuous high strength fibers usually embedded in a polymeric matrix is aimed at structural applications in concrete. At present this concerns glass,. aramid and carbon fibers impregnated in epoxy resin matrix. The strength capacities of these fibers are in the range of prestressing steels. Several other material characteristics differ considerably from those of the well known steels such as creep, relaxation, stress-strain relationship, behavior in alkaline environments etc.

Satisfactory application of these fibers as reinforcement can only be achieved, if the following basic requirements are considered:

- **adequate physical and mechanical properties,**
- **durability, and**
- **structural interaction with concrete.**

Aramid is an organic man-made fiber with a high degree of crystallinity. The molecular chains are aligned and made rigid by means of aromatic rings linked by hydrogen bridges. Very

high strength exhibited by these fibers is due to this type of molecular combination. There are three main producers of high performance aromatic polyamide fibers world-wide.

- Dupont in the U.S. (Kevlar-Aramid)
- Aramide Maatschappij v.o.f. in the Netherlands (Twaron-Aamid)
- Teijin in Japan (Technora-Aramid)

Normal, intermediate and high modulus are the three types of currently manufactured Twaron-aramid fibers. The discussions that follow hereafter, emphasize mainly on ARAPREE an aramid/epoxy tendon jointly developed by AKZO and HBG, based on Twaron HM. ARAPREE consists of Twaron filaments impregnated in epoxy resin.

Requirements for the reinforcement materials in prestressed concrete structures include high tenacity, low mechanical relaxation, proper toughness, high fatigue resistance and low weight in addition to high corrosion resistance. Among these, high tenacity and corrosion resistance, and low relaxation are most important. Materials confirming to these requirements include carbon, aramid and glass fibers, the physical properties of which are listed in Table 3.1.

Table 3.1 Physical properties of composite fibers

	Carbon(pan)	Aramid	E-glass	
	High tenacity	Kevlar	Technora	
Tensile strength (GPa)	4.2	2.8	3.5	2.2
Tensile modulus (GPa)	240	130	74	70
Elongation (%)	1.7	2.4	4.6	4.0
Density (g/cm3)	1.80	1.45	1.39	2.54
Diameter (pan)	7-8	12	12	12
Thermal decomposition temperature (°C)	3,000	600	500	800

Table 3.2 summarizes the currently available types of ARAPREE. Short term properties of aramid composite available in literature are shown in Table 3.3. It should be noted that "the strength and. stiffness are related to the net fiber cross section and not to the gross composite cross section. The former formulation gives a more accurate value, since this excludes the influence of varying fiber content (due to shape)" [Gerritse 1991].

Table 3.2 Currently available types of ARAPREE

Type	Shape of the cross section	Dimensions (mm)	Fiber cross section (mm `)	Characteristic force
f 100 000	rectangular	20 x 1.5	11.1	30 kN
f 200 000	rectangular	20 x 3.0	22.2	60 kN
f 400 000	rectangular	20 x 6.0	44.4.	120 kN
f 100 000	circular	dia 5.7	11.1	30 kN
f 200 000	circular	dia 7.9	22.2	60 kN

Table 3.3 Short term properties of aramid composite

Property	Average values
Axial tensile strength (N/mm^2)*	3000*
Modulus of elasticity(kN/mm^2)*	125-130
Failure strain (%)	2.3
Transverse compressive strength (N/mm^2)	ca. 150
Interlaminar shear strength (N/mm^2)	ca. 45
Poisson's ratio	0.38

* values related to the effective fiber cross section
** characteristic value: 2800 N/mm2

3.2 EXPERIMENTAL SETUP FOR DURABILITY STUDIES

Durability of **ARAPREE** tendons was assessed in simulated pore water alkalinity and marine environments. Accelerated testing methods were used to conduct these tests at an elevated range of temperatures. Totally, four sets of eight ARAPREE specimens each were used in the study. Two sets, each of tensioned and untensioned specimens, were exposed to alkali solution and sea water at elevated temperatures. Durability of the tendons was assessed based on strength retention after a specified period of continuous exposure and scanning electron microscope (SEM) analysis.

3.2.1 Experimental Setup for Untensioned Specimens

The ARAPREE tendons used in the present environmental studies is of rectangular type f 100,000. The test specimens were cut to specified length (30 in.), out of which a particular length (12 in.) was exposed to the environmentally hazardous conditions simulated by strong alkali solution and sea water. The test specimens were exposed with the help of a tank made of 1/2 in. thick polycarbonate material. The polycarbonate tank contains eight specimens exposed to sea water or alkali. Fig. 3.1 shows the arrangement of the test specimens in the polycarbonate tank. Fig. 3.2 shows ARAPREE specimens, heater and thermostat arranged in polycarbonate tank prior to the exposure tests. Alkali solution and sea water were heated to temperatures (40°C - 45°C) for accelerated degradation of the tendons. A circulation pump was used to ensure homogeneous temperature conditions throughout the tank. The arrangement was made in such a way so as to optimize space and also ensure uniform heating of all the tendons. A detailed description of the setup is as follows:

The following two test cases were considered:

a) Test specimens in strong alkali solution of pH 13,
b) Test specimens in sea water.

Fig. 3.1 ARAPREE specimens arranged in polycarbonate tank

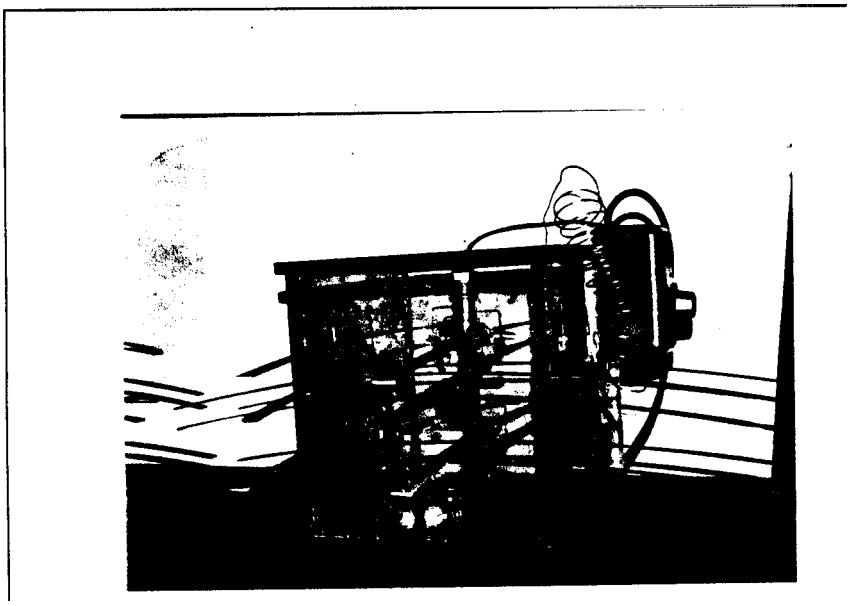

Fig. 3.2 Experimental, setup for exposure of ARAPREE specimens

Tank

Material of the tank	Polycarbonate(1/2 in. thick)
Volume of the tank	2250 CC.
Total quantity of the solution	5.93 gallons.
Approximate weight of solution	49.47 Lb.

Heater and thermostat

Manufacturer	Omega technologies Co.
Heater type	Screw plug immersion heater
Heater capacity	700 watts (RINO 130/120)
Range of thermostat	60-250 deg F
Accuracy of thermostat	± 4 deg F

Pump

Capacity of the pump	85 gal/hr

The alkali solution was formed by pre-measured mix of the following chemicals:

- Sodium hydroxide 40 gm / liter
- Calcium hydroxide 1 gm / liter

The solution needs to be stirred and circulated constantly to avoid sedimentation. This is achieved by circulating the solution continuously using the pump, which, in turn, also keeps the temperature of the solution homogeneous throughout the tank. The temperature of the alkali and sea water was maintained at an average temperature of 43-45 ˚C.

The polycarbonate plates constituting the tank were glued with PVC cement and the sides were sealed with liquid electrical tape (dielectric solution), which inhibits seepage of water. It was observed that this dielectric solution was not damaged and there was no sign of deterioration, in addition to being flexible enabling easy removal of tendons for testing. The tendons were inserted

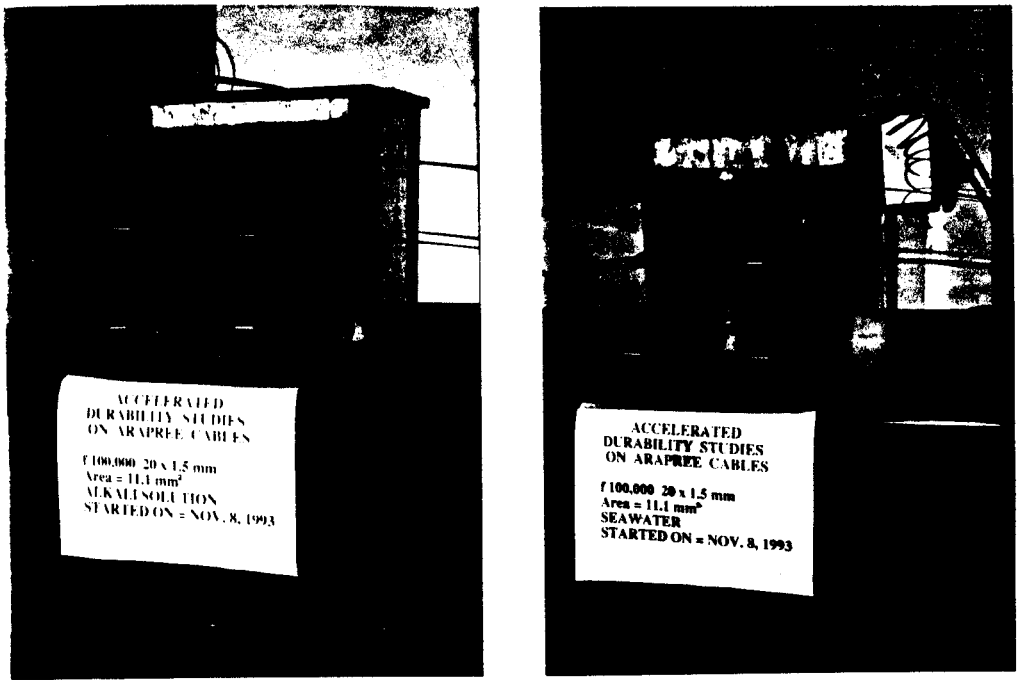

Fig. 3.3 ARAPREE tendons being exposed to sea water and alkali solution

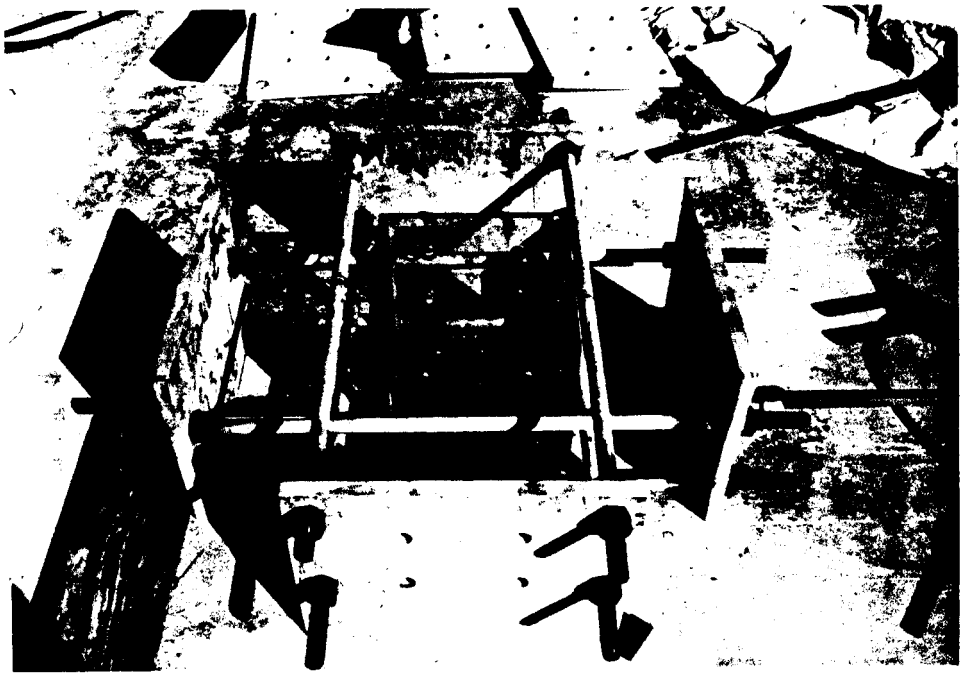

Fig. 3.4 Polycarbonate tank positioned between the tensioning frame

into the 1 in. diameter holes and the holes were first sealed by end plates using epoxy. Later on dielectric solution was applied (3 coats) on both sides. Filler material in the form of flexible adhesive was added. This was sealed once again with the dielectric solution. The total curing time for the dielectric solution and the filler adhesive was between 96 - 144 hrs.

Heater and thermostat were suspended from the top cover at the center of the tank. The pump was placed at the bottom of the tank with feeder pipe directing water towards the heater and the upward movement of water from the base of the tank ensured uniform temperature by way of moving colder water towards the heater to ensure homogeneity. Fig. 3.3 shows the untensioned ARAPREE tendons being exposed to alkali solution and sea water.

3.2.2 Experimental Setup of Tensioned Specimens

The ARAPREE tendons were tensioned to a force of about 30001bs. before being exposed to sea water or alkali solution. The polycarbonate tank setup similar to that for untensioned specimens is placed within a self straining frame. Fig. 3.4 shows the polycarbonate tank positioned within the self straining frame, before ARAPREE specimens were inserted.

3.2.2.1 Pretensioning of ARAPREE specimens

The ARAPREE tendon specimens were passed through the holes in the tank and the corresponding ones on the frame. A chair is held against the frame (at jacking end) so that the hole on the chair matches the hole on the frame through which ARAPREE specimen is inserted. A hollow core hydraulic jack is then placed against the chair, so that core axis of the jack coincides with the centers of the holes on the frame as well as the tank. The tendon is anchored at the dead as well as the jacking ends. Fig. 3.5 shows the jacking end, where the tendon is anchored in front of the hydraulic jack before tensioning the tendon. Force is then applied in the tendon by the jack while carefully adjusting the positions of the anchorages at dead and jacking ends so that the cable is not twisted nor bearing against walls of the frame or tank. Since the tendons used for the

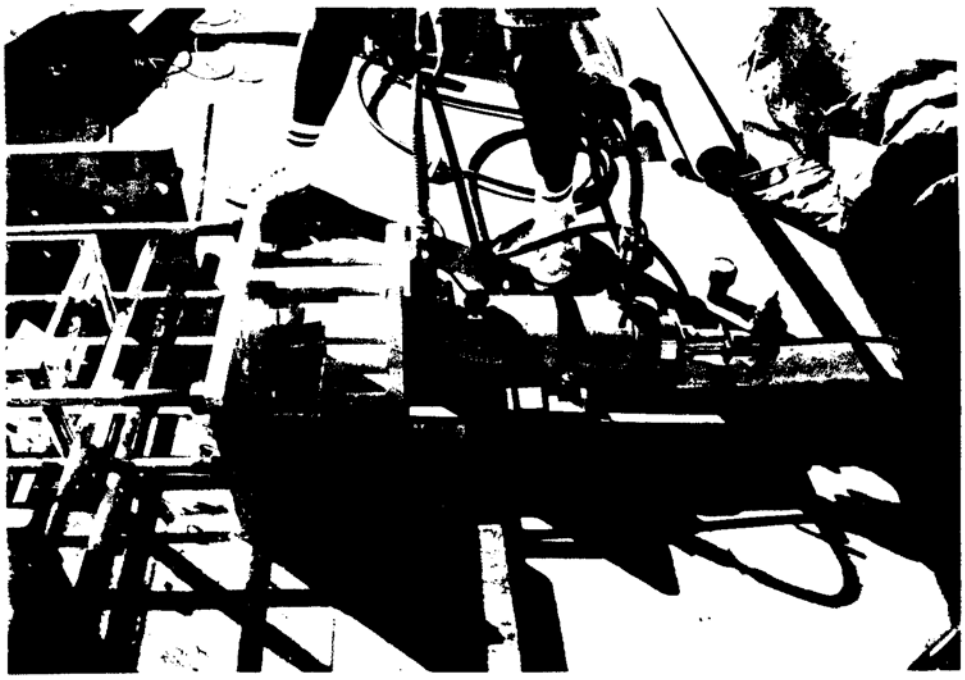

Fig. 3.5 Tendon anchored in front of the hydraulic jack before tensioning

Fig. 3.6 Tensioning of ARAPREE specimens in progress

durability study are rectangular shaped, and with a very small thickness. of 1.5 mm, due care should be taken to keep the tendon in perfectly horizontal or perfectly vertical position while being tensioned. Fig. 3.6 shows the tensioning operation in progress.

After the required jacking force is reached, the sleeve which is placed between chair and the frame, is wedged with two spacers between the frame and sleeve of the anchorage.. The polyamide wedges are properly arranged and then gently tapped into the sleeve as shown in Fig. 3.7. The two spacers which are placed between the anchorage and frame will be used to release the tension in the specimen after specified period of exposure. The jacking force is then released slowly letting the anchorage in front of the frame to set and the anchorage that is placed in front of the jack is removed by cutting the tendon as shown in Fig. 3.8. Fig. 3.9 shows an anchorage at jacking end after set in place. The jack is then shifted to the next tendon location so as to have symmetry in forces acting on the frame and the procedure described above is repeated.

Fig. 3.10 shows the jack arranged for pretensioning of a tendon at a higher elevation. Fig. 3.11 shows the self straining frame with all the eight cables pretensioned and ready for the exposure. The holes in the tank were sealed as in the case with untensioned specimens and cables within the tank were exposed to sea water. Similar frame is setup and cables pretensioned and exposed to alkali solution.

3.3 ULTIMATE TENSILE STRENGTH TESTS

3.3.1 Preliminary Tensile Testing of Pilot Specimens

Pilot ARAPREE specimens were tested to determine the ultimate tensile strength of the cables. This strength compared to those of the specimens exposed to sea water or alkali for a specified amount of time, would be indicative of the degradation of the tendon due to exposure. Tensile testing of ARAPREE was carried out on a Tinius Olsen universal testing machine. Fig 3.12 shows the testing machine with a ARAPREE specimen while tension testing is being carried out.

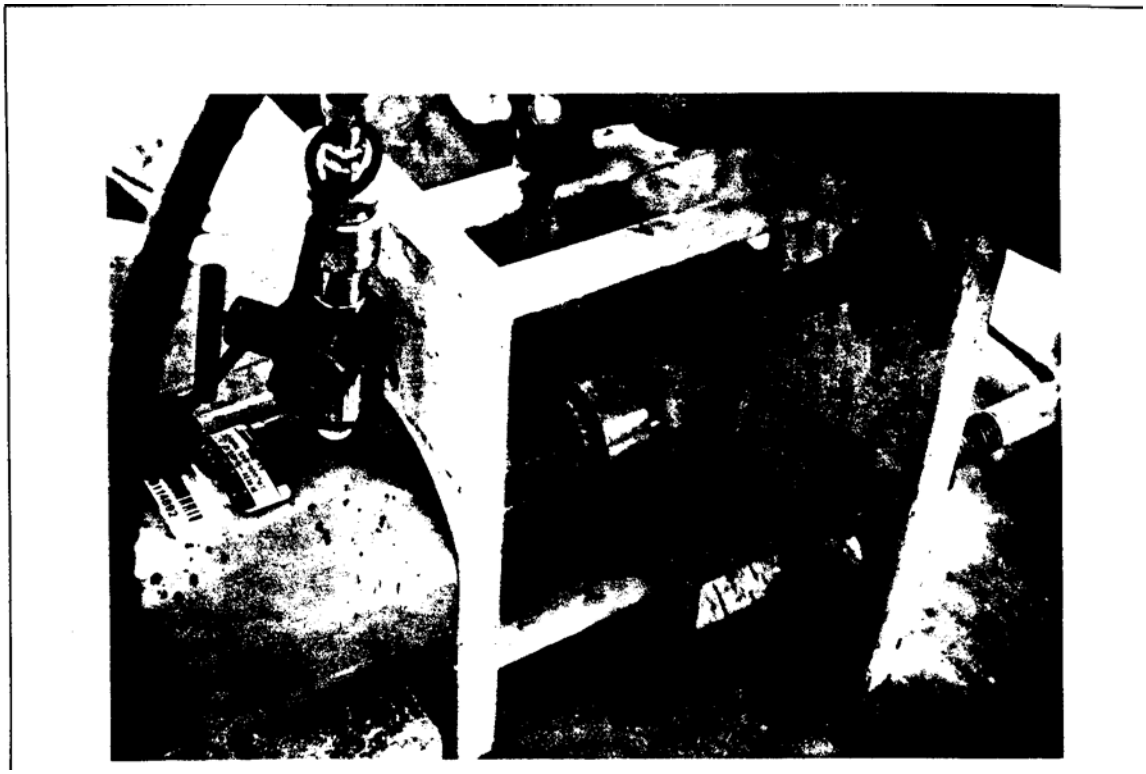

Fig. 3.7 Anchoring of polyamide wedges

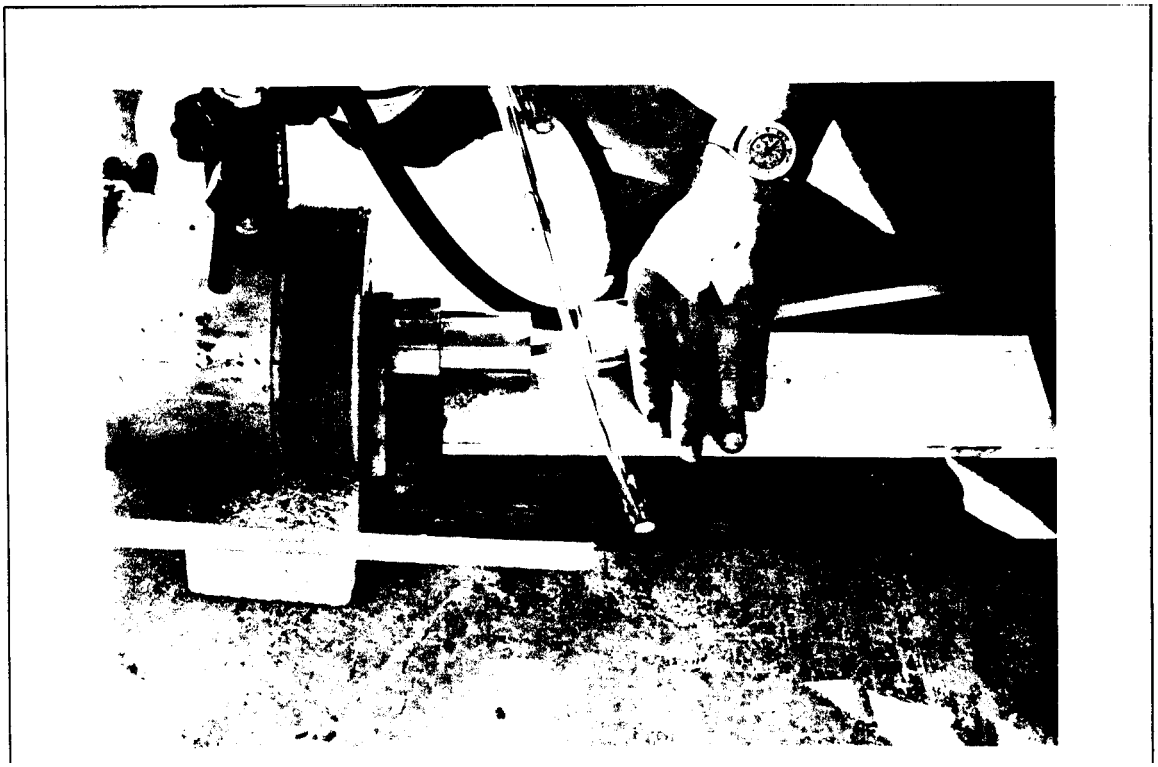

Fig. 3.8 Release of jacking anchorage by cutting the ARAPREE tendon

Fig. 3.9 Typical ARAPREE tendon anchored against the self straining frame

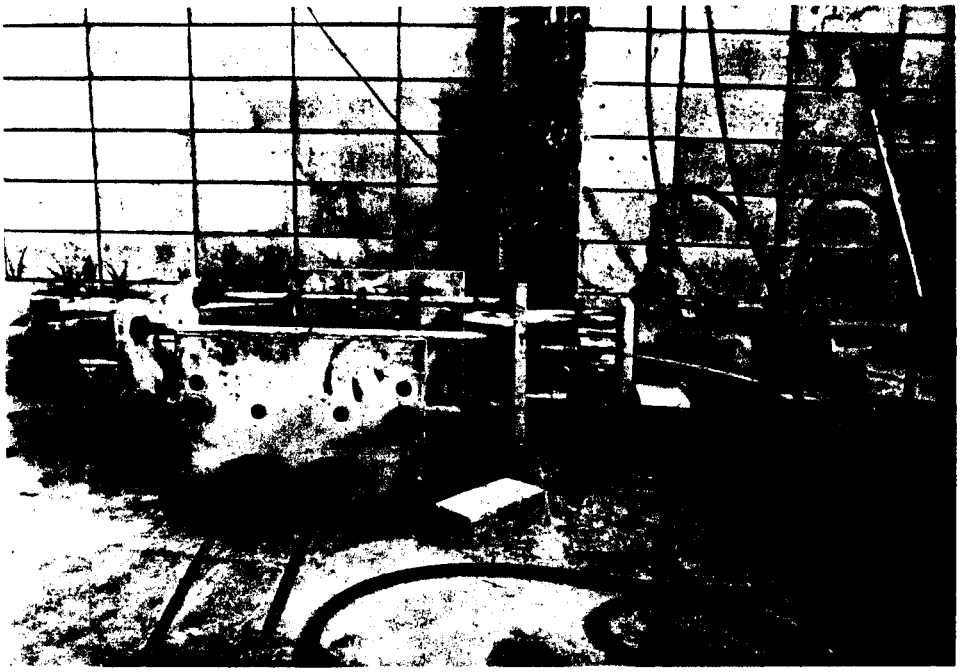

Fig. 3.10 Tensioning of ARAPREE specimen at a higher level

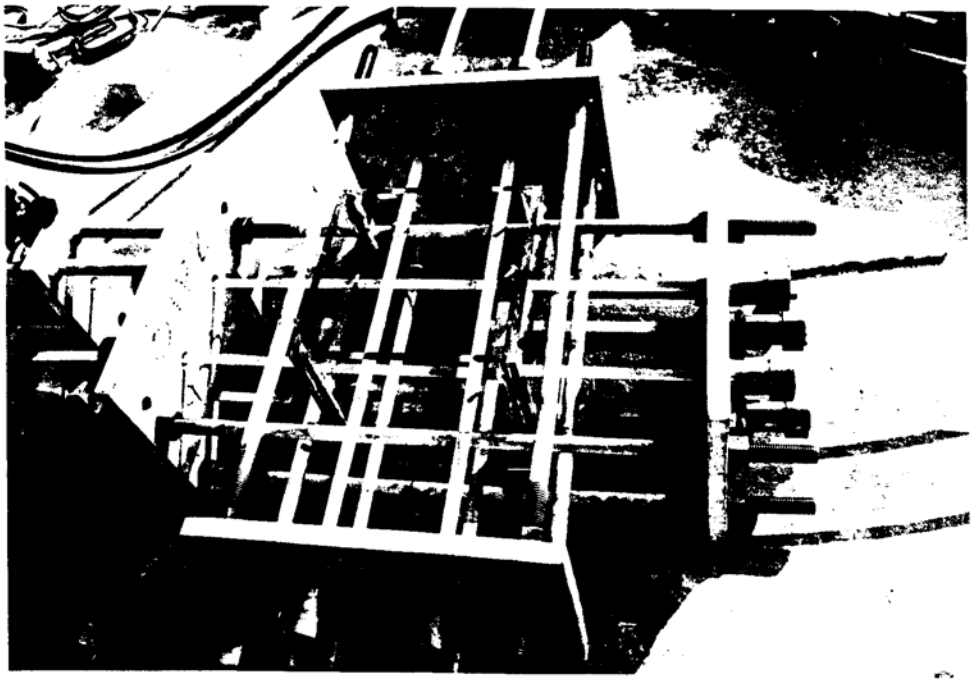

Fig. 3.11 Self straining frame with all eight tensioned specimens ready for exposure

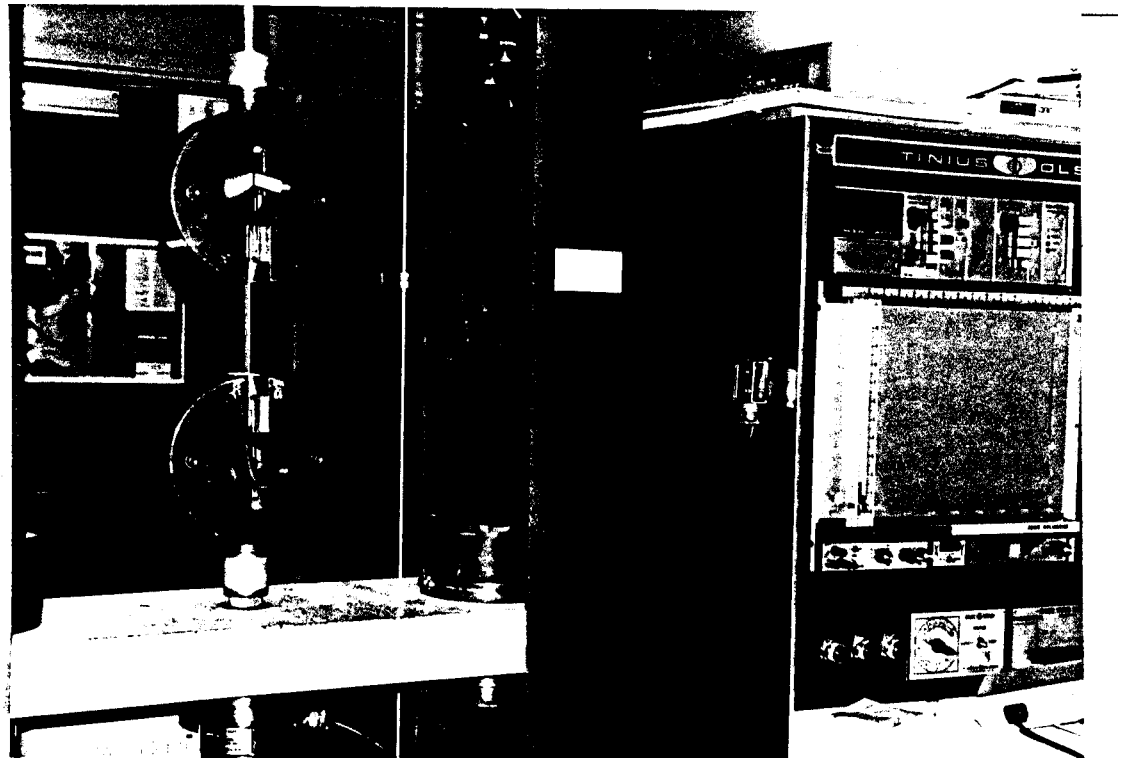

Fig. 3.12 Tensile testing of a typical ARAPREE specimen

The ASTM tension test specimen lay-ups and dimensions are given in Table 3.4. However, as the width of the ARAPREE composite is 20 mm, it could not be split to the width as specified by ASTM standards. Hence the width of 20 mm was considered for testing purposes.

Table 3.4 ASTM specifications for composite tensile test specimens

Fiber orientation	Width, mm	Number of plies	Length, mm
0 deg	12.7	6-8	229
90 deg	25.4	8-16	229
(± 45 deg)	25.4	8	229

3.3.2 Preparation of The Test Specimen

The surface of the composite is textured and hence surface treatment was necessary for testing purposes. The preparation of the test specimen includes sticking of tabs at both ends of the specimen for gripping purposes and installation of strain gage / strain rosette as described below:

i) The specimen was cut to desired length and sufficient care was taken to ensure that the longitudinal strands do not get separated in the specimen. The ends were smoothened out with the aid of a grinder.

ii) The initial rough texture of ARAPREE, where the end tabs are attached had to be smoothened, as it would prevent proper bonding of the glass / epoxy end tabs to the specimen.

iii) The surface was sanded in ± 45 degree motions with a coarse 320 grit paper. Final smoothening was carried out with 600 grade paper. The surfaces so sanded were cleaned under running water to remove any residual fibers or impurities.

iv) Degreaser was then sprayed on the surface to dissolve any greasy residuals and then, the surface swiped with cotton buds dipped in less concentrated acid solution followed by cleaning the surface with a neutralizer.

The surface of the specimens thus prepared is now ready for attaching the end tabs. Glass/epoxy material procured from NVF company was used for the end tabs, where the specimen is to be gripped by the serrated spring operated clamps on the tensile testing machine. The product used to prepare end tabs has following specifications:

Product number	EG-873
Sheet size	8 1/2 in. x 11 in.
Thickness	1/8 in. (3.2mm)
Material	Glass Epoxy

These end tabs were cut to a size of (length x width) 70mm x 20mm to suit the ends of the composite specimen. The sides were ground to ensure squared edges. A radius in addition to a slope of 60 degrees was provided to avoid stress concentration during testing (Fig. 3.13). Sufficient care has to be taken to avoid the glass fibers from getting burnt due to excessive heat during the grinding process which might lead to improper adhesion of the tab on to the composite specimen. Surface treatment was carried out on the end tabs, which was similar to that for on the Aramid composite specimen.

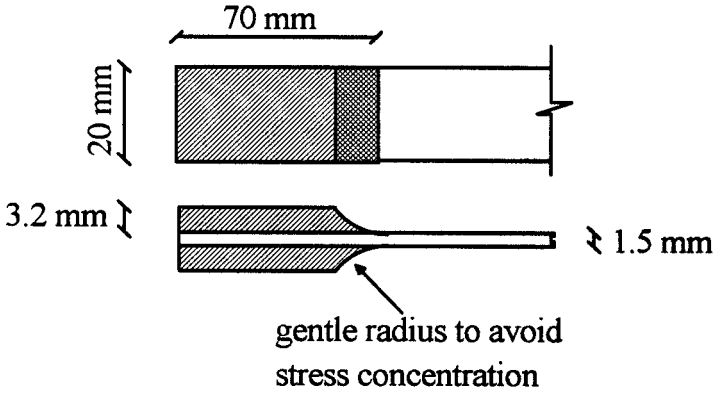

Fig. 3.13 End tab details

The epoxy, Hysol 9309 NA was used as adhesive to bond the end tabs to the specimen. Pre-measured quantities of the resin and hardener are mixed at a room temperature of 77 T. This adhesive was initially preferred because of its high shear and peel strength in addition to its environmental resistance.

TEST #1

Strain gages were not installed as this test was intended to determine only the ultimate load. The specimen details are as follows:

Specimen #1

Cross-sectional area = 11.1 mm^2.
Length = 9 in.

Observations

Upon loading, high pitched noises could be heard from the specimen at frequent load intervals., This could be due to the failure of the individual fibers/matrix. Loading was done at a uniform rate and the ultimate rupture occurred at 54701b. The failure was not consistent with the normal ultimate rupture behavior of a 0° composite specimen, where the fiber rupture takes place at the middle perpendicular to the longitudinal axis. In this test, the failure was dominated by the lap shear failure of the glass epoxy end tabs.

TEST #2

Two specimens of different lengths were tested to determine the failure load and understand the failure mode. Strain gages were affixed on to the specimen to observe the stress-strain behavior.

Specimen #1 Length = 9 in.

Specimen #2 Length = 16 in.

Observations

Specimen #1

The first fiber failure was recorded at 4000 lb. and then the strain gage ruptured at a measured load of 4750 lb. The ultimate load was recorded at 50001b. Fig. 3.14 shows the tensile test in progress for specimen # 1. The glass / epoxy end tabs failed due to interfacial slip, thus damaging the specimen at one of the ends.

Specimen #2

The first fiber failure was recorded at 24001b. and second major fiber rupture was observed at 3500 lb, when the strain gage stopped functioning. The ultimate failure was once again dominated by the end tab failure phenomena at a load of 51901b.

Test #3

In view of the lap shear failure of the end tabs, the ultimate load of the composite specimen was never reached. Thus the adhesion characteristics of the end tab to the specimen had to be improved. Hence, specimen #1 was bonded using the freshly acquired pre-measured sample of EA 9309 and specimen #2 using AE 10, the adhesive used to bond strain gages.

	Length	Bond type	Manufacturer
Specimen #1	16 in.	EA 9309	Hysol
Specimen #2	16 in.	AE 10	Measurements Group

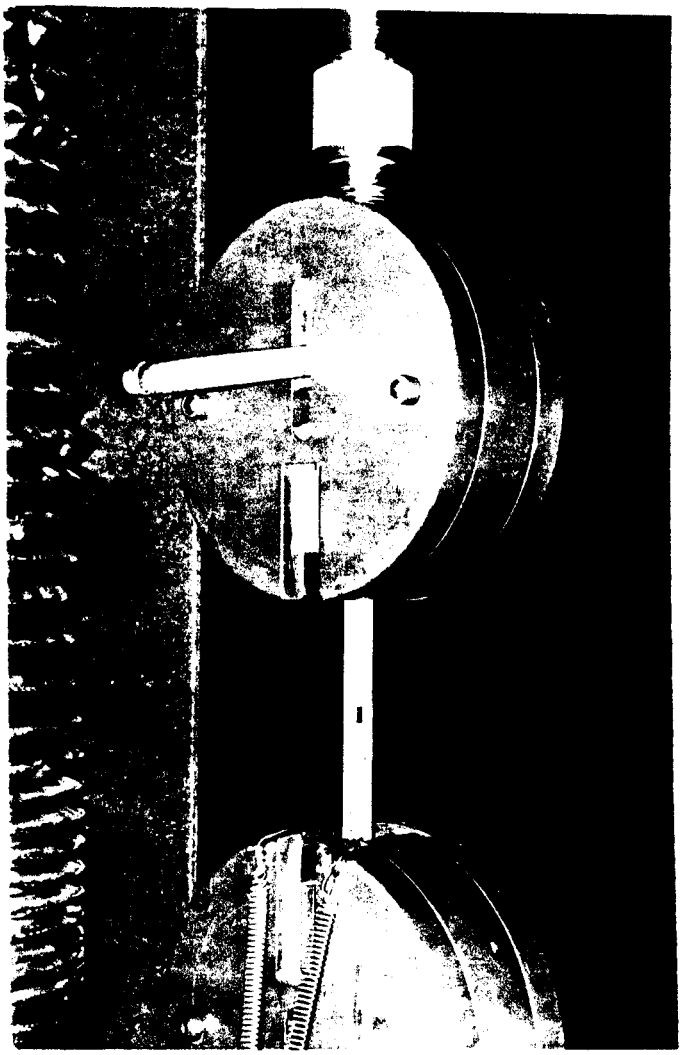

Fig. 3.14 Tensile test of ARAPREE specimen in progress

Observations

Specimen #62

First fiber rupture		17001b.
Subsequent fiber rupture		22001b.
Subsequent fiber rupture		2450 lb.
Subsequent fiber rupture		3350 lb.
Subsequent fiber rupture		36001b.
Ultimate failure	5250 lb.	(The failure of end tabs dictated the ultimate failure)

Specimen #2

First fiber rupture	380 lb.
Subsequent fiber rupture	6201b.
Subsequent fiber rupture	1060 lb.
Ultimate failure	61801b. (The failure of end tabs dictated the ultimate failure)

The ultimate failure limit was much higher than that of the earlier test specimens. The fact that the end tabs withstood higher levels of shear loading, justified the use of AE 10 as a suitable bonding agent for the end tabs. Some modifications were considered necessary to bring about a normal failure mode.

Test #4

In view of the end tab shear failure, the area of adhesion of the end tab was increased from 760 mm^2 to 1400 mm^2 bringing about a larger area of adhesion (84 °lo increase in area). The resultant dimension of the end tab after the change is 70 x 20 instead of the previous size 38 x 20.

In conformity with the specifications formulated by Japanese Society of Civil Engineers (JSCE), the length of the specimen was increased to 28 in. But the tension testing machine had a constraint, with a maximum specimen length of 17 in. Hence, the extension rod at the dead end of the clamp was extended from 9 in. to 20.25 in. This change in the extension rod could accommodate specimens upto 28 in. length, which could aid failure to occur in the center of the specimens. The following were the test parameters:

Length	28 in.
Bonding agent	AE 10
Curing time	70 hrs.
Effective area of end tabs	1400 mm^2.

Observations

Specimen #64

First fiber rupture	16001b.
Subsequent fiber rupture	1840 lb.
Subsequent fiber rupture	23301b.
Subsequent fiber rupture	34901b.
Ultimate failure	59201b. (Normal ultimate failure)

The ultimate failure was similar to the failure mode expected of a 0° composite specimen and hence the use of AE 10 as a bonding agent was found to be advantageous. The ultimate failure load was much higher than that of the earlier test specimens. Fig. 3.15 shows specimen # 1 at failure.

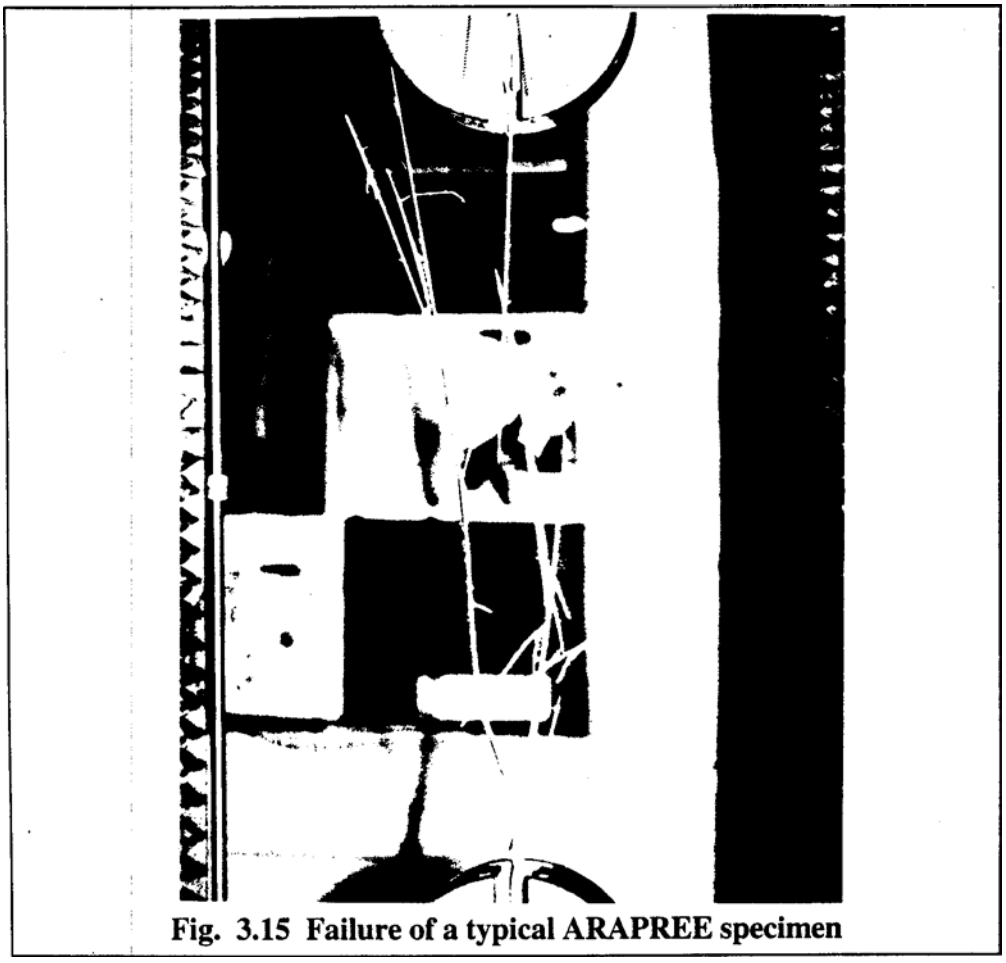

Fig. 3.15 Failure of a typical ARAPREE specimen

Observations

Specimen #65

First fiber rupture	10401b.
Subsequent fiber rupture	14001b.
Subsequent fiber rupture	1650 lb.
Subsequent fiber rupture	26001b.
Subsequent fiber rupture	3120 lb.
Ultimate failure	6 100 lb. (Normal ultimate failure)

The ultimate failures indicate consistency in the failure load magnitudes and the end tabs have better anchorage owing to using AE 10 as a bonding agent in addition to the larger effective area adopted. The length of the test specimens (28 in.) was considered to be a factor contributing to the consistency, as this is an important factor considering the effect of stress concentration near the end tabs upon loading. The outcome of these two tensile tests indicate that the testing process and parameters adopted could form the basis for further testing of test specimens. Fig. 3.16 shows typical types of failures encountered in tension testing of the specimens; a) failure of the specimen due to longitudinal split followed by slip of the end tab (top specimen), b) a normal failure as expected for a composite with 0 degree fiber orientation (middle specimen) and c) typical end tab slip followed by a sudden damage of tendon towards the end with undamaged end tab (bottom specimen).

3.4 EXPERIMENTAL AND SCANNING ELECTRON MICROSCOPE (SEM) ANALYSES OF SPECIMENS EXPOSED TO ALKALI SOLUTION AND SEA WATER

Untensioned ARAPREE specimens, which are exposed to alkali solution and sea water for 900 hrs., two specimens from each set, were tested in the tension testing machine to estimate the degradation due to exposure.

Fig. 3.16 Types of failure of ARAPREE specimens

Fig. 3.17 Removal of exposed untensioned ARAPREE specimens

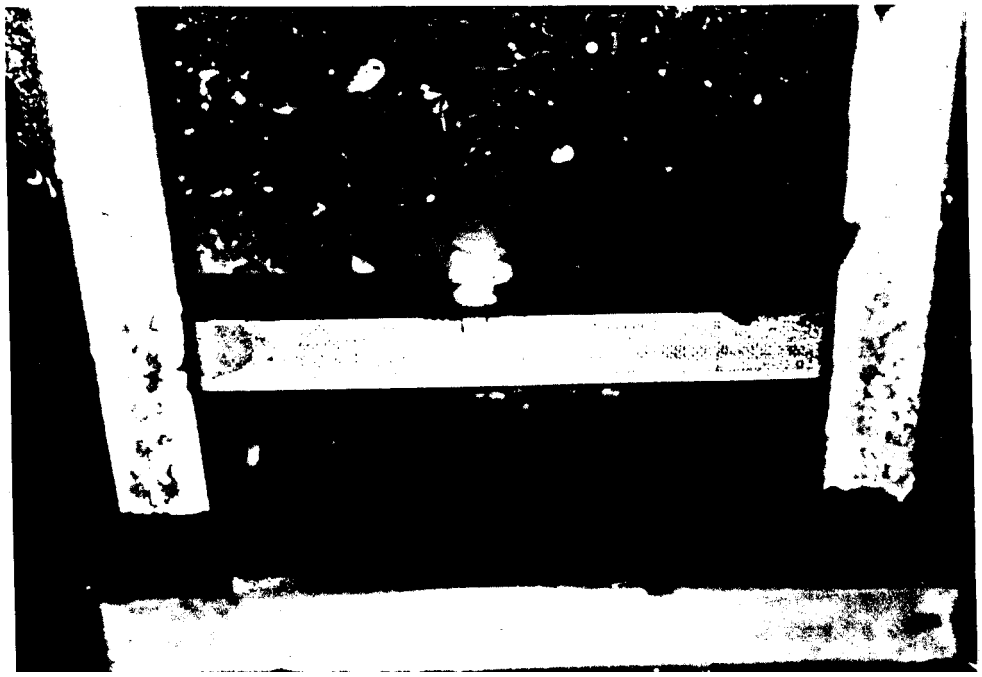

Fig. 3.18 Deposits on ARAPREE specimen exposed to Alkali solution

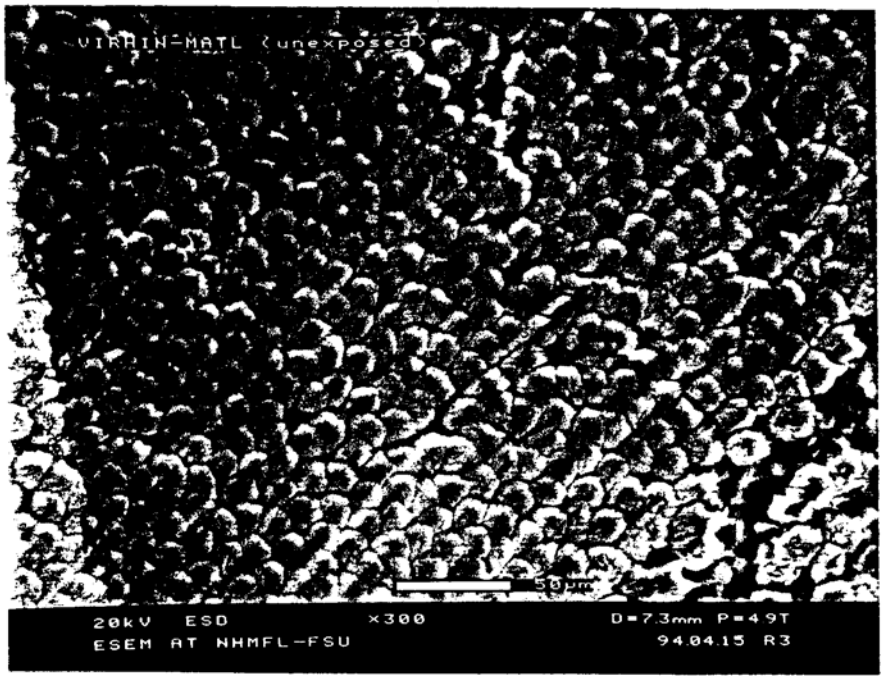

Fig. 3.19 SEM image of unexposed ARAPREE specimen

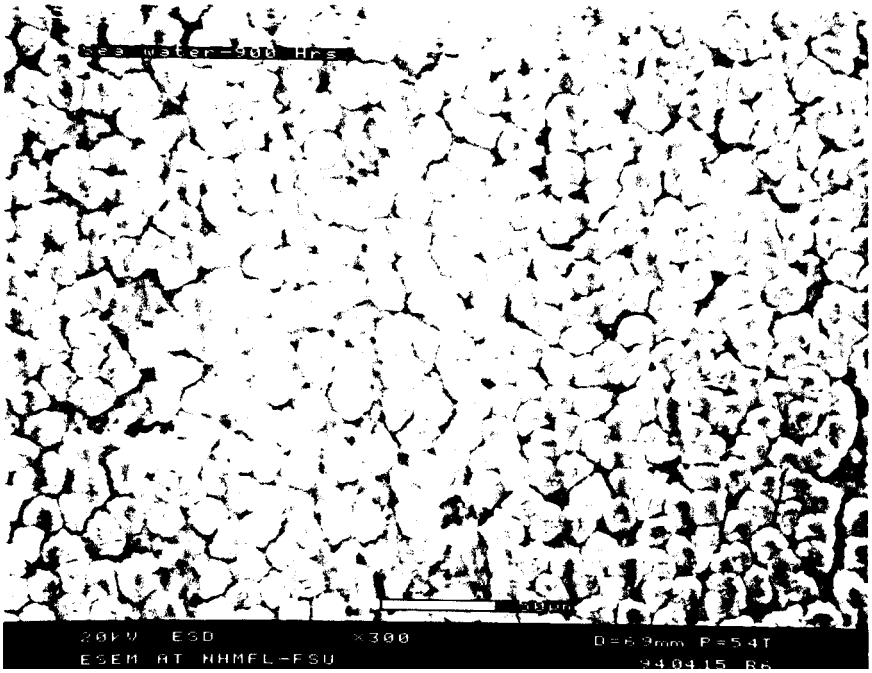

Fig. 3.20 SEM image of ARAPREE specimen exposed in sea water for 900 hrs.

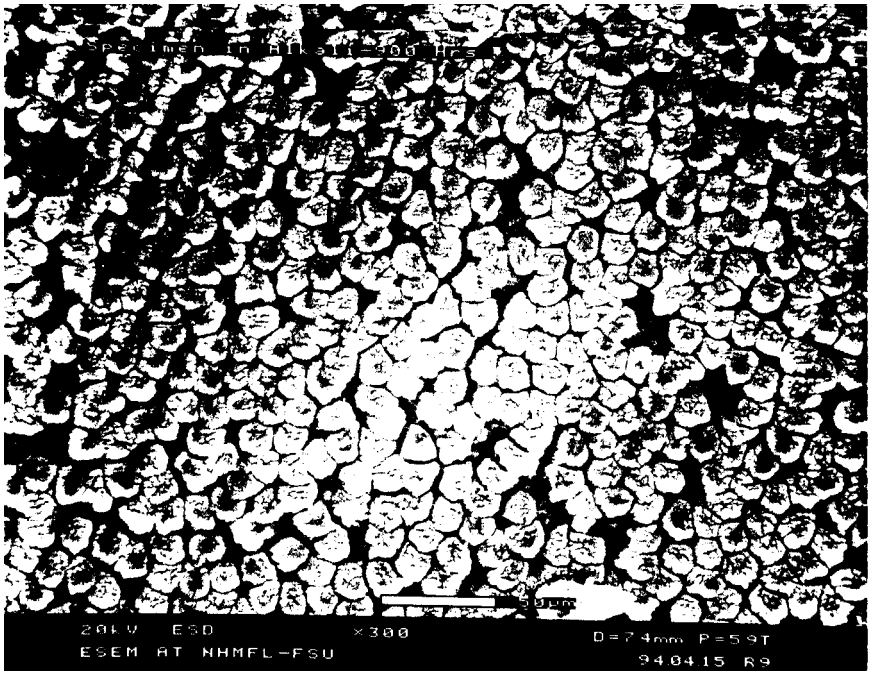

Fig. 3.21 SEM image of ARAPREE specimen exposed in alkali solution for 900 hrs.

Fig. 3.17 shows the exposed ARAPREE tendon being removed from the polycarbonate tank. It was observed that there was a significant amount of deposition on the cables exposed to alkali solution as shown in Fig. 3.18. The specimens for the tension test were prepared as explained in the preceding section using AE 10 epoxy, which gave good results in pilot tests. No conclusions could be made from these tensile tests, since in all the tests the failure was premature due to slip of the end tab. In view to avoid the loss of exposed specimens, tests were not conducted on the remaining exposed specimens.

The ARAPREE specimens exposed to alkali solution and sea water for 900 hrs. were also analyzed under a scanning electron microscope. Figs. 3.19 to 3.21 show the magnified cross sections of the unexposed specimen, and those exposed to alkali and sea water respectively. It can be observed that, at some locations, the space between the fibers for the specimen exposed to alkali solution is larger than that of unexposed and the one exposed to sea water. This observation is not adequate to make a firm conclusion about the degradation of the cables exposed to alkali solution.

CHAPTER 4

DESIGN AND CASTING OF DOUBLE-TEE BEAMS

4.1 INTRODUCTION

This chapter presents the design, fabrication of reinforcements including prestressing of tendons and casting of Double-Tee beams. Design principles for flexural members reinforced and / or prestressed with FRPs are not yet established. Lately significant research is directed towards the standardization of design concepts for applications of FRPs in concrete structures. The complexity in design arises from the fact that FRPs have varied range of material properties depending on type of fibers and resin matrix used in their manufacture. Many assumptions which are made in designing members with steel reinforcement will not be valid any more and hence the equations / specifications applicable to steel cannot be used directly in designing members with FRPs. For instance, if the reinforcing and / or prestressing elements are in multiple layers, the assumption of moment redistribution at ultimate conditions is not valid since the FRP tendons, being purely elastic in nature, will not yield like steel.

The CFRM design committee of 7SCE suggests (Okamura et al., 1992) that one way of designing members with FRPs / CFRM is to adopt safety factors for each and every unknown / undetermined design parameter. This committee also suggests that besides performing thorough analyses, vital material properties such as ultimate strength, Young's modulus etc. should be experimentally established prior to designing the member. In the present study, Double-Tee beam cross section is designed from first principles. Since the desired levels of the prestressing forces in the AFRP tendons was not possible to achieve, with the state-of-the-art anchorages provided, the design is based on the flexural capacity of the Double-Tee beams with the actual prestressing forces in the strands.

Casting of the Double-Tee beams was done at the Structures Research Center, FDOT, Tallahassee. Four beams were cast in two different castings, two at a time, using a 71 ft. long steel form work. U-shaped steel shear stirrups made with # 3 deformed steel bars were used as shear reinforcement due to unavailability of AFRP stirrups. The study focuses mainly on flexural behavior of members prestressed with AFRP (ARAPREE). The use of steel shear stirrups will not affect the flexural behavior of beam. The ARAPREE tendons were instrumented with strain gages to establish the stress strain relationships at the time of prestressing and prestress transfer. These gages were epoxy coated prior to concrete pouring to prevent any moisture from affecting the gages. Other external instrumentation includes strain and displacement transducers to measure various parameters such as deflections, strains, strand slip, etc.

4.2 COMPUTATION OF FLEXURAL CAPACITY'OF DOUBLE-TEE BEAMS

The properties of ARAPREE tendons used in the design of Double-Tee beams are presented in Table 4.1. ARAPREE tendons consist of Aramid fibers impregnated in epoxy resin.

Table 4.1 Properties of ARAPREE tendons

Description	Properties
Breadth x Depth	20 mm x 6 mm
Gross cross sectional area	120 mm^2
Net fiber cross sectional area	44.4 mm^2
Number of fibers	400,000

For analytical purposes the net fiber area is used in calculation of stress and Young's modulus of the tendon. The reason for this is that the force in tendon is carried by the Aramid fibers and not by the epoxy resin which holds them in place. The composite action of the tendon, i.e., the fibers and the epoxy, could also be considered in the analysis. In general, the values of stresses and Young's modulus computed using net fiber area will be higher than those computed using

the gross cross section area. Use of either of the areas would not cause any change in the analytical parameters such as ultimate moment capacity, moment-curvature or load-deformation behavior etc., if they are used consistently throughout the analysis. In the following section, ultimate moment capacity is calculated using both the areas and it has been shown that it would not make any difference in the final results.

Design of the Double-Tee beams is based on two types of failure modes, which are defined below:

(i) crushing of concrete in compression zone, and

(ii) rupture of ARAPREE tendons in tension zone.

Both the net fiber area and gross cross sectional area of the tendon are used in the calculations. The values corresponding to the gross cross sectional area are presented in square parentheses. The following properties are used in the computations:

Ultimate strength of ARAPREE, fp_u = 435 [160.95] ksi,
Ultimate tensile strain, eu = 2.3 %,
Young's modulus, Ep = 18,913 [6,997.81] ksi and
Cross sectional area of ARAPREE, AO = 0.06882 in^2 [0.186 in^2]

Fig. 4.1 shows the cross section of Double-Tee beam. The initial prestressing forces (the forces recorded by the load cells before concreting) in the tendons 1 to 5, averaged for both the stems are given below:

T_{it} = 10.395 kips

T_{it} = 10.71 kips

T_{i3} = 8.46 kips

Ti4 = 10.23 kips

Ti5 = 9.74 kips

Since the behavior of ARAPREE tendons is purely elastic and linear without any plastic deformation upto rupture and the tendons are positioned one above the other in the Double-Tee beams, all the tendons will not fail at the same time at ultimate conditions. Under ultimate stage, the lower most tendon at the beam bottom would reach the failure strain first. Hence the second failure mode was redefined as the rupture of the bottom most tendon for the computation of ultimate flexural strength, M_u.

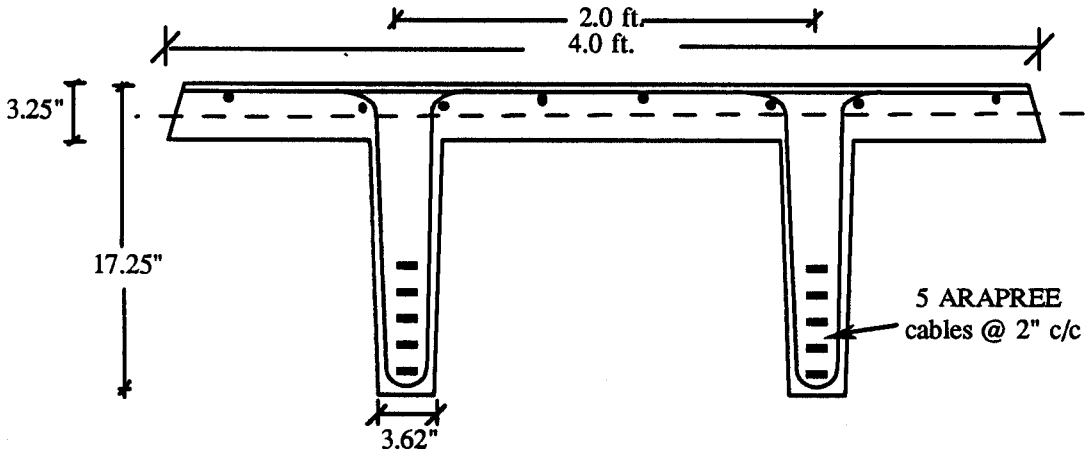

Fig. 4.1 Details of the model Double - Tee beam

Fig. 4.2 shows the assumed stress and strain distributions in the beam cross section for the calculation of ultimate flexural strength.

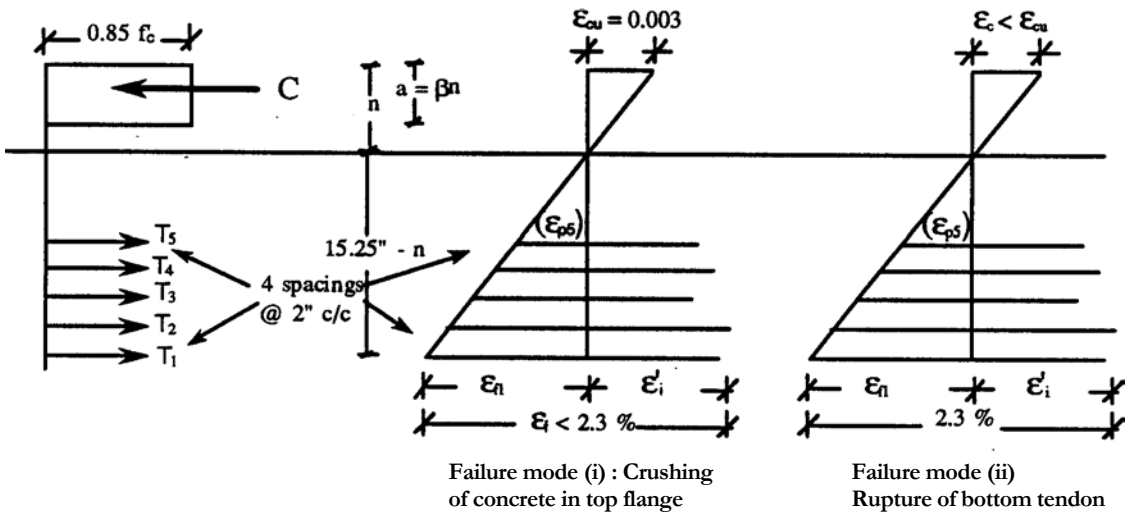

Fig. 4.2 Stress and strain diagrams in Double-Tee

beam Failure mode (i) : Crushing of concrete in top flange

Strains in the ARAPREE tendons are interpolated from concrete strain as

$$\varepsilon_1 = 0.003\frac{15.25-n}{n};$$

$$\varepsilon_2 = 0.003\frac{13.25-n}{n};$$

Similarly E3, E4 and E5 can be obtained. Forces in

the tendons are calculated as follows:

$T_i = \varepsilon_i E_p A_\phi$ (i=1 to 5).

At ultimate stage, the final force in the tendon is calculated as follows:

$$T_1 = \varepsilon_1 E_p A_\phi + T_{i1} = 3.905\frac{15.25-n}{n} + 10.395 kips$$

The calculated force in the tendons would result in the same value whether gross area or net fiber area is used in the above equation, since the product Ep Aϕ yields same value. Similar expressions were obtained for forces in the other tendons.

The total compressive force in concrete is C = (0.75 n) (0.85 f `$_c$) b

where f `$_C$ = 6.0 ksi and b = 24 in.

Thus, C = 91.8 n.

The depth of neutral axis n is found by equating ΣT_i and C, as n = 3.555 in. T_i was calculated using this value of n and shown below:

T_1 = 23.24 kips; T_2 = 21.36 kips; T_3 = 16.91 kips; T_4 = 16.48 kips; T_5 = 14.15 kips

The ultimate flexural strength was determined by taking moments of the individual forces about the centroid of the compression block as, M_u = 1,919.72 kip-in.

Failure mode (ii) : Rupture of bottom most tendon

Forces in the tendons are calculated as follows:

$T_i = \varepsilon_i E_p A_\phi$ (i=1to5).

For the bottom most tendon E1 is known (2.3 %), thus,

$T_i = \varepsilon_i E_p A_\phi$ = 0.023 x 18913 x 0.06882 = 29.94 kips.

[$T_i = \varepsilon_i E_p A_\phi$ = 0.023 x 6997.81 x 0.186 = 29.94 kips.]

For tendon 2, ε_2 is interpolated from strain diagram as

$$\varepsilon_2 = 0.01501 \frac{13.25 - n}{15.25 - n}$$

and thus,

$$T_i = \varepsilon_i E_p A_\phi + T_{i2} = 19.537 \frac{13.25 - n}{15.25 - n} + 10.71 \text{ kips}$$

Similar expressions were obtained for forces in the other tendons.

The total compressive force in concrete is C = (0.75 n) (0.85 f `$_c$) b

where f `$_c$ = 6.0 ksi and b = 24 in.

Thus, C = 91.8 n.

Following a similar procedure as in the failure mode with concrete crushing, n =1.299 in. and T_1 = 29.94 kips; T_2 = 27.446 kips; T_3 = 22.395 kips; T_4 = 21.365 kips; T_5 = 18.074 kips; and M_u = 2685.6 kip-in.

It is to be observed that in failure mode (i), tensile force in the bottom most tendon (T_1) is 23.24 kips, which is less than the breaking load (29.94 kips). This mode gives a lower M_u and hence might control the failure pattern. Failure mode (ii) yields a concrete strain of 0.0014 when the bottom most tendon ruptures.

4.3 FABRICATION OF SHEAR STIRRUPS AND TEMPERATURE AND SHRINKAGE REINFORCEMENT

Seventy feet long steel form work (Figs. 4.3a and 4.3b) was assembled and used to cast four 33 ft. long beams in two different castings. Due to the unavailability of AFRP shear stirrups in the required shape, #3 deformed steel bars were used for fabrication of double legged shear stirrups. Fig. 4.4 shows the steel shear stirrups tied to circular f100,000 ϕ 5.7 type ARAPREE hangar bars. The use of steel stirrups does not affect the overall objective of the study, since the scope includes mainly the flexural behavior of the beams prestressed with ARAPREE. Earlier studies have reported that the high Poisson's ratio of AFRP might cause cracking at the transfer zone (due to Hoyer effect). Hence the shear stirrups were spaced closer at beam ends (3 in.) than at center (6 - 12 in.) to ensure a crack free transfer zone and avoid the shear failure of the beams. Circular f100,000 ϕ 5.7 type ARAPREE was used in the form of an isotropic mesh (6 in.) as temperature and shrinkage reinforcement. Temperature and shrinkage reinforcement mesh was prepared as shown in Fig. 4.5 and the mesh was placed in position and tied to the hangar bars (Fig. 4.6).

Three of the four Double-Tee beams cast for the study were arranged side by side and transversely post-tensioned to form the half scale model bridge system. The post-tensioning strands for this purpose were inserted through the polyvinyl chloride (PVC) ducts placed in the

flanges of the Double-Tee beams. PVC ducts (internal and external diameters of 0.75 and 1.0 in. respectively) were placed at 30 in. centers all along the beam length (Fig. 4.7). Since the beams were not match cast (i.e., one beside the other with the PVC ducts through the flanges) extreme caution was taken to ensure that the PVC ducts were spaced exactly in the same position for both the casts. Fig. 4.7 shows the steel forms with PVC ducts, shear stirrups and temperature and shrinkage reinforcement in place before tensioning the Aramid FRP cables.

Fig. 4.3a Double-Tee steel forms being arranged in position using crane

Fig. 4.3b Double-Tee steel forms in place

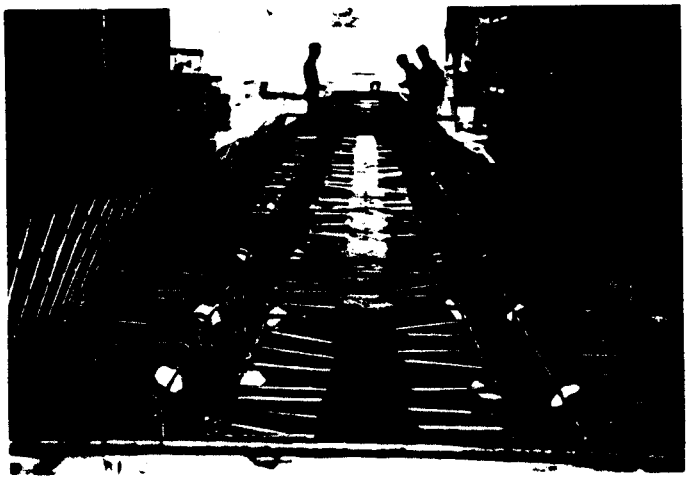

Fig. 4.4 Shear stirrups being tied with hangar bars

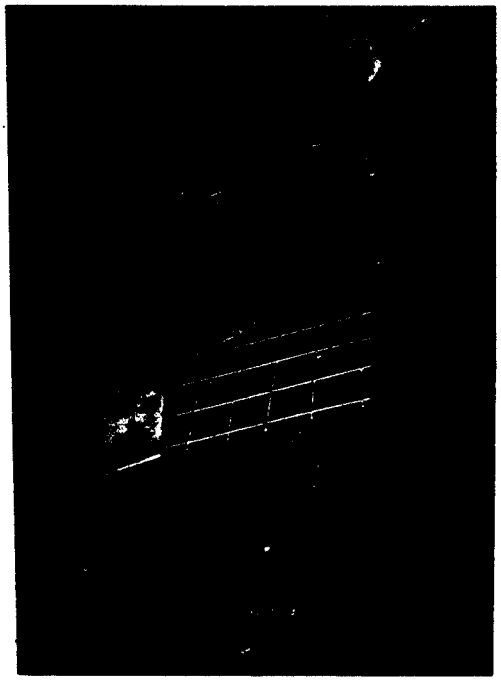

Fig. 4.5 Preparation of temperature and shrinkage mesh reinforcement

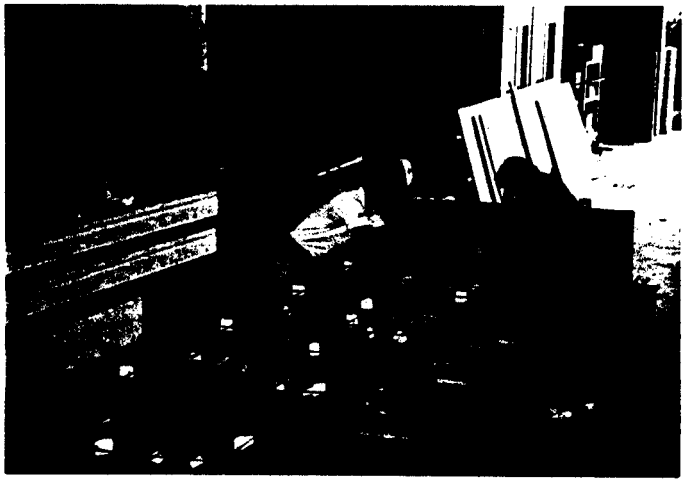

Fig. 4.6 Temperature mesh being tied with the hangar bars

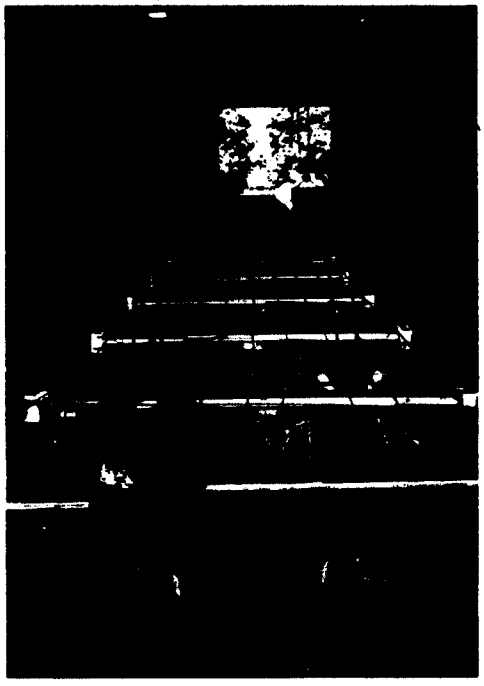

Fig. 4.7 PVC ducts, shear stirrups and shrinkage reinforcement arranged in position

4.4 PRETENSIONING OF ARAMID FRP CABLES AND DOUBLE-TEE BEAM CASTING

Five f-400,000 20 mm x 6.0 mm rectangular ARAPREE tendons were used as prestressing strands in each stem of Double-Tee beam. Prior to placing the temperature and shrinkage reinforcement, the ARAPREE tendons were inserted into the stems of the form work with great care to avoid any damage to the tendon (Fig. 4.8). Fig. 4.9 shows all the tendons in position, five in each stem of the Double-Tee steel form. Single wedge anchorages were used to tension as well as anchor the individual strands. The anchoring system (Figs. 4.10a and 4.10b) ' includes a metallic sleeve with a gentle inner taper and two polyamide wedges with rectangular grooves through which the cable is passed. Fine sand was adhered onto these grooves using epoxy and the cable gripped between these two wedges.

With the current anchorage system, it was not possible to attain and maintain the desired pretension of 55% of the characteristic force (0.55 F_u = 15 kips). In the first cast of the beams, the ARAPREE tendons were tensioned (Fig. 4.11) to a value of 0.5 F_u, (about 13.5 kips.) and the anchorage system failed suddenly, immediately after anchorage set. Two anchorages in series were then used with the tendon in an attempt to increase the capacity of the wedge system. However, technical difficulties were encountered in ensuring the proper anchorage set and transfer of tension.

Several attempts were made to increase the efficiency of the anchoring system, such as changing the type of epoxy used to adhere sand on the wedges, grade of sand used, and making the inner surface of the wedges rough before adhering sand. ARAPREE has very high tensile strength and comparatively low Young's modulus; hence under tension, these cables store high levels of strain energy. In the initial prestressing stages, when the cable was tensioned upto 13.5 kips, the anchorage at tensioning end slipped suddenly releasing enormous amount of energy. The temperature and shrinkage reinforcement, which was tied and placed in position before prestressing the cables, prevented the cable from flying and thereby creating a hazardous

condition. Fig. 4.12 shows an ARAPREE cable, which slipped through the anchorage and wound as a coil beneath the temperature reinforcement.

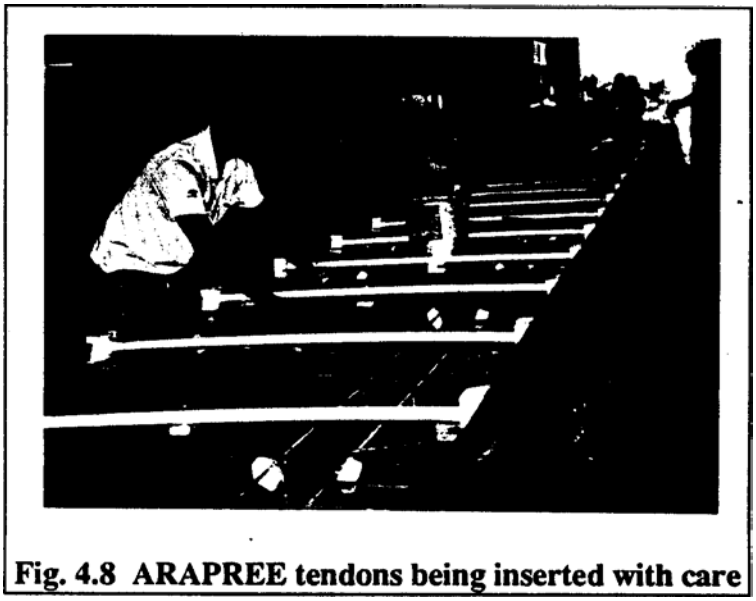

Fig. 4.8 ARAPREE tendons being inserted with care

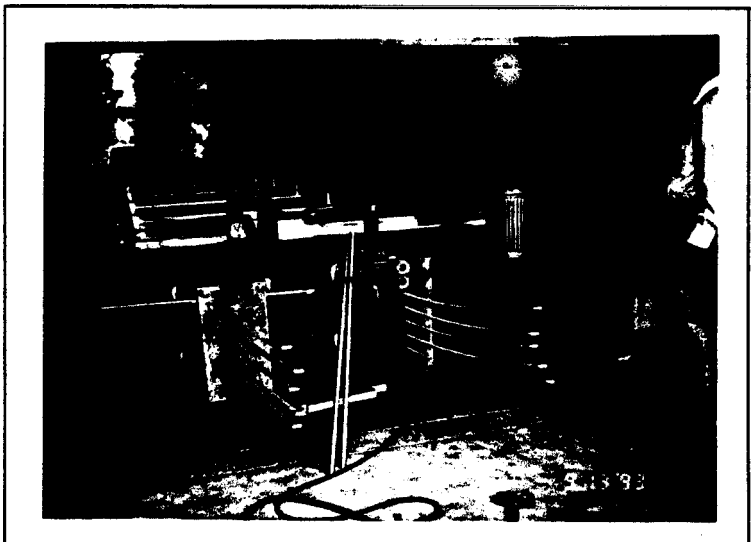

Fig. 4.9 Arrangement of ARAPREE tendons

Fig. 4.10a Anchoring system with polyamide wedges

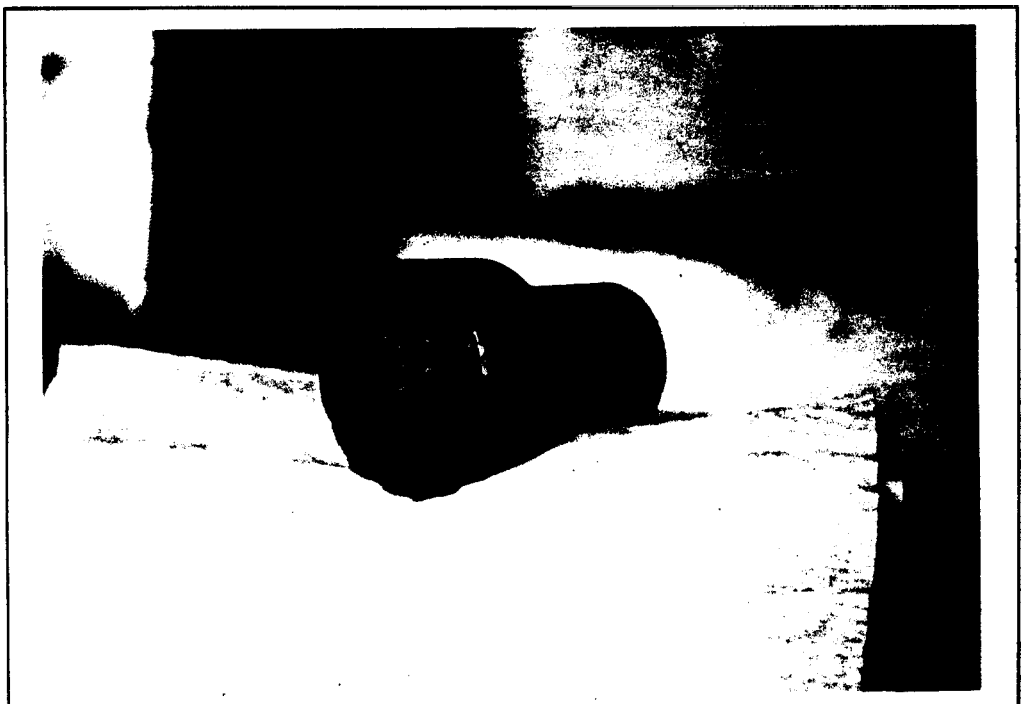

Fig. 4.10b End view of wedges

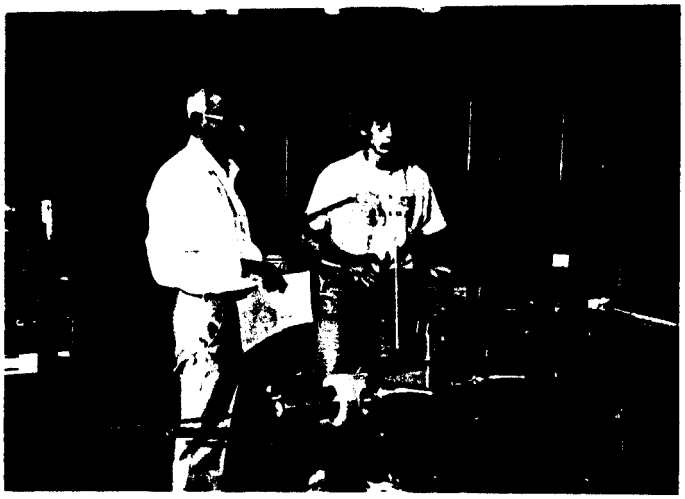

Fig. 4.11 Pretensioning of an ARAPREE tendon

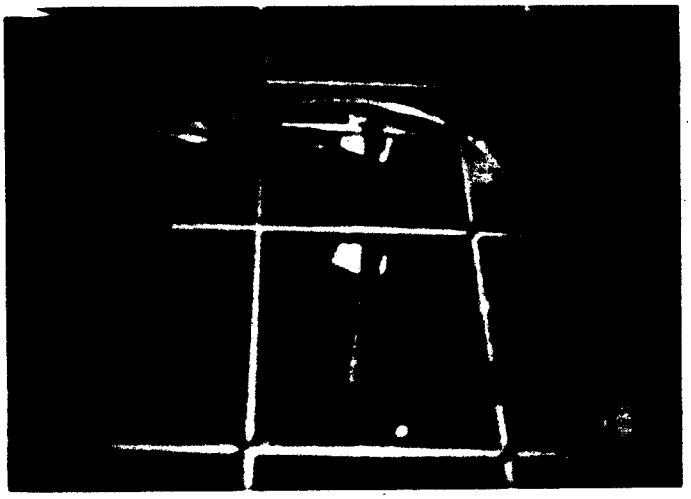

Fig. 4.12 ARAPREE tendon after wedge failure

Forces in the ARAPREE tendons were measured by calibrated load cells (Fig. 4.13) at the dead end. Load cells were placed at both dead and tensioning ends of one cable to monitor any difference in the forces between the two ends. It was observed that at jacking end the load was higher by about 1.5 kips. Probably, it was this difference in the load which caused the anchorage failure since these anchors, at their best, are designed to carry upto 65% of the characteristic force. Hence it was decided to prestress the ARAPREE tendons only upto 35 - 40 % of F_u.

At the desired pretensioning force (11 to 12 kips.) the elongation of ARAPREE cables was about 11.5 in. This elongation due to prestress together with the slack in the tendons prior to tensioning necessitated a long stroke in the jack. Hence, two jacks (Figs. 4.14a and 4.14b) were used to prestress the tendons, since available stroke of a single jack was not sufficiently long to achieve the desired force in the tendons. Fig. 4.15 shows cutting the excess length of the ARAPREE tendon after anchorage set. The load cells in front of the anchorages at the dead end and the anchorages at the jacking end are shown in Figs. 4.16a and 4.16b. The actual magnitudes of prestressing forces are summarized in the preceding Section 4.2.

Four ARAPREE **Double-Tee beams were cast in two castings. Prestressing the ARAPREE tendons in the second cast was less difficult owing to the know-how acquired during the prestressing of the cables in the first cast. In the second cast, the ARAPREE prestressing tendons were instrumented with strain gages (Figs. 4.17a and 4.17b) at different locations along the tendon length. Fig. 4.18 shows the schematic of positions of the strain gages on the ARAPREE cables. Great care was exercised to place the instrumented tendons in position without damaging the strain gage as well as the tendon (Fig. 4.19). The objective of instrumenting the ARAPREE cables was to achieve the following:**

a) To measure the strain in the cables at the time of prestressing, establish average strain in the tendon and compare it with the corresponding force in the cable recorded by the load cell,

b) To establish the transfer length at the time of prestress release,

c) To measure strains and establish strain profile at the time of static load test.

Fig. 4.13 Calibration of load cell

Fig. 4.14a Two-jack setup for prestressing

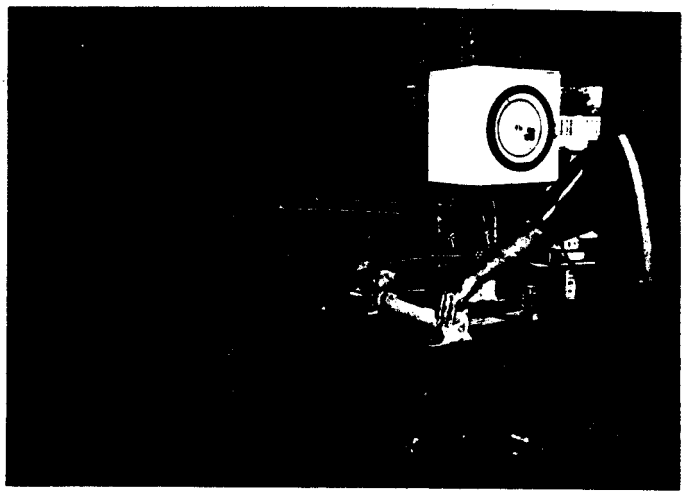

Fig. 4.14b Pressure gage recording the force in the hydraulic jack

Fig. 4.15 Excess length of ARAPREE tendon being cut

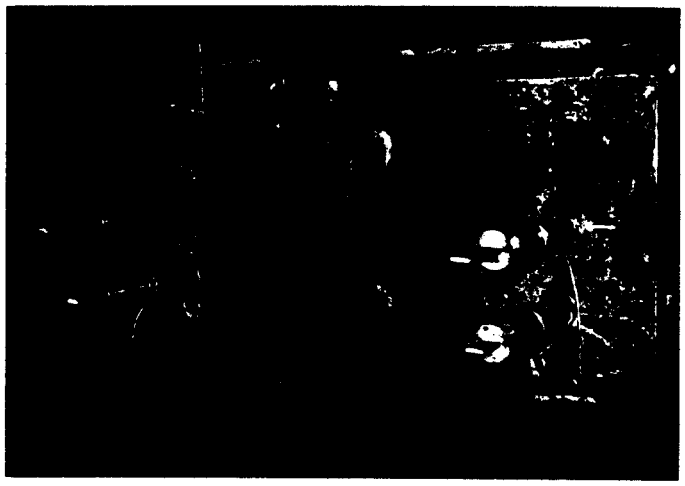

Fig. 4.16a Load cells and anchors at dead end

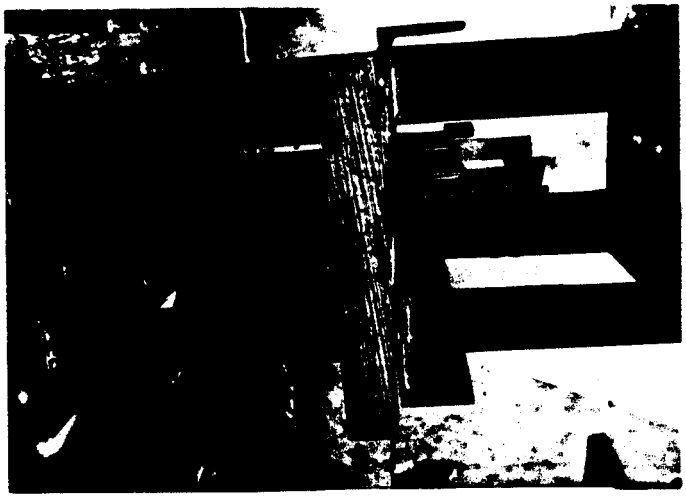

Fig. 4.16b Anchors at jacking end

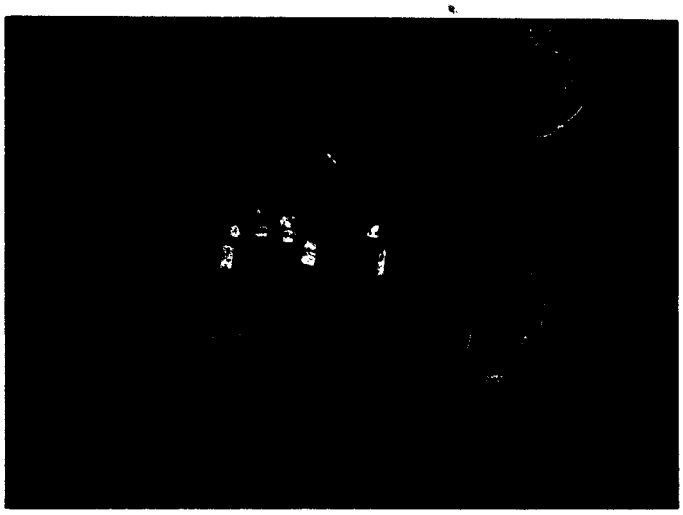

Fig. 4.17a Strain gages on the ARAPREE tendon being checked for continuity

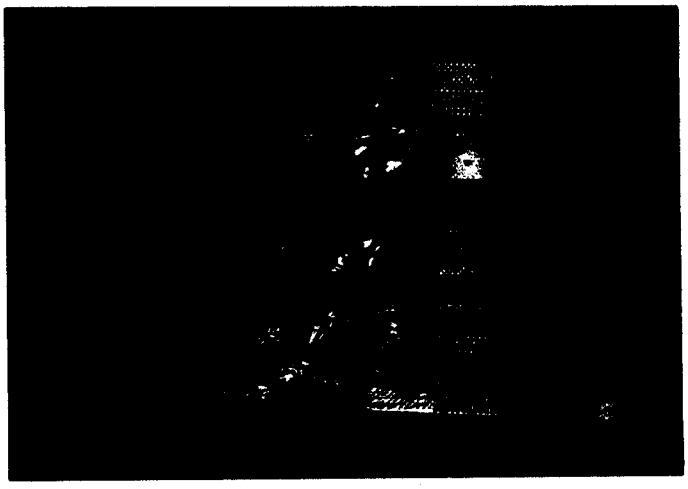

Fig. 4.17b ARAPREE tendon instrumented with strain gages

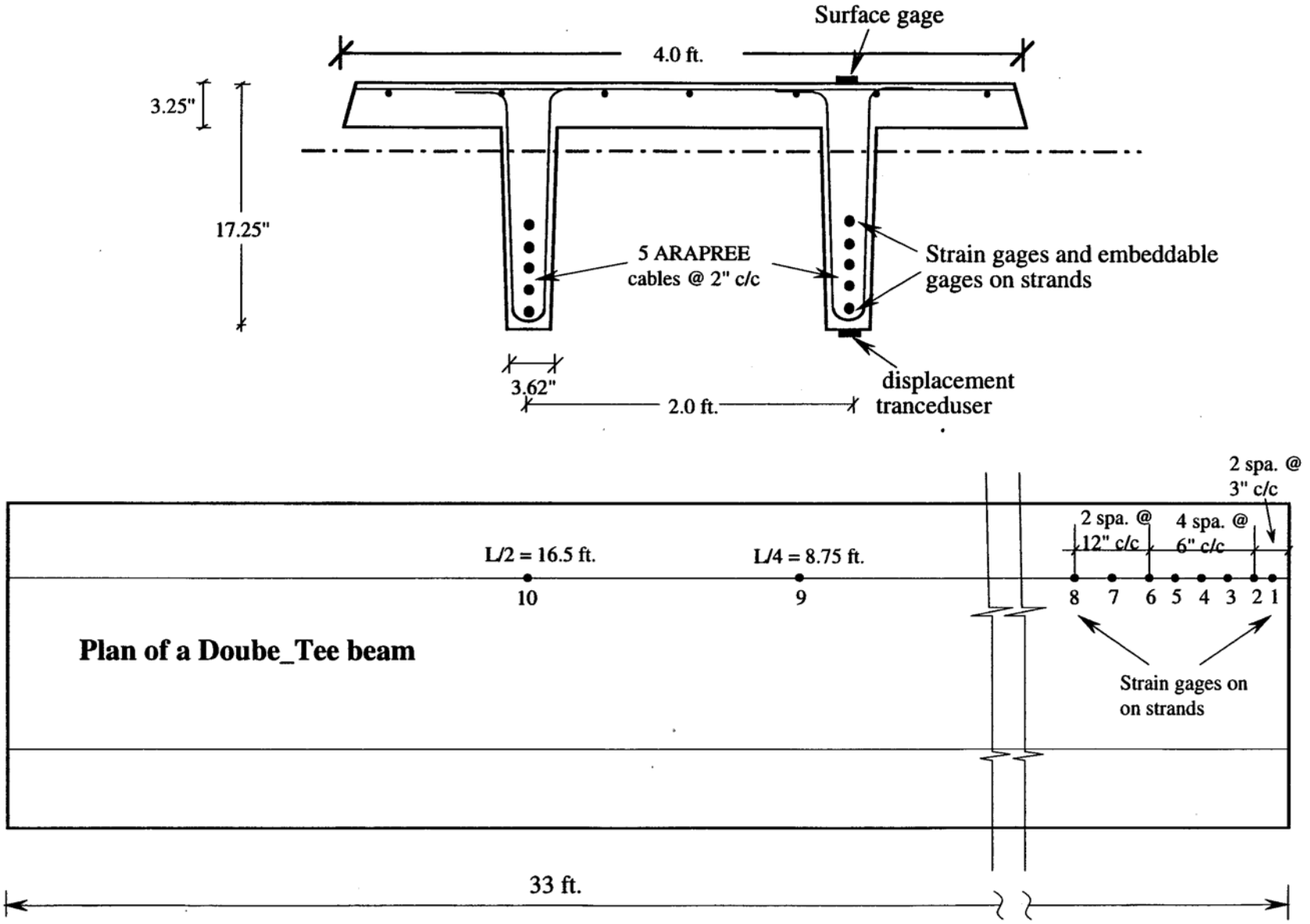

Fig. 4.18 Schematic of positions of strain gages on ARAPREE cables in Double-Tee beam

Fig. 4.19 Insertion of instrumented tendons in position

Fig. 4.20 MEGADAC data acquisition system

The Double-Tee beam consists of five ARAPREE tendons in each stem. The two stems are categorized as East and West stems. The two beams cast were designated as North and South beams. The East stem of the North beam and West stem of South beam were instrumented with strain gages. The tendons were numbered from top to bottom (top and bottom tendons designated as 1 and 5 respectively) in both East and West stems. The tendons were recognized as Cables-E1 (or 1E) through E5 (or 5E) in the East stem and Cables-W1 (or 1W) through W5 (or 5W) in the West stem of the Double-Tee beam.

The forces and strains in the tendons were recorded using MEGADAC data acquisition system (Fig. 4.20). Figs. 4.21a - 4.211 show the load - strain behavior of the ARAPREE tendons , at the time of prestressing. Four ARAPREE tendons out of ten (1E, 3E, 1W, and 3W) were instrumented using 8 to 10 strain gages for measuring transfer lengths. The other cables were instrumented with strain gages only at mid and quarter span points (Fig. 4.18). Hence, Figs 4.21a, 4.21c, 4.21e and 4.21g show recorded strains from gages on cables 1E, 3E, 1W, and 3W. It is evident from these graphs that the load (stress) strain relationship is linear. The texture of ARAPREE tendons is rough and uneven. To facilitate the installation of strain gages, tendon surface was coated with epoxy. Strain gages were then installed on the smooth surface of the epoxy. Though necessary care was taken to make this layer of epoxy as thin as possible, just enough to smoothen the surface texture, it was understood that the strain readings would slightly differ from the actual strains in the cables and those recorded by one strain gage relative to the other. This difference in the strain values recorded on the same cable for a given load level can be observed in Figs. 4.21a - 4.21i.

The load - strain plots shown in Figs. 4.21a to 4.21i were utilized to determine the Young's modulus (E) of the ARAPREE tendons. Young's modulus was calculated using the data from all the strain gages installed on each cable and were averaged. The averaged Young's moduli from all the ten cables were again averaged to arrive at the final value.

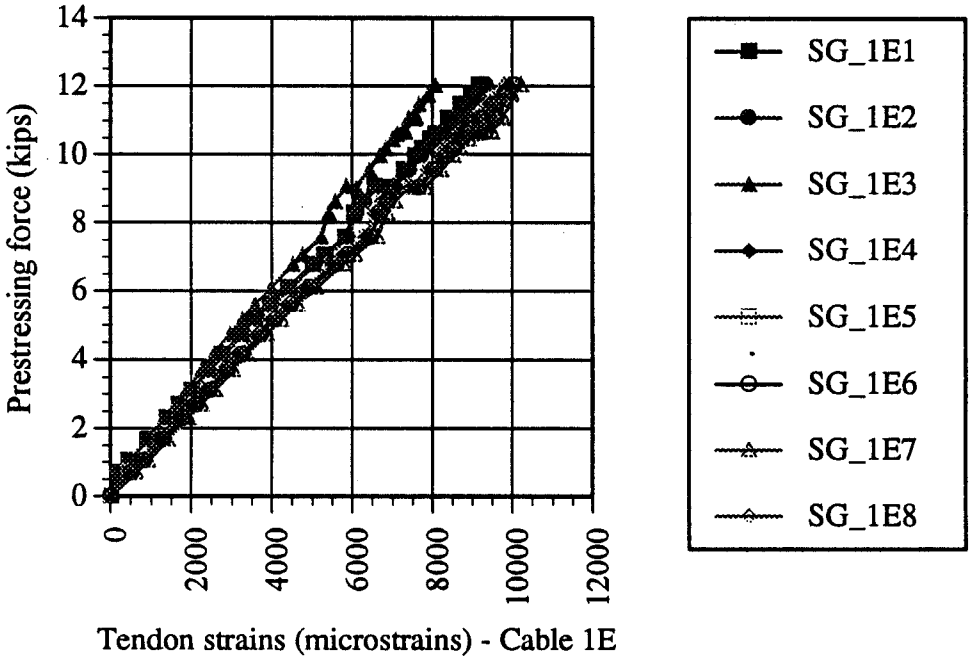

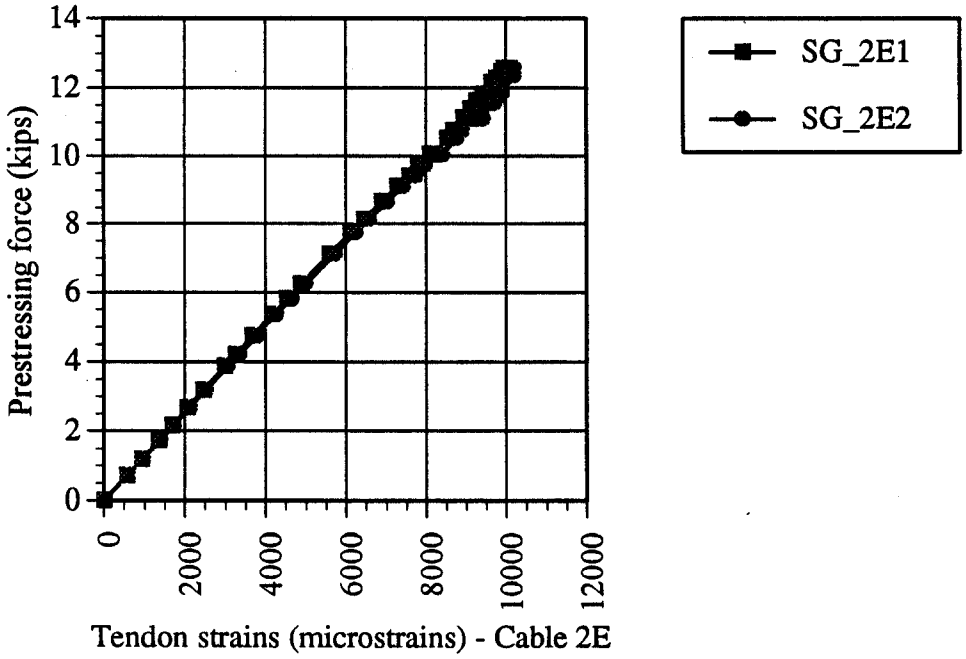

Figs. 4.21a and 4.21b Load vs strain relationships for cables lE and 2E

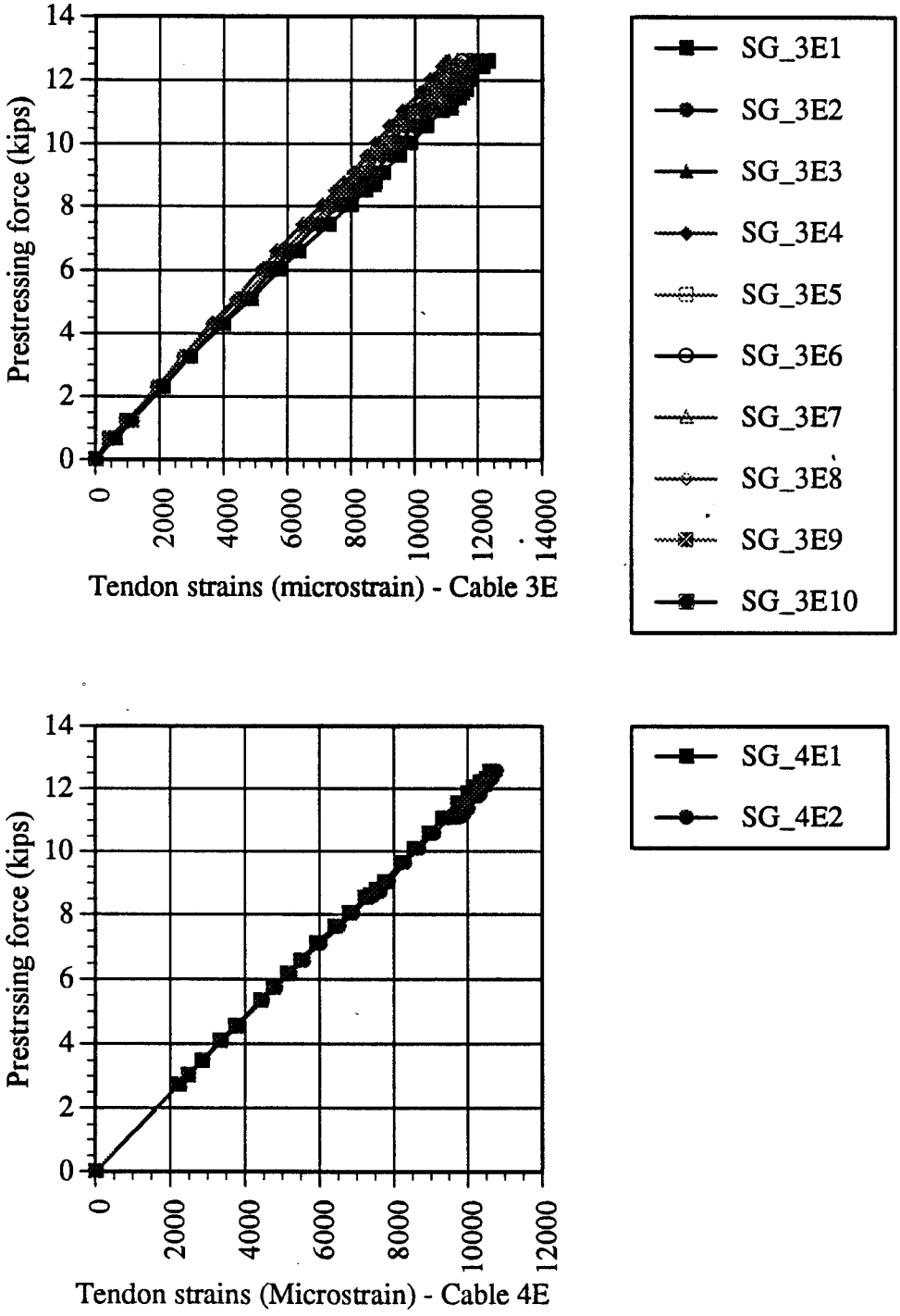

Figs. 4.21c and 4.21d Load vs strain relationships for cables 3E and 4E

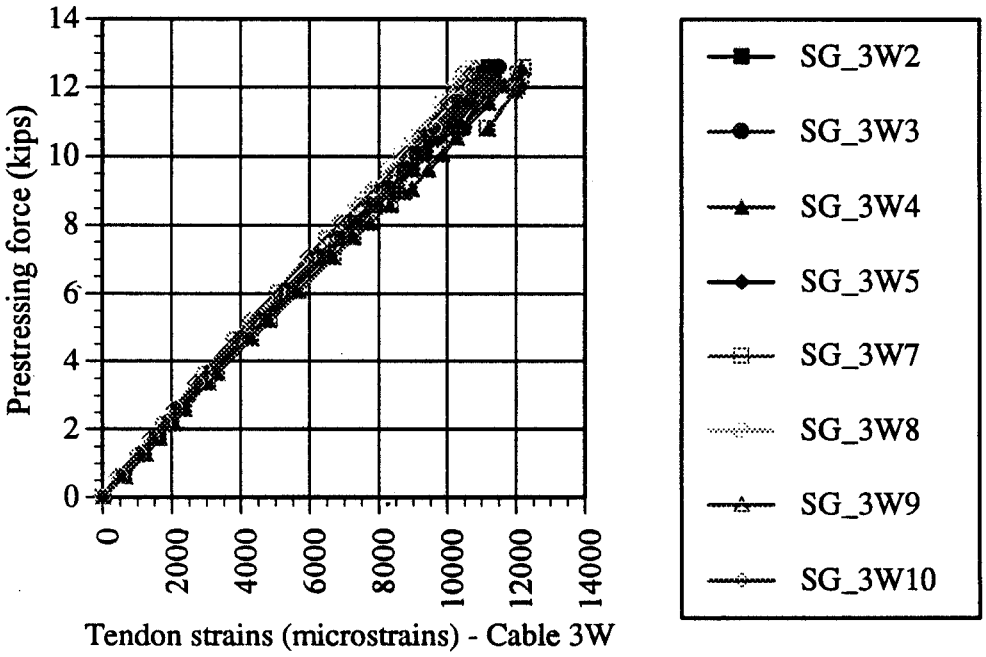

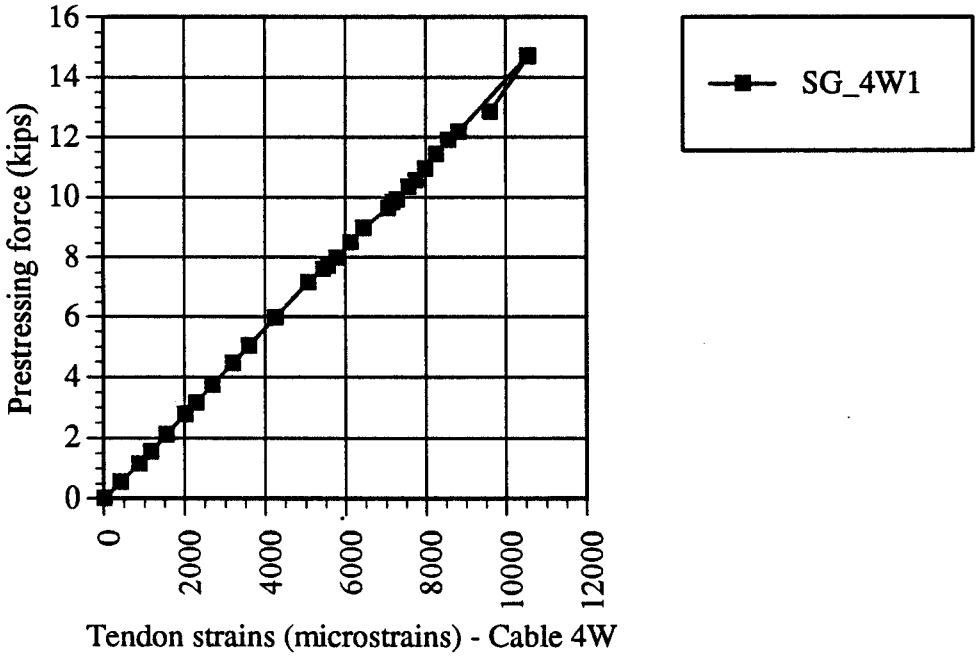

Figs. 4.21g and 4.21h Load vs strain relationships for cables 3W and 4W

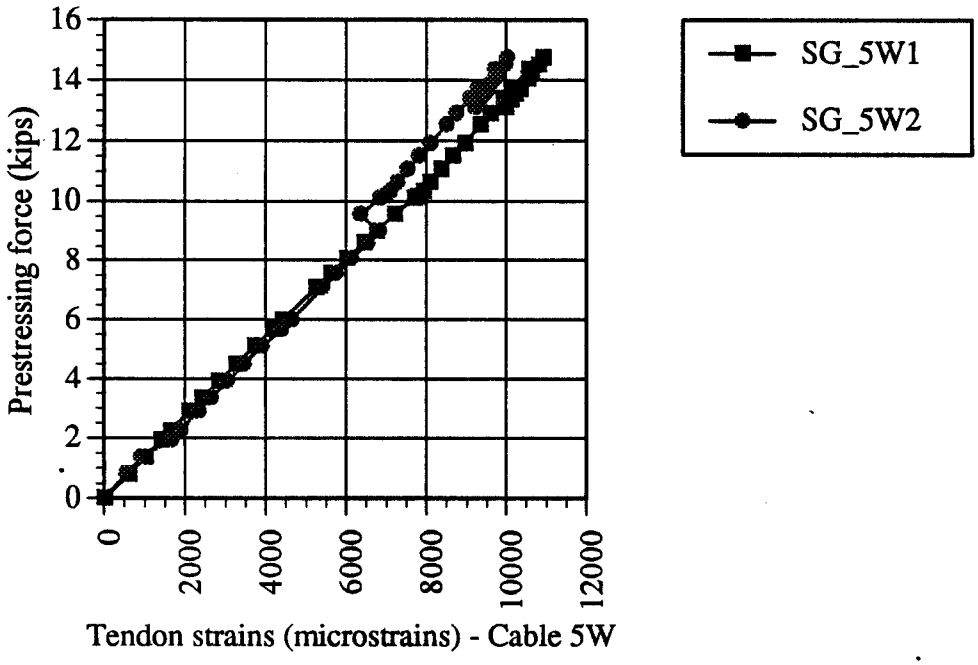

Figs. 4.211 Load vs strain relationship for cable 5W

Table 4.2 shows the computed value of Young's modulus. The value for Young's modulus published in the literature [A. Gerritse, 1989] is about 18,800 ksi. which is about 6 % greater than the computed value.

Fig. 4.22 shows the Double-Tee steel form work ready for casting after prestressing of ARAPREE cables. Double-Tee beams were designed to be cast using normal weight 6000 psi concrete with 3/4 in. aggregate and 5 in. slump. Figs. 4.23a and 4.23b show the concreting of the Double-Tee beams in progress. Curing of the beams was done by spreading burlap on the surface of the beams (Fig. 4.24) and keeping them wet continuously for three days. In the second cast of Double-Tee beams, an hour after concrete was poured, anchorage of one of the ARAPREE tendons slipped and prestress in the tendon was lost. This could probably be due to the following phenomenon: ARAPREE has negative linear thermal expansion coefficient (oc= $-2x10^{-6}$ to - $4x10^{-6}/^{\circ}C$), i.e., in effect, the tendon shrinks if the temperature is increased. The cables were pretensioned upto a force of about 13 kips, allowing for anchorage set losses. It is possible that this particular tendon was tensioned to a slightly larger force than that recorded by the load cell.

After the concrete pouring, the heat of hydration would substantially increase the temperature surrounding the cables resulting in an increase in tension in the tendons. This increase in tension, in addition to several other problems associated with the anchorages (as explained earlier in this section), might have resulted in tendon slip.

Table 4.2 Young's modulus calculated from measured stress - strain data

	Young's modulus [1] (average, ksi)	Young's modulus [2] (average, ksi)
Cable - lE	19,243.9	7,120.24
Cable - 2E	18,165.35	6,721.18
Cable - 3E	15,597.0	5,770.89
Cable - 4E	17,067.8	6,315.09
Cable - 5E	-	-
Cable - 1W	15,916.7	5,889.18
Cable -2W	17,452.7	6,457.5
Cable - 3W	16,060.2	5,942.27
Cable - 4W	18,924.4	7,002.03
Cable - 5W	19,290.8	7,137.6
Overall average	17,624.3	6,520.99

1 Net fiber area considered for stress calculation [A. Gerritse, 1989].

2 Gross cross sectional area considered for stress calculation.

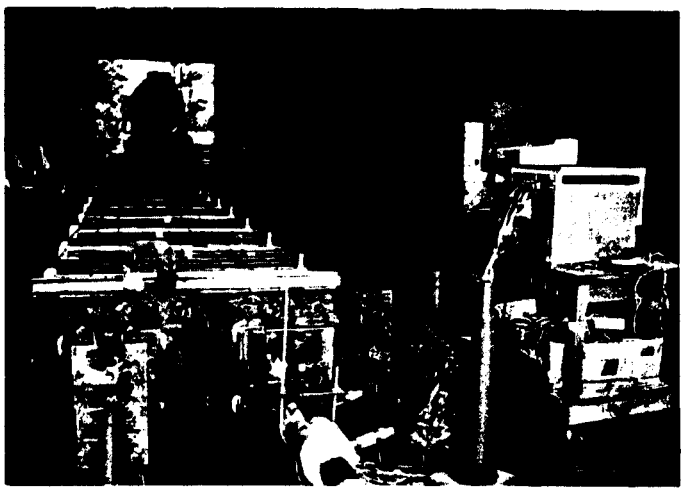

Fig. 4.22 Double-Tee beam form work with reinforcement ready for casting

Fig. 4.23a Concrete being poured using a bucket

Fig. 4.23b Surface finishing of the beam in progress

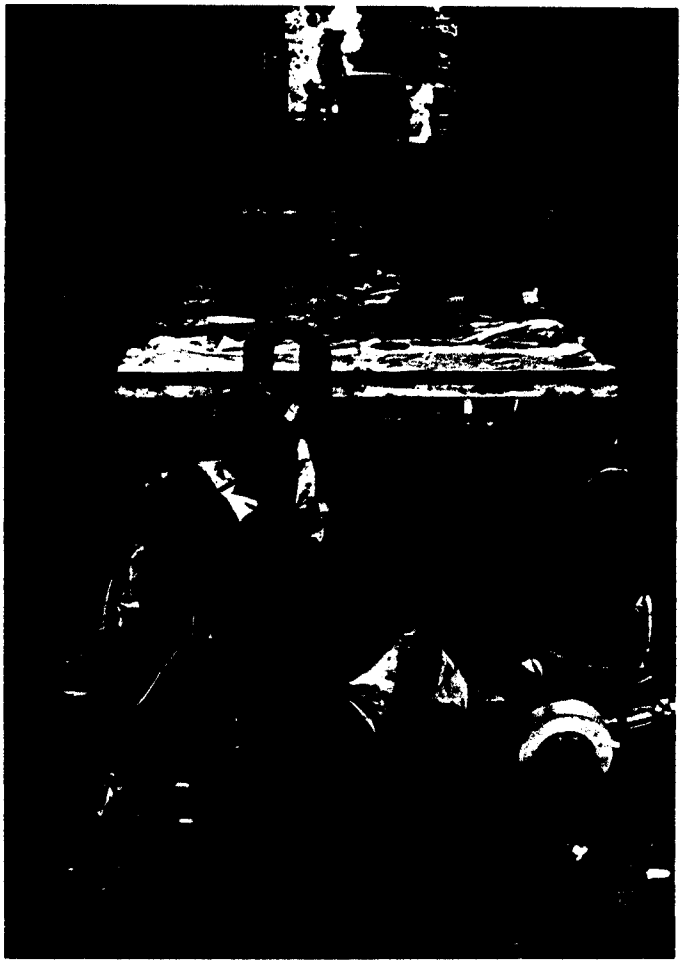

Fig. 4.24 Curing of the beams using burlap

4.5 RELEASE OF PRESTRESS

Two Double-Tee beams were cast at a time using 70 ft. long form work with about 2 ft. clearance between end faces of the beams. ARAPREE prestressed tendons were cut between the two beams to release the prestress, four days after concreting, when the concrete strength was about 4300 psi. Fig. 4,25a presents the variation of forces recorded by the load cells in ARAPREE tendons during the sequential release of prestress. It can be observed that there was little change in forces in the tendons'until prestress in all the tendons was released.

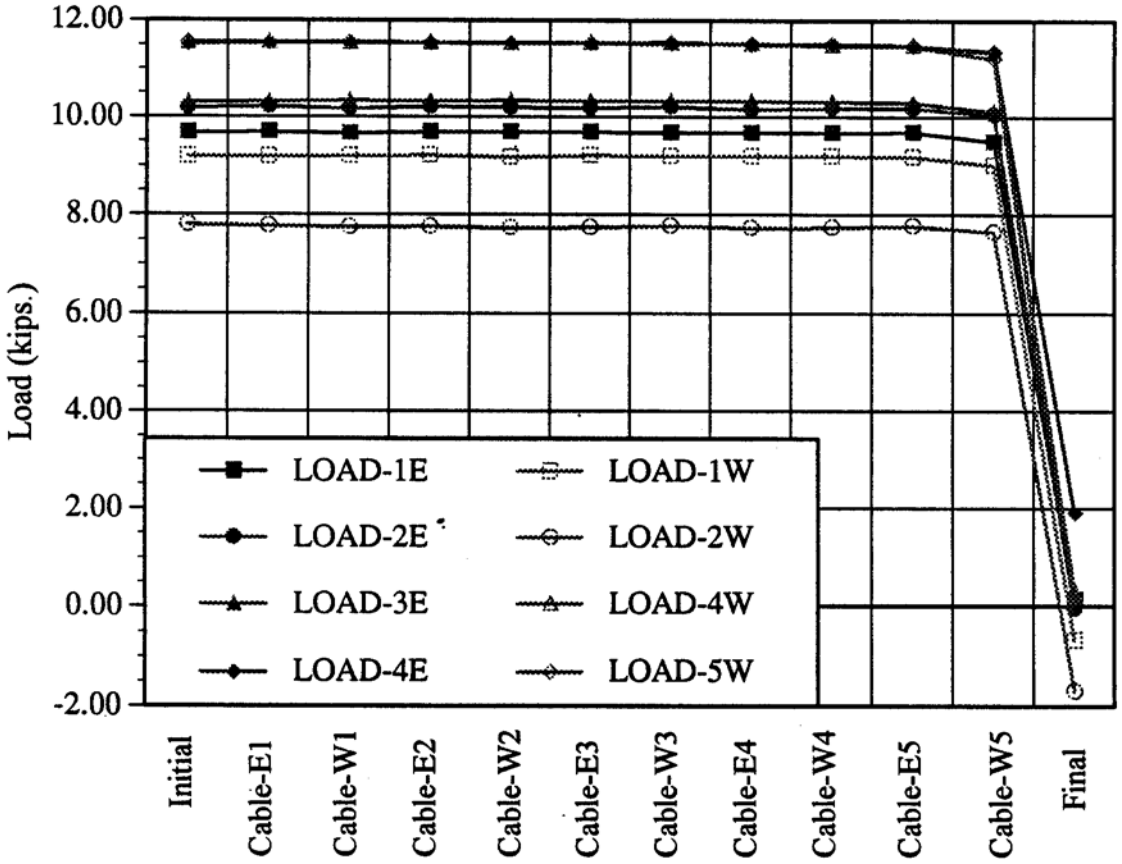

Fig. 4.25a Forces recorded in ARAPREE tendons during prestress release

Totally four out of ten ARAPREE tendons were instrumented with strain gages towards beam ends to measure transfer lengths. Due to impact resulting from sudden release of prestress, some of the strain gages very close to the end face of the beam were damaged. Figs. 4.25b to 4.25e show the strains recorded by the strain gages located on the cables with respect to the

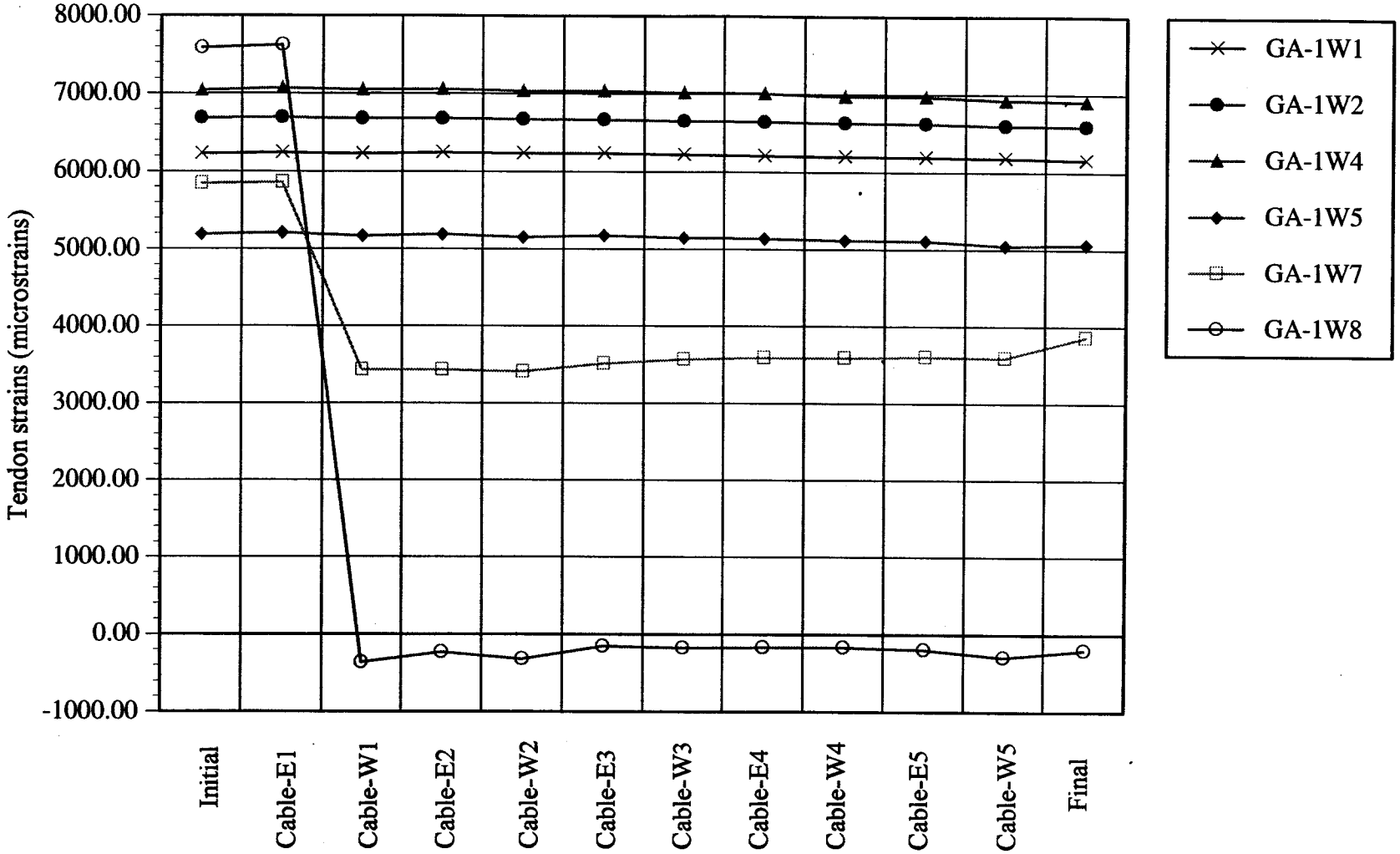

Fig. 4.25b Strains recorded in cable-W1 during prestress release

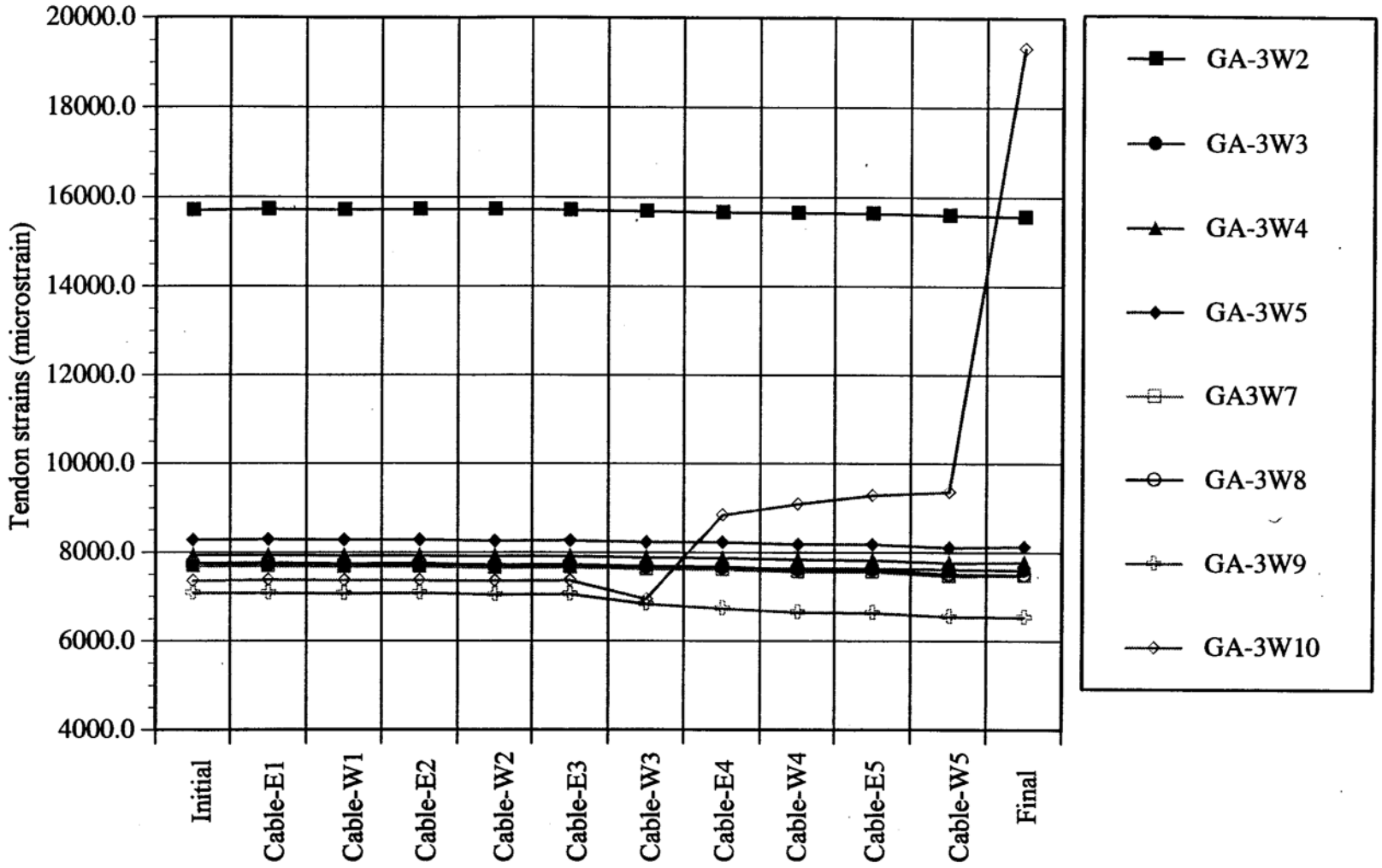

Fig. 4.25c Strains recorded in cable-W3 during prestress release

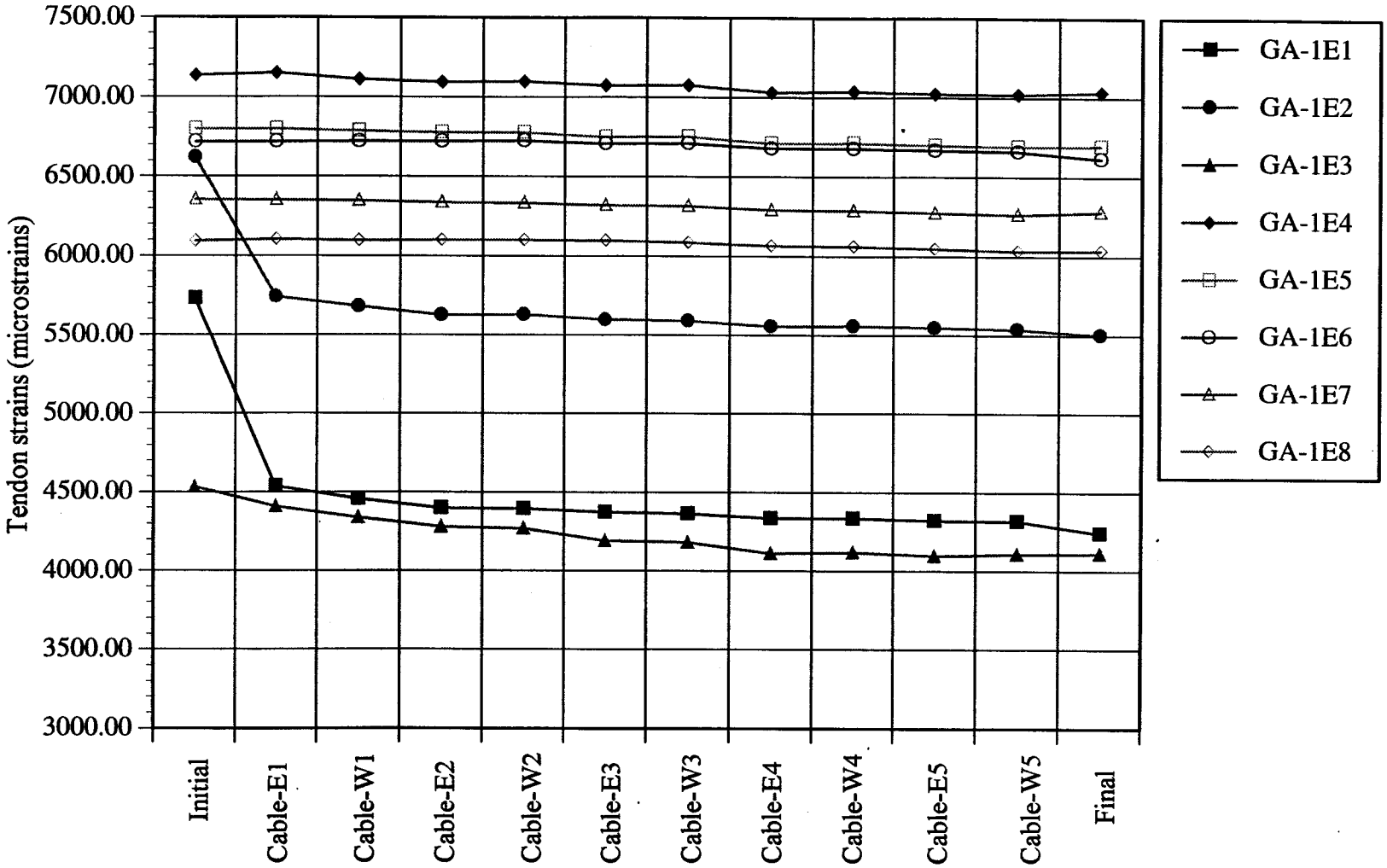

Fig. 4.25d Strains recorded in cable-E1 during prestress release

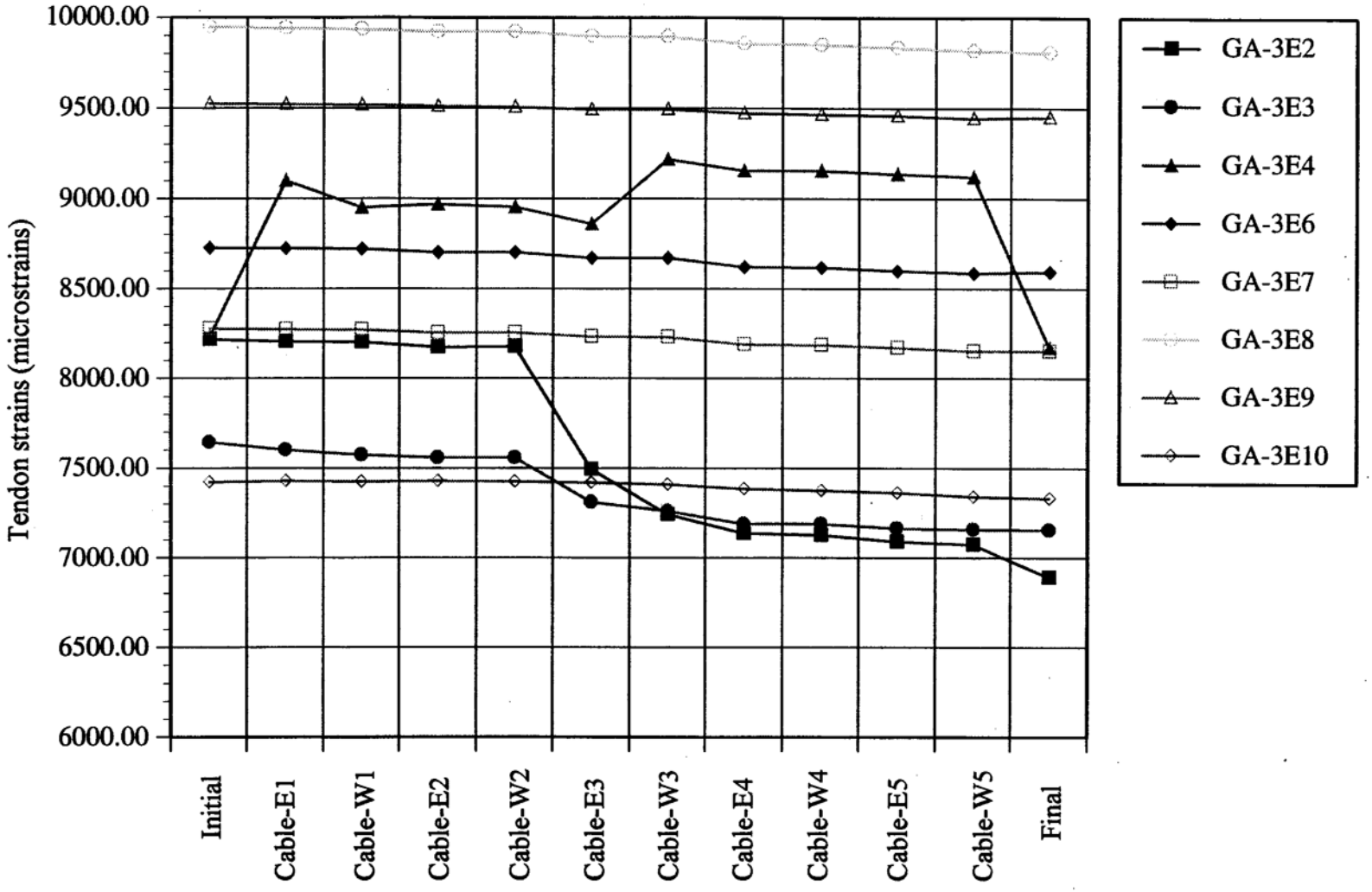

Fig. 4.25e Strains recorded in cable-E3 during prestress release

sequence of prestress release. During the release of prestress, a reduction in strain magnitudes was observed at strain gage locations far from the end face of the beam. This reduction could be attributed to the elastic shortening of the beam due to transfer of prestress. The relationships between change in strains with respect to the release of prestress establish a transfer length between 12 and 18 in. (Table 4.3). **These values of transfer length have a range of 12 to 18 in. because there were no strain gages between 12 to 18 in. from the end face and the strain gages at 24** in. **through midspan showed no change in the strain values.**

Table 4.3 Comparison of measured and theoretical transfer lengths

Description	Transfer length (in)
Steel strands[1]	**13.07**
ARAPREE[2]	**12.59**
ARAPREE[3]	**41.95**
ARAPREE[4]	4.66
ARAPREE[5]	**15.5**
ARAPREE[6]	**15.77**
ARAPREE[7]	**9.59**
Measured	**12.0-18.0**

Notes:

All the values (except measured for transfer length are calculated using ACI 318-89 formula.

1. 0.5 in. dia. 270 ksi steel strand

2. A_ϕ**=0.06882 in** d_b **= 6 mm**

3. A_ϕ**=0.06882 in** d_b **= 20 mm**

4. A_ϕ **=0.186 in** d_b **= 6 mm**

5. A_ϕ**=0.186 in** d_b = 20 mm

6. A_ϕ**=0.06882 in db~,ff = 0.296 in.**

7. A_ϕ**=0.186 in db~ff = 0.4866 in.**

where

$$d_{b-eff} = \sqrt{\frac{4A_\phi}{\pi}}$$

Fig. 4.26 shows the strains recorded in cables W1, El, W3 and E3 after release of prestress. It is not very clear from this graph to make conclusions regarding transfer length. However, Fig. 4.26 illustrates a general trend of strain variation in the cables Wl, E1, W3 and E3

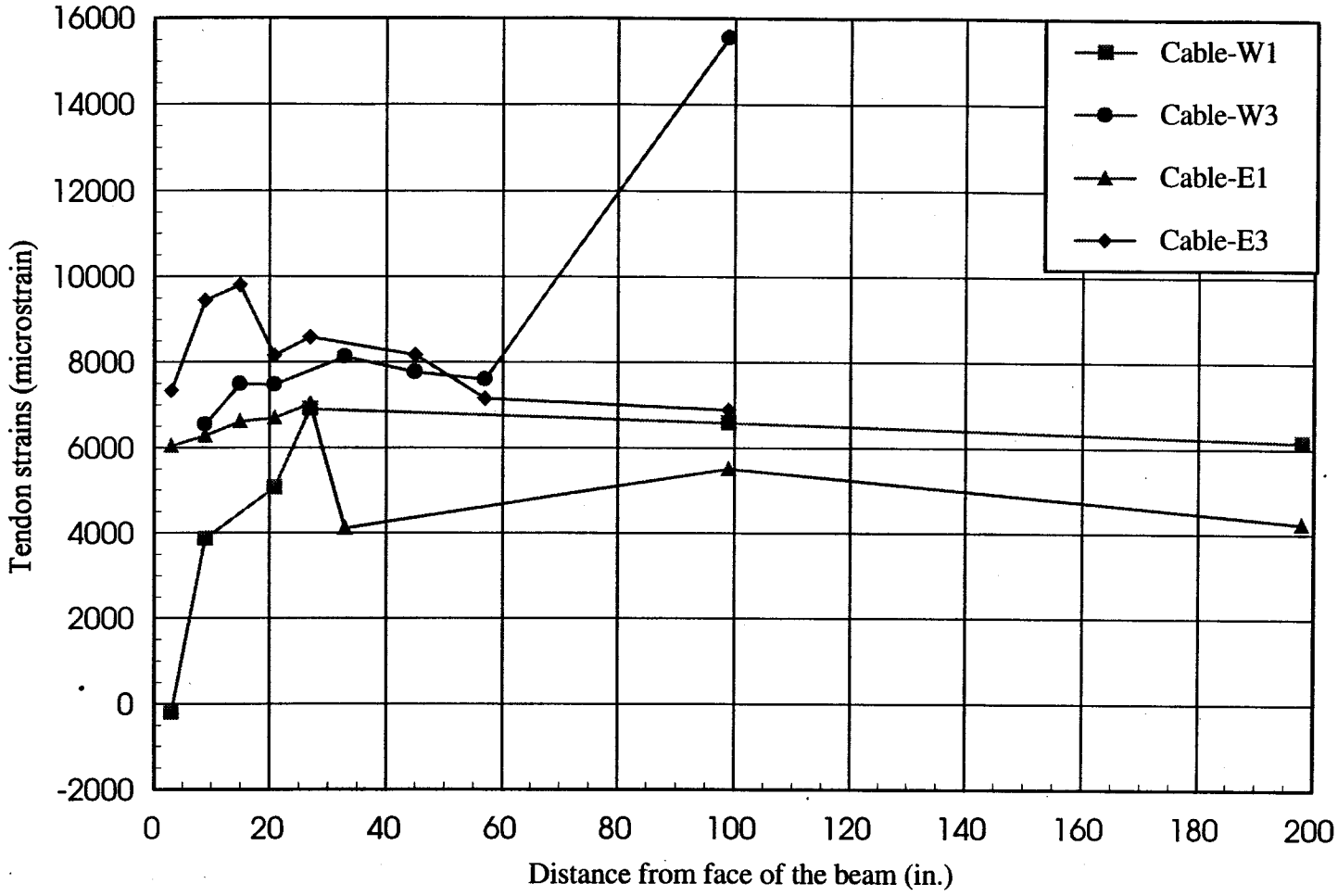

Fig. 4.26 Strains recorded in cables-W1, W3, E1 and E3 after release of prestress

after release of prestress. The reason for the inconsistent strain values can be attributed to the creep in epoxy coating.

The beams were removed from the forms eight days after concreting. Removal of Double-Tee beams was done by using the gantry girder system as shown in Figs. 4.27a and 4.27b. Fig. 4.28 shows the PVC ducts embedded into the top flange for the transverse post-tensioning strands.

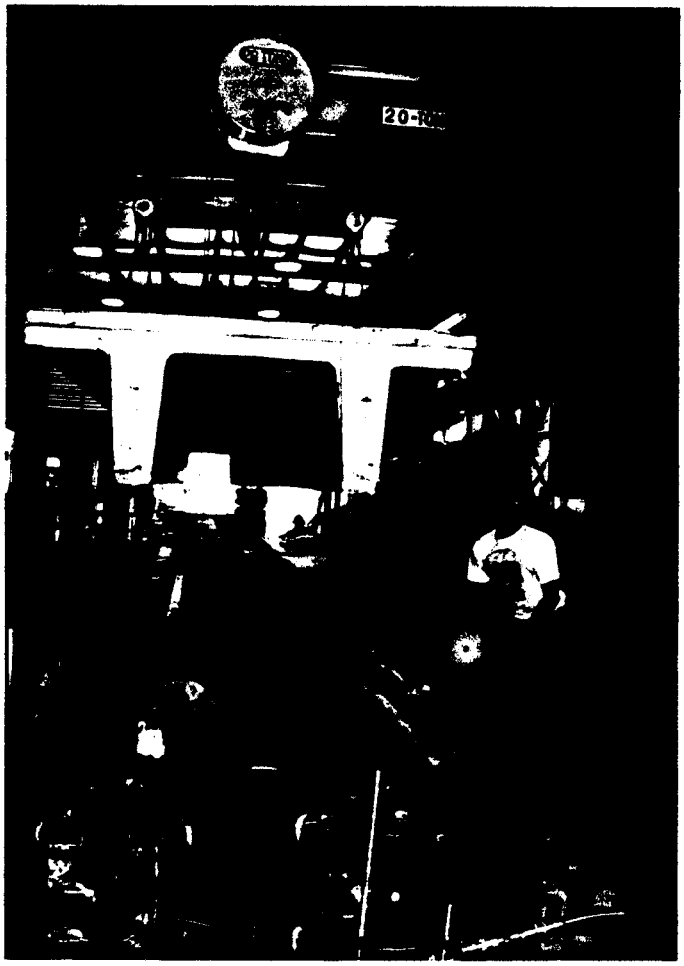

Fig. 4.27a Double-Tee beam being lifted from the steel form work

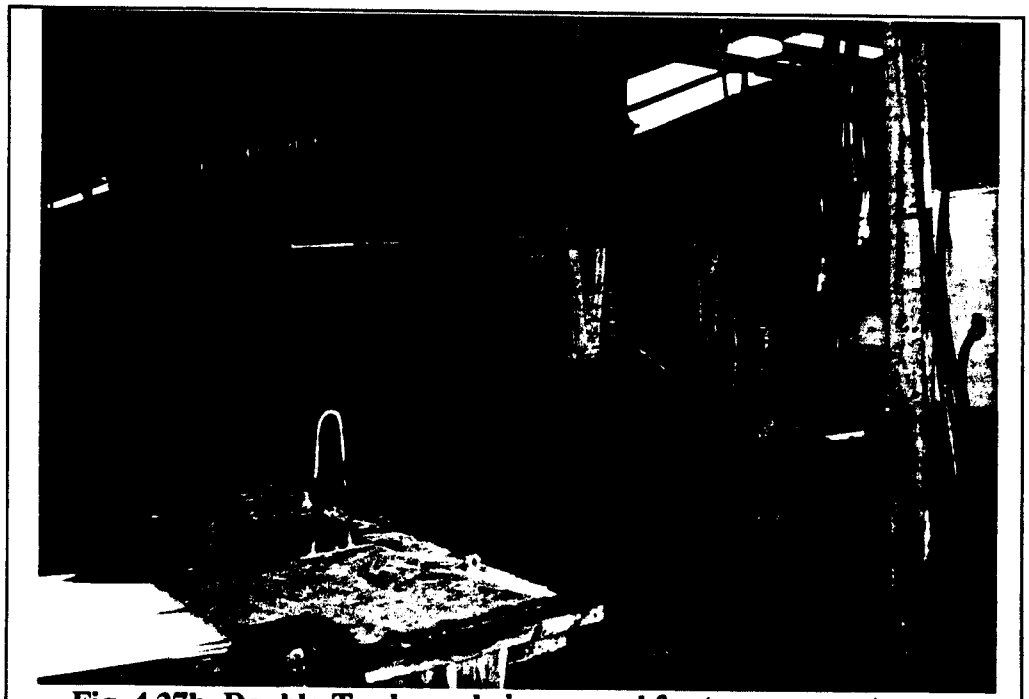

Fig. 4.27b Double-Tee beam being moved for temporary storage

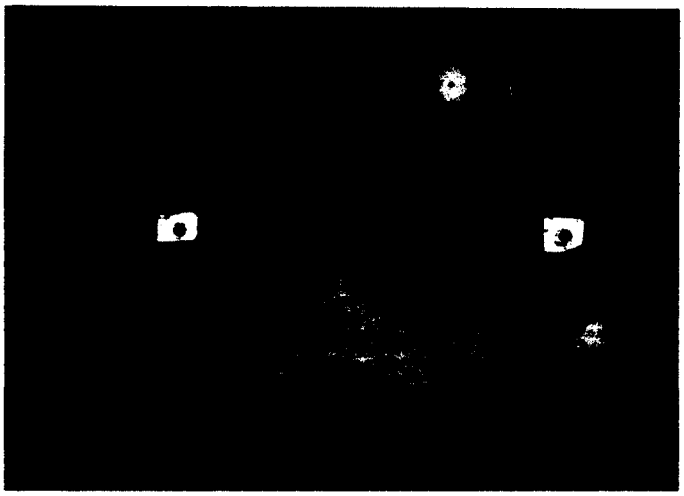

Fig. 4.28 PVC ducts in the top flange

CHAPTER 5

COMPUTER PROGRAM FOR FLEXURAL ANALYSIS OF SECTIONS PRESTRESSED WITH FRP : "FRPFLEX"

5.1 INTRODUCTION

A computer program "FRPFLEX" has been developed to perform flexural analysis of rectangular and Tee beam cross sections with single or multiple prestressed and / or reinforced FRP tendon layers. The linear elastic stress strain properties of FRPs and parabolic stress strain relationship of concrete are taken into account in the formulation. Tension stiffening of concrete in tension zone is also taken into account upto 85 % of ultimate tensile strain in the reinforcing / prestressing layers. FRPFLEX is developed for IBM compatible computers in FORTRAN language and compiled using Microsoft Power Station. The following sections explain the theory and analytical procedures in the development of computer code (FRPFLEX) followed by numerical illustrations.

5.2 LOAD DEFORMATION RELATIONSHIP

The program first determines complete moment - curvature relationship for any given cross section for both pre-cracked and post-cracked stages. Moment and curvature diagrams are obtained for the beam for increments of applied load. The curvature diagram is then numerically integrated along the span to obtain the deflections. The applied load is increased in small increments until the applied moment equals the ultimate moment of resistance of the cross section. This section describes the theoretical details of computing moment - curvature and moment - deflection relationships. Fig. 5.1 presents the general layout of the program in the form of a flowchart.

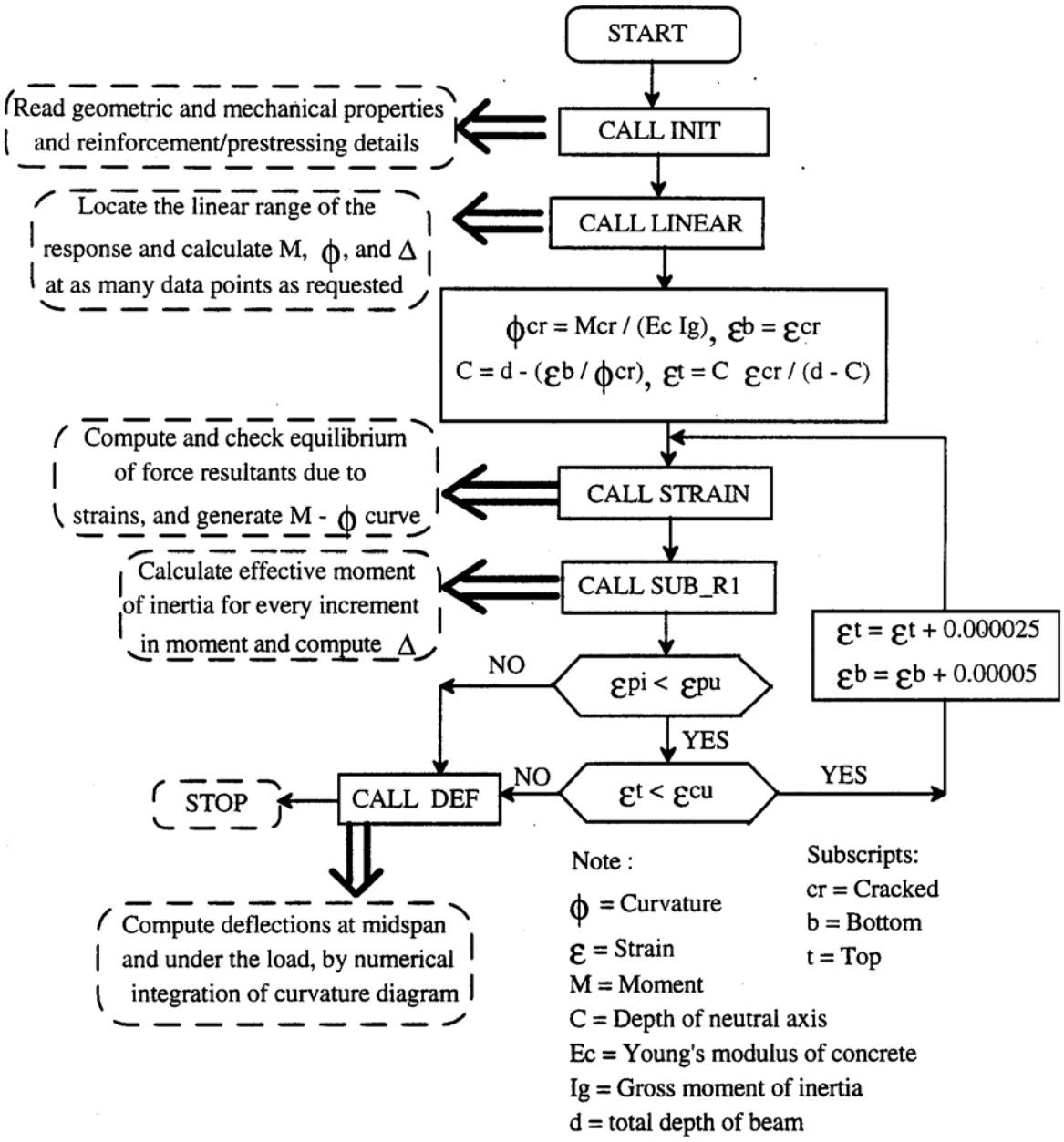

Fig. 5.1 General flowchart for the program

"FRPFLEX" 5.2.1 Stress Block Factors

At any section of a beam the required sectional forces moment, M and internal force, N calculated as follows:

$$\int_{Ac} f_c dA_c + \int_{As} f_s dA_s + \int_{Ap} f_p dA_p = N \qquad \text{.....(5.1)}$$

$$\int_{Ac} f_c y dA_c + \int_{As} f_s y dA_s + \int_{Ap} f_p y dA_p = -M \qquad \text{.....(5.2)}$$

Eqns. 5.1 and 5.2 are evaluated with the aid of stress block factors. Instead of using the actual non-linear stress distributions in concrete, equivalent uniform stress distributions are used in the computation of N and M (Fig. 5.1). For the compressive stress distribution, the stress block factors α_1 and β_1 (rectangular sections) and α_2 and β_2, (flanged sections), are determined using the known strain values at top and bottom layers, so that the magnitude and location of the resultant force are the same in the equivalent uniform stress distribution as in the actual distribution.

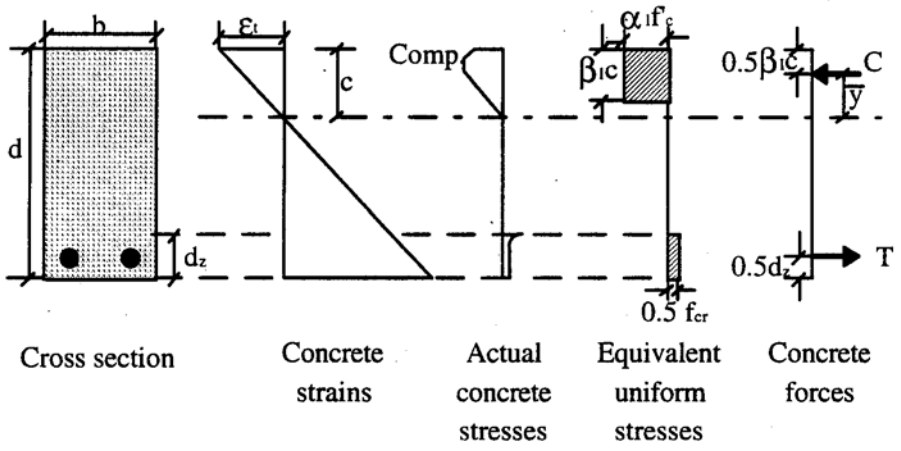

Fig. 5.2 Stress-block factors

The magnitude the compressive force in concrete, C, is given by Eqn. 5.3 and location of the resultant force is expressed by Eqn. 5.4. The parabolic stress strain relationship of concrete is given by Eqn. 5.5. Using Eqns. 5.3 to 5.5, Eqns. 5.6 and 5.7 are derived for a constant width section and Eqns. 5.8 and 5.9 for a flanged section. Eqns. 5.6 and 5.7 or Egns. 5.8 and 5.9 can be used to find the stress block factors for a given state of strains, for a constant width or flanged section respectively.

The compressive force in concrete based on the parabolic stress strain relationship can be equated to the value using the stress block and given by

$$\int_0^c f_c b dy = \alpha f'_c \beta c b \qquad \text{.....(5.3)}$$

The actual location of the resultant compressive force is determined from

$$\bar{y} = \frac{\int_0^c f_c b y dy}{\int_0^c f_c b dy} \qquad \textbf{.....(5.4)}$$

The parabolic stress strain relationship of concrete is assumed a

$$\frac{f_c}{f'_c} = 2\frac{\varepsilon_{cf}}{\varepsilon'_c} - \left(\frac{\varepsilon_{cf}}{\varepsilon'_c}\right)^2 \qquad \textbf{.....(5.5)}$$

where

f_c = stress in concrete corresponding to strain Ecf,

b = width of rectangular section,

d = depth of rectangular section,

c = depth of neutral axis from top fiber,

ε_t = strain in top layer,

ε_b = strain in bottom layer,

ε'_c = concrete strain at compressive strength, f '$_c$,

$\alpha_{1,\ bi}$ = stress block factors for constant width section.

For a rectangular section, the conditions given by Eqns. 5.3 and 5.4 together with Eqn. 5.5 give

$$\alpha_1\beta_1 = \frac{\varepsilon_t}{\varepsilon'_c} - \frac{1}{3}\left(\frac{\varepsilon_t}{\varepsilon'_c}\right)^2 \qquad \textbf{.....(5.6)}$$

$$\beta_1 = \frac{4 - \varepsilon_t / \varepsilon'_c}{6 - 2\varepsilon_t / \varepsilon'_c} \qquad \textbf{....(5.7)}$$

For a flanged section the corresponding α and β values are

$$\alpha_2 = \frac{A}{d_f b_f + (\beta_2 c - d_f) b_w} \qquad .....(5.8)$$

where

$$A = \frac{\varepsilon_t}{c\varepsilon_c'}\left[(c-d_f)^2(b_w-b_f)+b_f c^2\right] - \frac{1}{3}\left(\frac{\varepsilon_t}{c\varepsilon_c'}\right)^2\left[(c-d_f)^3(b_w-b_f)+b_f c^3\right]$$

and β_2 can be evaluated by solving the following quadratic equation:

$$\beta_2^2 \frac{b_w c^2}{2} - \beta_2\left(b_w c - \frac{B}{A} b_w c\right) - d_f\left[\left(c-\frac{d_f}{2}\right)(b_f-b_w) - \frac{B}{A}(b_f-b_w)\right] = 0$$

..... (5.9)

where

$$B = \frac{2}{3}\frac{\varepsilon_t}{c\varepsilon_c'}\left[(c-d_f)^3(b_w-b_f)+b_f c^3\right] - \frac{1}{4}\left(\frac{\varepsilon_t}{c\varepsilon_c'}\right)^2\left[(c-d_f)^4(b_w-b_f)+b_f c^4\right]$$

bf = flange width
df = flange depth

b_w = web width

b_w = web depth

α_2, β_2 = stress block factors for flanged section.

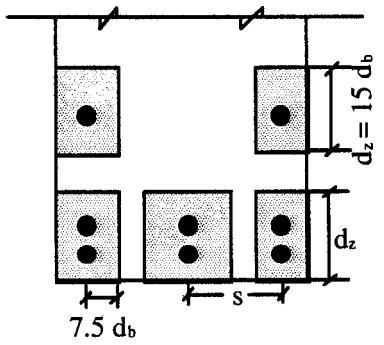

Fig. 5.3 Definition of d z

After the formation of cracks in pure bending region, unlike in the pre-cracked stage, the local curvatures differ along the length with high curvatures occurring at crack locations. Concrete stress at these cracks is zero while the reinforcement carries high stresses. The tensile stress carried by concrete between cracks stiffens the beam. This stiffening effect in concrete

between the cracks is approximated by a uniform stress of 0.5 f_{cr} acting over that part of the "embedment zone" in tension. The effective embedment zone, dz, is defined in Fig. 5.3. Consideration of tension stiffening in flexural analysis would result in computation of the average curvatures / deflections. This would give an accurate estimate of most of the flexural response. Towards the ultimate conditions, analysis at a crack would yield accurate response since failure occurs mostly at a crack. The failure of flexural members with multiple layers of FRP tendons due to tendon rupture, is defined as the failure of bottom most tendon layer. Hence in estimation of the load deformation behavior, tension stiffening effect is considered until the strain in the bottom most tendon reaches 85% of its failure strain.

5.2.2 Moment Curvature Relationship Using Stress Block Factors

Computation of moment-curvature relationship using the stress block factors derived in the earlier section is presented here. The methodology of computing the moment-curvature relationship is presented in Fig. 5.4. Before occurrence of any flexural cracks in a beam member, moment curvature relationship is linear. The moment at which the first flexural crack appears, is termed as cracking moment, M_{cr}. In the case of pretensioned members with prestressing tendons in multiple layers, the cracking moment can be theoretically calculated by

$$M_{cr} = f_{cr} S_b + \left(\Sigma Pi S_b / A_g\right) + \Sigma P_i e_i - M_d \qquad \text{..... (5.10)}$$

Where

f_{cr} = tensile strength of concrete,

S_b = bottom section modulus,

P_i and e_i = force and eccentricity of i^{th} tendon layer, and

M_d = moment due to self weight of the beam.

The program "FRPFLEX" prompts the user to enter the number of data points (moment and corresponding curvature) required in the linear range. Then, the moments are incremented from the initial moment value up to the cracking moment depending on the number

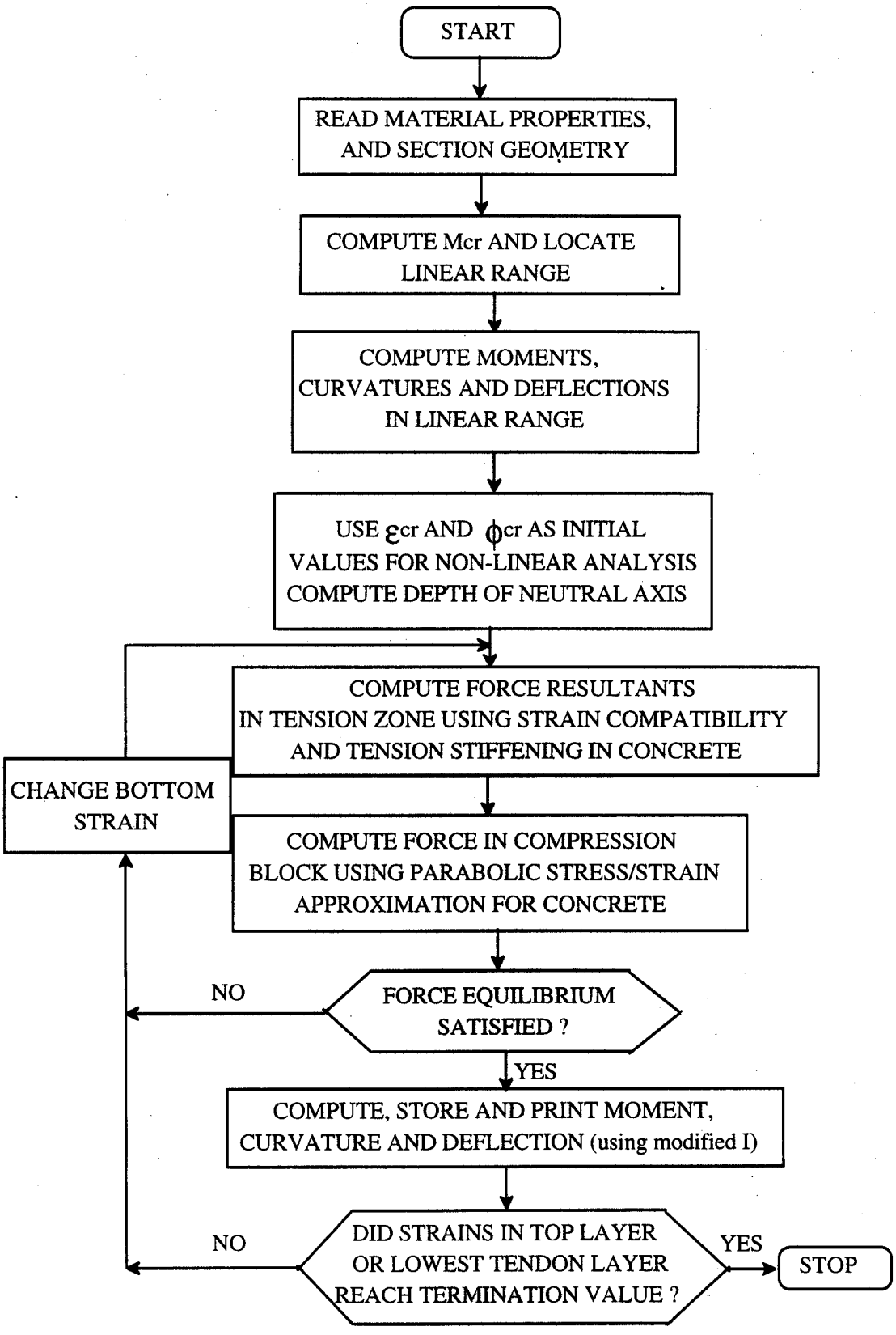

Fig. 5.4 Flowchart for computation of moment-curvature relationship

of data points. For initial and each incremented moment value, the corresponding curvature (0) is **computed as follows:**

$$\phi = \frac{M}{E_c I_g} \qquad \text{..... (5.11)}$$

When the incremented value of the moment equals the cracking moment, further analysis is performed assuming the strains in top and bottom layers, as illustrated in the following equations:

$$\varepsilon_b = \varepsilon_{cr}$$

$$\phi_{cr} = \frac{M}{E_c I_g}$$

$$c = d - \frac{\varepsilon_b}{\phi_{cr}} \text{ and} \qquad \text{..... (5.12)}$$

$$\varepsilon_t = \frac{c\varepsilon_b}{d - c}$$

Depending on whether the section is of constant width or flanged, and the neutral axis is falling in the web or the flange, the stress block factors are computed using Eqns. 5.6 to 5.9. **From the values of the top and bottom strains and depth of the neutral axis, the strains in the prestressing and / or reinforcing layer(s) are interpolated, and then added to the initial prestressing strain to obtain the total strain. The corresponding force(s) in prestressing and / or reinforcing layer(s) is then calculated using the following equation:**

$$F_i = \varepsilon_i A_i E$$

where

F_i = **total force in the ith tendon layer,**

A_i **= total area of the ith tendon layer, and**

E = Young's modulus of the tendons.

The forces in all the tendon layers are then added to get the total tensile force in tendon layers. Tensile force imparted by the concrete in tension zone, i.e., tension stiffening effect is also computed as explained in the earlier section. Then using the stress block factors and Eqn. 5.1, the

resultant force N is computed (assuming tensile and compressive forces to be positive and negative respectively). If the resultant force is zero, the internal moment is computed by taking moments of the forces in the prestressing and / or reinforcing layers and tensile force in concrete, about the point where the compression force is acting in the compression block (Eqn. 5.2). If the resultant force, N, is not zero, then the bottom or top strain is increased depending on whether the resultant force is positive or negative, in small increments. Then, all the above mentioned computations are repeated with the new set of top and bottom strains in an iterative manner until the resultant force is zero. For the set of strains when the resultant force is zero, the internal moment is computed together with the corresponding curvature as follows:

$$\phi = \frac{\varepsilon_t}{c} \qquad \textbf{(5:13).}$$

The internal moment computed and corresponding curvature (5.13) will constitute one data point on the moment - curvature relationship. Then, both top and bottom strains are incremented and the next set of iterations is performed to obtain the next data point. The preceding computations are repeated, before program terminates, until one of the following occurs:

i) concrete in the compression zone fails by crushing (i.e., value of top strain is equal to the crushing strain in concrete which is specified by the user),

ii) bottom most tendon layer has ruptured (i.e., the strain in this tendon layer has reached the ultimate tensile strain which is specified by the user) and the user opted to terminate the program at this point,

iii) all the tendon layers are ruptured.

At this point the complete response of the section is printed as output by the program in the first output file that contains moments, and corresponding midspan deflections (computed using ACI bilinear formulation), curvatures, and strains in top layer in concrete and in tendon layers.

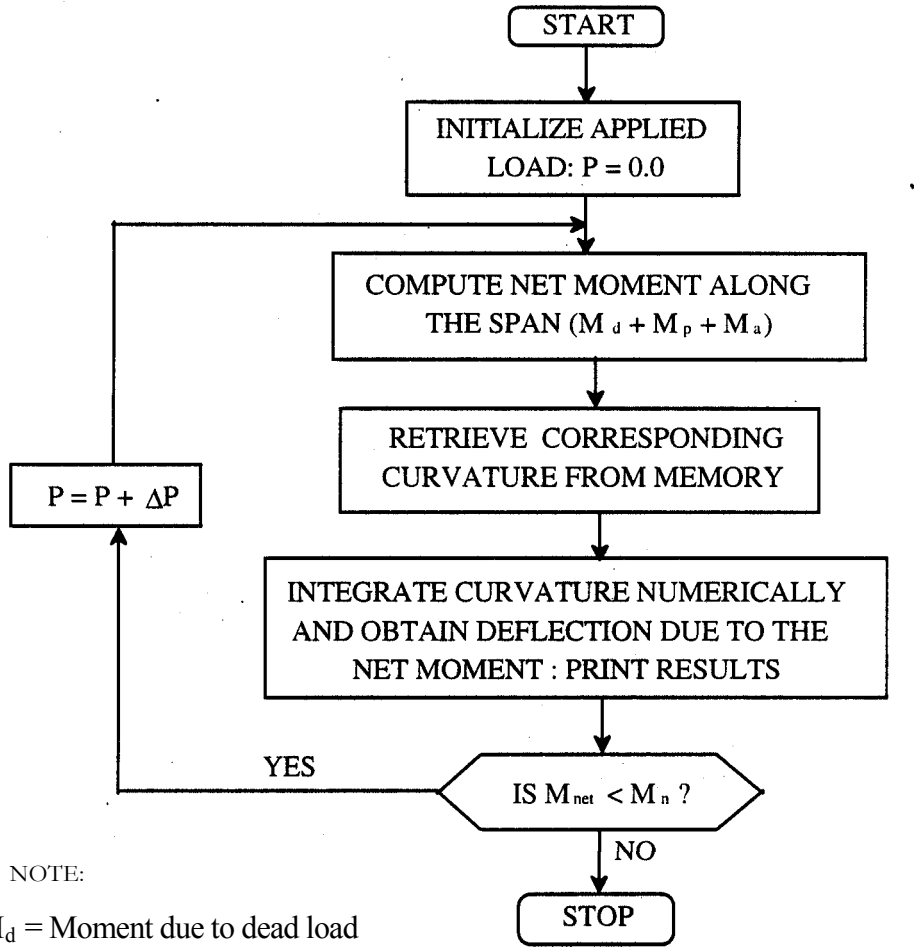

Fig. 5.5 Flow chart for computation of deflections

5.2.3 Moment Deflection Relationship by Integration of Curvature

The program computes moment-deflection relationship for a beam with symmetric four point applied loading. Fig. 5.5 presents the flowchart for computation of deflections by integration of curvature diagram. The distance from the beam end to the first load point and distance thereafter upto midspan are divided into ten portions each. Thus, upto the midspan, the beam is discretized into twenty parts using twenty one points. The applied load is first initialized

to zero and then the net bending moment (including dead load, live load, and prestressing moments) is obtained at each of the twenty one points. The curvatures corresponding to these computed net moments are calculated at each point from the moment curvature relationship.

The curvature diagram is then numerically integrated from the beam end upto midspan to obtain the deflections at midspan. The applied load is increased in small increments, until the net moment at any section equals the ultimate moment of resistance of the cross section. Once the net moment equals the ultimate moment capacity, the program closes the second output file, which contains the moments and the corresponding deflections.

5.3 NUMERICAL EXAMPLES

Flexural response analyses of members prestressed and/or reinforced with FRPs were performed using "FRPFLEX" and the results of these analyses presented in this section. Example #1 deals with the flexural analysis of a beam with square cross section prestressed with two CFRP tendons at the same level, example #2 considers a rectangular beam with multi-layered AFRP prestressing tendons and example #3 presents analysis of a rectangular beam pretensioned with GFRP tendons.

5.3.1 Example # 1 : Beam with Single Layer Prestressing Tendons

Fig. 5.5 shows the cross sectional details of the beam used in the analysis. The properties of materials used are as follows:

concrete compressive strength, f', = 6,000 psi.,

concrete strain at f',, E'_c **= 2.13E-3;**

concrete tensile strength, f_c**, = 310 psi,**

concrete strain at f, F, = 7.56E-5,

Young's modulus, E, = 4,098,000 psi,

concrete crushing strain = 0.003,

rupture strength of CFRP, fpu = 307,000 psi.,

rupture strain of CFRP, F_u = 0.0157,

Young's modulus, E_{pu} = 20,467,000 psi.

The prestressing details are as follows:

number of prestressing layers = 1,

depth of the prestressing layer from top fiber of the section = 8.25 in,

effective prestressing force in the layer = 40,000 lbs.,

prestressing strain = 0.00863.

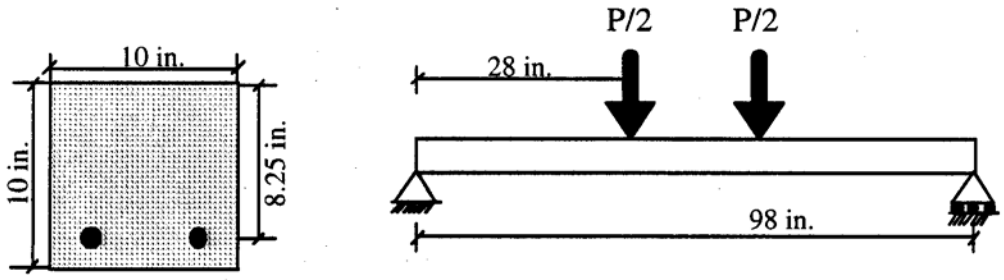

Fig. 5.6 Square beam prestressed with CFRP

Figs. 5.7a and 5.7b present the predicted moment-curvature and moment-deflection relationships respectively. It was predicted by "FRPFLEX" that the beam failure would be due to rupture of the prestressing tendons. The flexural moment capacity and the moment deflection relationships compare very well with the experimental results that are performed at Florida Atlantic University [Arockiasamy, 1994].

5.3.2 Example #2: Rectangular Beam with Multi-Layered Prestressing Tendons

Fig. 5.8 shows the cross sectional details of the beam used in the analysis.

The properties of materials used are as follows:

concrete compressive strength, f_c = 6,000 psi.,

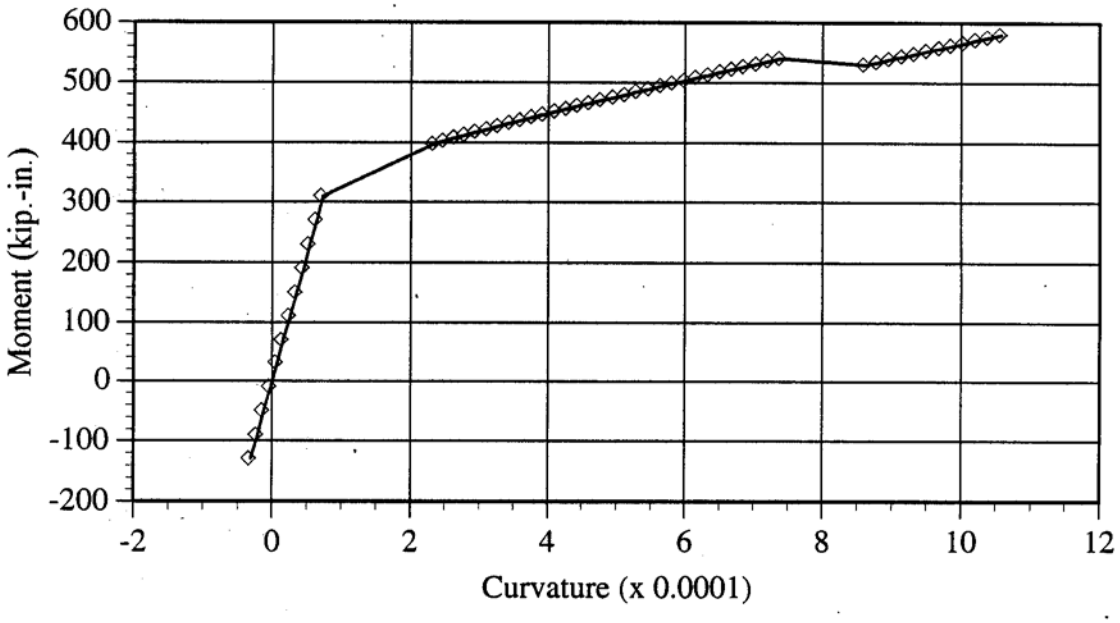

Fig. 5.7a Predicted moment-curvature relationship : Example # 1

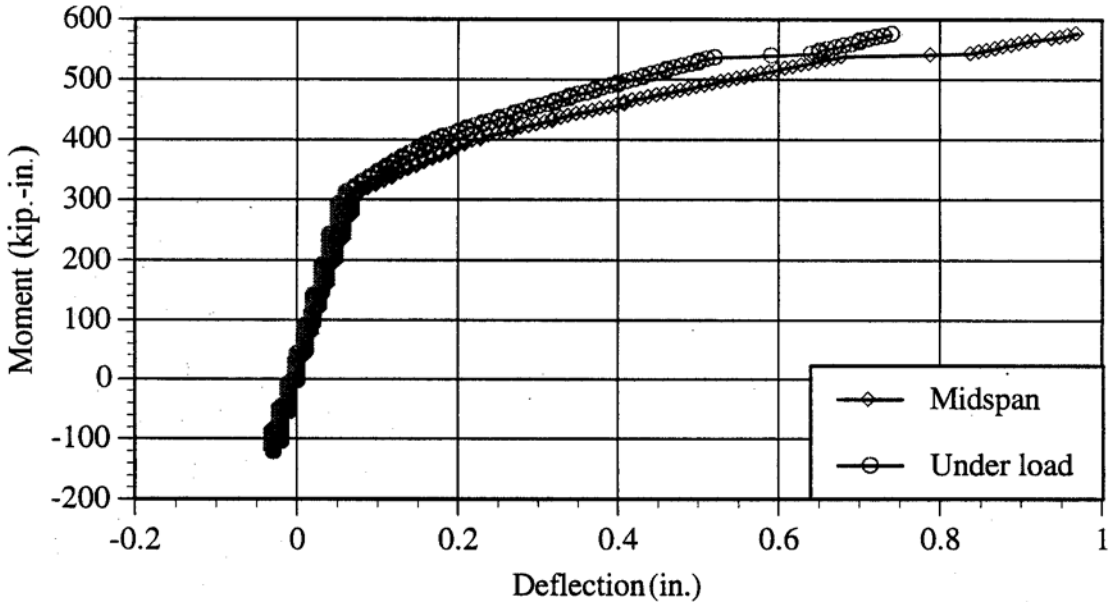

Fig. 5.7b Predicted moment-deflection relationship : Example # 1

concrete strain at f'_c, e'_c = 2.13E-3,

concrete tensile. strength, f_a = 310 psi.,

concrete strain at f_a, F_r = 7.56E-5,

Young's modulus, E, = 4,098,000 psi.,

concrete crushing strain = 0.004,

rupture strength of AFRP, $f_{p,,}$ = 435,000 psi.,

rupture strain of AFRP, $e_{c,,}$ = 6.023,

Young's modulus, E_p = 18,913,000 psi.

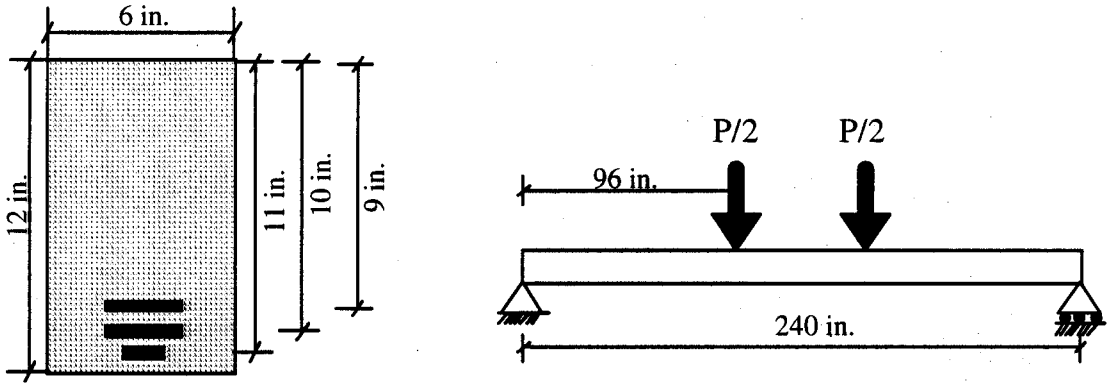

Fig. 5.8 Rectangular beam prestressed with multiple layers of AFRP tendons

The prestressing details are as follows:
number of prestressing layers =

3. *First layer:*

depth of the first prestressing layer = 11 in, area of

the prestressing layer = 0.06882 in^2, effective

prestressing force in the layer = 15,000 lbs.,

prestressing strain in the layer = 0.0115.

Second layer:

depth of the second prestressing layer = 10 in., area

of the prestressing layer = 0.13764 in^2., effective

prestressing force in the layer = 20,0001bs.,

prestressing strain in the layer = 0.00767.

Third layer:
depth of the third prestressing layer = 9 in.,

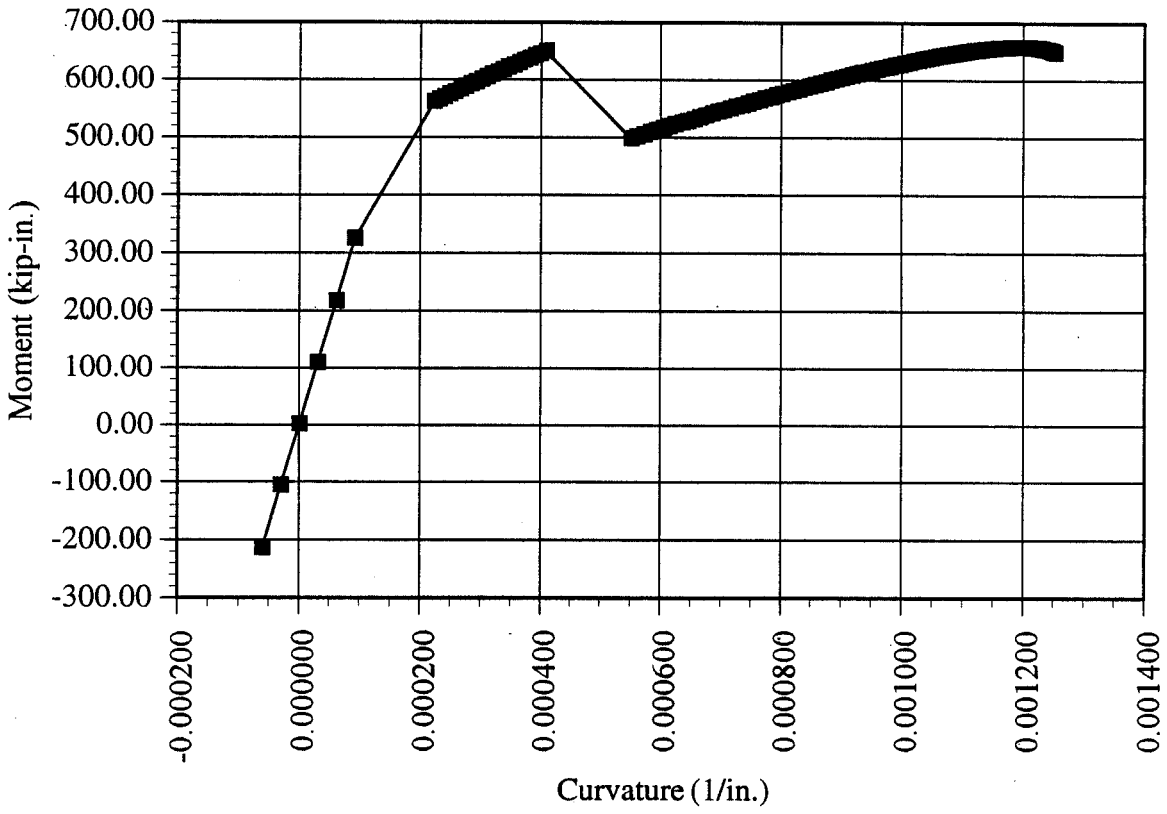

Fig. 5.9a Predicted moment-curvature relationship : Example # 2

area of the prestressing layer = 0.13764 in^2.,
effective prestressing force in the layer = 20,0001bs.,

prestressing strain in the layer = 0.00767.

This example demonstrates the capability of the program to analyze beams with multilayered prestressing tendons. The program continues the analysis until all prestressing layers are ruptured or concrete in the compression zone crushes. In this example, the bottom most tendon layer ruptures before the top concrete strain reaches the ultimate value. The analysis is opted to be continued at this point and the beam finally fails by crushing of concrete in compression zone. Figs. 5.9a and 5.9b present the predicted moment-curvature and moment-deflection relationships respectively. The decrease in moment magnitude and continual increase in the deformation, seen in the graphs (Figs. 5.9a and 5.9b) after the rupture of the bottom most tendon, shows the

capability of the program to compute response of beams with multi-layered FRP prestressing tendons.

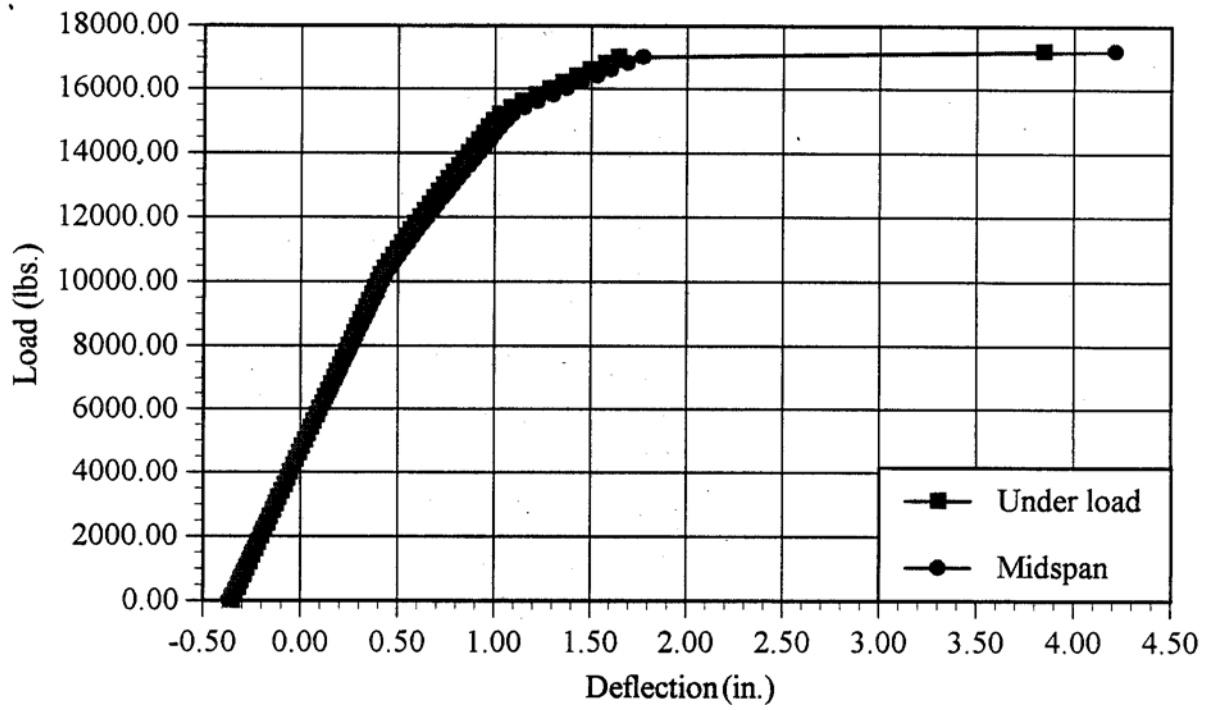

Fig. 5.9b Predicted moment-deflection relationship : Example # 2

5.3.3 Example #3: Rectangular Beam Prestressed with GFRP Tendons

Sen [1992] tested a series of beams prestressed with GFRP tendons to estimate the load carrying capacity after exposing the beam specimens to marine environment. In this illustration, load-deflection behavior of a typical. beam (designated as FG-M9) is estimated and compared with the experimental results. The prestressing forces after losses were considered in the analysis. Fig. 5.10 **shows the cross sectional details of the beam used in the analysis.**

The properties of materials used are as follows:

concrete compressive strength, f , = 6,840 psi.,

concrete strain at f'$_c$, ε'_c = 2.13E-3,

concrete tensile strength, f$_{cr}$ = 434 psi.,

concrete strain at f_z, ε_c, = 6.87143E-5,

Young's modulus, E_c = 4,714,144.7 psi.,

concrete crushing strain = 0.003,

rupture strength of GFRP, fpu = 285,760 psi.,

rupture strain of GFRP, ε_{cu} = 0.0304, Young's

modulus, E_{pu} = 9.4E6 psi.

The prestressing details are as follows:

number of prestressing layers = 1,

depth of the prestressing layer from top fiber of the section = 6.0 in.,

effective prestressing force in the layer (inclusive of all the tendons) = 24509.0 lbs.,

average prestressing strain = 0.01024.

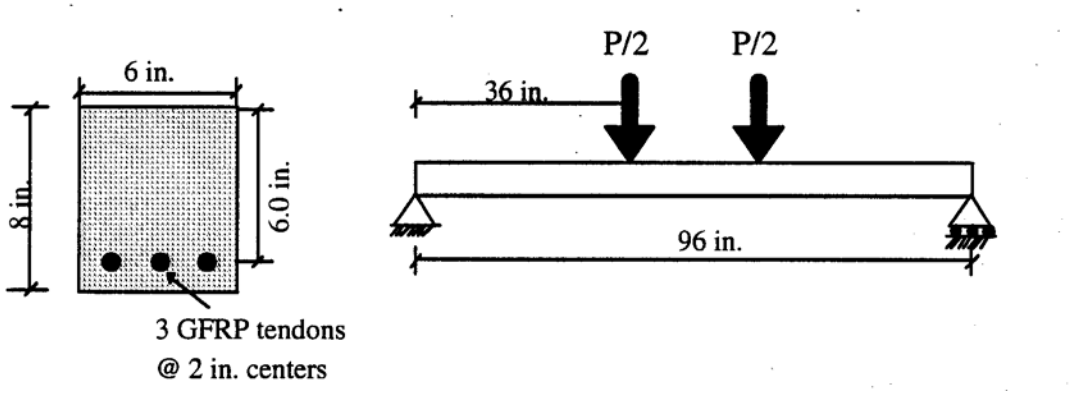

Fig. 5.10 Rectangular beam prestressed with GFRP

Fig. 5.11 shows the experimental load deflection behavior [Sen, 1992]. The predicted load-deflection relationship is shown in Fig. 5.12. It can be seen from the comparison of the Figs. 5.11 and 5.12, that predicted load-deflection relationship compares well with that of the experiment.

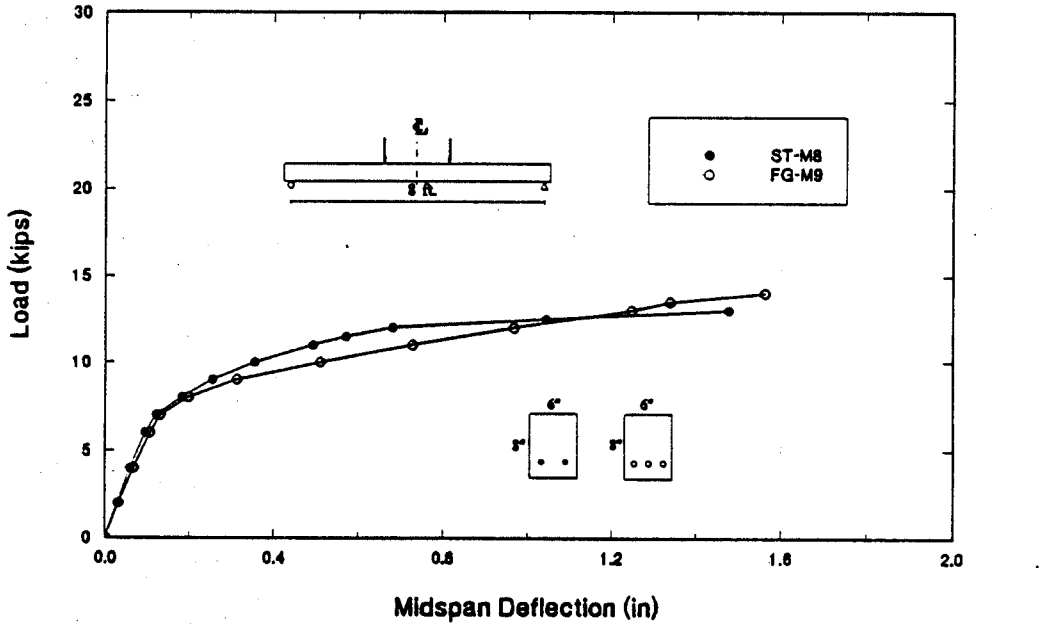

Fig. 5.11 Load-deflection behavior of rectangular beam prestressed with GFRP

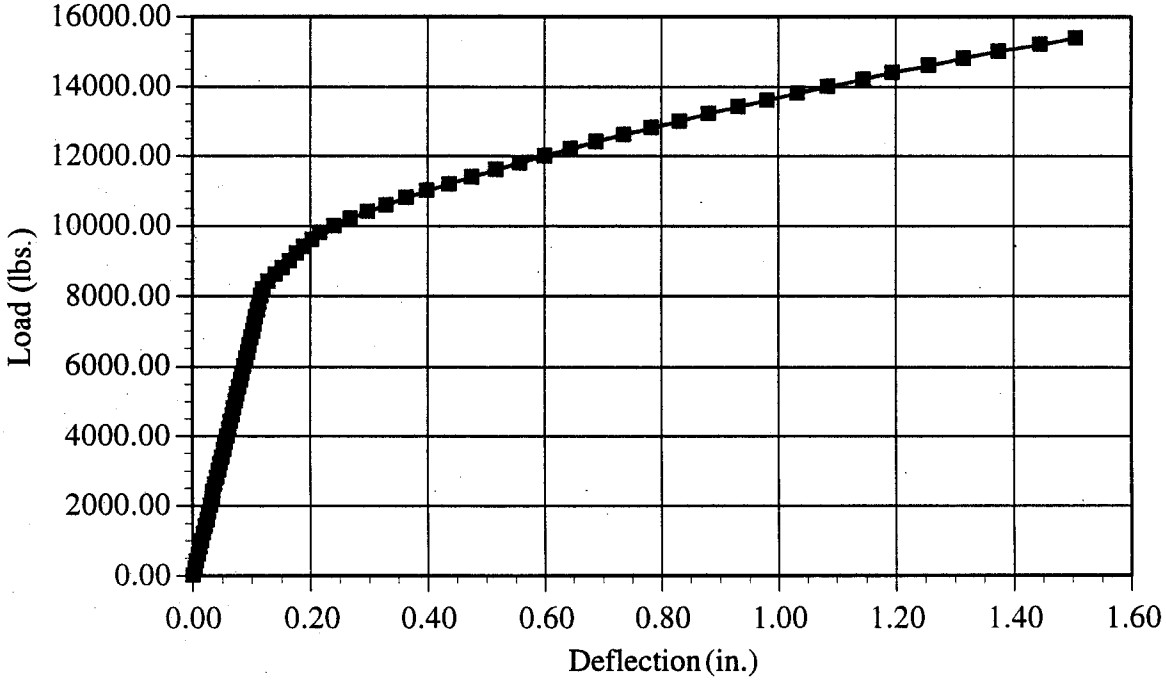

Fig. 5.12 Predicted load-deflection relationship : Example # 3

The input data prepared for the analysis of the rectangular beam shown in Fig. 5.10 is given in section 5.3.2.1. Section 5.3.2.2 presents the output data files created by "FRPFLEX" for moment-curvature and load-deflection relationships.

5.3.3.1 Input data file

6.0 8.0 6840 2.13E-3 434.197 6.87143E-5 4714144.7

1

285760 10.1 le6 0.0304 0.003

0.375 6.0 0.2106 24509.0 0.01024

36.0 96.0 4.167

10 { number of data points requested in the linear range }

5.3.3.2 Output data files

Load-deflection relationship

MID .M	DEFM	LOAD .M	DEFQ	Load
-.442E+05	-.440E-01	-.445E+05	-.411E-01	.000E+00
-.406E+05	-.411E-01	-.409E+05	-.385E-O1	.200E+03
-.370E+05	-.383E-01	-.373E+05	-.358E-01	.400E+03
-.334E+05	-.354E-01	-.337E+05	-.332E-01	.600E+03
-.298E+05	-.325E-01	-.301E+05	-.305E-01	.800E+03
-.262E+05	-.296E-01	-.265E+05	-.279E-01	.100E+04
-.226E+05	-.267E-01	-.229E+05	-.252E-01	.120E+04
-.190E+05	-.238E-01	-.193E+05	-.226E-01	.140E+04
-.154E+05	-.209E-01	-.157E+05	-.199E-01	.160E+04
-.118E+05	-.181E-01	-.121E+05	-.173E-01	.180E+04
-.822E+04	-.152E-01	-.852E+04	-.146E-01	.200E+04

Load-deflection relationship(continued)

MID -M	DEFM	LOAD -M	DEFQ	Load
-.462E+04	-.123E-01	-.492E+04	-.120E-01	.220E+04
-.102E+04	-.941E-02	-.132E+04	-.934E-02	.240E+04
.258E+04	-.652E-02	.228E+04	-.669E-02	.260E+04
.618E+04	-.364E-02	.588E+04	-.404E-02	.280E+04
.978E+04	-.755E-03	.948E+04	-.139E-02	.300E+04
.134E+05	.213E-02	.131E+05	.125E-02	.320E+04
.170E+05	.501E-02	.167E+05	.390E-02	.340E+04
.206E+05	.790E-02	.203E+05	.655E-02	.360E+04
.242E+05	.108E-01	.239E+05	.920E-02	.380E+04
.278E+05	.137E-01	.275E+05	.118E-01	.400E+04
.314E+05	.166E-01	.311E+05	.145E-01	.420E+04
.350E+05	.194E-01	.347E+05	.171E-01	.440E+04
.386E+05	.223E-01	.383E+05	.198E-01	.460E+04
.422E+05	.252E-01	.419E+05	.224E-01	.480E+04
.458E+05	.281E-01	.455E+05	.251E-01	.500E+04
.494E+05	.310E-01	.491 E+05	.277E-01	.520E+04
.530E+05	.339E-01	.527E+05	.304E-01	.540E+04
.566E+05	.367E-01	.563E+05	.330E-01	.560E+04
.602E+05	.396E-01	.599E+05	.357E-01	.580E+04
.638E+05	.425E-01	.635E+05	.383E-01	.600E+04
.674E+05	.454E-01	.671 E+05	.410E-01	.620E+04
.710E+05	.483E-01	.707E+05	.436E-01	.640E+04
.746E+05	.512E-01	.743E+05	.463E-01	.660E+04
.782E+05	.541 E-01	.779E+05	.489E-01	.680E+04
.818E+05	.569E-01	.815E+05	.516E-01	.700E+04
.854E+05	.598E-01	.851E+05	.542E-01	.720E+04
.890E+05	.627E-01	.887E+05	.569E-01	.740E+04

Load-deflection relationship (continued)

MID -M	DEFM	LOAD -M	DEFQ	Load
.926E+05	.656E-01	.923E+05	.595E-01	.760E+04
.962E+05	.685E-01	.959E+05	.622E-01	.780E+04
.998E+05	.714E-01	.995E+05	.648E-01	.800E+04
.103E+06	.742E-01	.103E+06	.675E-01	.820E+04
.107E+06	.827E-01	.107E+06	.749E-01	.840E+04
.111E+06	.947E-01	.110E+06	.855E-01	.860E+04
.114E+06	.107E+00	.114E+06	.961E-01	.880E+04
.118E+06	.119E+00	.117E+06	.107E+00	.900E+04
.121E+06	.131E+00	.121E+06	.117E+00	.920E+04
.125E+06	.144E+00	.125E+06	.129E+00	.940E+04
.129E+06	.158E+00	.128E+06	.142E+00	.960E+04
.132E+06	.172E+00	.132E+06	.154E+00	.980E+04
.136E+06	.195E+00	.135E+06	.175E+00	.100E+05
.139E+06	.223E+00	.139E+06	.199E+00	.102E+05
.143E+06	.253E+00	.143E+06	.225E+00	.104E+05
.147E+06	.285E+00	.146E+06	.254E+00	.106E+05
.150E+06	.319E+00	.150E+06	.283E+00	.108E+05
.154E+06	.354E+00	.153E+06	.315E+00	.110E+05
.157E+06	.392E+00	.157E+06	.349E+00	.112E+05
.161 E+06	.431 E+00	.161 E+06	.383E+00	.114E+05
.165E+06	.472E+00	.164E+06	.419E+00	.116E+05
.168E+06	.513E+00	.168E+06	.456E+00	.118E+05
.172E+06	.555E+00	.171E+06	.494E+00	.120E+05
.175E+06	.599E+00	.175E+06	.533E+00	.122E+05
.179E+06	.644E+00	.179E+06	.573E+00	.124E+05
.183E+06	.691E+00	.182E+06	.615E+00	.126E+05
.186E+06	.738E+00	.186E+06	.658E+00	.128E+05

Load-deflection relationship

MID -M	DEFM	LOAD M	DEFQ	Load
.190E+06	.787E+00	.189E+06	.701E+00	.130E+05
.193E+06	.836E+00	.193E+06	.745E+00	.132E+05
.197E+06	.886E+00	.197E+06	.790E+00	.134E+05
.201E+06	.936E+00	.200E+06	.836E+00	.136E+05
.204E+06	.988E+00	.204E+06	.882E+00	.138E+05
.208E+06	.104E+01	.207E+06	.929E+00	.140E+05
.211 E+06	.110E+01	.211 E+06	.979E+00	.142E+05
.215E+06	.115E+01	.215E+06	.103E+01	.144E+05
.219E+06	.121E+01	.218E+06	.108E+01	.146E+05
.222E+06	.127E+01	.222E+06	.114E+01	.148E+05
.226E+06	.133E+01	.225E+06	.119E+01	.150E+05
.229E+06	.140E+01	.229E+06	.125E+01	.152E+05
.233E+06	.146E+01	.233E+06	.131E+01	.154E+05

Moment - curvature

DELTA	PHI	M	**e -tendon**	**e -t**
-.42973E-01	-.40617E-04	-.49018E+05		
-.31052E-01	-.27881E-04	-.33648E+05		
-.19131E-01	-.15145E-04	-.18277E+05		
-.72095E-02	-.24089E-05	-.29071E+04		
.47115E-02	.10327E-04	.12463E+05		
.16633E-01	.23063E-04	.27833E+05		
.28554E-01	.35800E-04	.43204E+05		
.40475E-01	.48536E-04	.58574E+05		
.52396E-01	.61272E-04	.73944E+05		
.64317E-01	.74008E-04	.89315E+05		

Moment - curvature relationship (continued)

DELTA .76238E-01	PHI .86744E-04	M .10468E+06	e -tendon	e -t
END OF LINEAR				
.52639E+00	.22900E-03	.13263E+06	.10989E-01	.62524E-03,
.54276E+00	.24531E-03	.13420E+06	.11062E-01	.65024E-03
.55904E+00	.26198E-03	.13573E+06	.11137E-01	.67524E-03
.57522E+00	.27898E-03	.13724E+06	.11214E-01	.70024E-03
.59135E+00	.29630E-03	.13872E+06	.11293E-01	.72524E-03
.60746E+00	.31390E-03	.14018E+06	.11373E-01	.75024E-03
.62357E+00	.33177E-03	.14162E+06	.11455E-01	.77524E-03
.63969E+00	.34990E-03	.14304E+06	.11539E-01	.80024E-03
.65585E+00	.36828E-03	.14446E+06	.11624E-01	.82524E-03
.67205E+00	.38687E-03	.14585E+06	.11711E-01	.85024E-03
.68832E+00	.40568E-03	.14724E+06	.11799E-01	.87524E-03
.70462E+00	.42467E-03	.14862E+06	.11888E-01	.90024E-03
.72101E+00	.44385E-03	.14999E+06	.11978E-01	.92524E-03
.73748E+00	.46320E-03	.15135E+06	.12069E-01	.95024E-03
.75401E+00	.48269E-03	.15270E+06	.12161E-01	.97524E-03
.77062E+00	.50232E-03	.15405E+06	.12254E-01	.10002E-02
.78731E+00	.52209E-03	.15539E+06	.12347E-01	.10252E-02
.80407E+00	.54196E-03	.15672E+06	.12442E-01	.10502E-02
.82091E+00	.56195E-03	.15805E+06	.12536E-01	.10752E-02
.83782E+00	.58203E-03	.15937E+06	.12632E-01	.11002E-02
.85481E+00	.60219E-03	.16069E+06	.12728E-01	.11252E-02
.87186E+00	.62243E-03	.16200E+06	.12824E-01	.11502E-02
.88898E+00	.64273E-03	.16330E+06	.12921E-01	.11752E-02
.90616E+00	.66309E-03	.16460E+06	.13018E-01	.12002E-02
.92340E+00	.68351E-03	.16589E+06	.13116E-01	.12252E-02

Moment - curvature relationship

DELTA	PHI	M	e_tendon	e_t
.94070E+00	.70396E-03	.16718E+06	.13213E-01	.12502E-02
.95804E+00	.72444E-03	.16846E+06	.13311E-01	.12752E-02
.97542E+00	.74495E-03	.16973E+06	.13409E-01	.13002E-02
.99284E+00	.76547E-03	.17100E+06	.13508E-01	.13252E-02
.10103E+01	.78602E-03	.17227E+06	.13606E-01	.13502E-02
.10278E+01	.80656E-03	.17352E+06	.13704E-01	.13752E-02
.10453E+01	.82710E-03	.17477E+06	.13802E-01	.14002E-02
.10628E+0 l	.84764E-03	.17602E+06	.13901E-01	.14252E-02
.10804E+01	.86816E-03	.17725E+06	.13999E-01-	.14502E-02
.10979E+01	.88866E-03	.17848E+06	.14097E-01	.14752E-02
.11154E+0 l	.90914E-03	.17971 E+06	.14195E-01	.15002E-02
.11330E+01	.92959E-03	.18092E+06	.14292E-01	.15252E-02
.11505E+01	.95000E-03	.18213E+06	.14390E-01	.15502E-02
.11680E+01	.97039E-03	.18333E+06	.14487E-01	.15752E-02
.11855E+01	.99071E-03	.18452E+06	.14584E-01	.16002E-02
.12030E+01	.10110E-02	.18570E+06	.14681E-01	.16252E-02
.12204E+01	.10312E-02	.18688E+06	.14777E-01	.16502E-02
.12378E+01	.10514E-02	.18805E+06	.14873E-01	.16752E-02
.12551E+01	.10715E-02	.18921E+06	.14969E-01	.17002E-02
.12724E+01	.10916E-02	.19036E+06	.15064E-01	.17252E-02
.12896E+01	.11116E-02	.19150E+06	.15159E-01	.17502E-02
.13068E+01	.11315E-02	.19264E+06	.15254E-01	.17752E-02
.13239E+01	.11513E-02	.19376E+06	.15348E-01	.18002E-02
.13409E+01	.11711E-02	.19487E+06	.15441E-01	.18252E-02
.13579E+01	.11908E-02	.19598E+06	.15534E-01	.18502E-02
.13748E+01	.12104E-02	.19708E+06	.15627E-01	.18752E-02
.13915E+01	.12299E-02	.19816E+06	.15719E-01	.19002E-02

Moment - curvature relationship

DELTA	PHI	M	e_tendon	e_t
.14082E+01	.12493E-02	.19924E+06	.15811E-01	.19252E-02
.14248E+01	.12686E-02	.20030E+06	.15902E-01	.19502E-02
.14413E+01	.12879E-02	.20136E+06	'. 15992E-01	.19752E-02
.14577E+01	.13070E-02	.20241E+06	.16082E-01	.20002E-02
.14740E+01	.13260E-02	.20344E+06	.16171 E-01	.20252E-02
.14901 E+O 1	.13449E-02	.20447E+06	.16259E-01	.20502E-02
.15061 E+O 1	.13638E-02	.20548E+06	.16347E-01	.20752E-02
.15220E+01	.13825E-02	.20648E+06	.16435E-01	.21002E-02
.15378E+01	.14011E-02	.20747E+06	.16521E-01	.21252E-02
.15534E+01	.14196E-02	.20845E+06	.16607E-01	.21502E-02
.15689E+01	.14379E-02	.20942E+06	.16692E-01	.21752E-02
.15843E+01	.14562E-02	.21038E+06	.16777E-01	.22002E-02
.15995E+01	.14743E-02	.21133E+06	.16861E-01	.22252E-02
.16145E+01	.14923E-02	.21226E+06	.16944E-01	.22502E-02
.16294E+01	.15102E-OZ	.21318E+06	.17026E-01	.22752E-02
.16441 E+O 1	.15280E-02	.21409E+06	.17108E-01	.23002E-02
.16586E+01	.15456E-02	.21499E+06	.17188E-01	.23252E-02
.16730E+01	.15631E-02	.21588E+06	.17268E-01	.23502E-02
.16872E+01	.15804E-02	.21675E+06	.17347E-01	.23752E-02
.17012E+01	.15977E-02	.21761E+06	.17426E-01	.24002E-02
.17151E+01	.16148E-02	.21846E+06	.17503E-01	.24252E-02
.17287E+01	.16317E-02	.21929E+06	.17580E-01	.24502E-02
.17422E+01	.16485E-02	.22011E+06	.17656E-01	.24752E-02
.17554E+01	.16652E-02	.22092E+06	.17731E-01	.25002E-02
.17685E+01	.16817E-02	.22172E+06	.17805E-01	.25252E-02
.17814E+01	.16981E-02	.22250E+06	.17878E-01	.25502E-02
.17940E+01	.17143E-02	.22326E+06	.17951E-01	.25752E-02

Moment - curvature relationship

DELTA	PHI	M	e -tendon	e t
.18065E+01	.17304E-02	.22402E+06	.18022E-01	.26002E-02
.18187E+01	.17463E-02	.22476E+06	.18093E-01	.26252E-02
.18307E+01	.17621E-02	.22548E+06	.18162E-01	.26502E-02
.18425E+01	.17777E-02	.22619E+06	.18231E-01	.26752E-02
.18541E+01	.17931E-02	.22689E+06	.18299E-01	.27002E-02
.18654E+0 l	.18084E-02	.22757E+06	.18365E-01	.27252E-02
.18765E+01	.18236E-02	.22824E+06	.18431E-01	.27502E-02
.18874E+01	.18385E-02	.22889E+06	.18496E-01	.27752E-02
.18980E+01	.18534E-02	.22953E+06	.18560E-01	.28002E-02
.19084E+01	.18680E-02	.23015E+06	.18623E-01	.28252E-02
.19185E+01	.18825E-02	.23076E+06	.18685E-01	.28502E-02
.19284E+01	.18968E-02	.23135E+06	.18745E-01	.28752E-02
.19380E+01	.19109E-02	.23192E+06	.18805E-01	.29002E-02
.19474E+01	.19249E-02	.23248E+06	.18864E-01	.29252E-02
.19565E+01	.19387E-02	.23303E+06	.18922E-01	.29502E-02
.19654E+0 1	.19523E-02	.23355E+06	.18978E-01	.29752E-02
.19740E+01	.19657E-02	.23406E+06	.19034E-01	.30002E-02

CHAPTER 6

EXPERIMENTAL STUDIES ON FLEXURAL BEHAVIOR OF SINGLE DOUBLE-TEE BEAM

6.1 INTRODUCTION

Fiber reinforced plastic reinforcements in the form of bars, tendons and strands are being explored in reinforced and prestressed concrete for two types of applications in new structures and repair of existing structures. Prestressing, bonded or unbonded seems a natural field of application of FRPs in new structures because of their distinct advantages. This chapter presents the flexural behavior of single Double-Tee beam prestressed with ARAPREE tendons. One Double-Tee beam with an reinforcing index of approximately 0.09 was cast and tested under four point loading. The beam curvature, load deflection characteristics, crack pattern, strains in ARAPREE tendons at typical locations and ultimate strength are investigated in this study. The test results are compared with predicted analytical values using the computer code "FRPFLEX".

6.2 EXPERIMENTAL SETUP AND INSTRUMENTATION

Static ultimate test was performed on a single Double-Tee beam at the Structural Research Center, FDOT, Tallahassee, Florida. The objective of this test was to investigate the flexural behavior of the beam and correlate the results with those of the experimental model bridge system. The clear span of the test beam was 30 ft. with 9 in. wide end supports. The load was applied simultaneously by two hydraulic jacks, each located at 7.5 ft. away from the center of the beam (Fig. 6.1). This particular loading pattern on the beam would result in a constant applied moment within the midspan region.

Fig. 6.1 Hydraulic jacks positioned on Double-Tee beam for static test

Assessing the feasibility of a non-metallic prestressing element, ARAPREE in traditional civil engineering structures, would require a comprehensive study of several important parameters. This static ultimate test was designed such that all necessary data would be acquired for a detailed examination of the flexural behavior of the beam. Comprehensive instrumentation plan was carried out on the test beam (Fig. 6.2). The parameters under study were deflections, concrete strains across the cross section, tendon strains and slip. Owing to the high ultimate elongation of ARAPREE and the long span of the Double-Tee beam, large deflections were expected and hence the quarter and midspan locations were instrumented with deflection transducers, which had a range of 8 in.

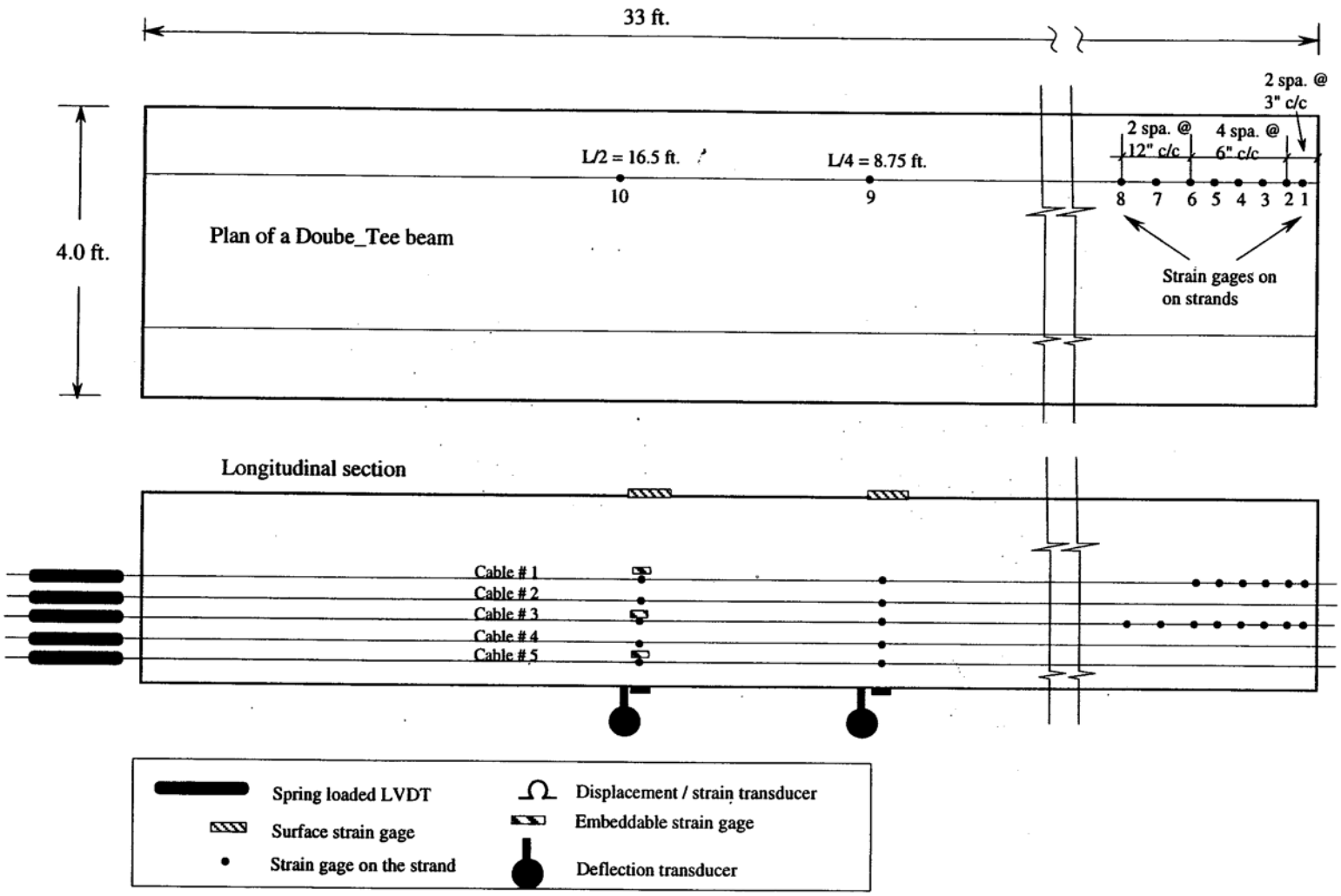

Fig. 6.2 Instrumentation details for single Double-Tee beam

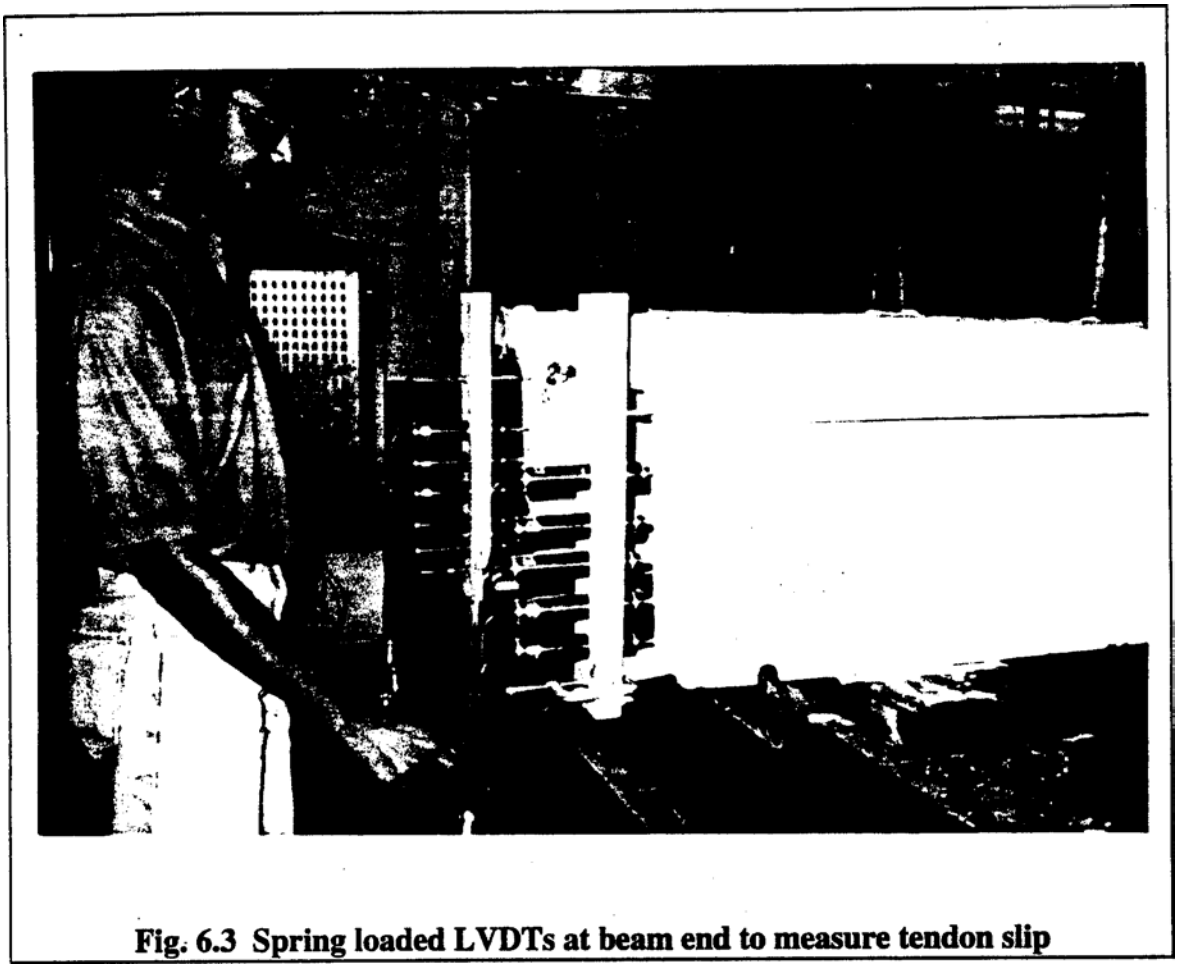

Fig. 6.3 Spring loaded LVDTs at beam end to measure tendon slip

Slip of a prestressing tendon is a measure of the tendon bond with concrete. At both ends of the beam, the ARAPREE tendons were instrumented with spring loaded LVDTs (Fig. 6.3) to measure the tendon slip. Strain gages were attached to all the prestressing tendons at mid and quarter spans to establish the strain profile at various load stages. Three out of five ARAPREE tendons (top, middle and bottom layers) were also instrumented with Carlson strain gages. Strain data recorded by these Carlson gages were compared with those measured by the gages on the ARAPREE cables (Fig. 6.4). The data acquisition was carried out using MEGADAC system, manufactured by OPTIM.

Fig. 6.4 Strain gages installed on ARAPREE cables

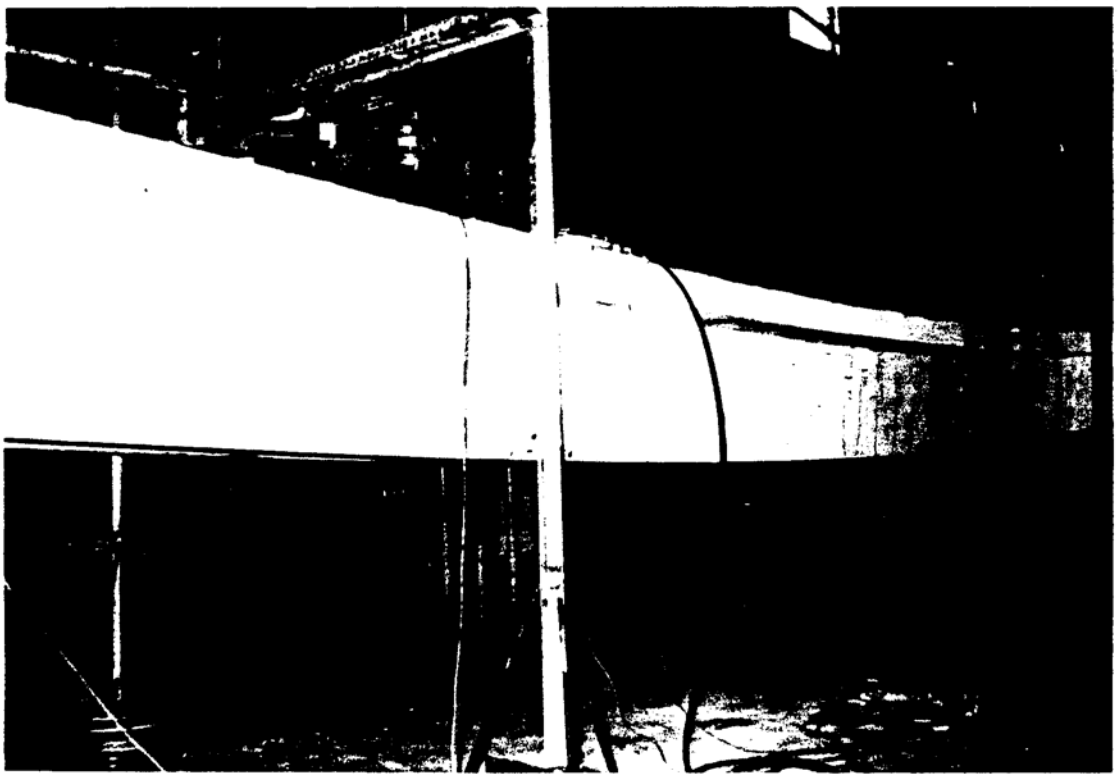

Fig. 6.5 Double-Tee beam static flexural test in progress

6.3 TEST PROCEDURE

The four point static test was performed on a single Double-Tee beam. Load was applied using two hydraulic jacks placed 7.5 ft. away from the center of the beam. The distance between the load points (15 ft.) was representative of the simulated value of the rear axle spacing of HS 20-44 truck. The single Double-Tee beam was tested in three load stages. Fig. 6.5 shows the flexural test in progress. Fig. 6.6 presents the positions of hydraulic jack for loading and typical LVDT for measuring deflection. During the first load stage, the maximum applied load at each jack position was 10.5 kips. The first crack was observed in the constant bending moment region between the jack positions at a load of 5.5 kips. The maximum deflection was more than 3.1 in. and the LVDTs had to be reset before continuing with further loading. Therefore, the beam was unloaded gradually

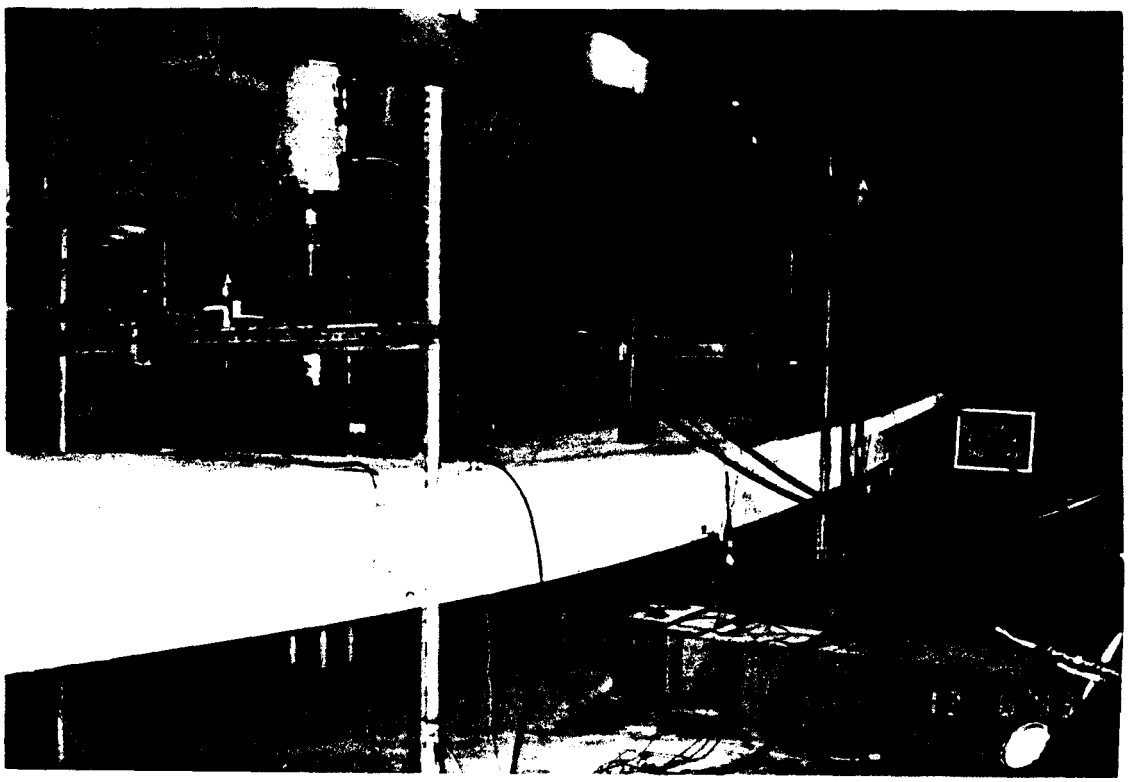

Fig. 6.6 Positions of hydraulic jack for load and LVDT for deflection measurement

to zero and reloaded in the second stage to the maximum value of 16.0 kips. The maximum deflection at this load was about 7.2 in., which necessitated resetting of both the LVDTs and the hydraulic jacks. During the third load stage, the maximum applied load at the ultimate stage was 18.8 kips. This load does not correspond to the ultimate collapse load of the Double-Tee beam. The maximum deflection recorded in the third load stage was about 8.5 in. During the second and third load stages, steel plates of known thicknesses were inserted between the LVDTs and the beam to enable measurement of the excessive deflections.

6.4 RESULTS AND DISCUSSIONS

6.4.1 Concrete and Tendon Strains

The concrete strains on the compression face and the tendon strains at different levels are plotted and shown in Fig. 6.7. The tendons are bonded to the concrete and therefore, the variations iii the tendon strains are used to obtain the strain profiles across the beam depth. This strain variation can be seen to be almost linear across the depth of the cross section. The first crack was observed at a load of 5.5 kips. at each load point. The strains recorded by the strain gages installed on the tendons were comparable to those from Carlson gages embedded in concrete at the level of the tendons until the formation of the first crack. However, with the onset of first crack, the two strains were found to vary significantly with further increase in the applied load and hence only the tendon strains were considered to obtain the strain variation.

Just prior to the first crack, the strain variation in the concrete is linear as observed from Fig. 6.7. The strain variations corresponding to the maximum loads of 10.0, 15.7, and 18.8 kips, in the three load stages are also shown in Fig. 6.7. The compressive strains in concrete on the top surface and typical tendon strains could be seen to increase with applied loading (Figs. 6.8a and 6.8b).

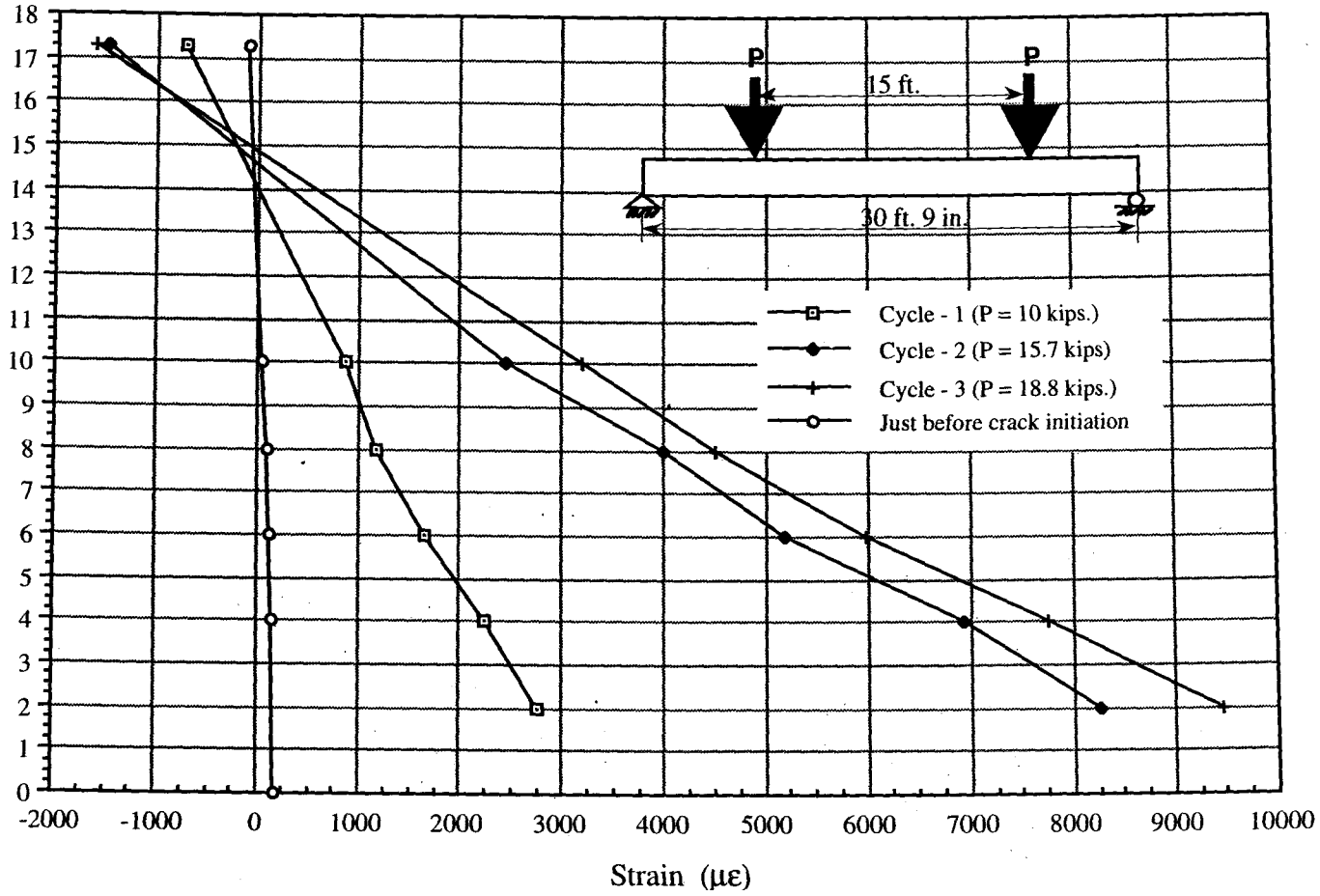

Fig. 6.7 Strain profiles corresponding to maximum loads in the three load stages

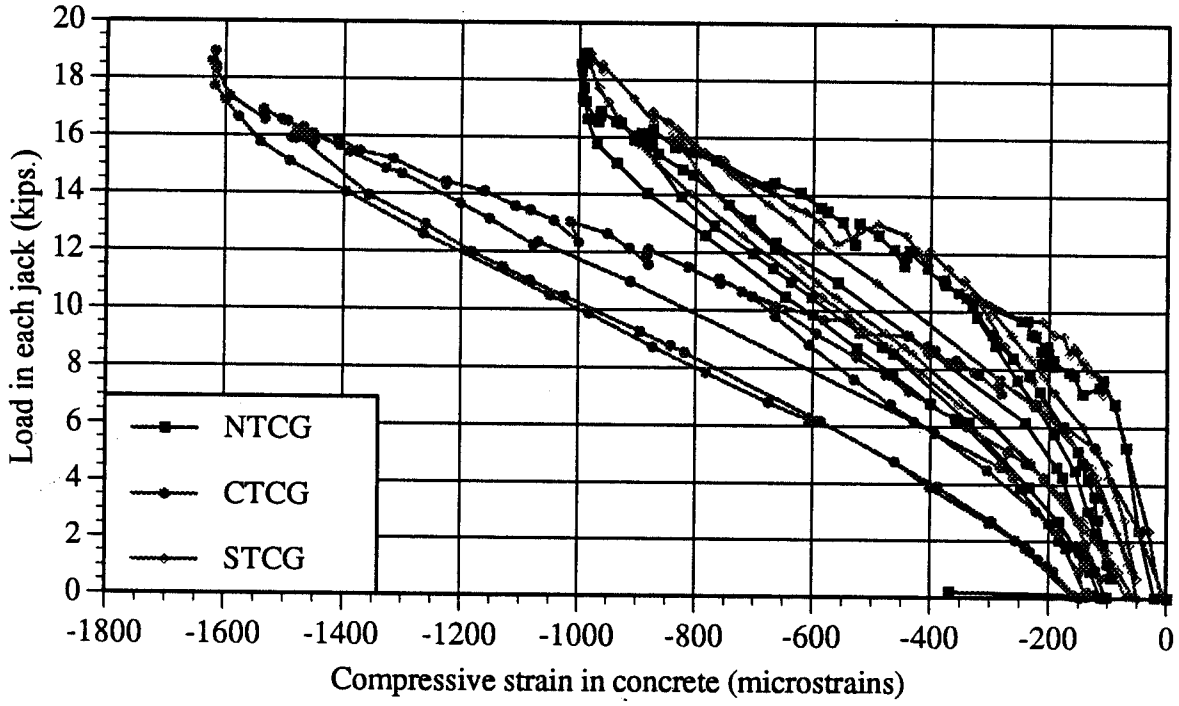

Fig. 6.8a Measured concrete strains at mid (CTCG), north-quarter (NTCG) and south-quarter (STCG) spans

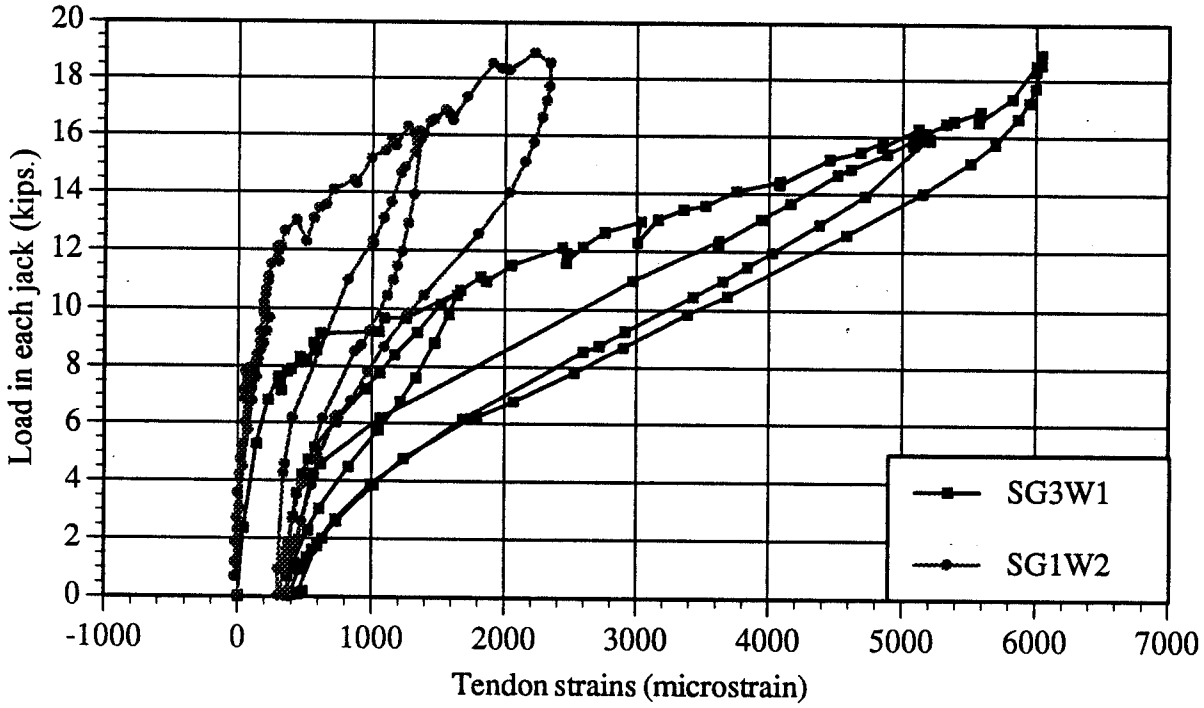

Fig. 6.8b Measured strains in typical tendons at mid (SG3W1) and quarter (SG1W2) spans

This variation shows the initial elastic and linear behavior with changes into the non-linear range with a transition zone between the linear and the non-linear regime. The maximum strain values due to the applied loading are 1600 and 9500 microstrains in concrete and the tendon respectively.

Concrete strains recorded at north and south quarter. spans exhibit uniform and similar bilinear behavior (Fig. 6.8a). Also, at midspan location concrete strains vary bilinearly with increased strain values for the same load in subsequent load stages. An average permanent compressive strain of about 150 and 175 microstrains is observed at mid and quarter span locations respectively. Variation of typical tendon strains with respect to the applied loading in all three load stages is shown in Fig. 6.8b. Similar to concrete strain variations, the behavior of tendon strains was also bilinear in all three load stages. Rate of increase of tendon strains in all the load stages was larger at midspan than that at quarter span location. Tendon strains also showed reduced stiffness in subsequent load stages up to the strain' value corresponding to maximum applied load in the previous load stage. An average permanent tensile strain of about 400 microstrains was observed in tendons after third load stage.

6.4.2 Load Deflection Characteristics

Figs. 6.9a - 6.9c show the load deflection relationships recorded under both the loads and mid-span for all the three load stages. It is observed that the load deflection relationship is bilinear with a short transition zone between the two linear portions. The load deflection relationship is linear upto the first crack load of 5.5 kips. in the first load stage. Although the section is cracked during the first load stage, the beam exhibits limited linear behavior in the second and third load stages possibly due to the prestress upto a applied load of about 4.0 kips in each jack. Small decreases in the applied load were observed in Figs. 6.9a -6.9c while the beam was being loaded. This could be due to the formation of additional cracks with applied load that cause decrease in the load values. It could be observed that the load-deflection behavior was similar at all the three locations. Reduced stiffnesses and resulting increase in the rate of change of deflections were observed at all the locations in subsequent load stages.

Figs. 6.10a - 6.10c show the comparison of the load-deflection relationships at south and north quarter spans for the three load stages. Similar load-deflection relationship is observed at north and south quarter spans in the first load stage. In the second load stage, a higher maximum deflection and consequently a higher permanent deflection was observed at south quarter span. It was observed in Fig. 6.10c that the rate of increase of deflection, at north and south quarter span locations, with respect to applied load was similar and uniform. The larger permanent deflection at south quarter span location in second load stage could be attributed to the deviation in deflections observed between north and south quarter spans (Fig. 6.10c).

Figs. 6.11 a, 6.11b and 6.11c show the measured load-deflection variations at midspan for first, second and third load stages respectively. The beam exhibits reduced stiffness in each successive load stage. - This is due to the cracks formed in the previous load stage which contributes to larger deflection. It is observed that the point corresponding to maximum load and deflection values for the first load stage is coincident exactly on the load deflection curve for the second load stage. The same observation could be made for the load deflection curves for the load stages two and three. The deflection recovery in all the three loading cycles was excellent, wherein a final permanent deflection of only about 0.4 in. was observed. The elastic nature of ARAPREE tendons with ability to carry load efficiently at very high strain levels can be attributed to this behavior. Fig. 6.12 shows the deflected shape of the Double-Tee beam. The Double-Tee beam deflected shape near the maximum load during the ultimate load test is shown in Fig. 6.13.

6.4.3 Crack Pattern and Bond Behavior

The crack pattern in the web of the Double-Tee beam at the maximum applied load is shown in Fig. 6.14. It is seen that the flexural cracks are uniformly spaced within and some distance beyond the applied load points. The flexural cracks were almost vertical within the constant bending moment region and somewhat inclined from the vertical outside the points of load application.

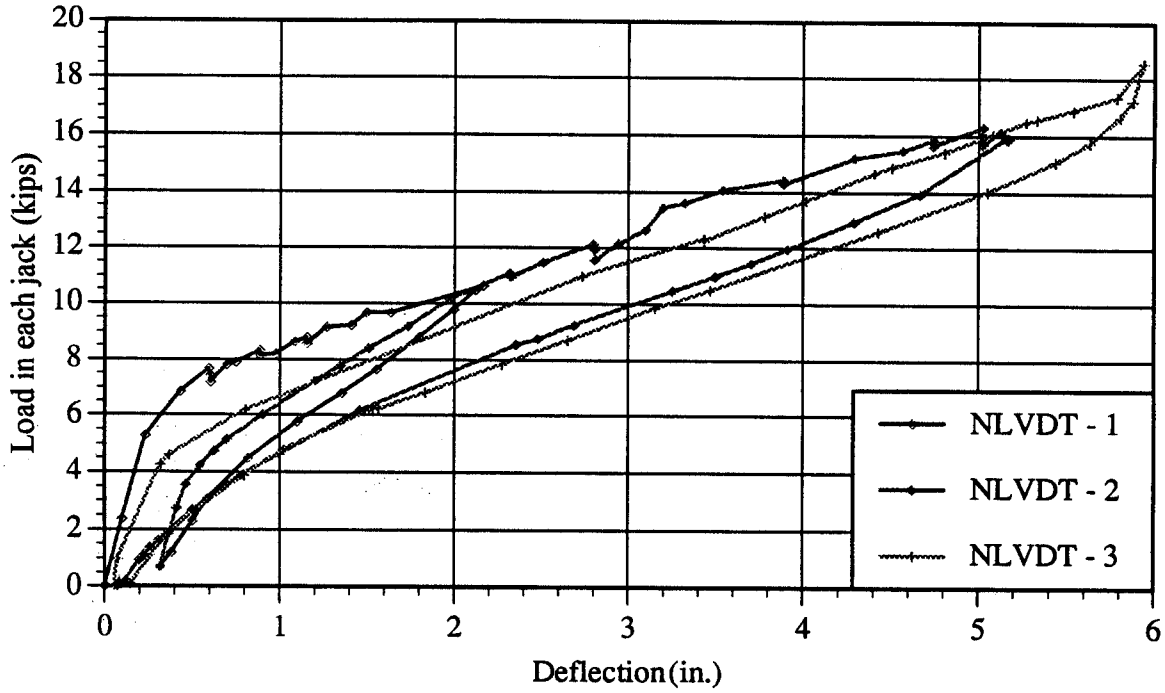

Fig. 6.9a Measured load deflection relationship at north-quarter span

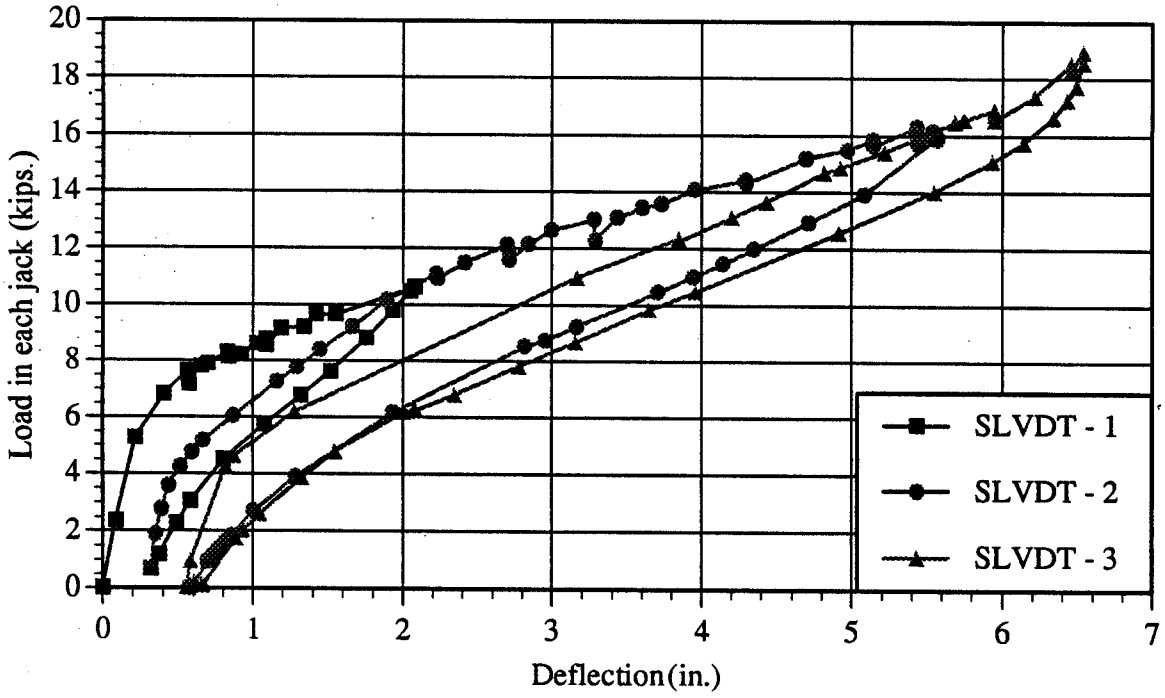

Fig. 6.9b Measured load deflection relationship at south-quarter span

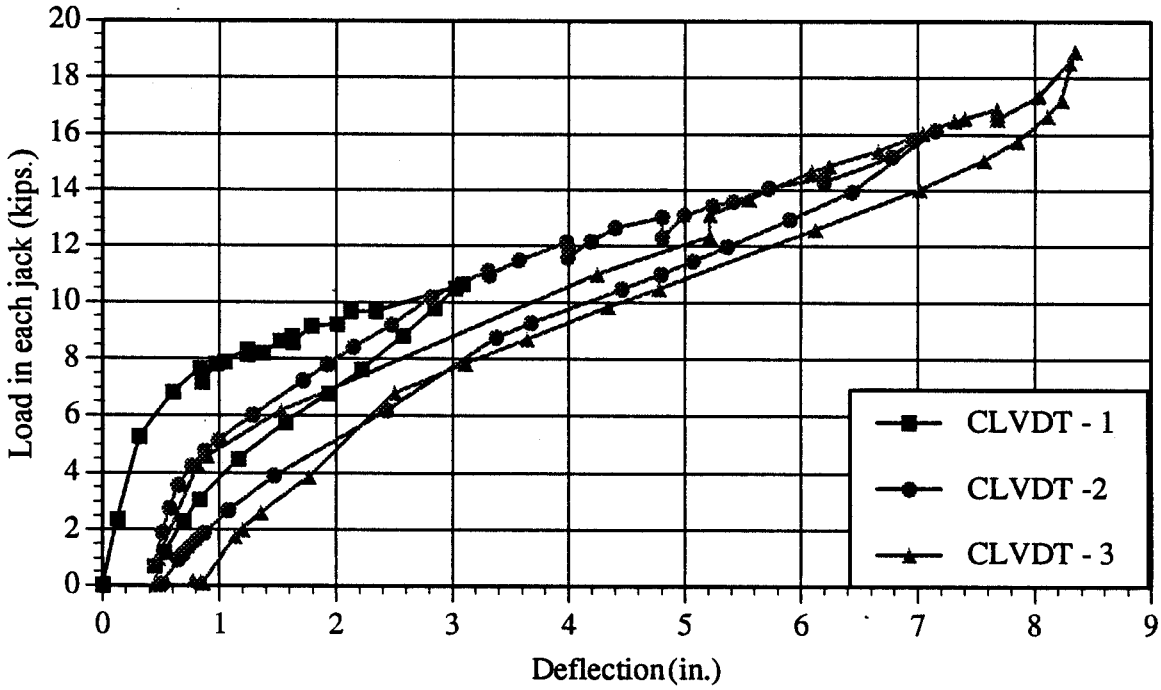

Fig. 6.9c Measured load deflection relationship at midspan

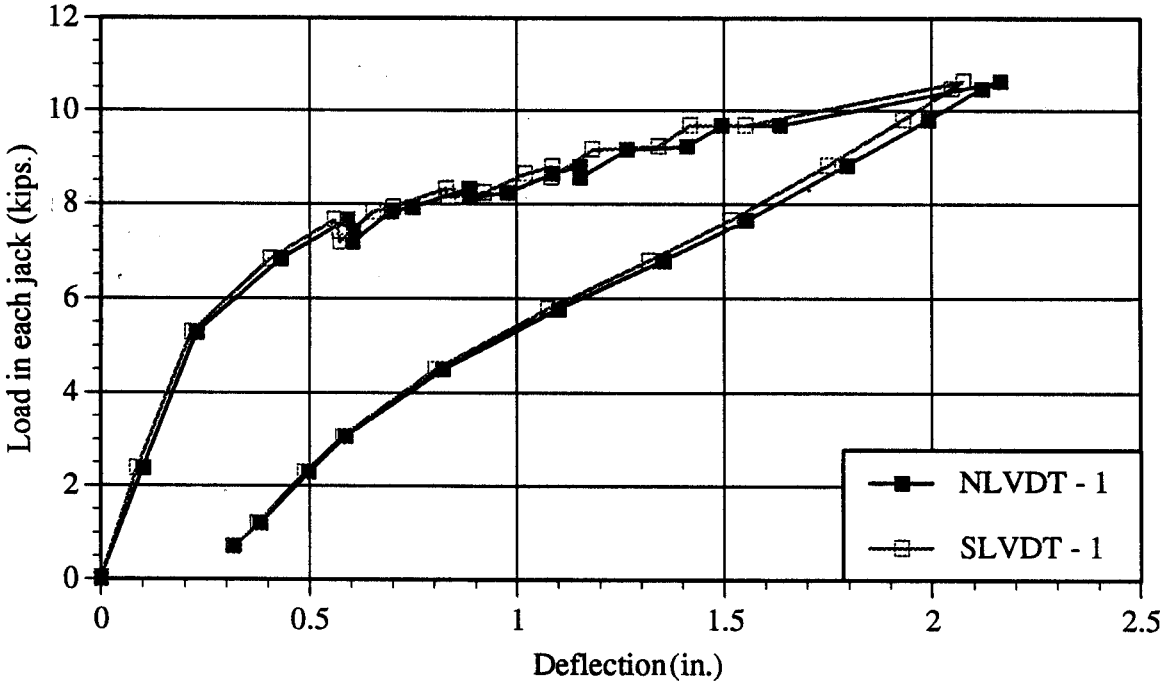

Fig. 6.10a Load deflection relationships at south and north-quarter spans : Load stage # 1

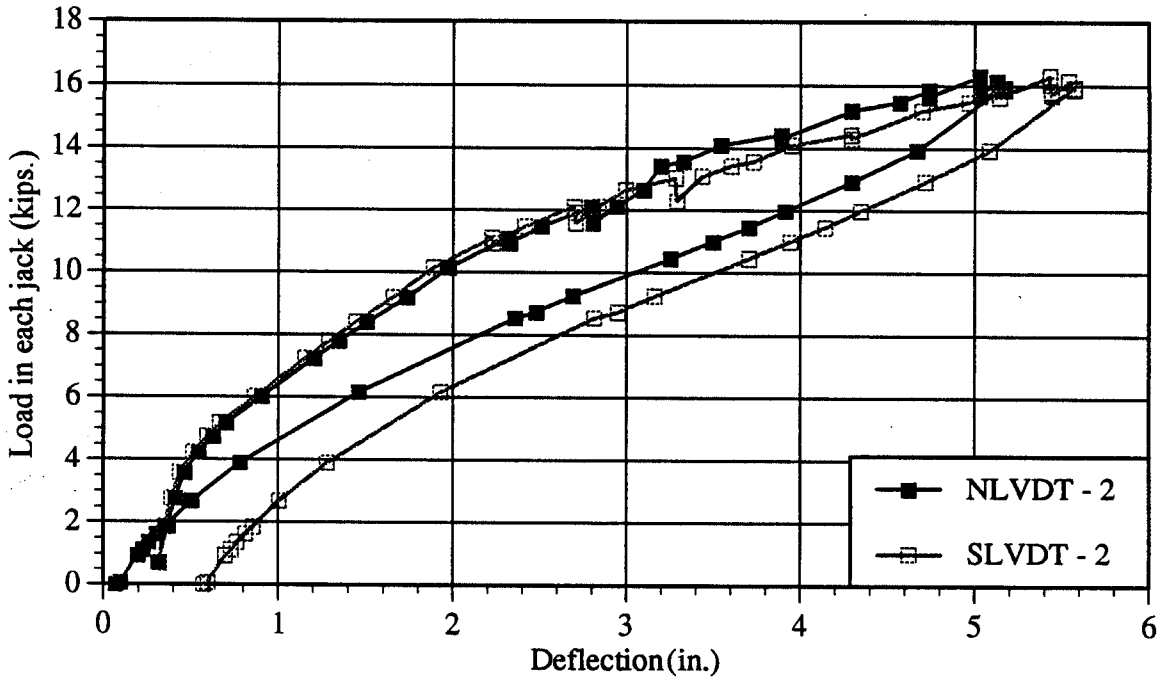

Fig. 6.10b Load deflection relationships at south and north-quarter spans : Load stage # 2

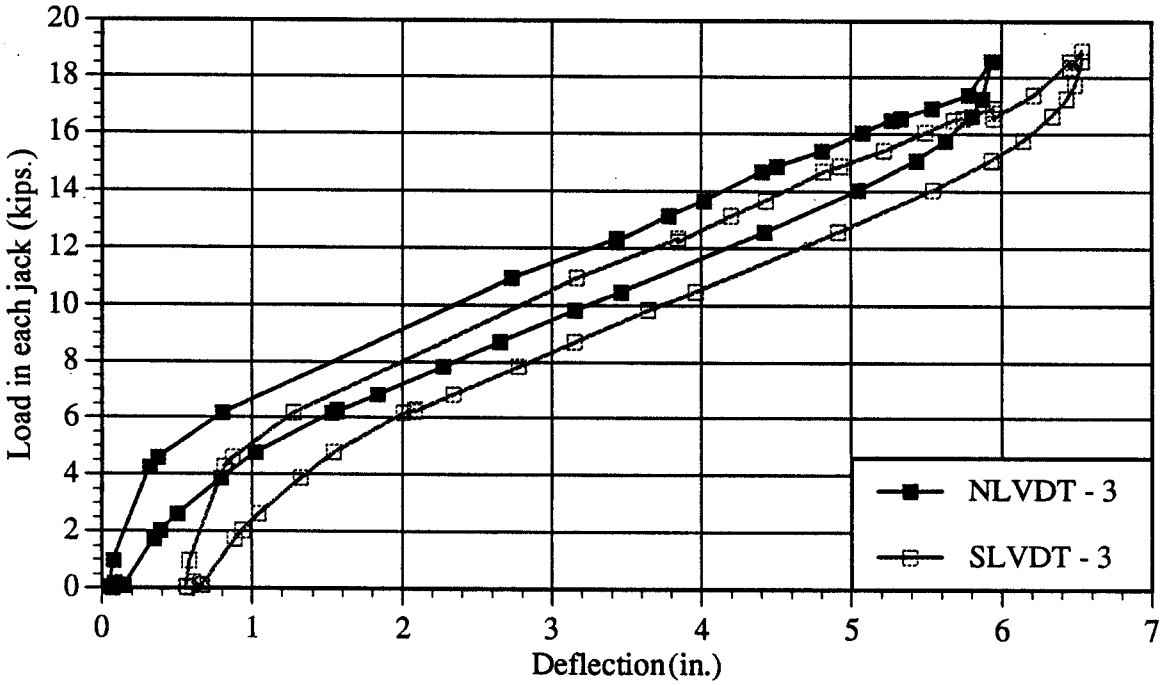

Fig. 6.10c Load deflection relationships at south and north-quarter spans : Load stage # 3

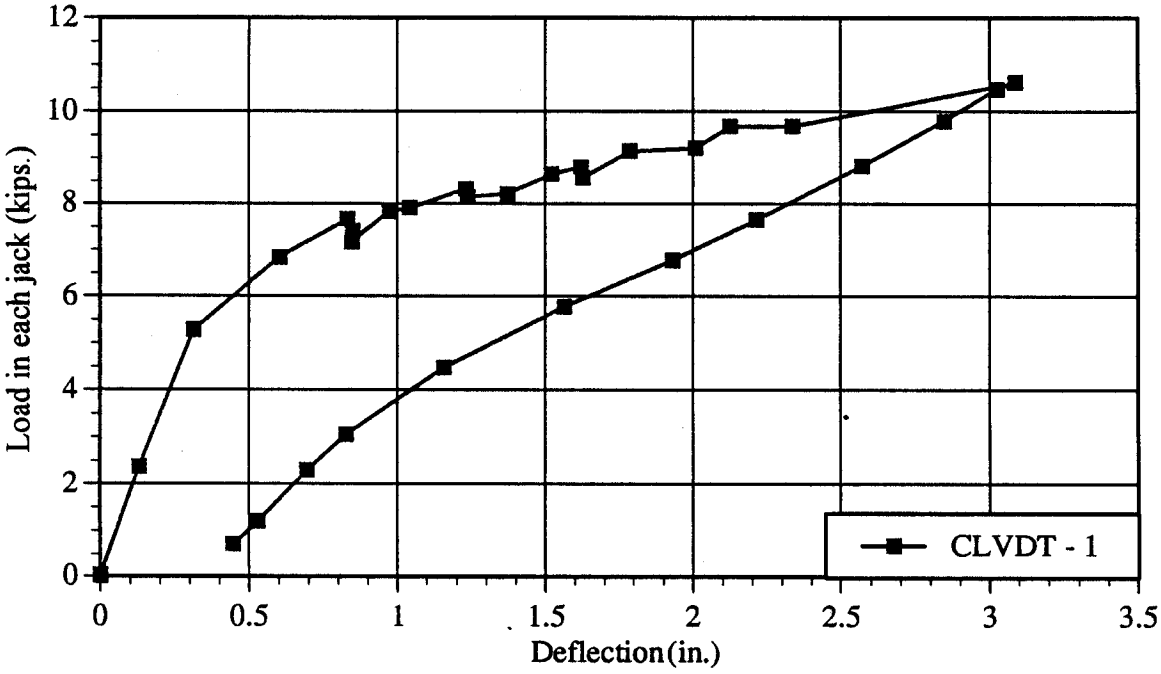

Fig. 6.11a Load deflection relationship at midspan : Load stage # 1

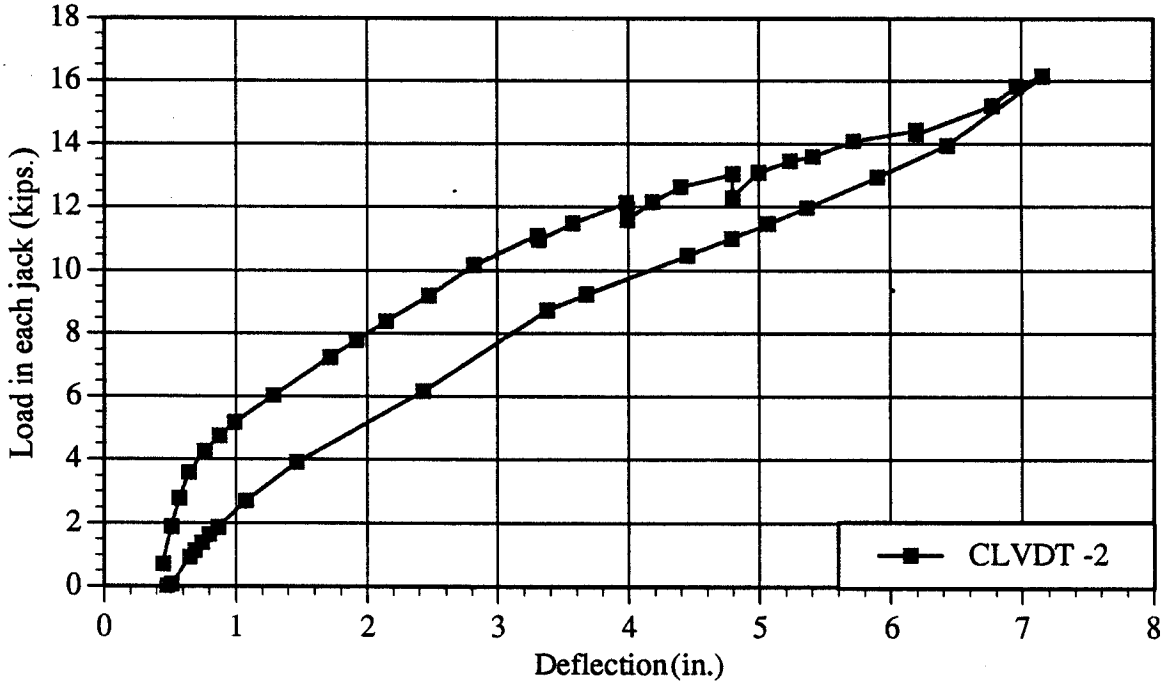

Fig. 6.11b Load deflection relationship at midspan : Load stage # 2

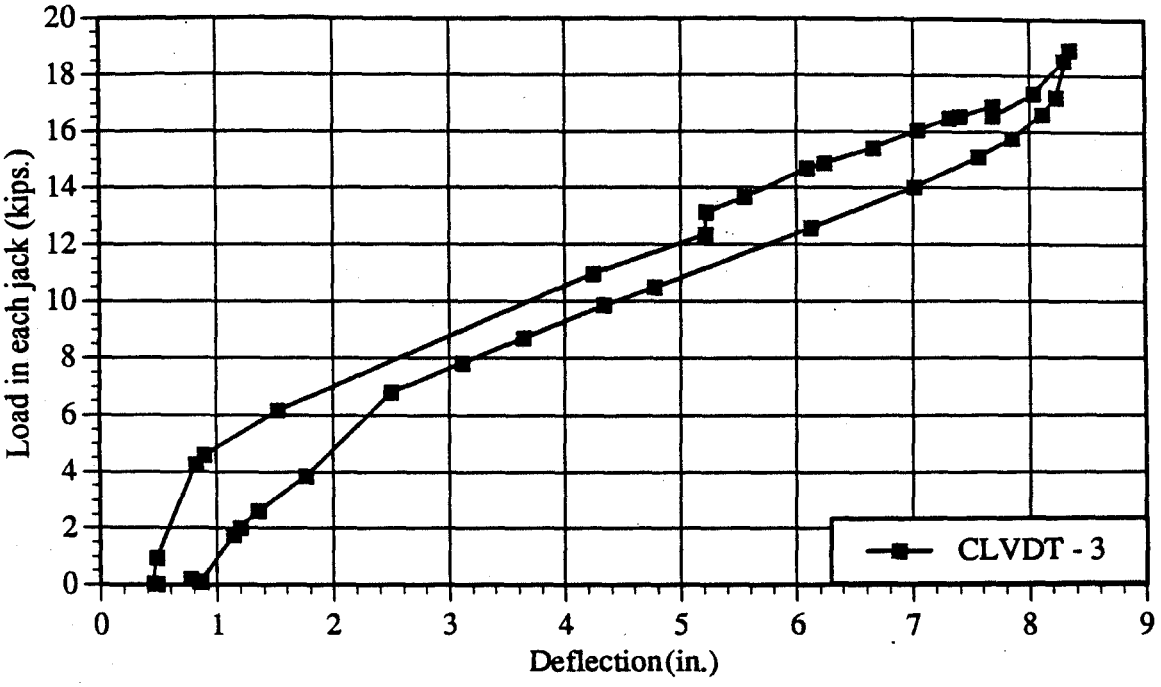

Fig. 6.11c Load deflection relationship at midspan : Load stage # 3

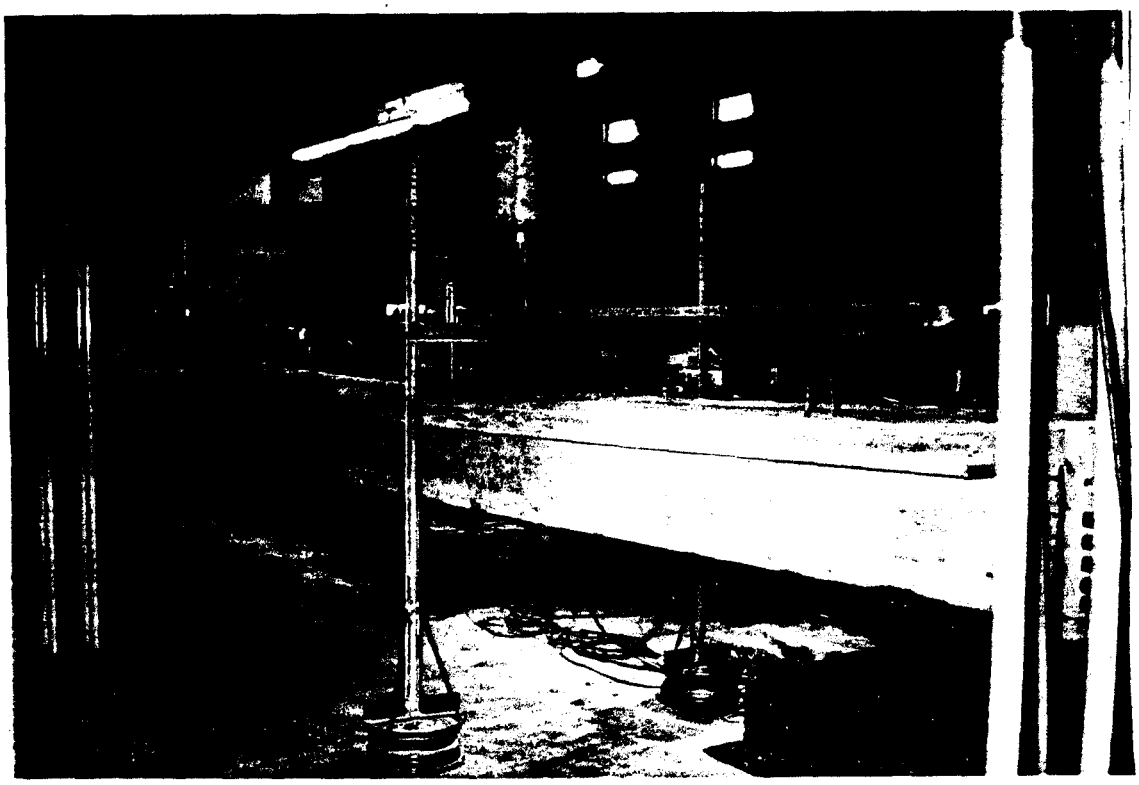

Fig. 6.12 Deflected shape of Double-Tee beam during static flexural test

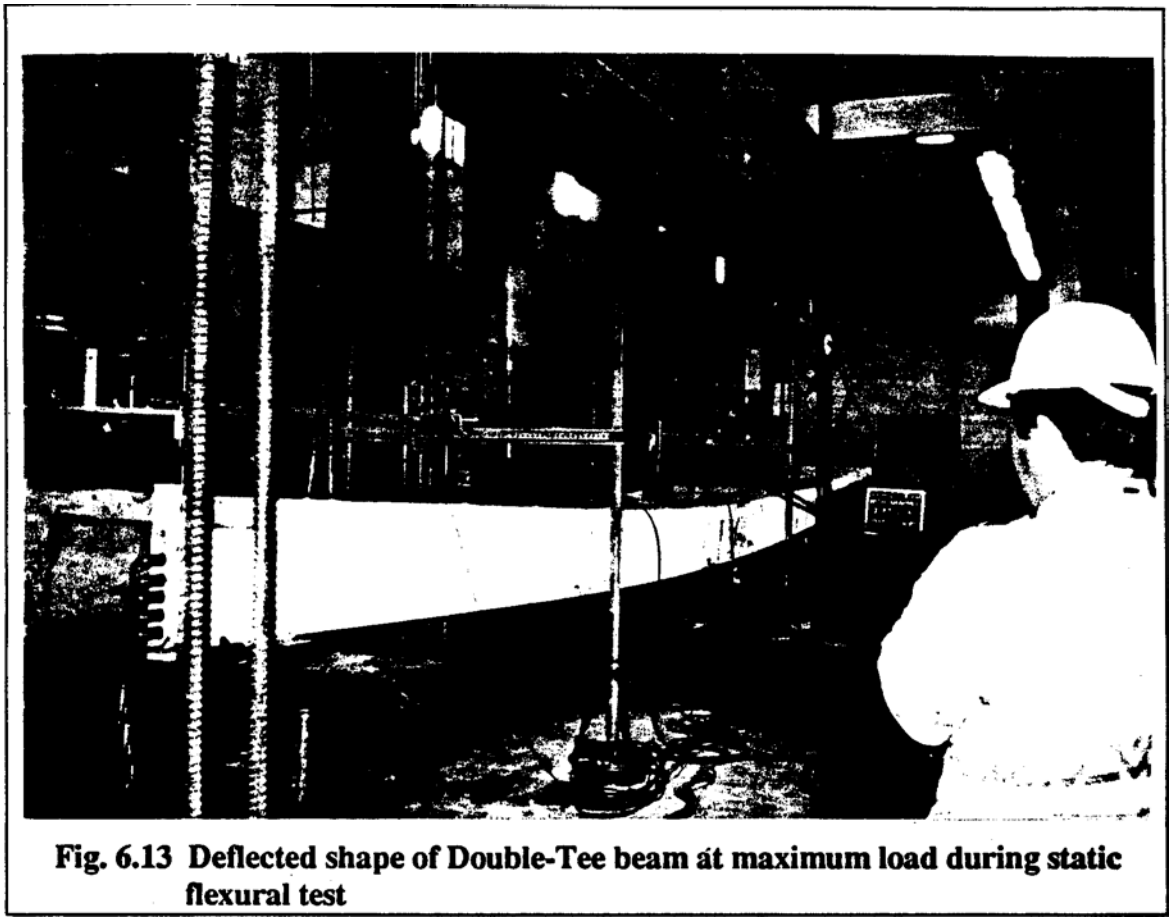

Fig. 6.13 Deflected shape of Double-Tee beam at maximum load during static flexural test

During the application of the loads in steps, new flexural cracks formed accompanied with sudden loud noises. The LVDTs mounted against the tendons at the beam ends did not show any deformation during the test. The fact that flexural cracks were uniformly spaced is a clear indication that there was no bond failure between ARAPREE tendons and concrete. Besides, the observation that there was no tendon slippage confirms the above conclusion.

Table 6.1 shows the loading stages, forces in the hydraulic jacks and corresponding maximum moments. The summary of observations made at these loading stages are also presented in Table 6.1.

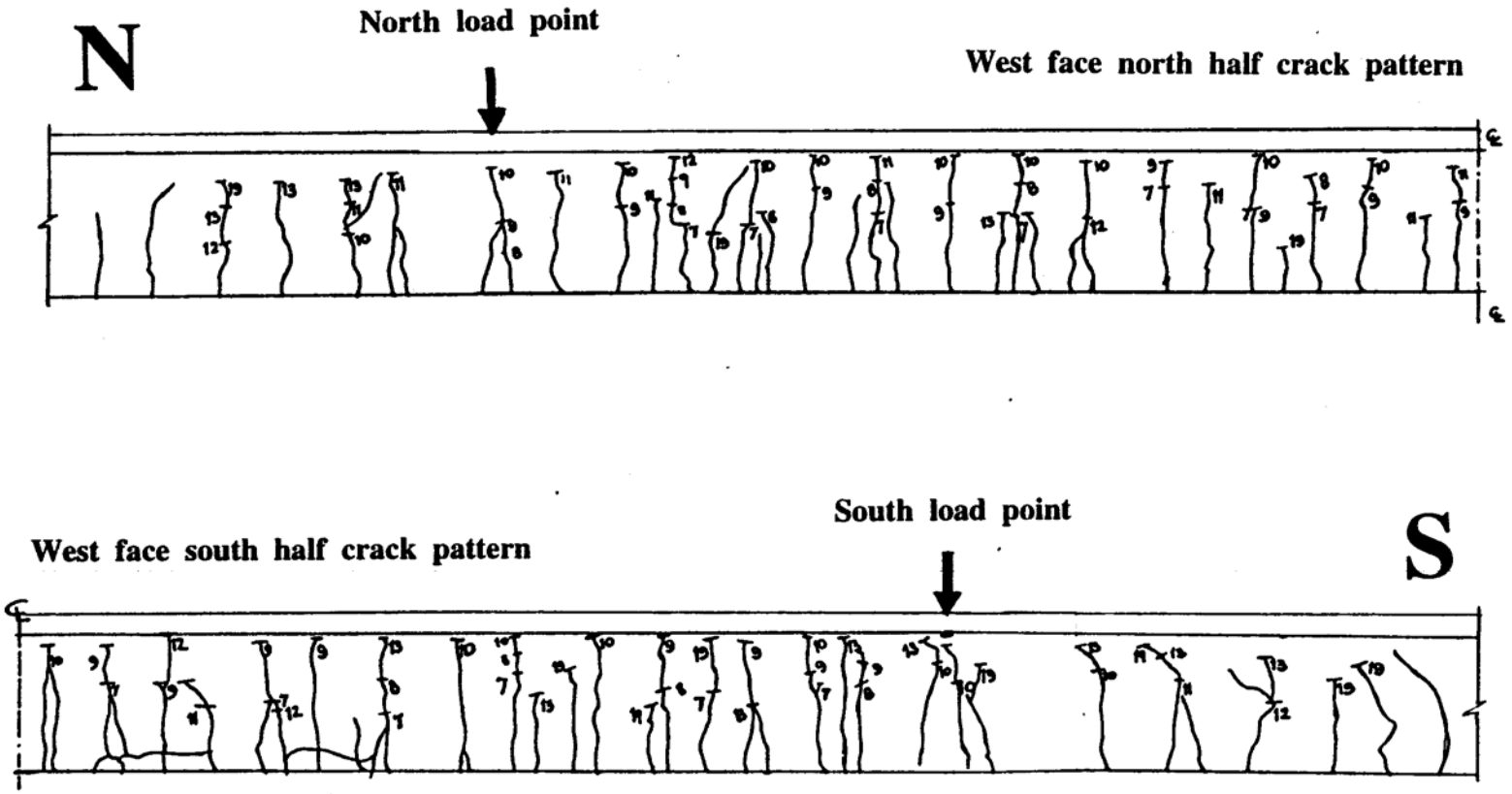

Fig. 6.14 Distribution of cracks - ultimate load test of single Double-Tee beam

Table 6.1 Single Double-Tee beam flexural test

Load stage no.	Load in each jack, P (kips)	Maximum moment in pure bending zone (kips-ft.)	Observations
1	0 to 10	7.735	• Flexural hairline cracks appeared at P = 6 kips and were distributed uniformly • No slip of tendons • Maximum central deflection =3.12 in.
2	0 to 15.7	123.64	• New cracks appeared, while old cracks propagated up to flange-web junction with no increase in the crack width • No slip of tendons • Maximum central deflection ==47.2 in.
3	0 to 18.8	148.05	• New cracks formed beyond bending region. No significant increase in the crack width • No slip of tendons

6.4.4 Analytical Results

6.4.4.1 Comparison of experimental deflections with predicted values

The predicted deflections from the computer code "FRPFLEN7" are based on the moment-curvature relationship which requires concrete strength, prestressing tendon tensile strength, effective prestressing force, section properties etc. The concrete used in the casting of the

Double-Tee beam had a design strength,- f,, of 6000 psi., whereas the actual 28 day average cylinder strength was approximately 5500 psi. Table 6.2 presents the tendon forces as measured by the load cells just before the prestress release and those based on the tendon strain values immediately after prestress release.

Table 6.2 Prestressing forces in ARAPREE cables

	Prestressing forces (kips) based on		
	Load cells[1]	Strain gages[4]	
Cable # 1 W	9.01	8.04	
Cable # 2W	7.65	7.91	
Cable # 3W	9.20[2]	8.14	
Viable # 4W	11.34	9.18	
Cable # 5W	11.22	8.56	
Cable # lE	9.49	7.98	
Cable # 2E	10.05	8.34	
Cable # 3E	10.12	10.91	
Cable # 4E	11.37	9.28	
Cable # 5E	0.00[3]	0.00	

1 **Recorded just before prestress release of the last cable**
2 **Based on pressure gage reading**
3 **Total loss of prestress due to anchorage failure after concreting**
4 **Based on average strain in respective cables after prestress release**

The forces recorded from the load cells differ on an average of about 11 % from the forces computed from the strain data. The tendon forces from the strain data are considered in the theoretical analyses since they represent the actual forces in the tendons after prestress release. The load deflection relationship for the Double-Tee beam has been established considering two concrete strengths of 4000 psi and 5500 psi as well as, (a) the tendon forces as obtained from the strain data and (b) the tendon forces from the strain data with an assumed 10 % prestress loss.

Figs. 6.15 - 6.18 show the results of the analyses and comparison with the experimental values is shown Figs. 6.19 - 6.21.

All the predicted load-deflection relationships (Figs. 6.15 - 6.18) are almost identical and trilinear showing three distinct regions prior to the beam collapse. The three regions are:

i) Pre-cracking stage where the Doable-Tee beam is crack free,

ii) Post-cracking stage at which the beam develops controlled cracking both in crack distribution and width,

iii) Post-serviceability cracking stage when the tendon strain approaches the rupture limit.

The analytical model prediction of the beam collapse identified the tendon # 5W to reach the rupture limit first, followed by the failure of the remaining tendons in succession. The points of discontinuity in the curves prior to the beam collapse denote this phenomenon of the bottom most tendon failure. Moreover, it can be observed that the beam has still a certain amount of reserve capacity to carry additional load beyond the first tendon failure.

6.4.4.2 Energy absorption and ductility

Ductility factor is usually expressed as the ratio of the ultimate deformation to the deformation at first yield. Reinforced and prestressed concrete members are designed to be ductile because their energy absorption is due to the inherent capacity of the steel to deform so as to have adequate ductility. The ductility factor is an index to express the deformation capacity and consequently indicates the energy absorption. In the case of FRP prestressed / reinforced concrete members the ductility factor has to be evaluated from a different perspective, based on energy absorption, since the FRPs, unlike prestressing steel, do not have an yield point before rupture. Therefore, energy absorption evaluation of FRP reinforced/ prestressed concrete is an important consideration in the design.

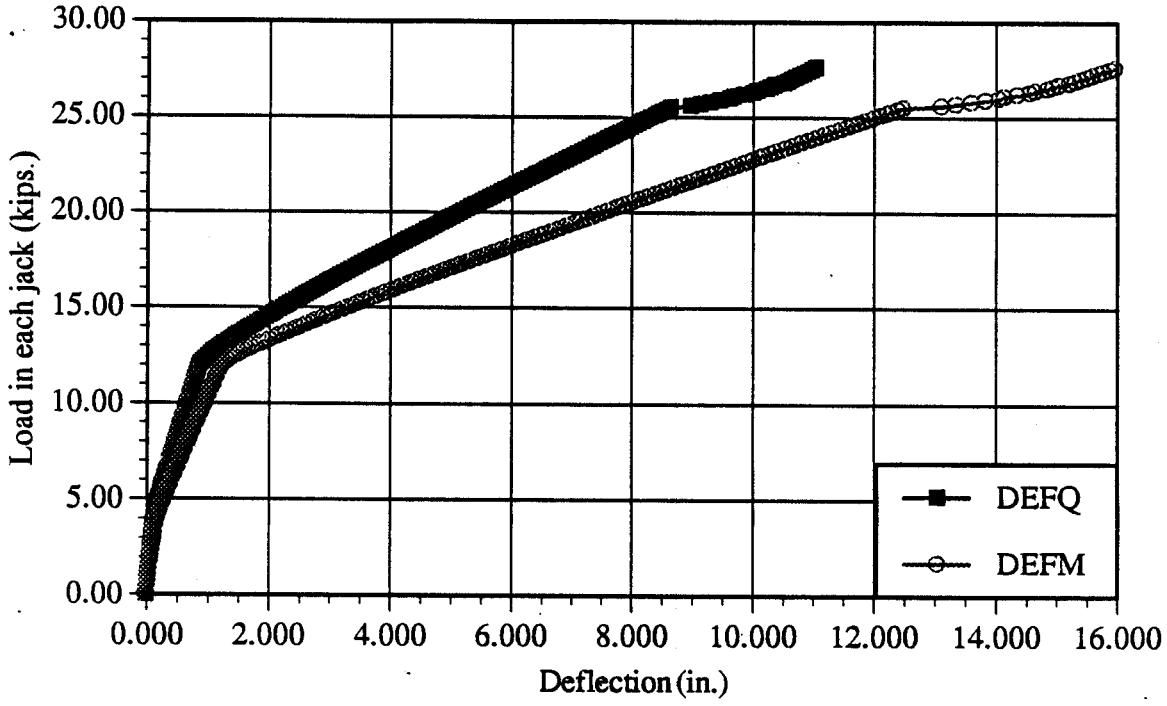

Fig. 6.15 Predicted load deflection relationship at mid and quarter spans, concrete strength = 5500 psi; prestress with no losses

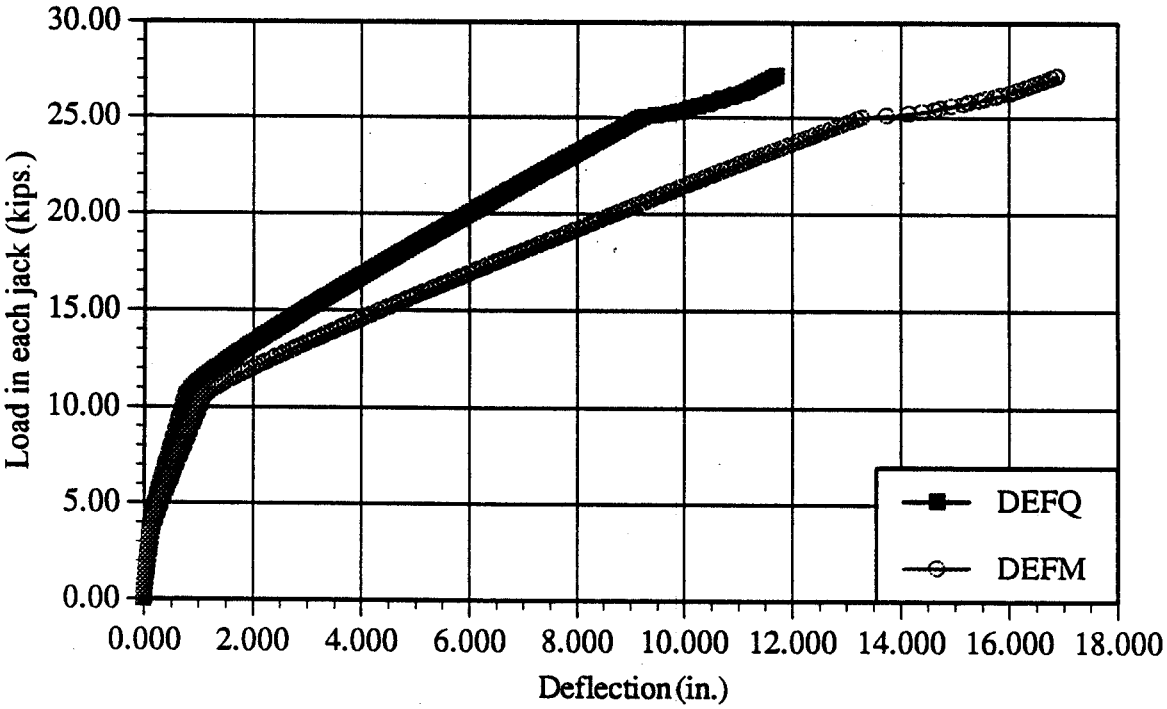

Fig. 6.16 Predicted load deflection relationship at mid and quarter spans, concrete strength = 5500 psi; prestress with 10 % loss

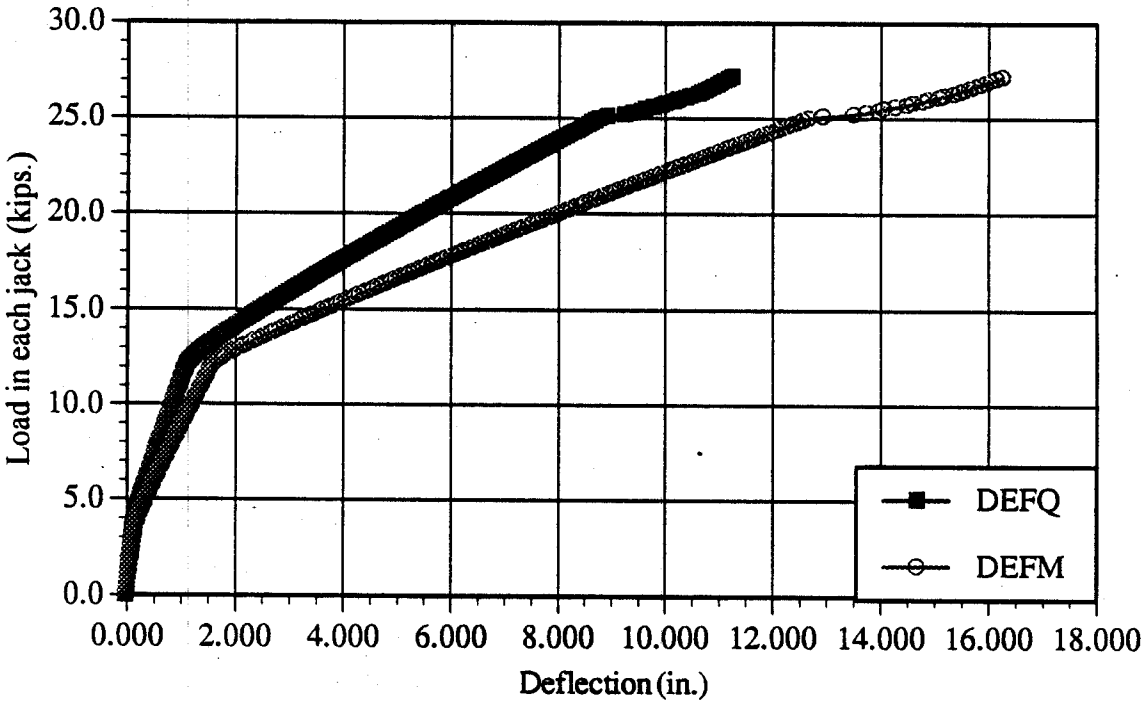

Fig. 6.17 Predicted load deflection relationship at mid and quarter spans, concrete strength = 4000 psi; prestress with no losses

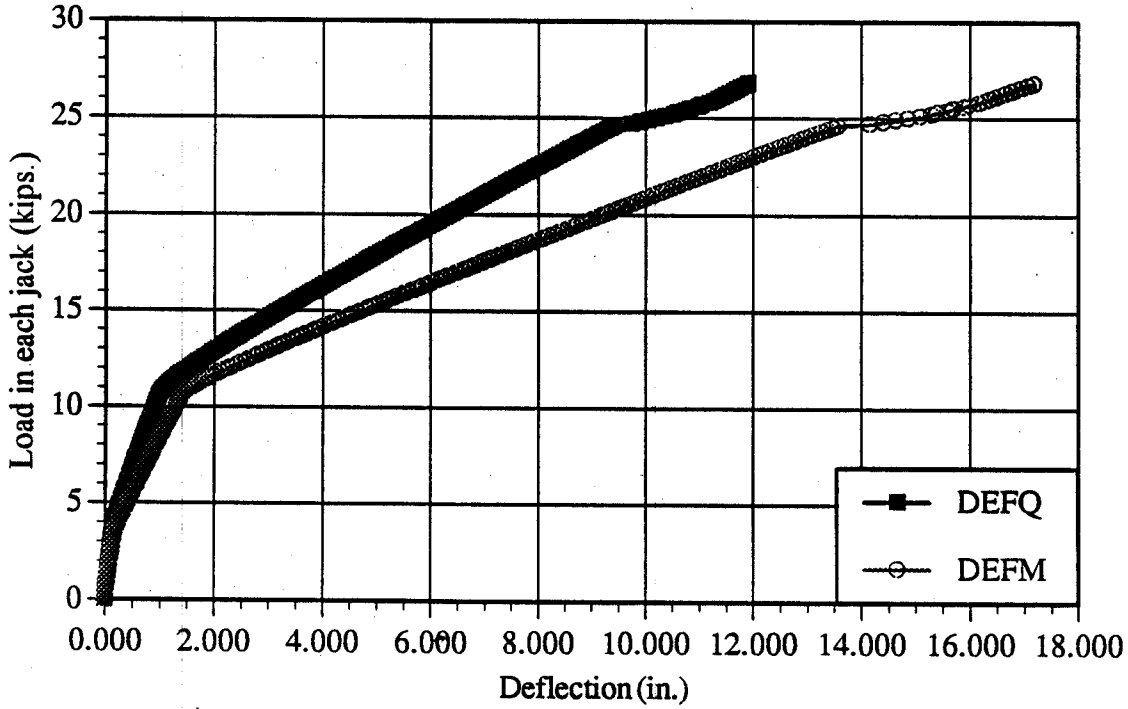

Fig. 6.18 Predicted load deflection relationship at mid and quarter spans, concrete strength = 4000 psi; prestress with 10% loss

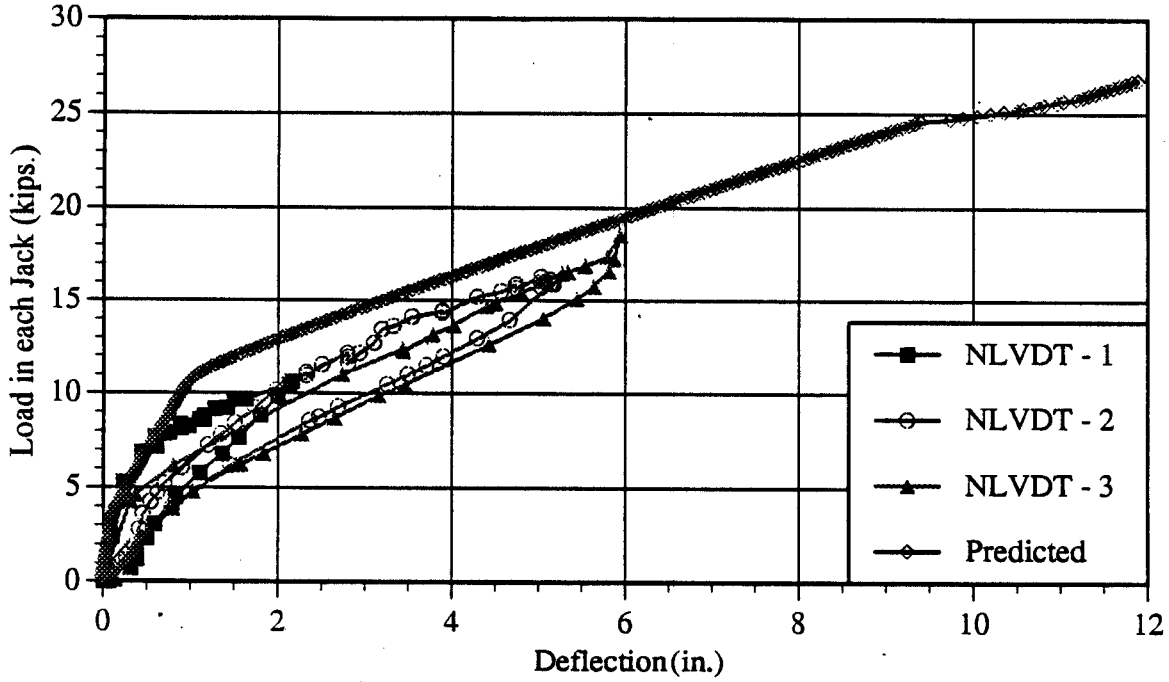

Fig. 6.19 Comparison of predicted and measured load deflection relationships at north-quarter span

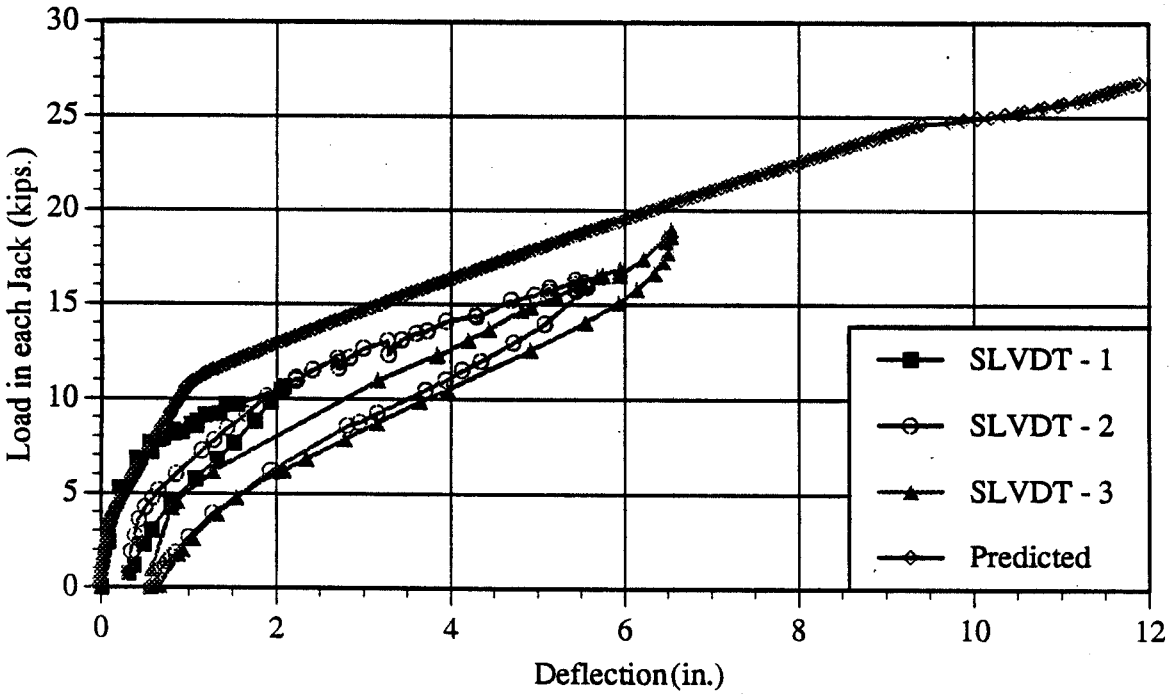

Fig. 6.20 Comparison of predicted and measured load deflection relationships at south-quarter span

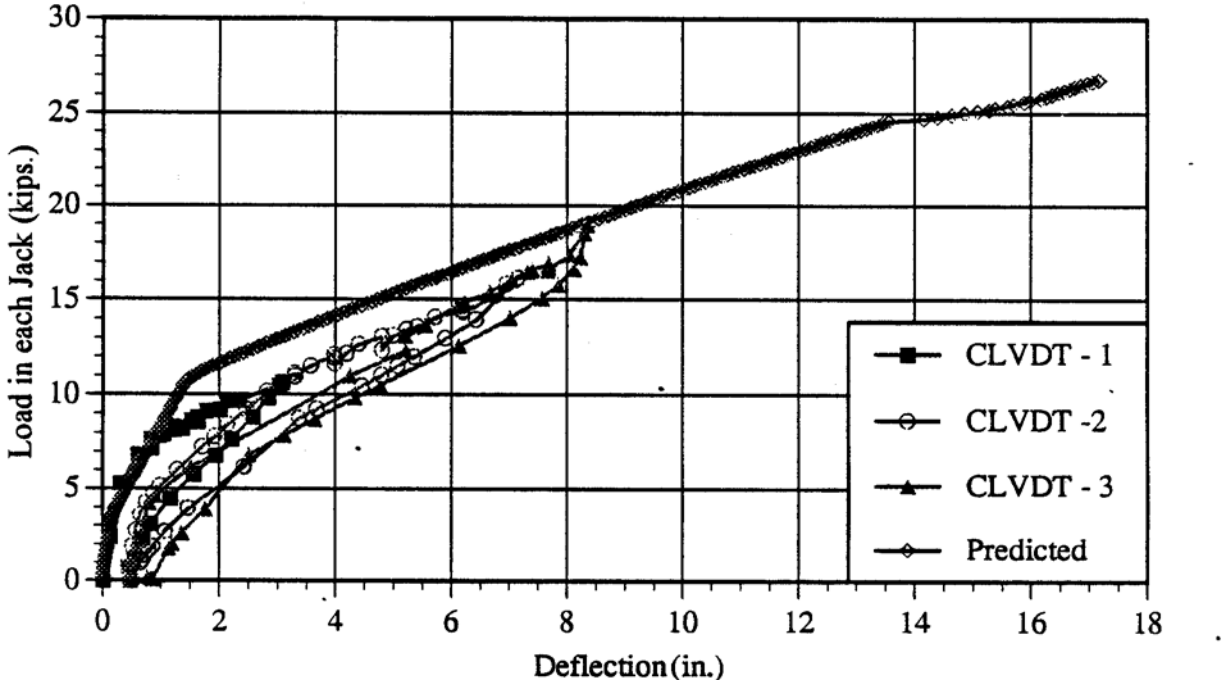

Fig. 6.21 Comparison of predicted and measured load deflection relationships at midspan

Figs. 6.22 - 6.25 show the moment - curvature relationships of the single Double-Tee beam corresponding to two concrete strengths of 4,000 and 5,500 psi as well as, (a) the tendon forces as obtained from the strain data and (b) the tendon forces from the strain data with an assumed 10 % prestress loss. The decrease in the moment values as seen in the above graphs corresponds to loss of tension stiffening in the concrete, and bottom most tendon rupture, which is followed by complete collapse of the beam. The area enclosed under the curve bounded by the ordinates corresponding to the rupture of the bottom most tendon and complete beam collapse is the energy in reserve before the ultimate collapse. The energy absorbed before and after the bottom most tendon rupture could be calculated from both the load deflection and moment curvature relationships. Table 6.3 presents the absorbed energy values as well as the ratios of the energies based on the energy absorbed before and after the bottom most tendon rupture.

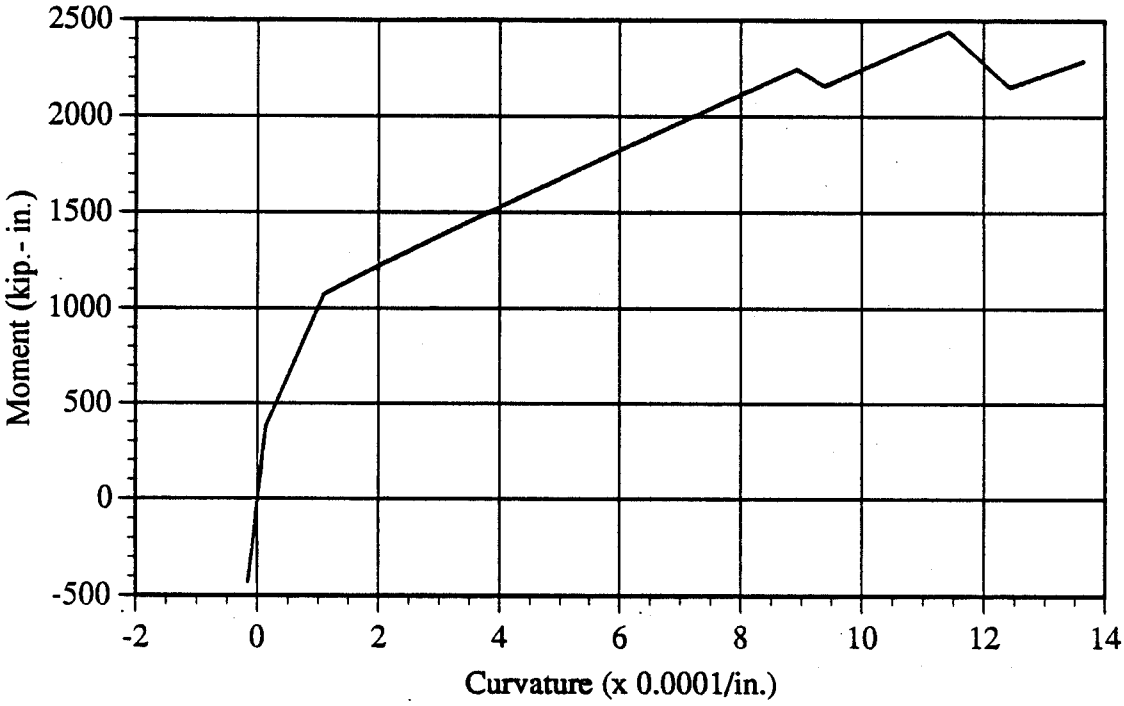

Fig. 6.22 Predicted moment-curvature relationship , concrete strength = 4000 psi; prestress with no losses

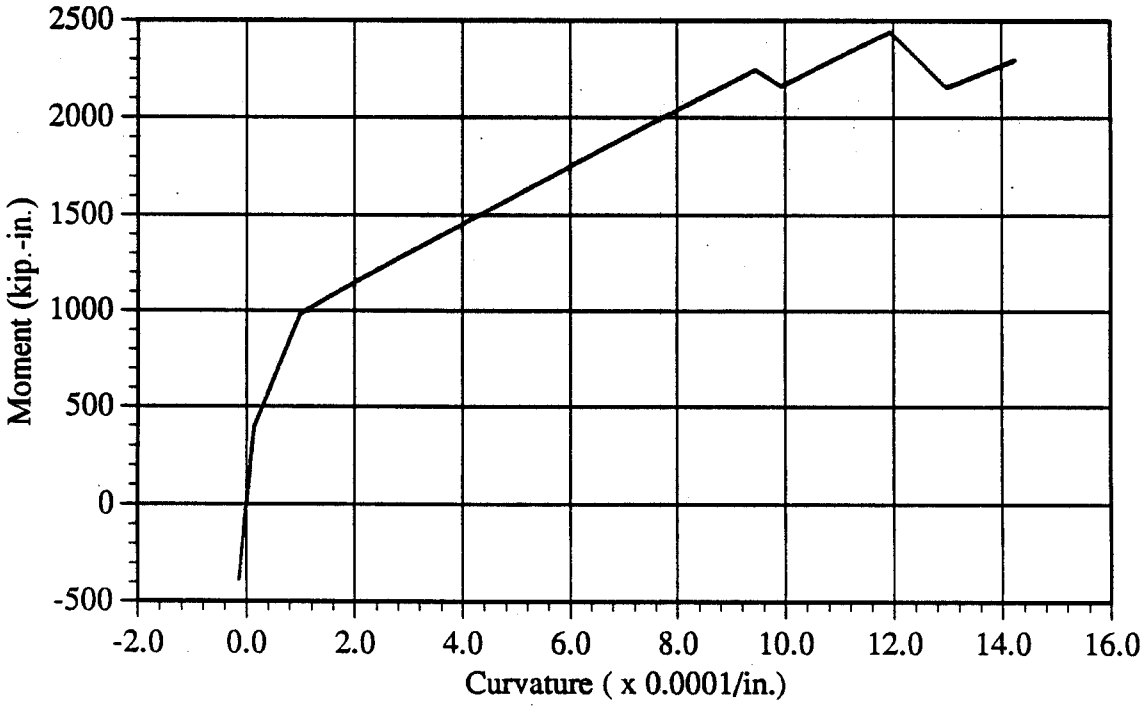

Fig. 6.23 Predicted moment-curvature relationship , concrete strength = 4000 psi; prestress with 10 % loss

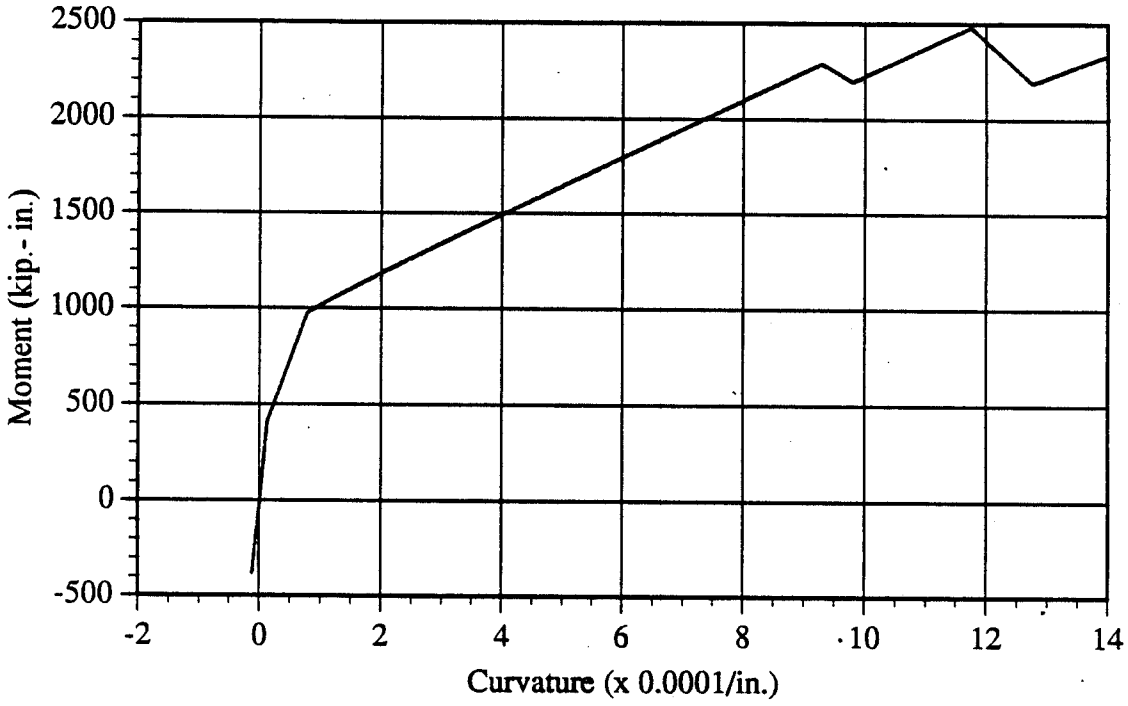

Fig. 6.24 Predicted moment-curvature relationship , concrete strength = 5500 psi; prestress with 10 % loss

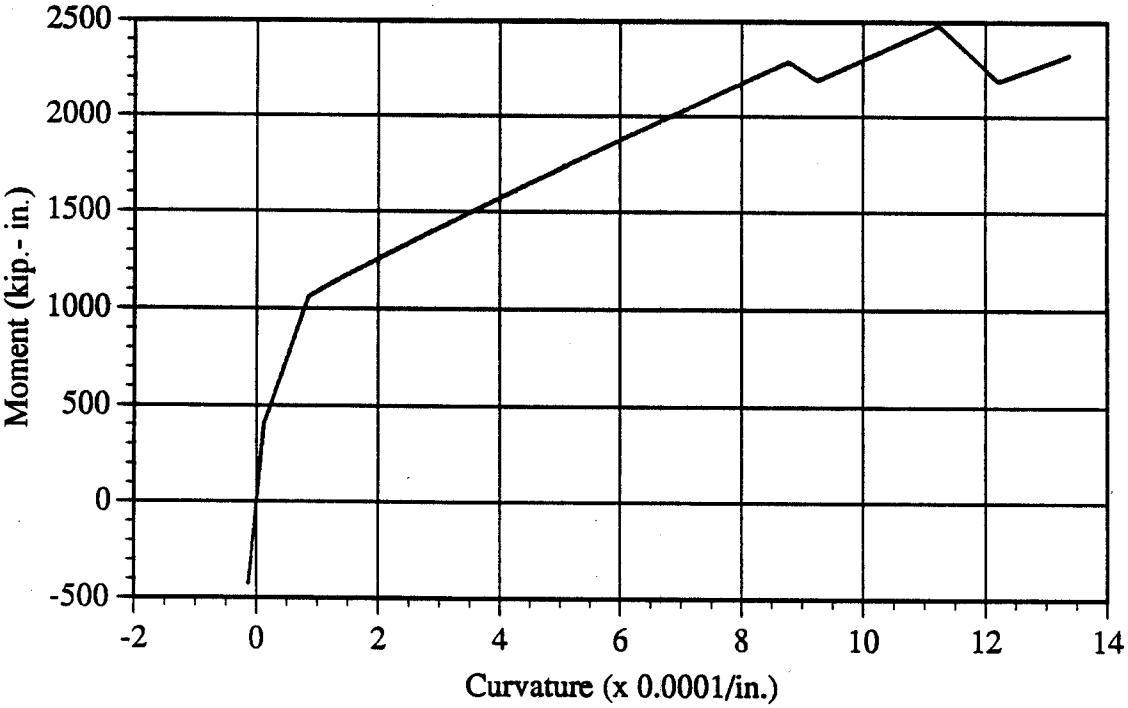

Fig. 6.25 Predicted moment-curvature relationship , concrete strength = 5500 psi; prestress with no losses

Table 6.3 Predicted energy absorption

	Energy absorbed with respect to bottom most tendon		
	Before rupture kip-in (1)	After rupture kip-in (1)	Ratio (2) / (1)
Case (Fig. 6.15)	219.25	93.625	0.427
Case (Fig. 6.16)	224.15	93.265	0.425
Case (Fig. 6.17)	219.313	98.8	0.451
Case (Fig. 6.18)	221.42	95.275	0.430

CHAPTER 7

EXPERIMENTAL INVESTIGATION OF FATIGUE AND ULTIMATE LOAD BEHAVIOR OF DOUBLE-TEE BRIDGE SYSTEM

7.1 INTRODUCTION

Double-Tee beams have been frequently used in bridges in the past for rural and secondary roads. However, because of their structural strength, cost effectiveness and ease of construction, there is growing interest in using Double-Tee beams in longer spans (upto 80 ft.). Nevertheless, with large load requirements, coupled with more slender structural members and higher working stresses, there is a need to check the fatigue behavior and ultimate strength of Double-Tee structural systems. The emerging trend of using FRPs in prestressed concrete bridges adds another new dimension in the design of these systems.

The studies on static and fatigue behavior of bridge systems prestressed with FRP rods / tendons are not reported, although limited experimental work has been published on the fatigue behavior of FRP rods alone under cyclic tension. This chapter presents the details of the experimental investigation on static, fatigue and ultimate load behavior of a 1:2 scale model Double-Tee bridge system prestressed with ARAPREE tendons. The assembly of the precast Double-Tee beams to form the bridge system, the details of the experimental setup, instrumentation and data acquisition and HS 20-44 truck load simulation are described together with the discussions of the results from the static, fatigue and ultimate load tests.

7.2 ASSEMBLY OF DOUBLE-TEE BRIDGE SYSTEM

Fig. 7.1 shows the Double-Tee beams arranged one over another before assembly in the Structure Research Center, Florida Department of Transportation, Tallahassee. One of the beams was used in the study of flexural behavior (Chapter 6) and the remaining three beams were assembled to form the bridge deck system. Double-Tee beams were placed on neoprene bearing pads resting on the support walls (Fig. 7.2). The beams were arranged side by side on the support forming longitudinal V joints between them (Figs. 7.3 - 7.6).

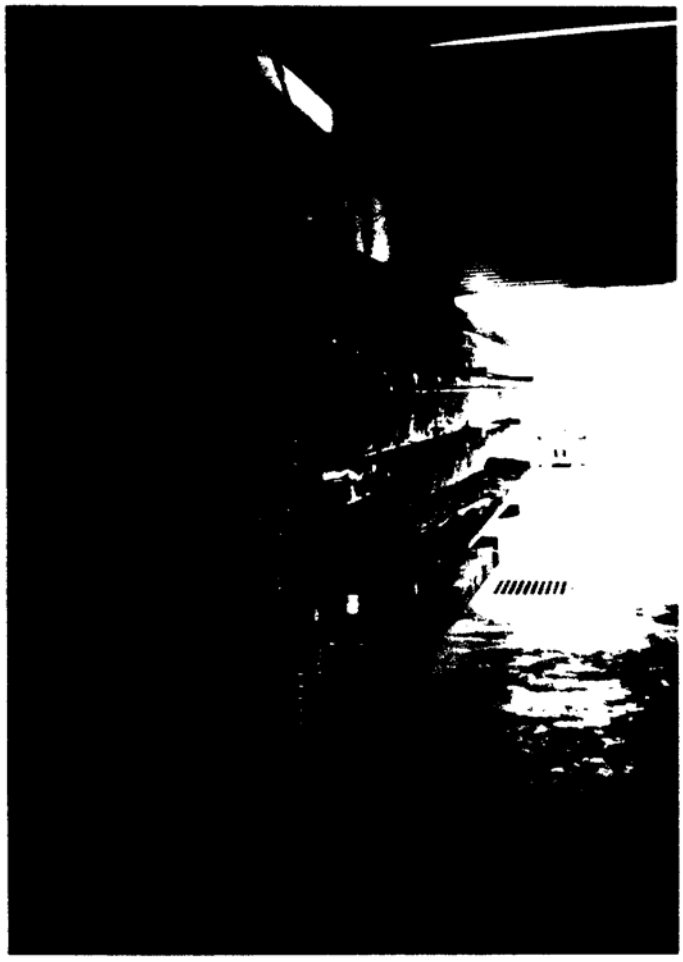

Fig. 7.1 Four Double-Tee beams stored before assembly

Fig. 7.2 Support of Double-Tee beam

Fig. 7.3 Top view of longitudinal joint between two Double-Tee beams

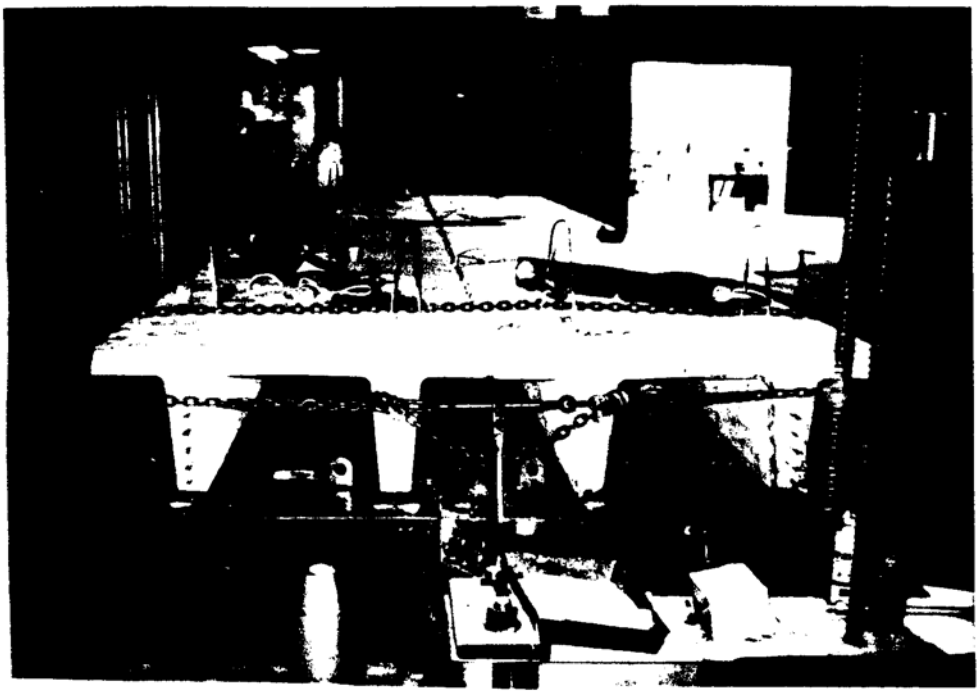

Fig. 7.4 End view of Double-Tee beams arranged side by side

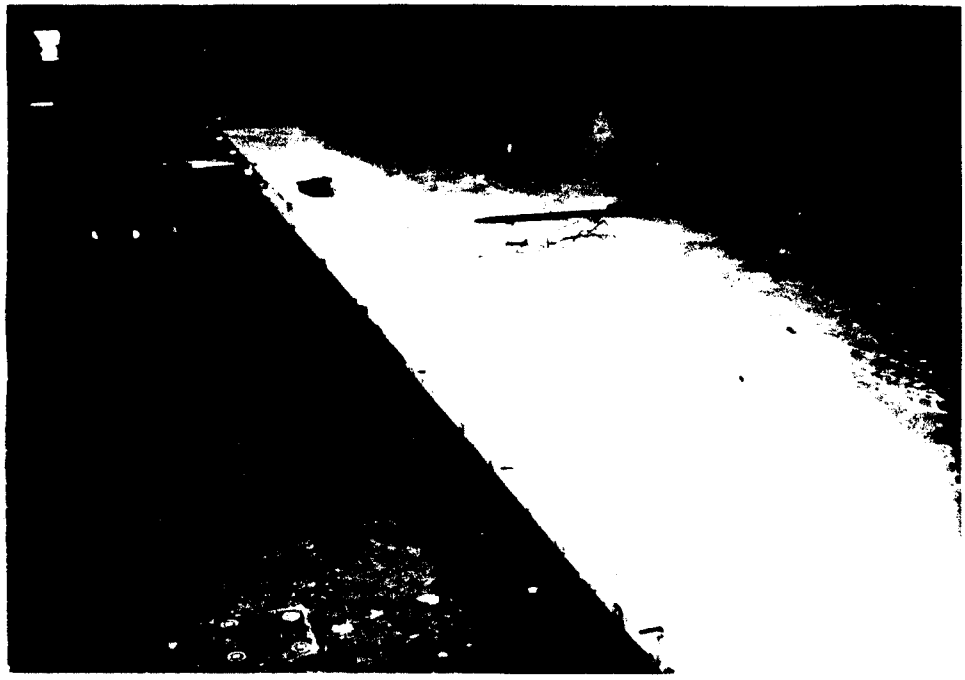

Fig. 7.5 Front view of Double-Tee beams arranged side by side

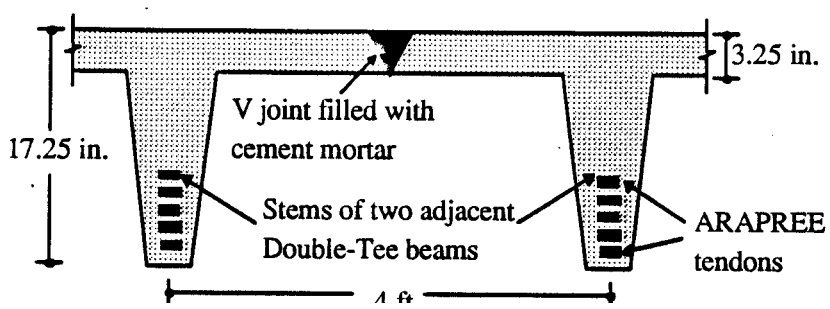

Fig. 7.6 Schematic of the V joint between two Double-Tee beams

Transverse post-tensioning would ensure the monolithic action of the three individual beams to form a two lane bridge deck. Initially, f 200,000 circular f 7.9 mm, ARAPREE was proposed to achieve a contact pressure of 250 psi. between the flanges. However, the spacing of the f 200,000 ARAPREE tendons was determined to be very. small and hence impractical. Therefore, seven wire steel strands were used for transverse post-tensioning.

Half an inch diameter seven wire steel strands were inserted through PVC ducts spaced at 31 in. centers (Fig. 7.7) through the flanges of Double-Tee beams along the span. Figs. 7.8 and 7.9 show the prestressing steel strand being cut to appropriate length and inserted through the ducts. The V joints between the Double-Tee beams were filled with mortar. Figs. 7.10 and 7.11 show the wooden form underneath and along the longitudinal joint ready for placing the mortar. Fig. 7.12 shows filling in a joint with mortar in progress and the two longitudinal joints after completion are shown in Fig. 7.13. Fig. 7.14 shows an end view of the mortar-filled -V joint between the Double-Tee beams. Figs. 7.15 and 7.16 show the transverse post-tensioning of the bridge deck system in progress. Fig. 7.17 shows the end view of the bridge system and the complete assembled bridge deck is shown in Fig. 7.18.

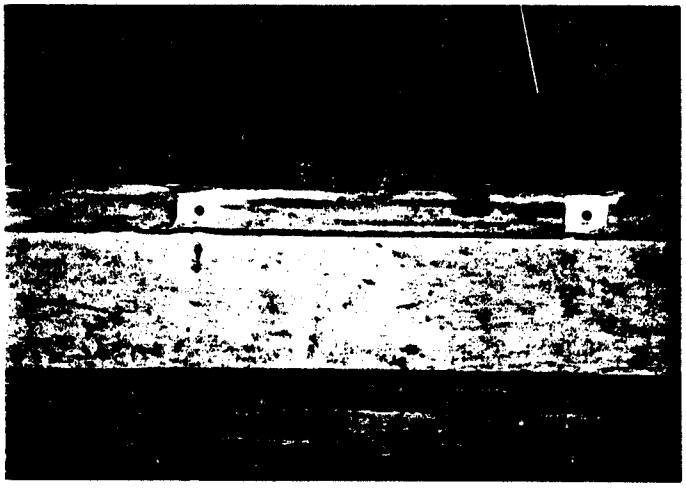

Fig. 7.7 PVC duct in flanges of Double-Tee beams

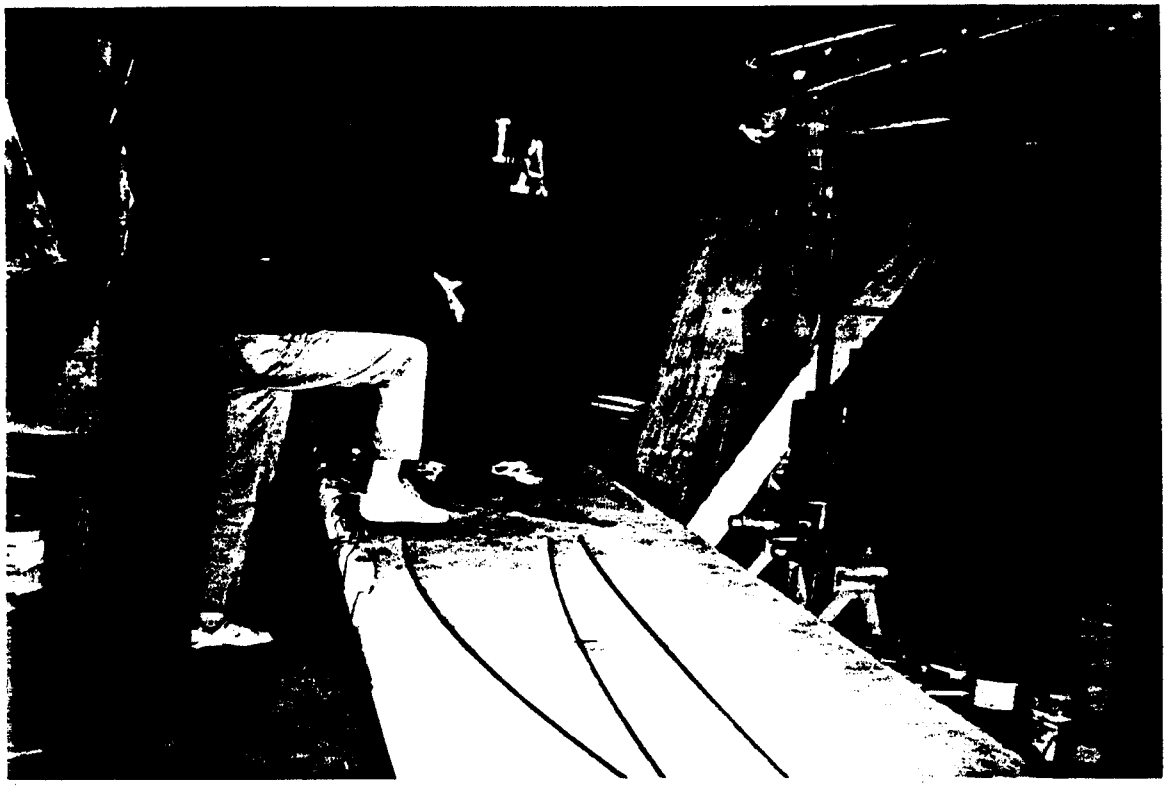

Fig. 7.8 The prestressing steel strands being cut in appropriate lengths

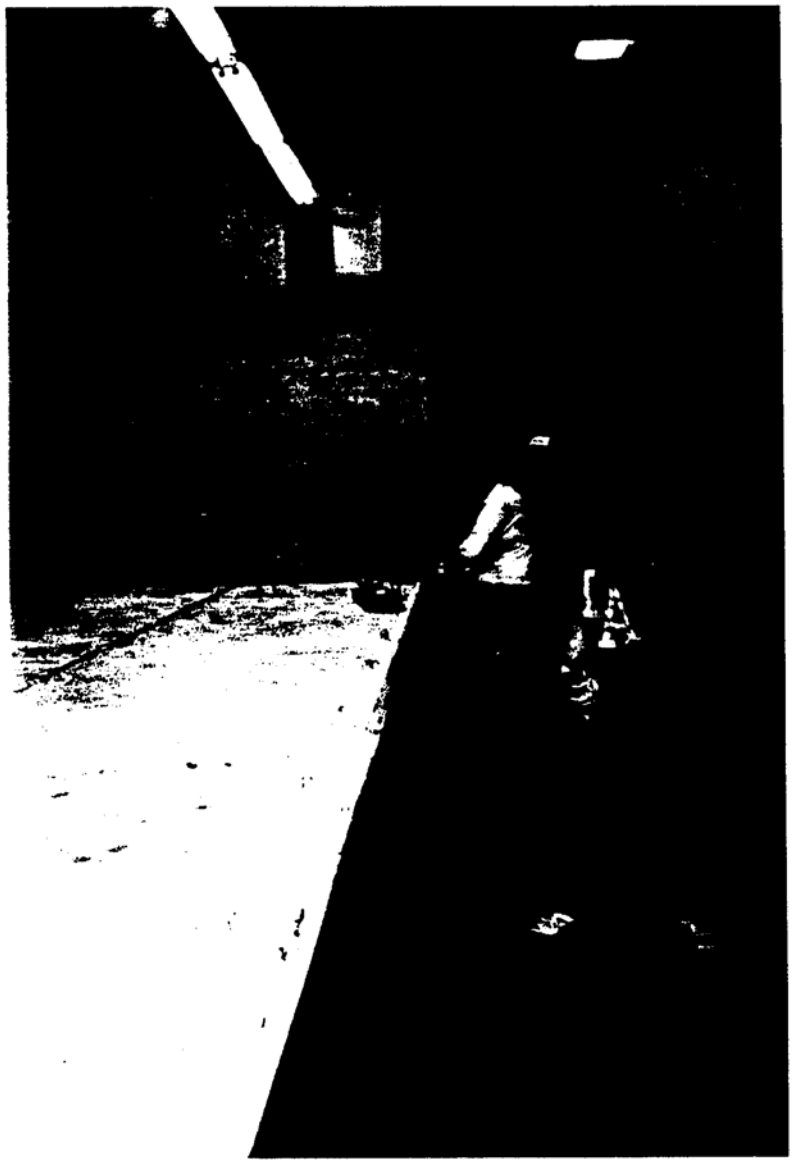

Fig. 7.9 The prestressing steel strand being inserted through the ducts

Fig. 7.10 The wooden form underneath and along the longitudinal joint of Double-Tee bridge ready for placing mortar

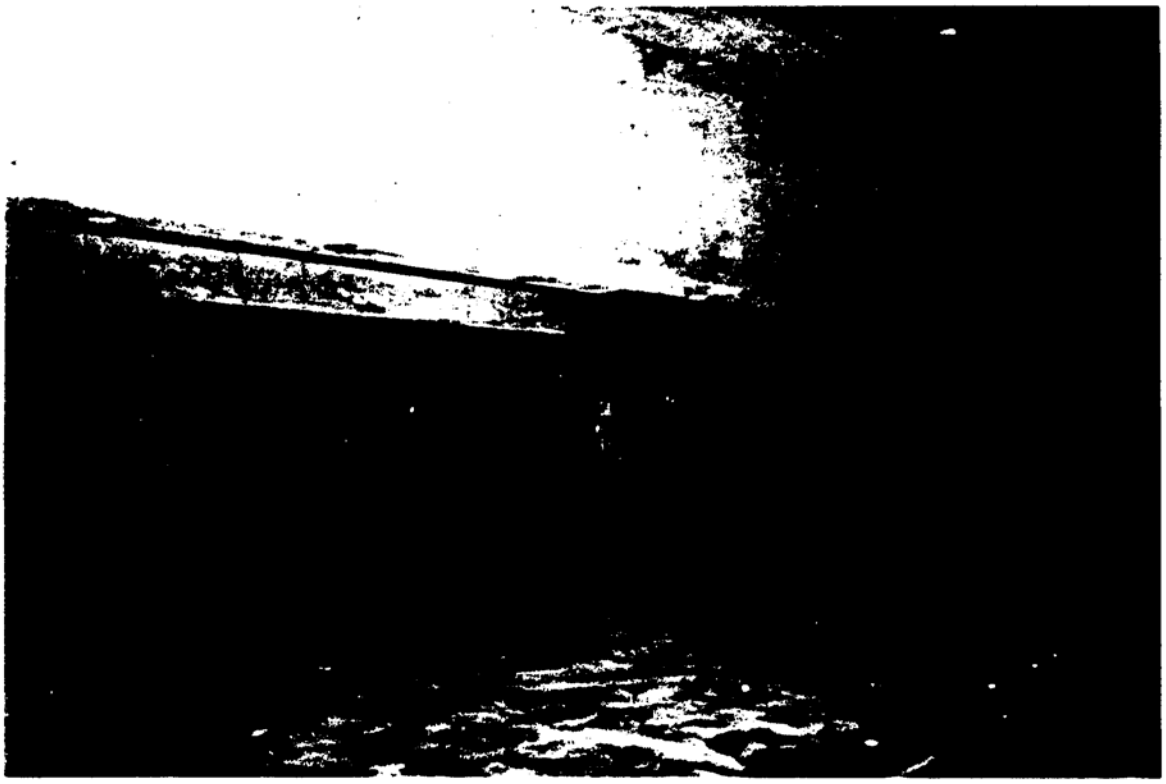

Fig. 7.11 The overall view of the wooden form underneath and along the longitudinal joint ready for placing the mortar

Fig. 7.12 Filling a V-joint with mortar in progress

Fig 7.13 The two longitudinal joints filled with mortar

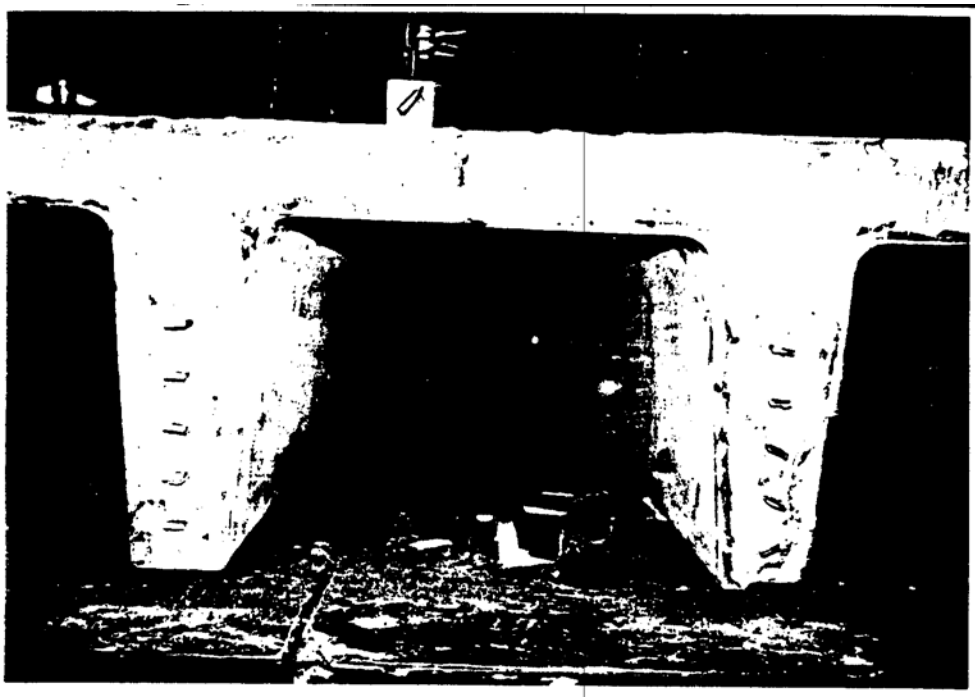

Fig. 7.14 End view of the mortar-filled-V joint between the Double-Tee beams

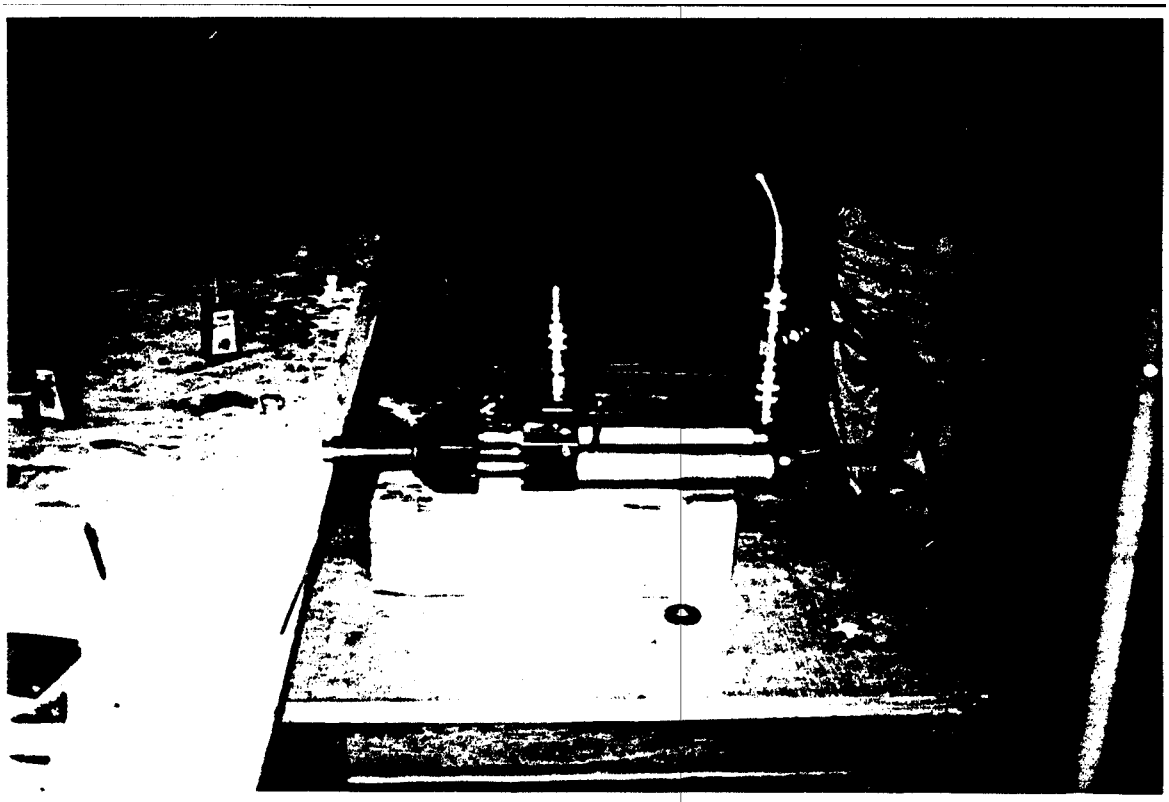

Fig. 7.15 Set-up for transverse post-tensioning

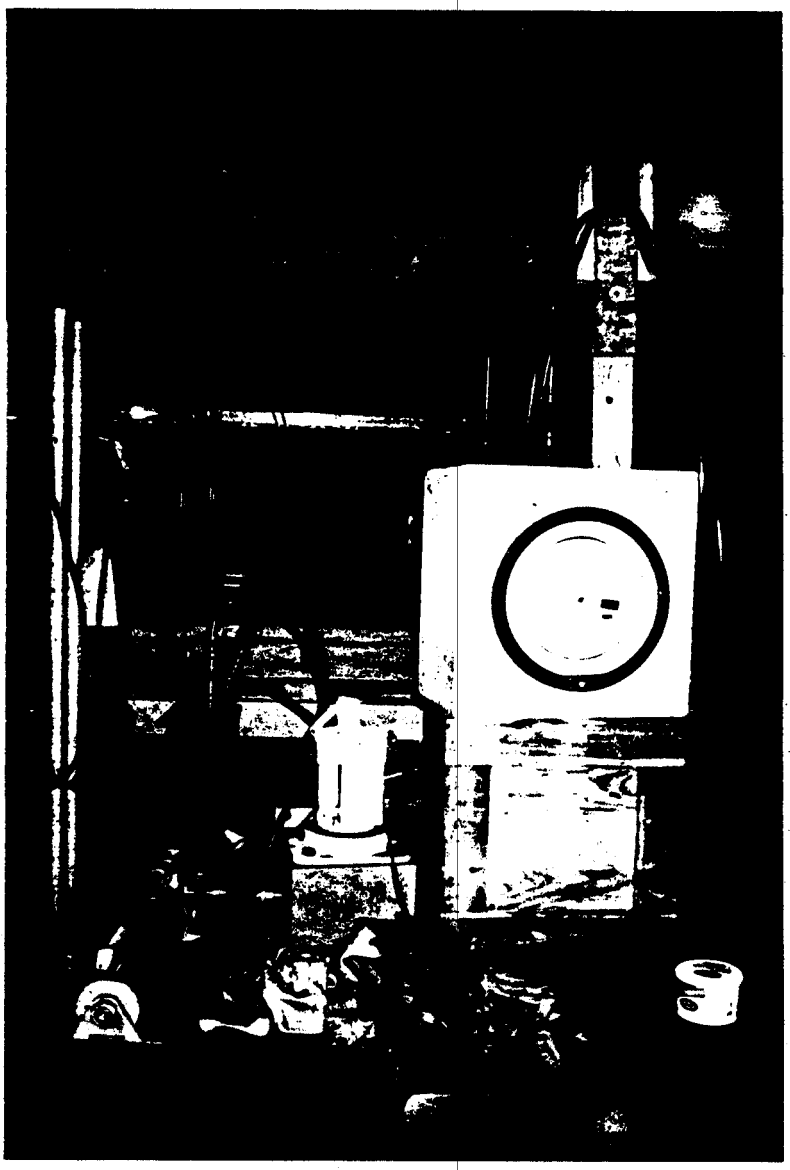

Fig. 7.16 Transverse post-tensioning of the bridge deck system in progress

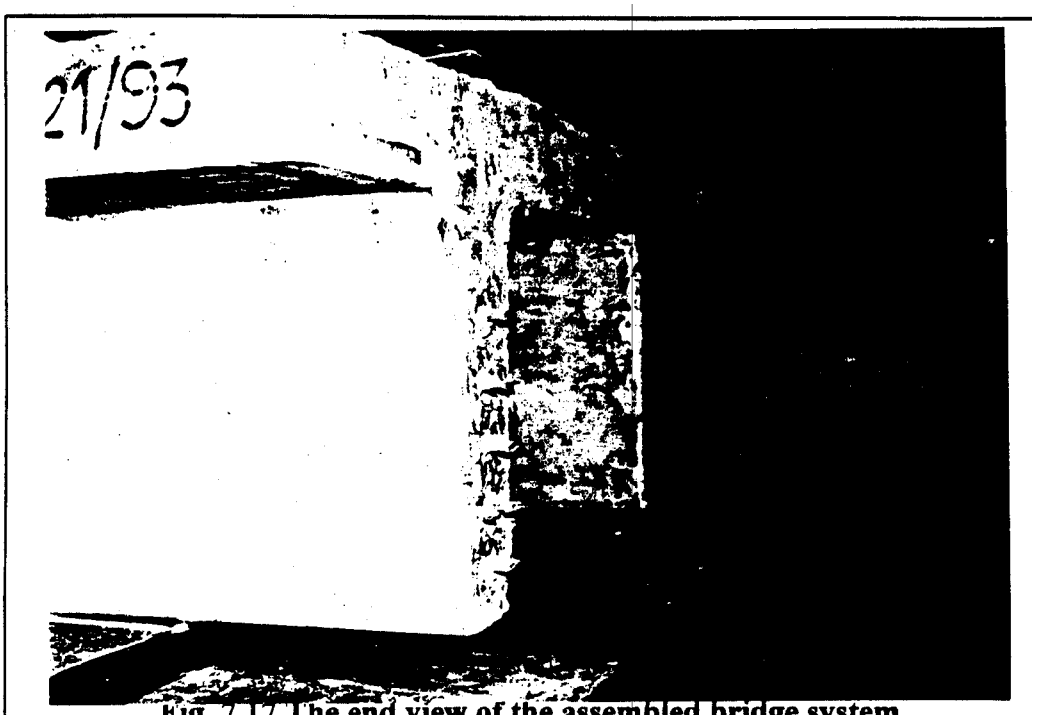

Fig. 7.17 The end view of the assembled bridge system

Fig. 7.18 The assembled bridge deck

7.3 FATIGUE BEHAVIOR

The model bridge system was subjected to a cyclic loading simulating the presence of two HS20-44 trucks on the two lanes. The static tests we performed at regular intervals of fatigue loading to evaluate the stiffness degradation of the bride deck. The deflections, concrete strains, distribution of cracks and crack widths were monitored in the bridge system. The details of the experimental setup, instrumentation, test procedure an the results and discussions are presented in the following sub-sections.

7.3.1 Experimental Setup and Instrumentation

The Double-Tee bridge system is a 1:2 scale model of a two lane bridge. The live loads (two HS20-44 trucks) on the model were positioned symmetrically with respect to the center of the span and eccentrically with respect to the bridge width. Fig. 7.19 shows a schematic of the bridge system and load positions simulating the HS20- AASHTO trucks. The load distribution frame on the east side was placed so as to have east- nt and the east-rear wheels exactly over the stem and the other two wheels over the longitudinal joint. The load flame on the west side was positioned so as to have the east-front and east-rear wheels of the simulated truck exactly over the stem (Fig. 7.19). Figs. 7.20a and 7.20b show the load distribution frames arranged on the model bridge system. Two **electro-mechanically controlled 55 kips. MTS actuators were mounted on the frame as shown in Fig. 7.21a and the load control was achieved using MTS 458.91 Micro profiler (Fig.7.21b). Fig. 7.22 presents e complete overview of the Double-Tee bridge system ready for the fatigue test.**

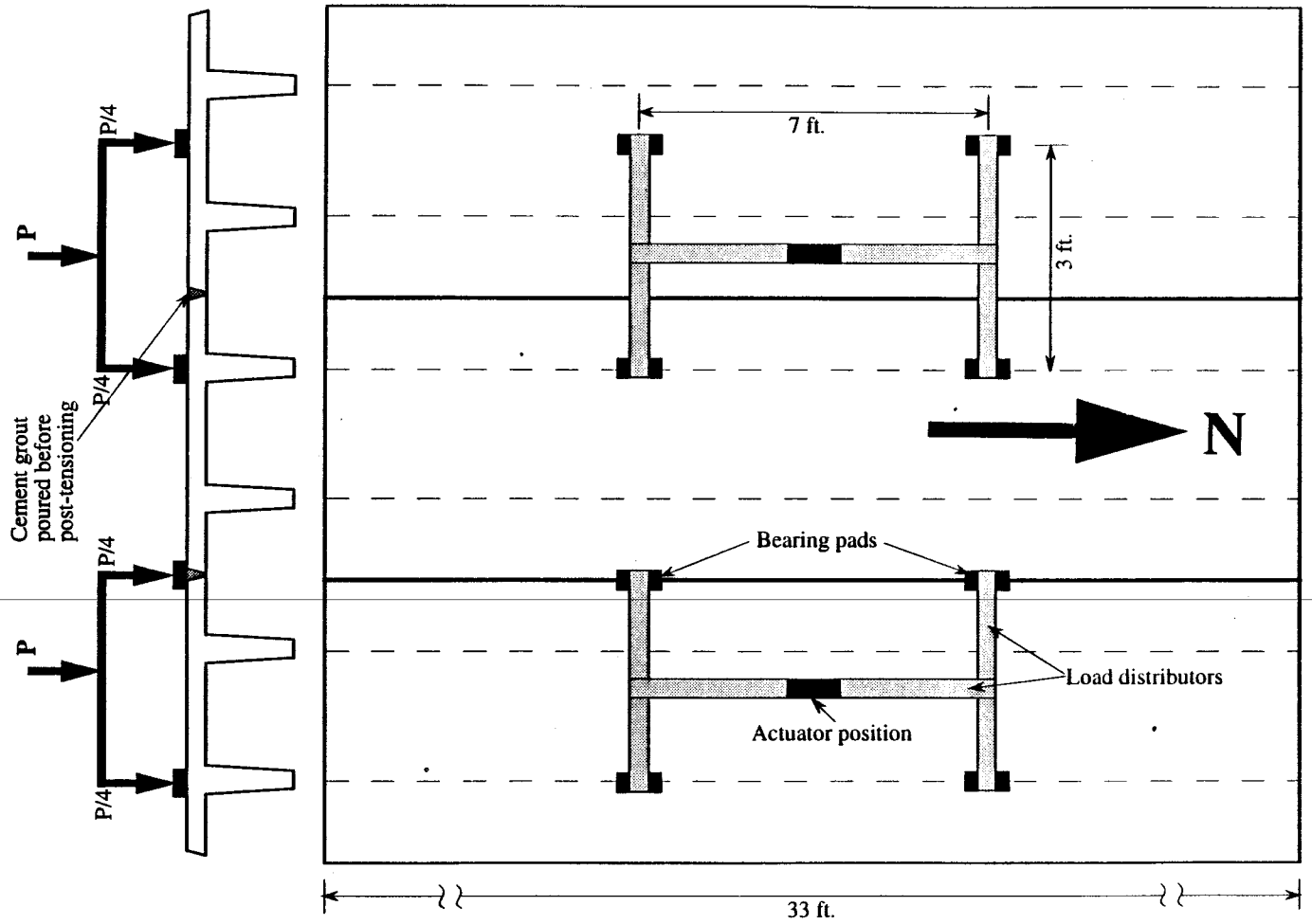

Fig. 7.19 Schematic of bridge system and load positions simulating HS20-44 trucks

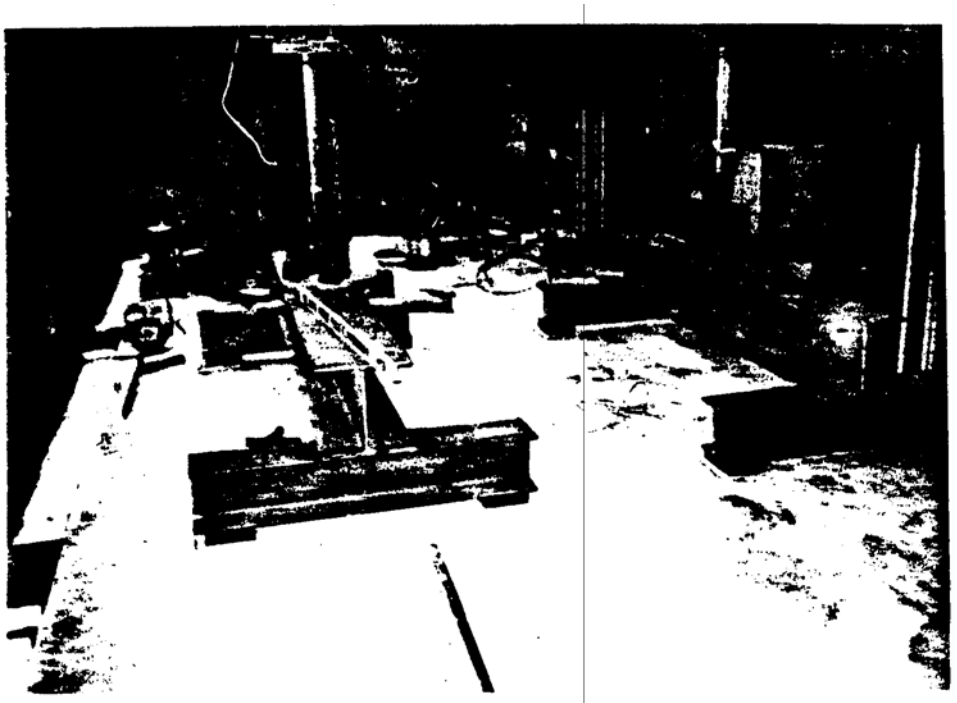

Fig. 7.20 a

Fig. 7.20 b

The load distribution frames arranged on the model bridge system

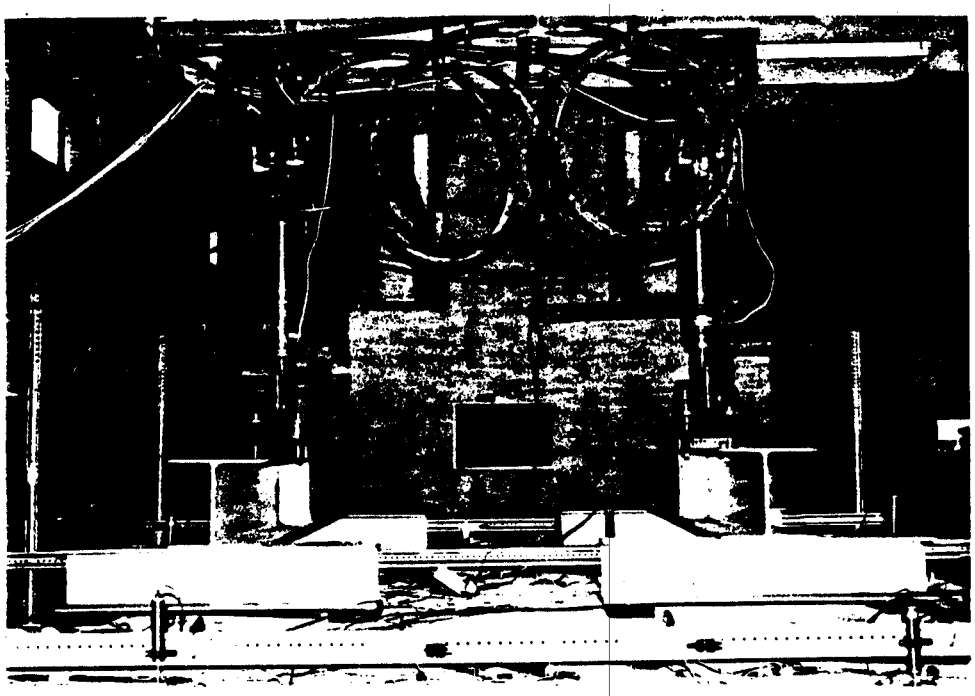

Fig. 7.21a MTS actuators mounted on the frame

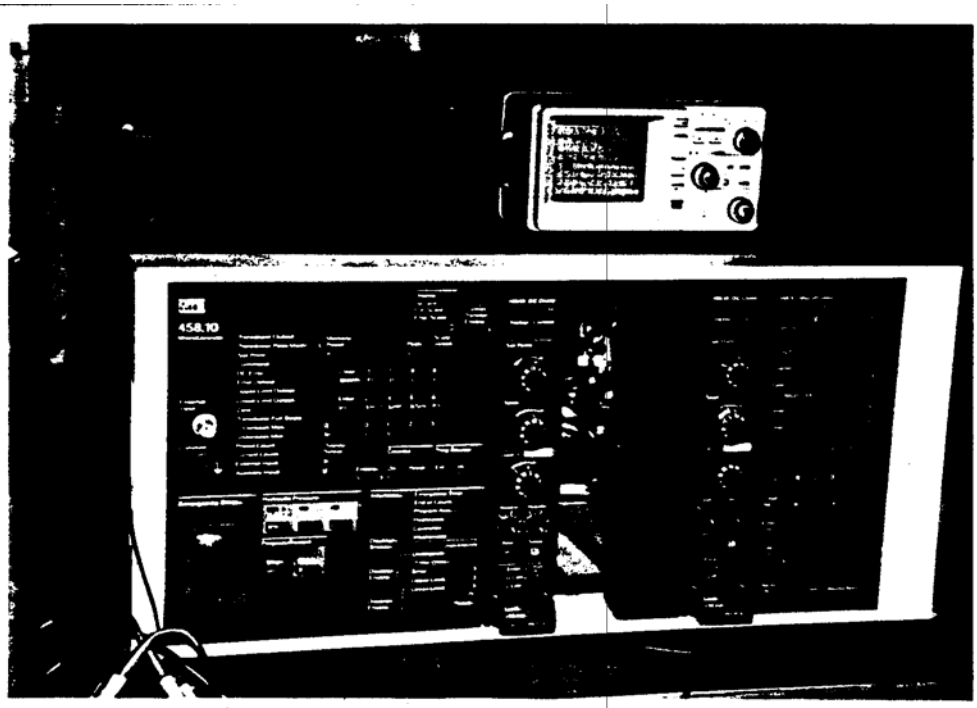

Fig. 7.21b MTS 458.91 Micro profiler

Fig. 7.22 Overview of the Double-Tee bridge system ready for the fatigue test.

Instrumentation was setup for measuring concrete strains, deflections and crack widths. The instrumentation details of the bridge system are shown in Fig. 7.23. One set of six LVDTs was positioned for measuring deflections along the bridge width over the deck system at one quarter span sections and midspan. Two strain transducers were mounted one on the deck and another directly underneath and at the bottom of each Double-Tee stem across the bridge width at one quarter span sections and midspan. Figs. 7.24 and 7 25 show the typical positions of LVDTs and strain transducers on the deck for measuring deflecti ns and compressive strains in concrete.

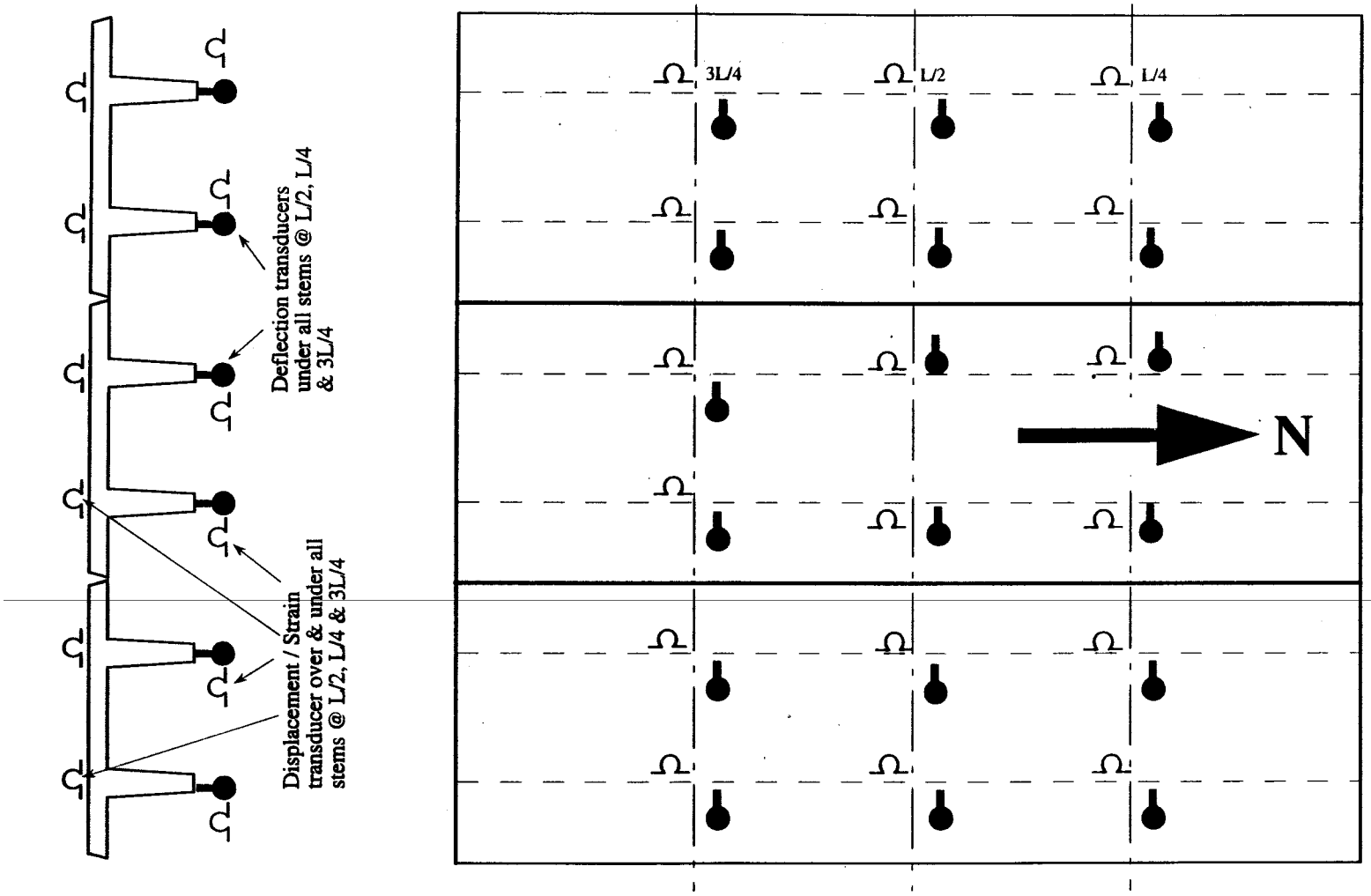

Fig. 7.23 Instrumentation details of the bridge system

Fig. 7.24 Instrumentation for measurement of deflections

Fig. 7.25 Instrumentation for measuring compressive strains in concrete

7.3.2 Test Procedure

A static test was conducted on the model bride system to evaluate the load-deflection behavior prior to subjecting the deck to fatigue loading The fatigue test was carried out in two stages; in the first stage, the model bridge was subjected, to a maximum of two million cycles at a frequency of 1.1 Hz. The maximum and minimum loads applied with each actuator were 11.0 and 4.0 lips respectively. Cyclic loading was carried out using load control method. The minimum load of 4.0 kips in the fatigue load range was chosen t take into account the partial dead load compensation for the scaled model bridge. The maxim load of 11.0 kips is representative of about 60% of the scaled loading of a single HS20-44 A SHTO truck. The effective prestressing forces of about 9.0 kips. in each tendon (as explained in Chapter 4) were about 40 % less than the design forces (15.0 kips in each tendon) due to limitations in the anchorage system. Hence, the maximum load value in the fatigue range had to be reduced by about 40 % in order to investigate the fatigue behavior.

The Double-Tee bridge system exhibited satisfactory fatigue behavior in the first stage cyclic testing. This led to continue to the investigation with a higher load range in the second stage testing. The second stage fatigue loading was c ed out upto one million cycles at a lower frequency of 0.33 Hz. after the completion of two million cycles in the first stage. The maximum and minimum loads in the second stage cyclic loading were 18.0 and 6.0 kips. respectively in each actuator. The recommended frequency range in e cyclic loading of bridge decks for investigation of fatigue behavior is 1.0 to 4.0 Hz. The model bridge system exhibited relatively a large midspan deflection of 1.4 in. at the load of 18.0 kips. With this large deflection, the maximum possible frequency with the MTS system was only 0.33 Hz. The static tests were conducted at regular intervals of cyclic loading in both. the first and second stage fatigue load tests. Deflections and strain measurements were taken pto the maximum loads in the two load ranges.

7.3.3 Results and Discussions

This section presents the details of analysis, res is from the first and second stage fatigue tests and detailed discussions. The effect of cyclic load' g on the stiffness of the bridge system is evaluated in terms of load-deflection behavior and distri ution and width of cracks.

7.3.3.1 Static test

The model and prototype bridge systems were first analyzed using the grillage analogy for i) self weight and u) unit loads at positions corresponding to HS20-44 trucks on the two lanes of the bridge deck system. Fig. 7.26 shows the typical di cretization of the bridge for the grillage analogy. Table 7.1 presents the summary of the analyse for the model and prototype bridges.

Table 7.1 Bending moments at critical element ends in kip.-ft. units

Model bridge system			
Element no.	**Self weight**	**Unit loads at points corresponding to HS20-44 truck**	**Prototype bridge system - self weight**
4	**17.89**	**8.576**	**262.0**
12	**17.89**	**8.113**	**262.0**
20	**17.89**	**7.659**	**262.0**
28	**17.89**	**7.27**	**262.0**
36	**17.89**	**6.831**	**262.0**
44	**17.89**	**6320**	**262.0**

Based on the above moments a partial dead load compensation was calculated as 4.0 kips. for each actuator representing a truck per lane. The first crack load of 9.8 kips. was calculated

based on 15 percent losses in prestress, concrete strength of 4000 psi and the moments for the critical element 4. But, the first crack in the experimental bridge system was observed at a load of 8.5 kips. in each actuator. However, the static test was continued up to a maximum load of 11.0 kips. in each actuator. Then the bridge system in a precracked condition was subjected to the first stage fatigue loading. Fig. 7.27 shows the load-deflection relationships for all the six stems of the bridge system at south and north quarter and midspan locations. The decrease in the slope of the load-deflection relationships can be observed after the initiation of the first crack. The bridge system was then unloaded after the maximum load and a permanent deflection of about 0.02 in. and 0.05 in. was observed at quarter and midspan sections respectively.

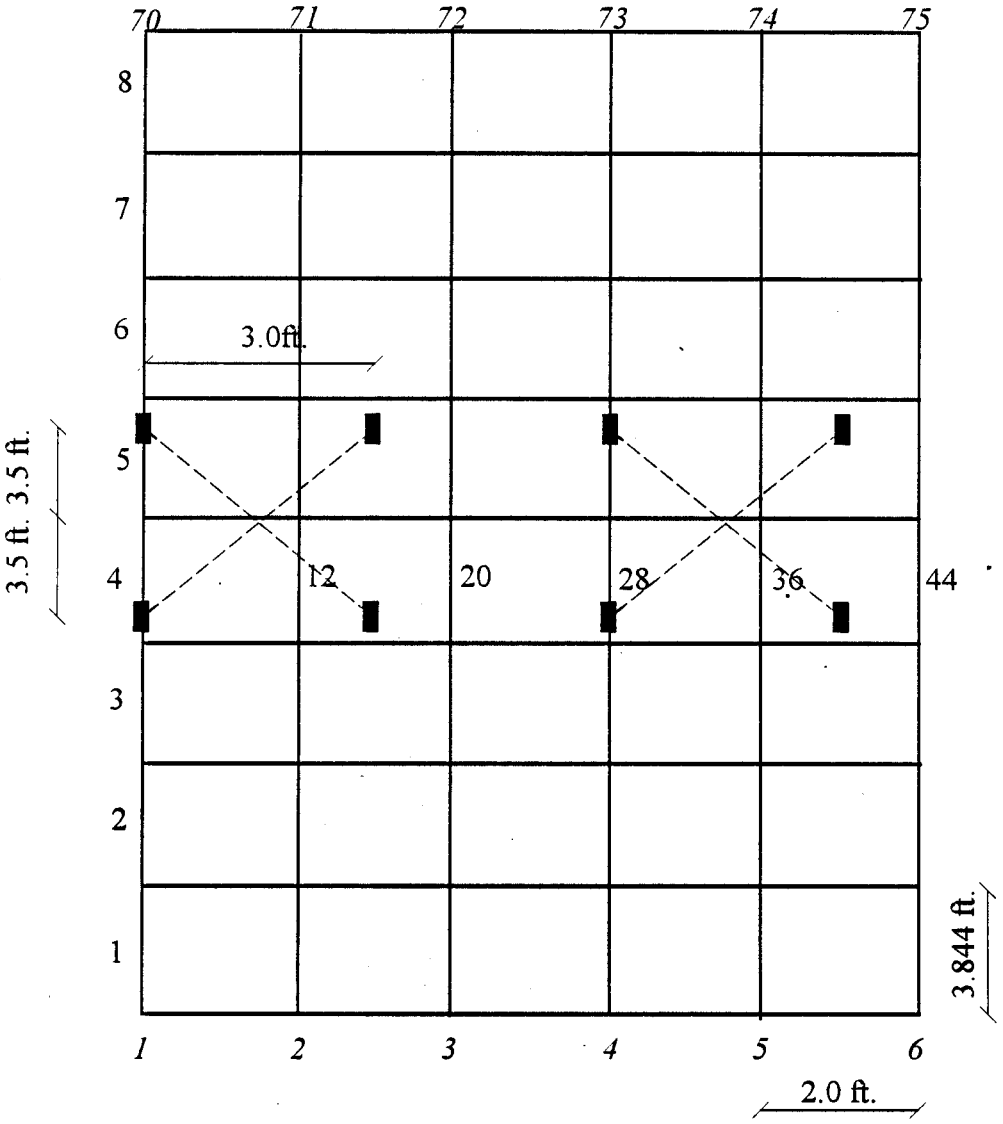

Note:

1, 2, 3, ... = Element numbers

1, 2, 3, ... = Node numbers

▮ = Wheel of simulated HS20-44 truck

Scale:

Widthwise - 1 in. = 0.4 ft.

Spanwise - 1 in. = 6.15 ft.

Fig. 7.26 Typical discretization of the bridge for grillage analogy

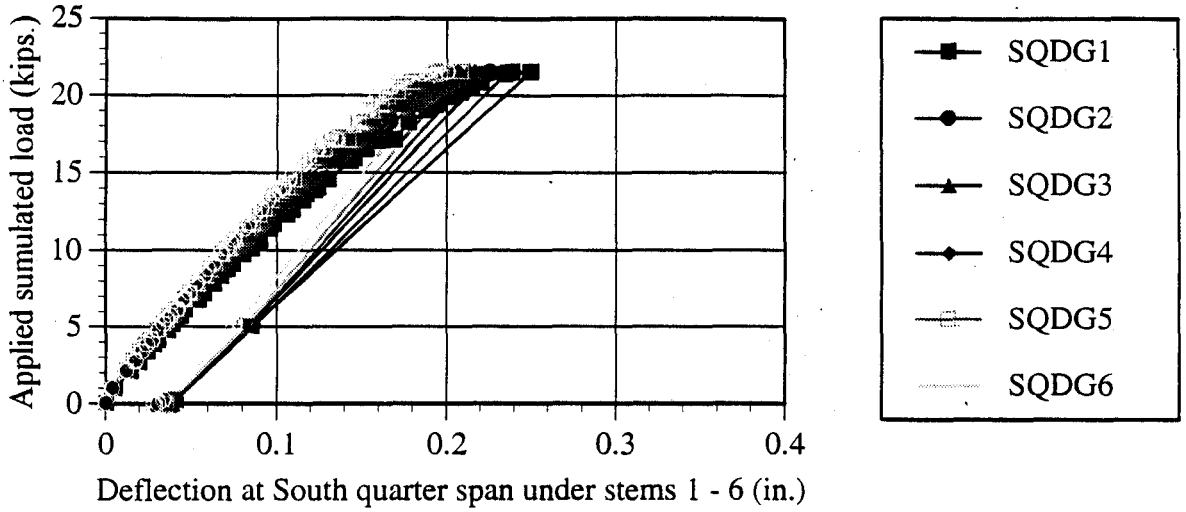

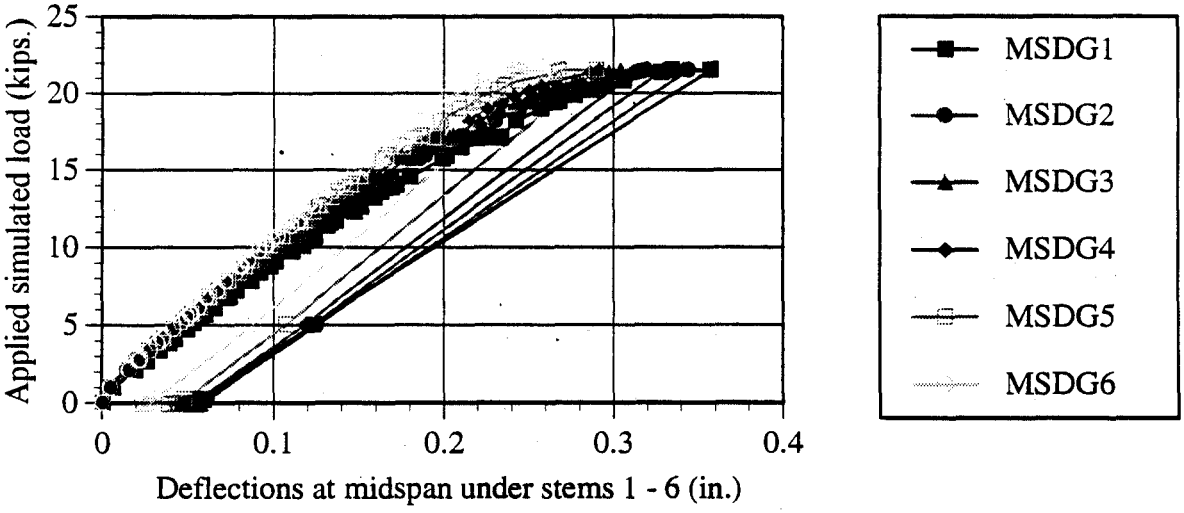

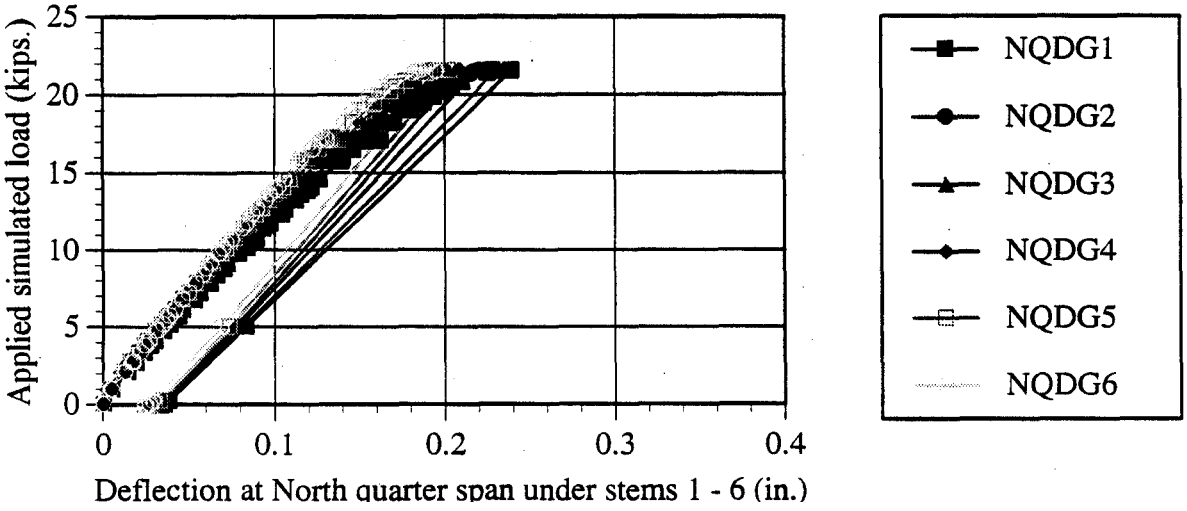

Fig. 7.27 Pmax = 22 kips; Pmin = 8 kips
Load deflection of AFRP Double Tee bridge system: 0 Cycles

7.3.3.2 First stage fatigue test

As explained in the earlier section, the first stage fatigue test was conducted with the load range of 4.0 to 11.0 kips. in each actuator. Static tests were conducted at regular intervals of 75,000 to 80,000 cycles of fatigue loading upto two million cycles. The load carrying capacity, and distribution and size of cracks were evaluated throughout the fatigue test. The first stage fatigue test in progress is shown in Fig. 7.28.

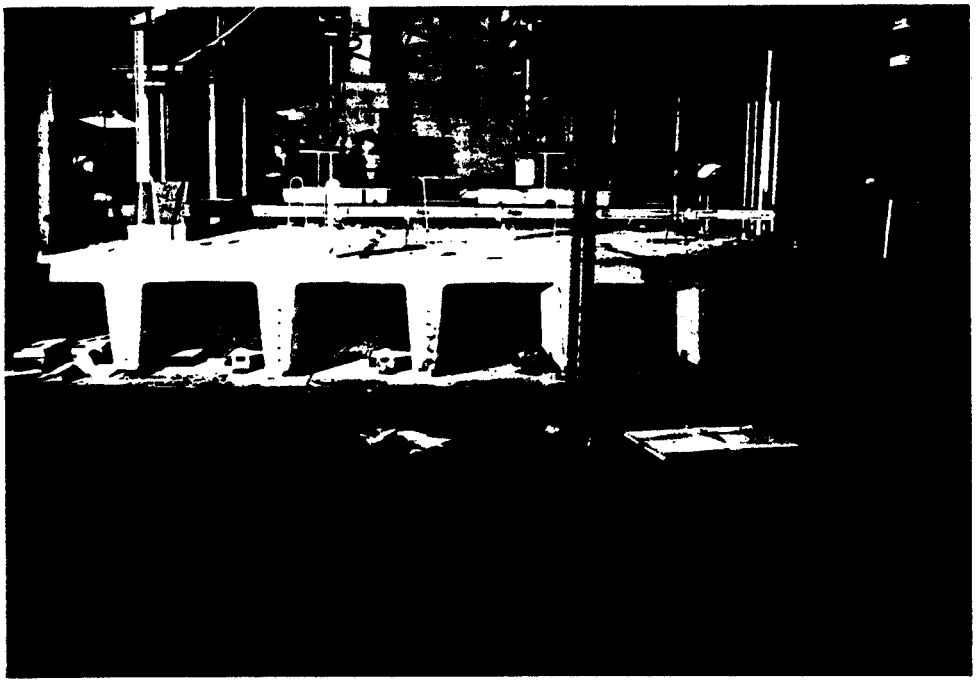

Fig. 7.28 The first stage fatigue test in progress

The deflections were measured during all the static tests conducted at regular intervals. The load-deflection relationships were examined to evaluate the stiffness degradation due to cyclic loading. Load-deflection relationships at south and north quarter and midspan sections for typical intervals of cyclic loading are given in Figs. 7.29 to 7.33. Fig. 7.34 presents the deflected shape of the bridge deck after 56,000 cycles at the maximum load of the fatigue load range (11 kips. in each actuator), in the form of isometric, side and end views. Deflections were measured under all the stems across the width of bridge deck upto 56,000 cycles. A significant reduction

in stiffness could be observed after the first 56,000 cycles of fatigue loading. However, thereafter the increase in deflections resulting from the change in stiffness. was small and hence displacements were monitored only at certain selected locations on the bridge deck upto two million cycles. Consequently Figs. 7.31 to 7.33 show load-deflection relationships recorded by only two or three LVDTs. Also, from Fig. 7.33 it can be observed that the permanent deflection after completion of two million cycles of fatigue loading, is not significantly different from that observed before the commencement of fatigue testing. This behavior certainly exhibits the good fatigue and bond characteristics of ARAPREE cables when used as prestressing tendons in concrete structures. The slight increase in deflections and reduction in slope of load deflection relationships over the period of first stage fatigue testing could be attributed to the propagation of existing cracks and / or. formation of a very limited number of new cracks. The deflection contours shown in the isometric view of Fig. 7.34 illustrates the unsymmetric deflected profile due to the eccentric loading pattern, while side and end views complement the above observation.

Figs. 7.35 and 7.36 show the load-deflection relationships at south and north quarter span sections of stems 6 and 1 respectively. Figs. 7.37 and 7.38 show the load-deflection relationships of stems 1 and 6 at midspan. The load-deflection relationships after completion of typical number of cycles are compared in Figs. 7.35 to 7.38 to evaluate the stiffness degradation due to fatigue loading. It is observed that significant increase in deflection is caused after 56,000 cycles resulting from stiffness reduction. However, the increase in deflection beyond 56,000 cycles was only marginal.

The longitudinal deflection profiles of stem 1 are shown in Fig. 7.39 corresponding to the minimum (8 kips.) and maximum (22 kips.) loads representative of the two HS20-44 trucks, for different cycles of fatigue loading. Fig. 7.40 shows the longitudinal deflection profiles of stem 6 corresponding to the total maximum load of 22 kips. The deflection increase at south and north quarter and midspan sections of stems 1 and 6 is shown in Fig. 7.41. Figs. 7.39 to 7.41 also demonstrate the significant increase in deflection at 56,000 cycles and subsequent marginal deflection increase up to two million cycles.

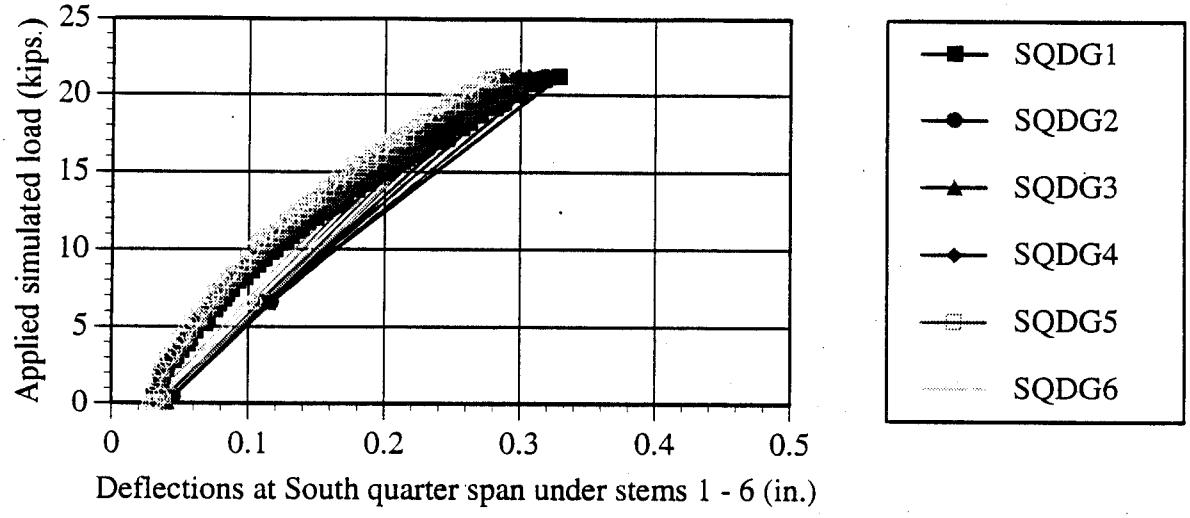

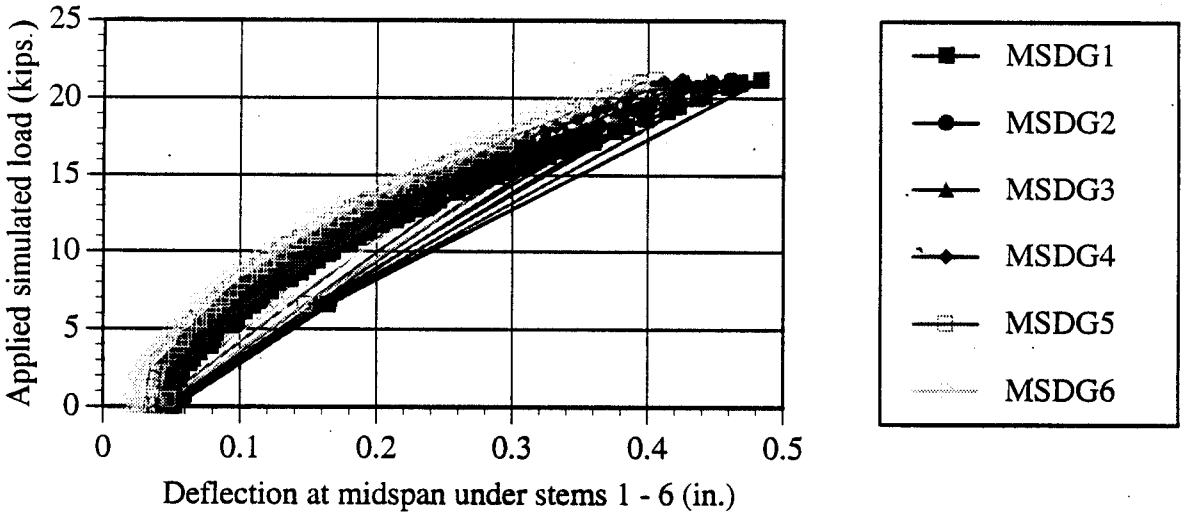

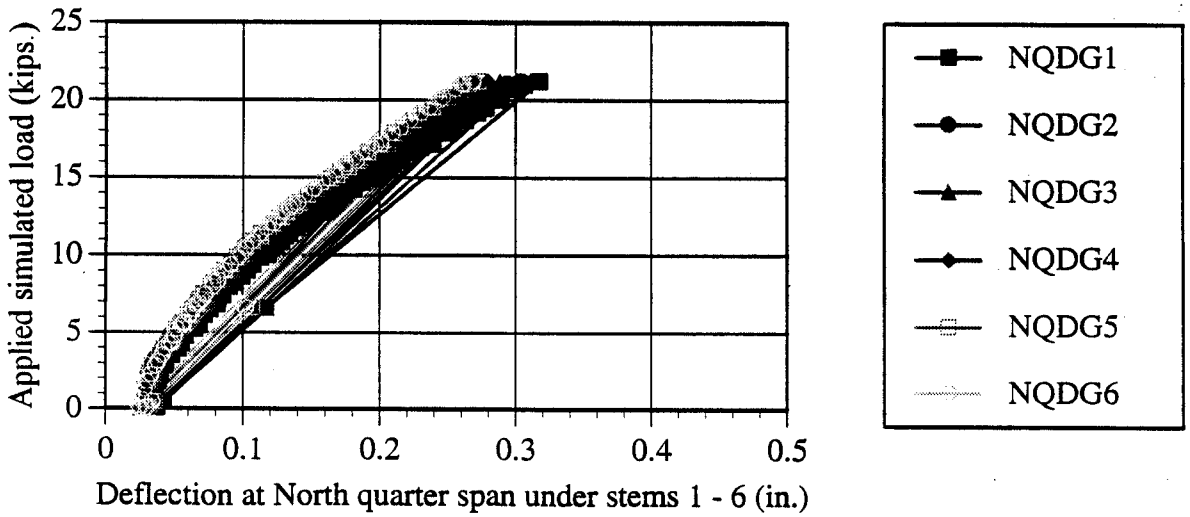

Fig. 7.29 P_{max} = 22 kips; P_{min} = 8 kips

Load deflection of AFRP Double Tee bridge system : 56,000 Cycles

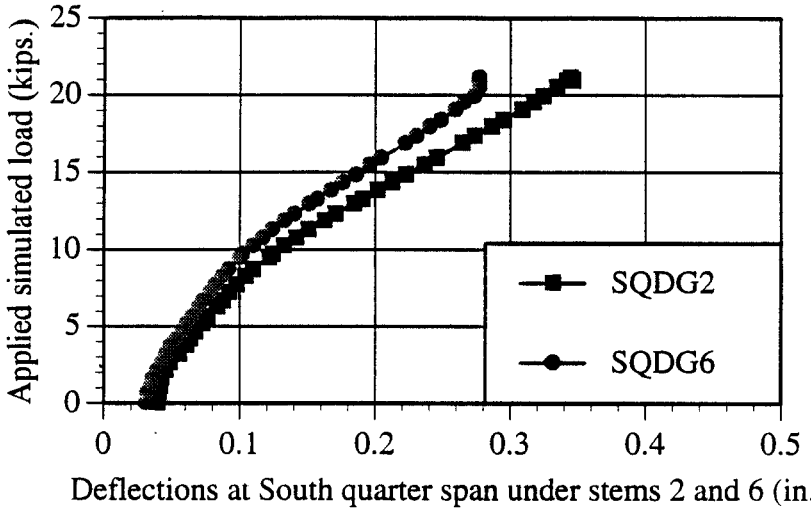

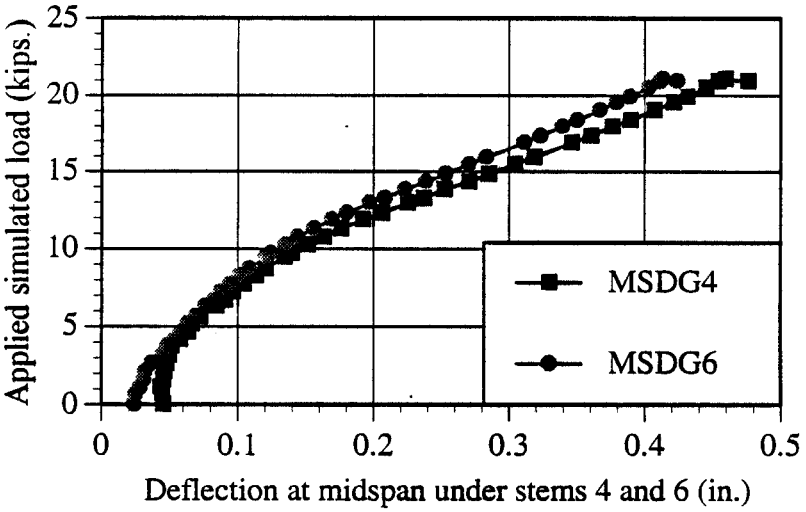

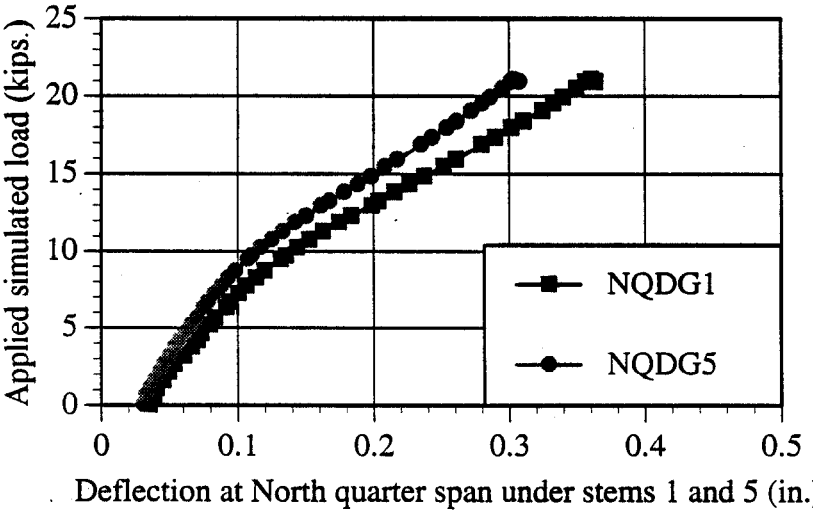

Fig. 7.30 P_{max} = 22 kips; P_{min} = 8 kips
Load deflection of AFRP Double Tee bridge system : 490,000 Cycles

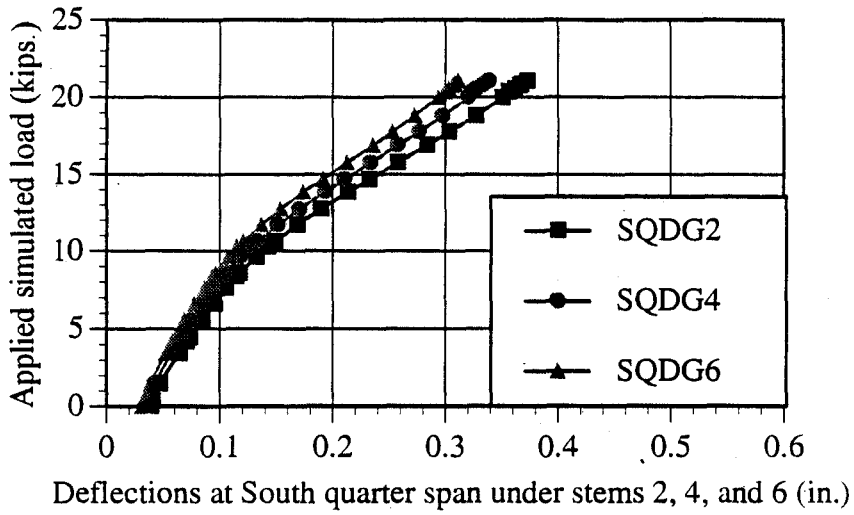

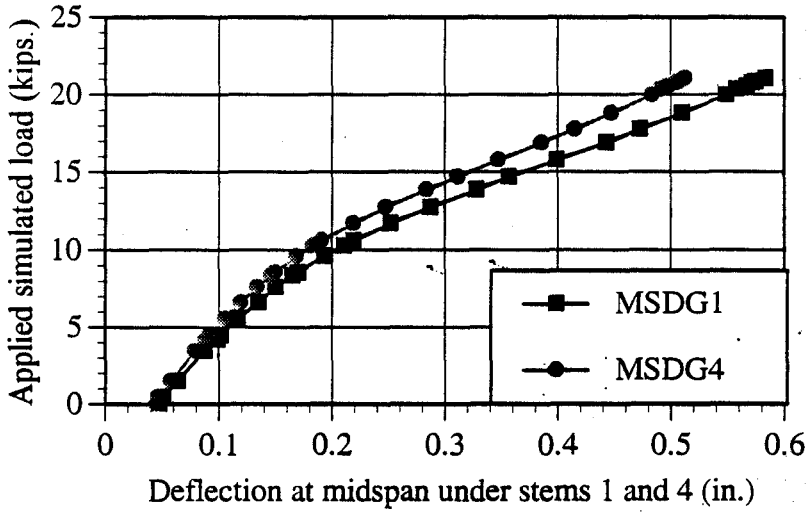

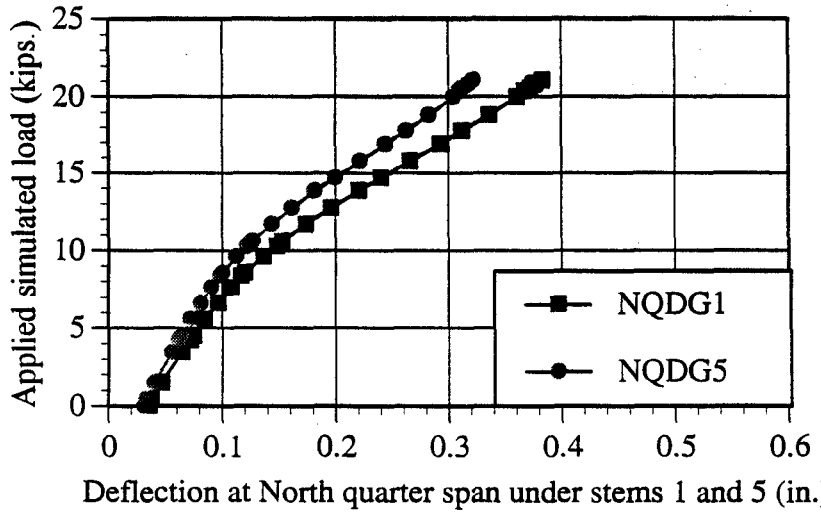

Fig. 7.31 P_{max} = 22 kips; P_{min} = 8 kips
Load deflection of AFRP Double Tee bridge system : 990,000 Cycles

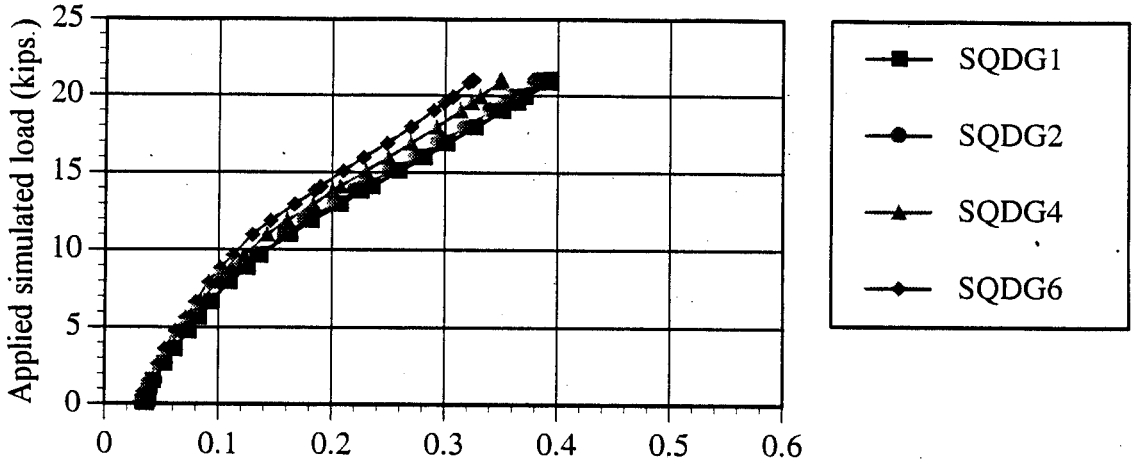

Deflections at South quarter span under stems 1, 2, 4, and 6 (in

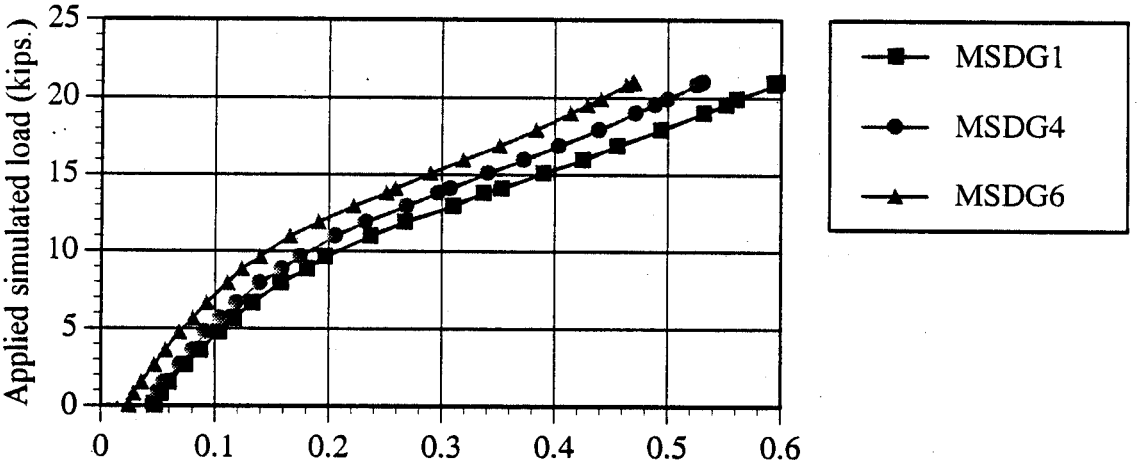

Deflection at midspan under stems 1, 4 and 6 (in.)

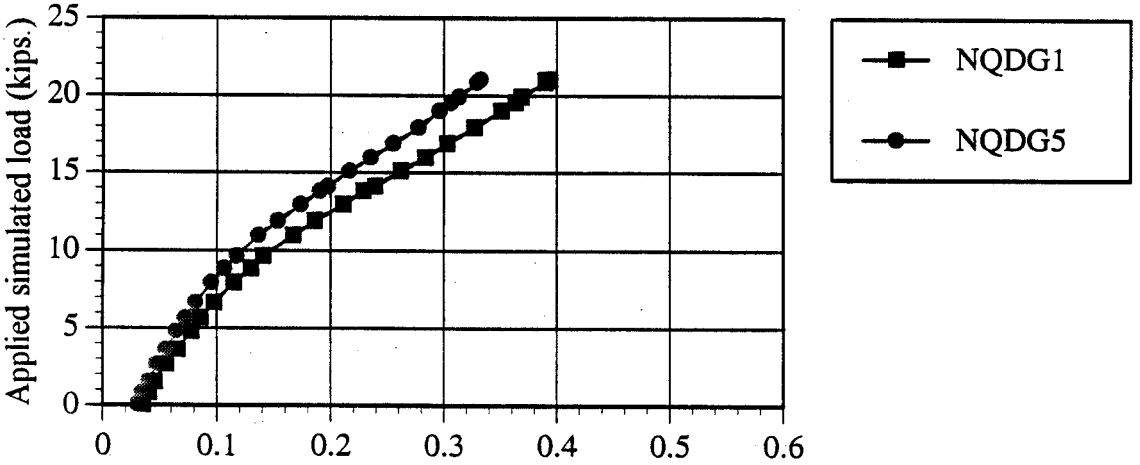

Deflection at North quarter span under stems 1 and 5 (in.)

Fig. 7.32 P_{max} = 22 kips; P_{min} = 8 kips
Load deflection of AFRP Double Tee bridge system : 1,500,000 Cycles

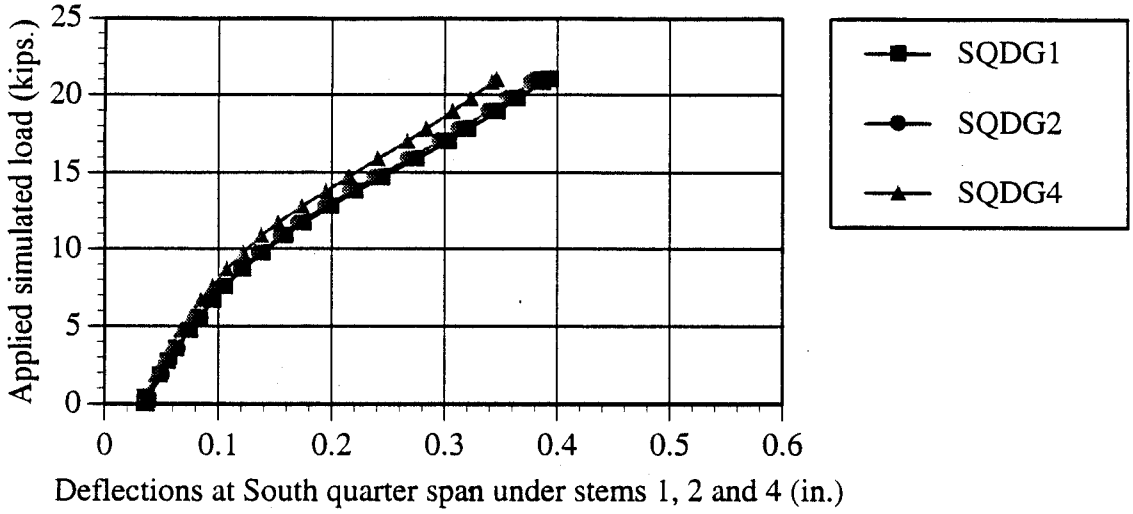

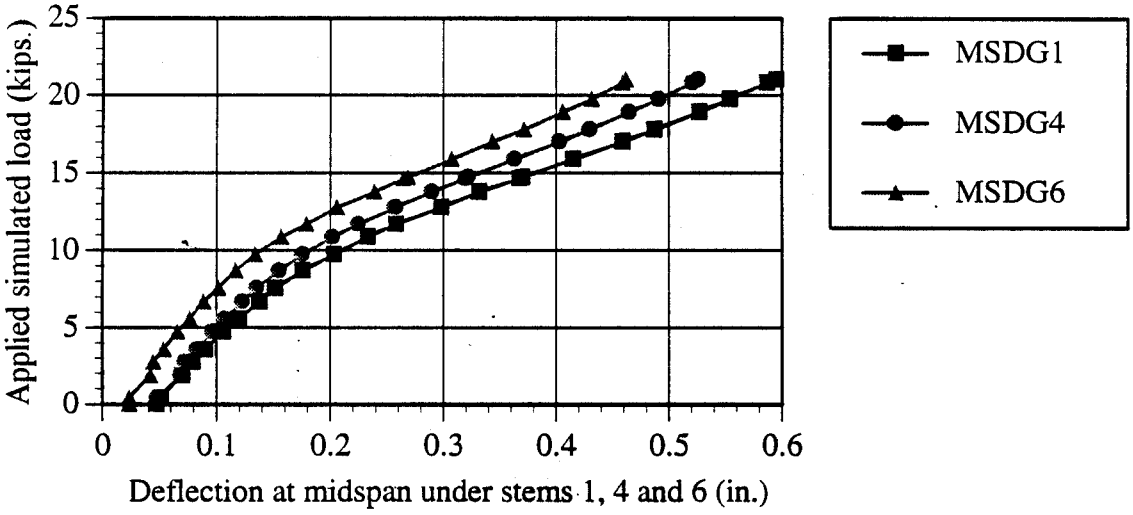

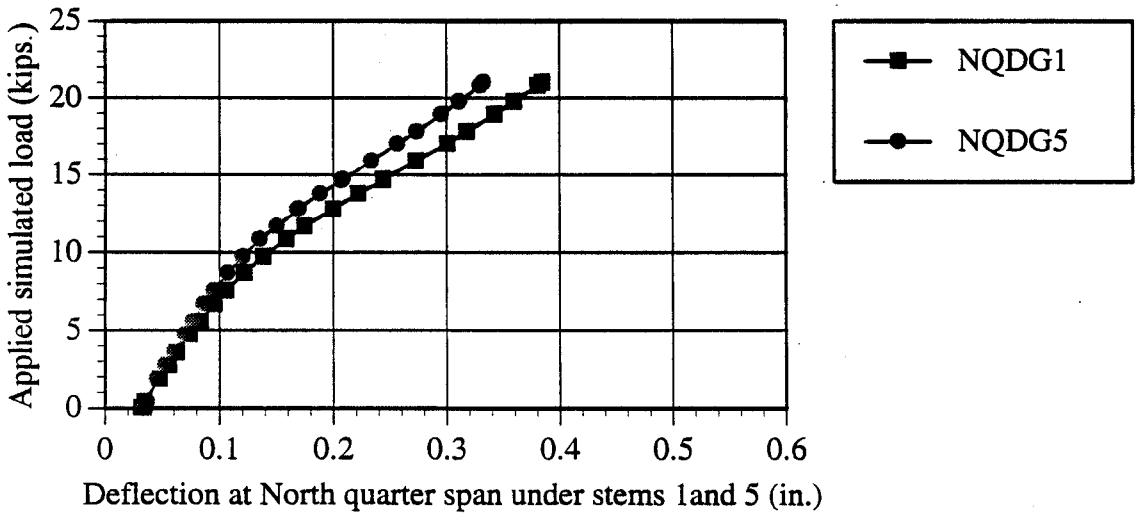

Fig 7.33 P_{max} = 22 kips; P_{min} = 8 kips

Load deflection of AFRP Double Tee bridge system : 2,000,000 Cycles

Fig. 7.34 The deflection shape of the bridge deck after 56,000 cycle loading at load of 22 kips

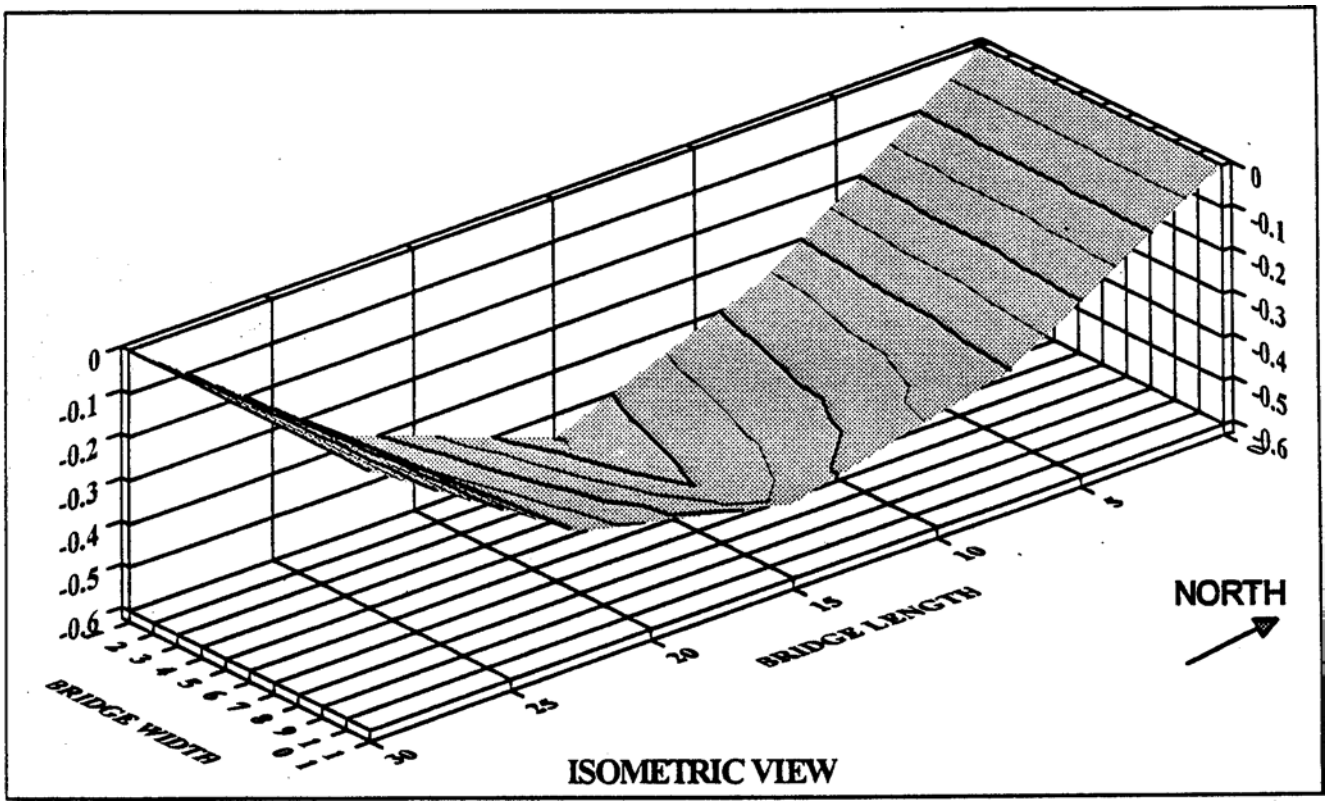

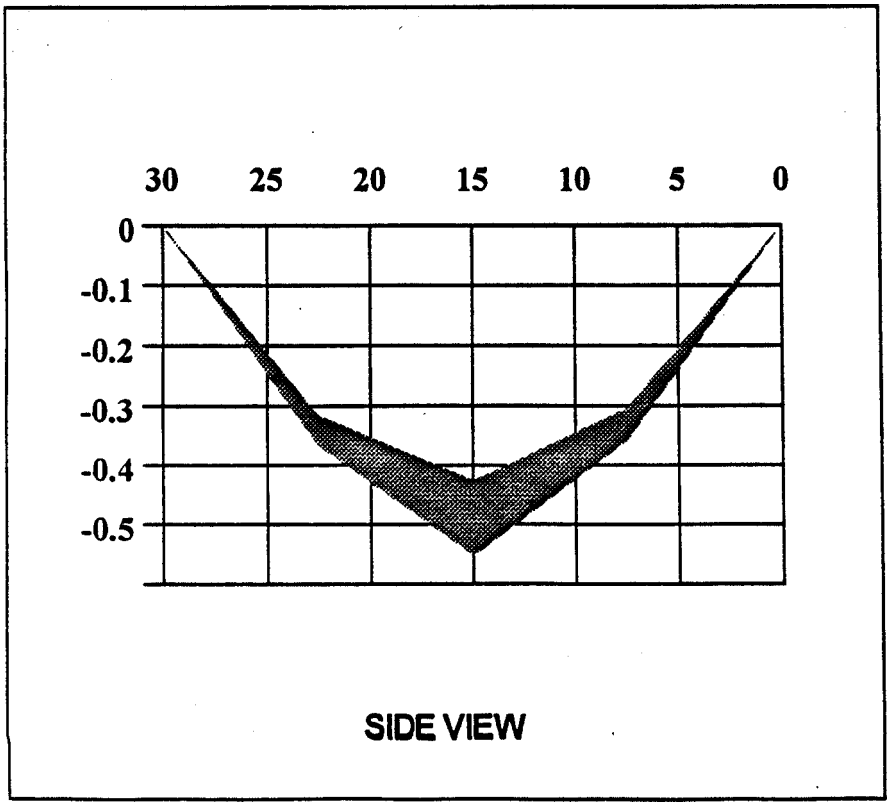

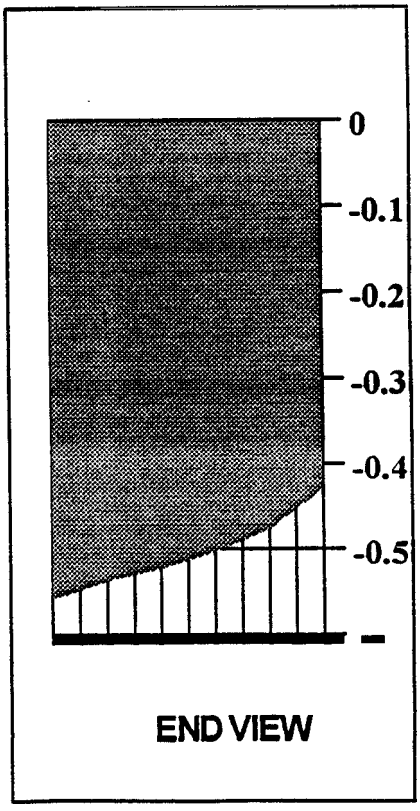

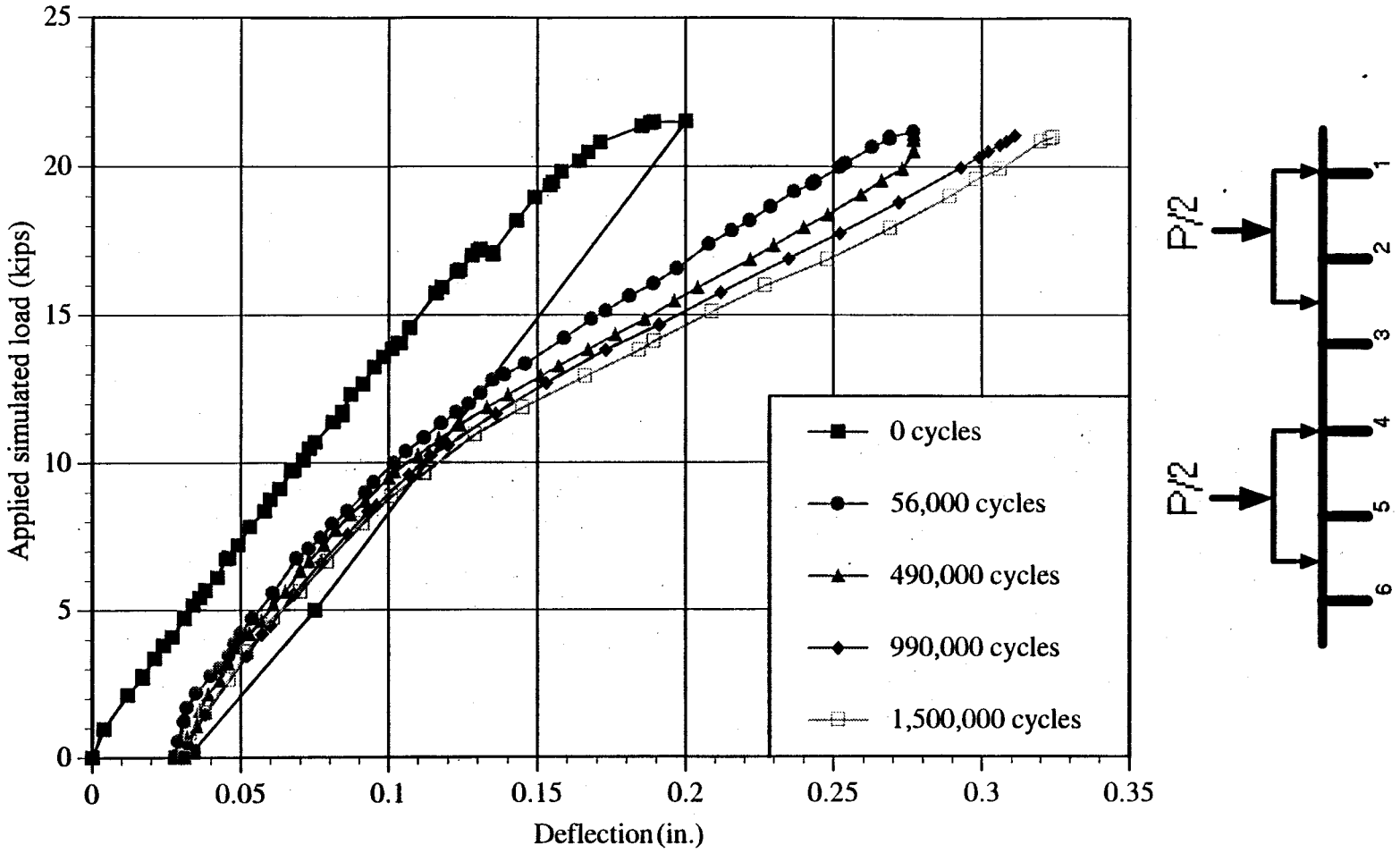

Fig 7.35 P_{max} = 22 kips; P_{min} = 8 kips
Load deflection at South quarter span of stem 6 during various stages of fatigue testing

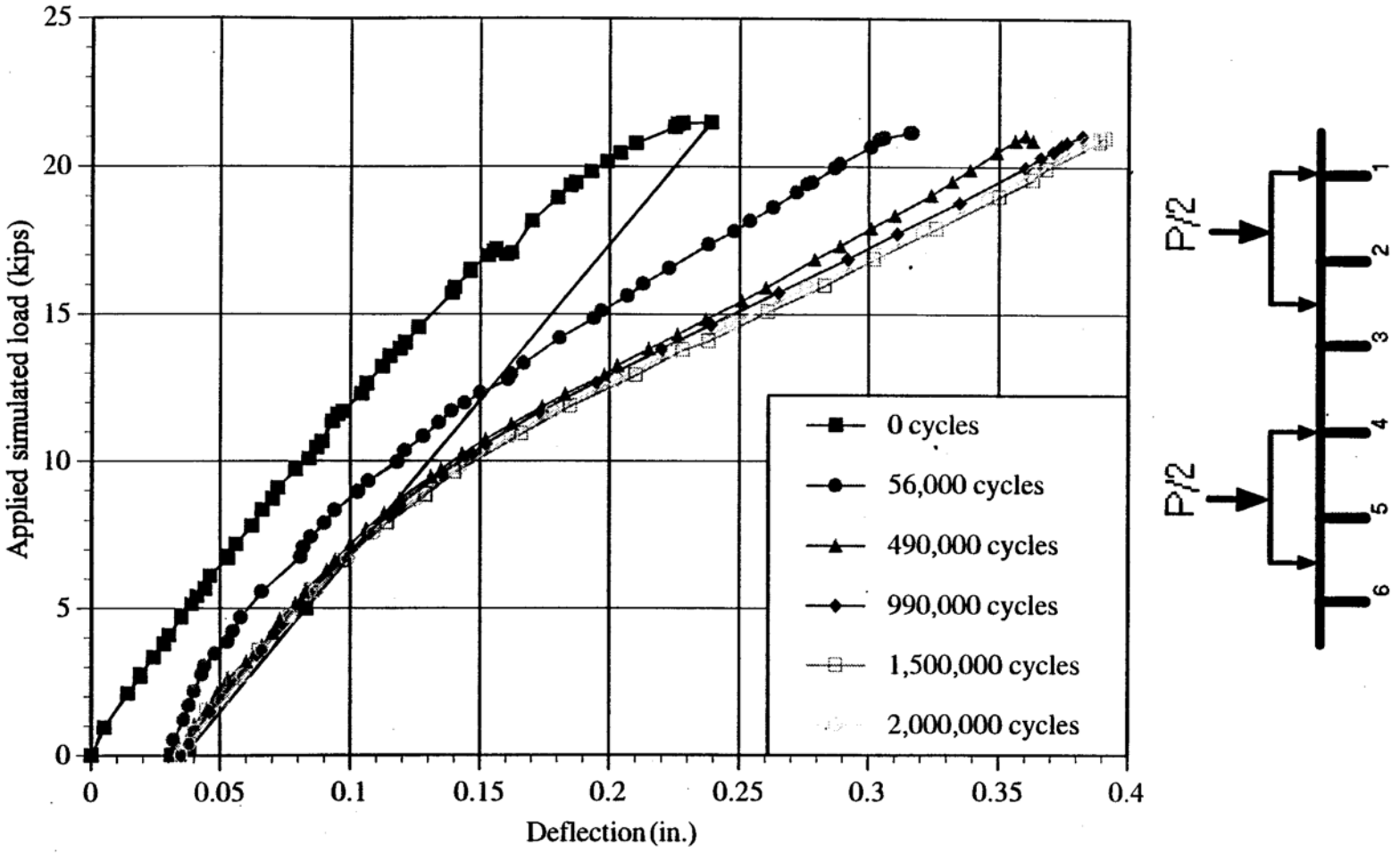

Fig. 7.36 P_{max} = 22 kips; P_{min} = 8 kips
Load deflection at North quarter span of stem 1 during various stages of fatigue testing

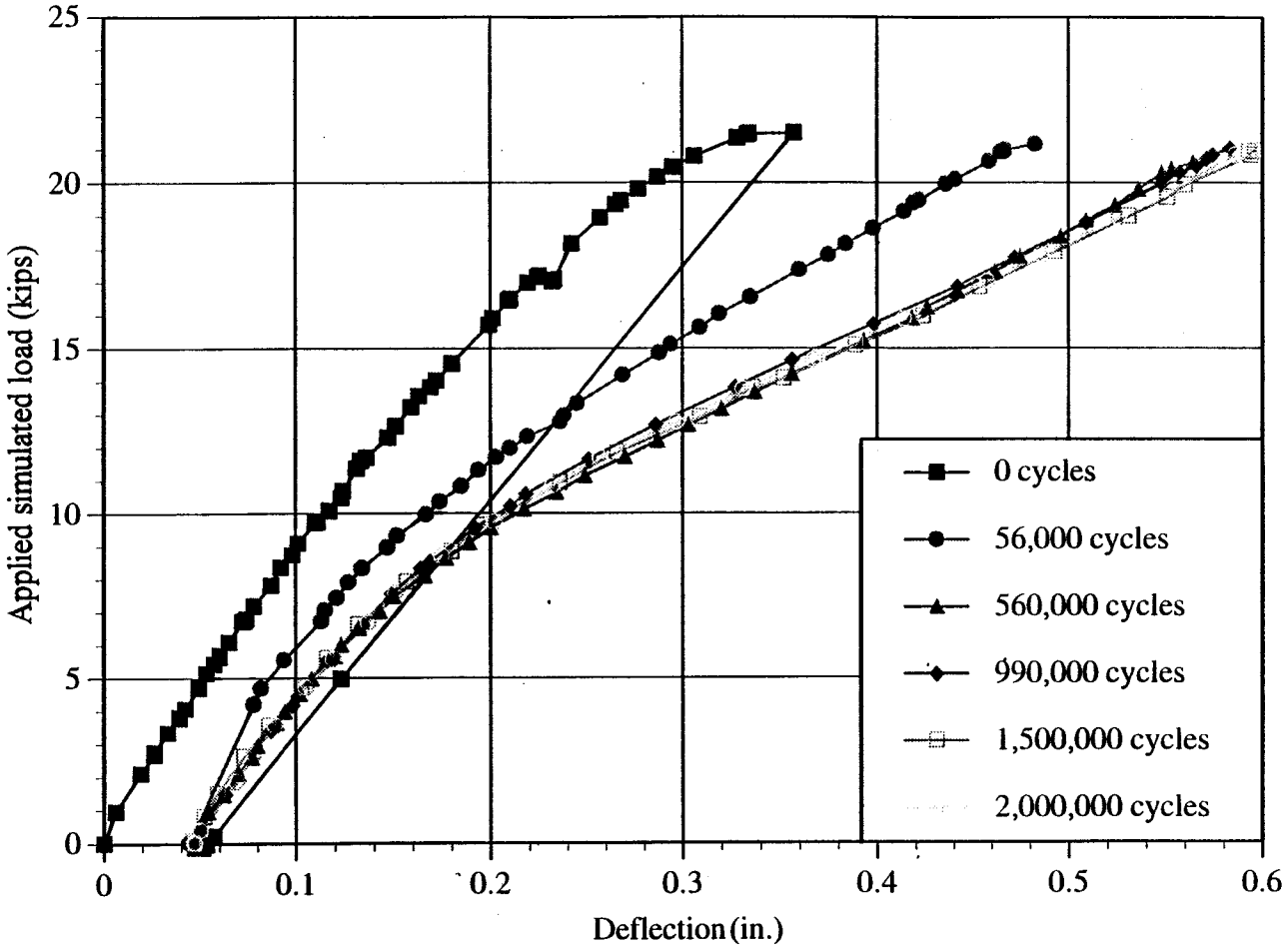

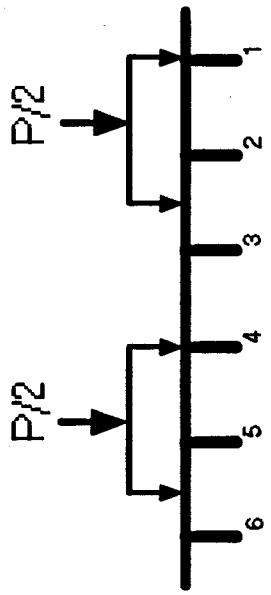

Fig. 7.37 P_{max} = 22 kips; P_{min} = 8 kips
Load deflection at midspan of stem 1 during various stages of fatigue testing

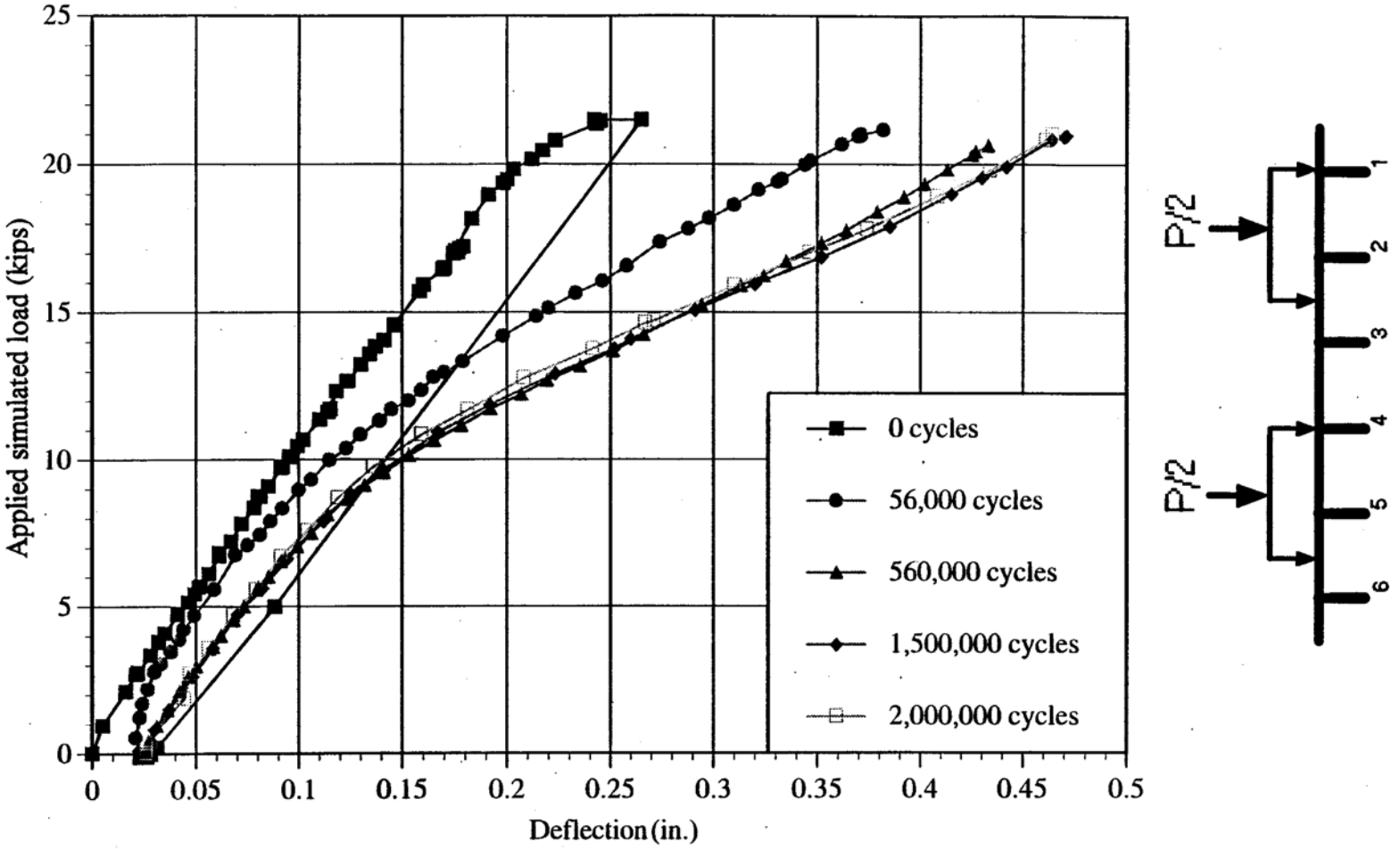

Fig. 7.38 P_{max} = 22 kips; P_{min} = 8 kips
Load deflection at midspan of stem 6 during various stages of fatigue testing

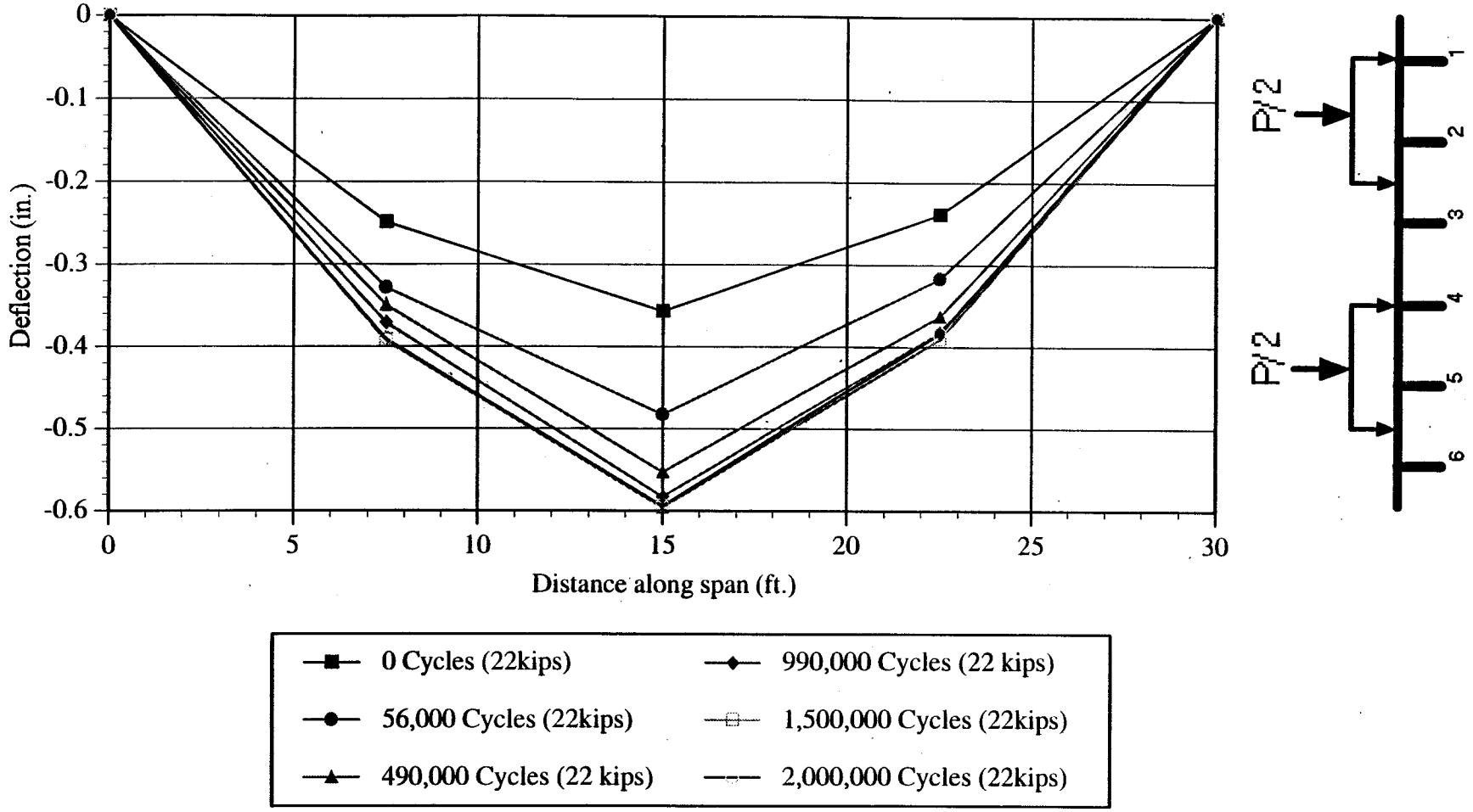

Fig. 7.39 Longitudinal deflection profile of stem 1 after being subjected to fatigue loading (Applied simulated load = 22 kips, fatigue load range : 8 to 22 kips)

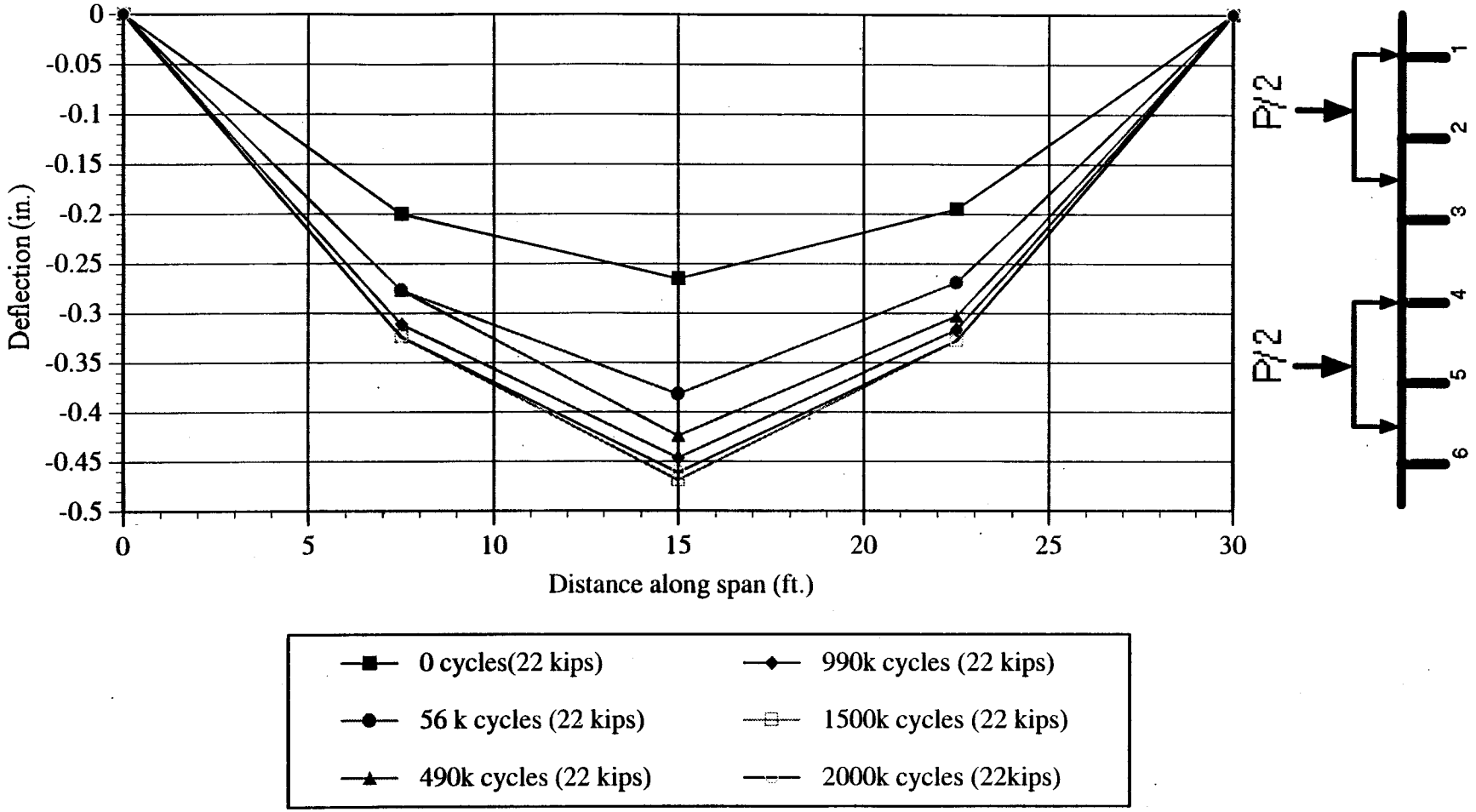

Fig. 7.40 Longitudinal deflection profile of stem 6 after being subjected to fatigue loading (Applied simulated load = 22 kips, fatigue load range : 8 to 22 kips)

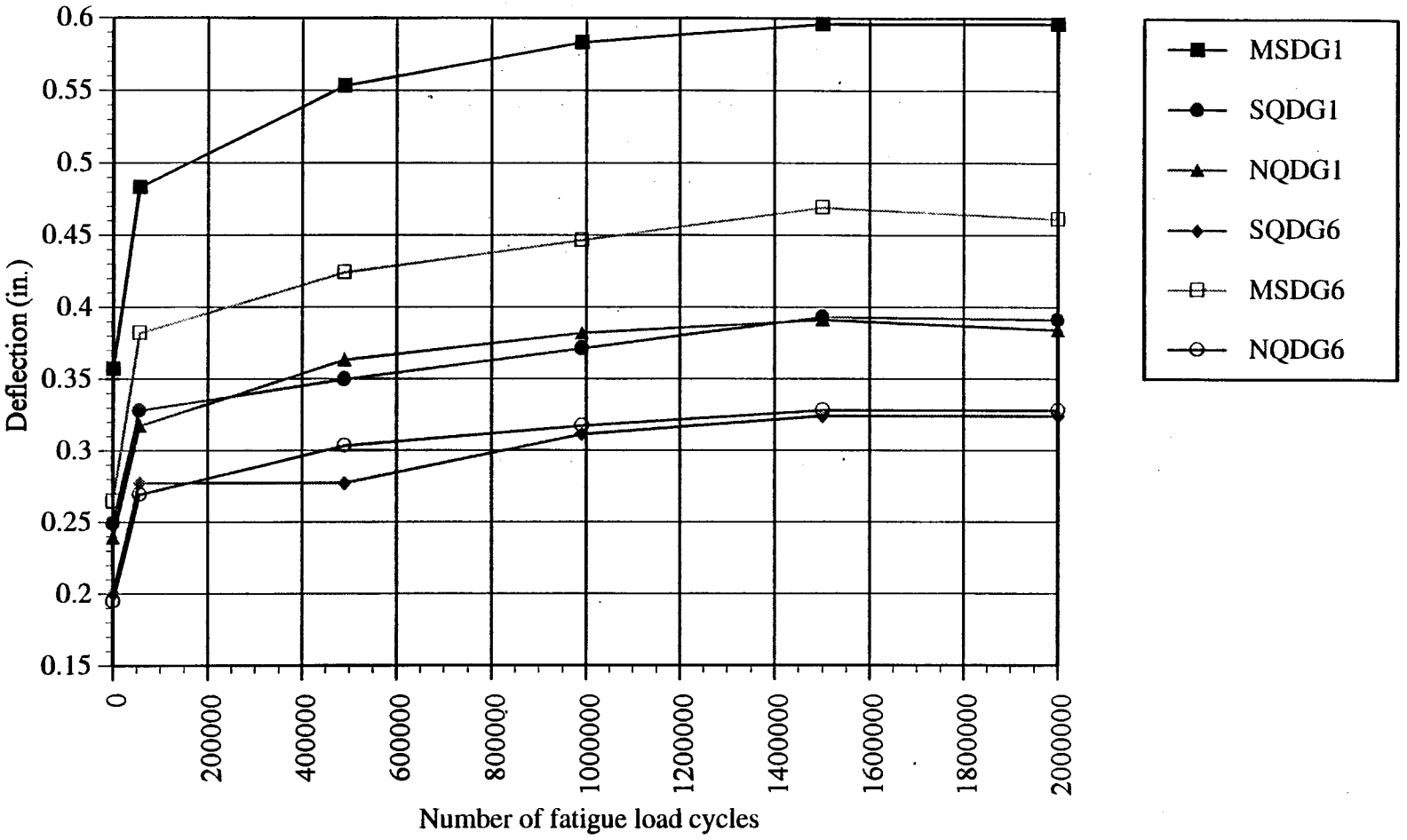

Fig. 7.41 Deflection increase at mid, South and North quarter spans of stems 1 and 6 with number of cycles (Applied simulated load = 22 kips : fatigue load range = 8 to 22 kips)

7.3.3.3 Second stage fatigue test

At the conclusion of the first stage fatigue test with two million cycles, a static test was conducted with a maximum load of 18.0 kips. in each actuator. This load corresponds to the scaled down value of a HS20-44 truck on a single lane of the two lane bridge model. The load-deflection behavior from the static load test is shown in Fig. 7.42. It can be observed that the curve almost coincides with the load-deflection graph upto a load of 11 kips. corresponding to the maximum value of the load range in the first stage fatigue test; the deflections increase faster beyond this load exhibiting the nonlinear trend resulting from the formation of new cracks. New cracks initiated along with widening of pre-existing cracks when the load was maintained constant at 18.0 lips. Fig. 7.43 shows the load-deflection relationships corresponding to typical stems at south and north quarter and midspan sections. The permanent deflection at south and north quarter span sections was approximately 0.2 in., whereas the value under the, midspan section was in the range of 0.2 to 0.3 in.

After the completion of the static test, the bridge model was then subjected to second stage fatigue test with a load range of 6.0 to 18.0 lips. in each actuator. The deflections and strains were monitored at regular intervals during the second stage upto one million cycles. Figs. **7.44 to 7.47 show the load-deflection graphs obtained from the static tests conducted at typical intervals during the second stage fatigue test. The load-deflection relationships corresponding to static tests after completion of 0, 58000, 350000, 500000, and 1 million cycles are compared in Figs. 7.48 and 7.49 for stems 1 and 6 at midspan section. The stiffness degradation was significant at 58,000 cycles and the change in stiffness beyond was marginal upto one million cycles. This behavior is quite similar to that observed during the first stage fatigue testing. The permanent deformation of the bridge system remained the same as that observed at the end of the first static test carried out at zero cycles prior to the commencement of the second stage fatigue testing.**

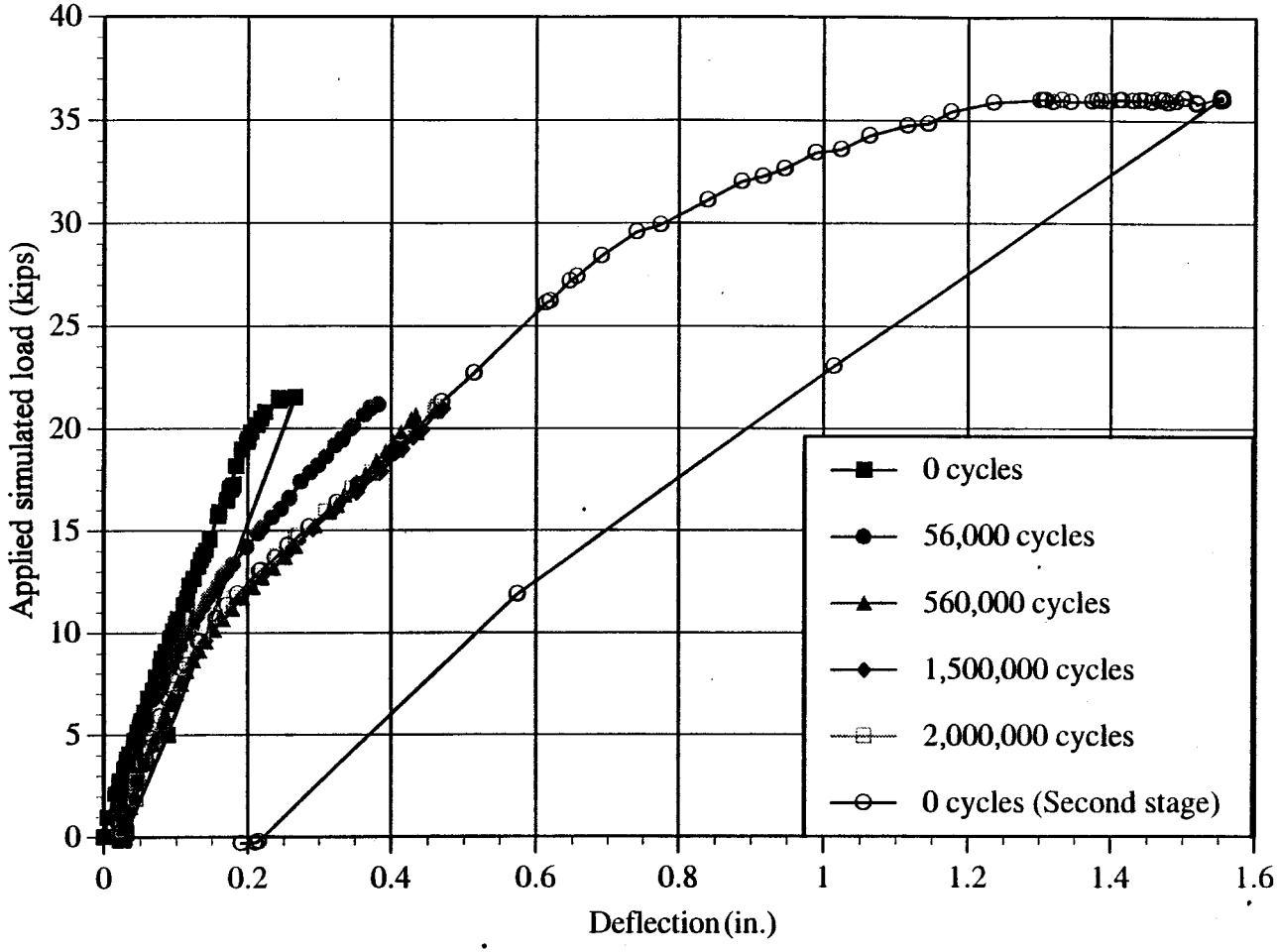

Fig. 7.42 Load-deflection relationships at midspan under stem 6 at the begining of second stage fatigue loading

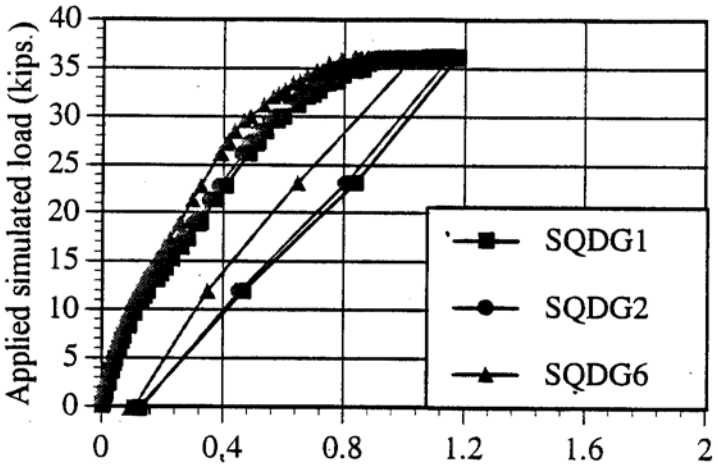

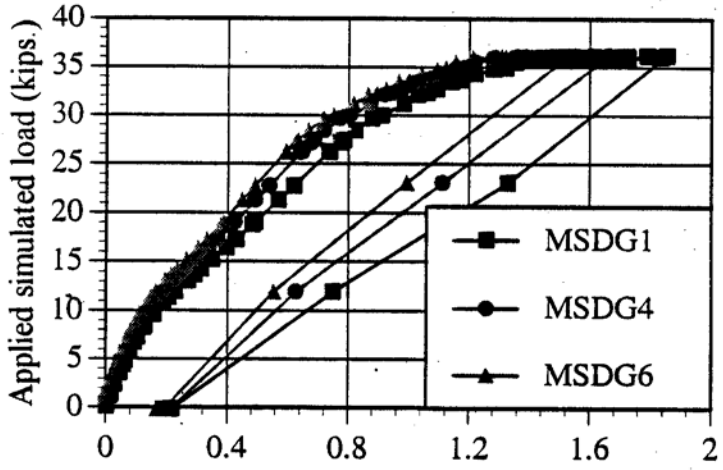

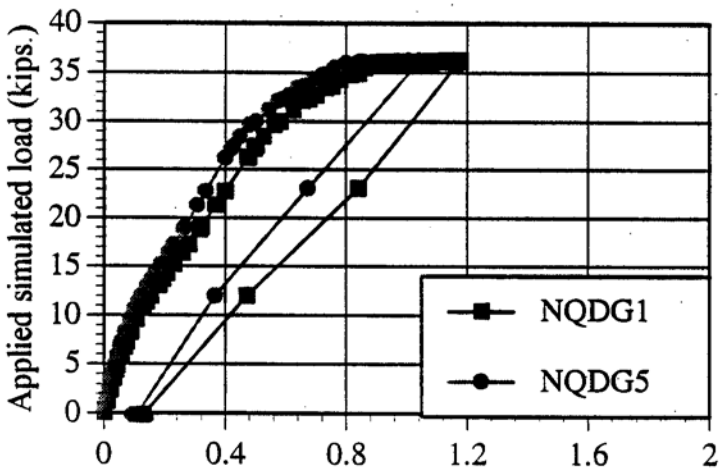

Fig. 7.43 Pmax = 36kips; Pmin = 12 kips
Load deflection of AFRP Double Tee bridge system : 0 Cycles

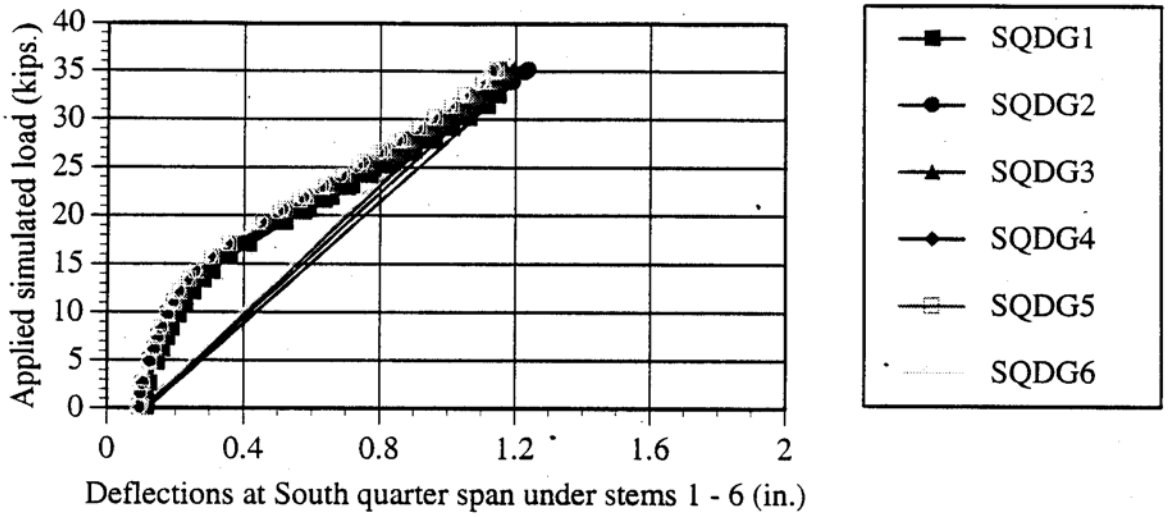

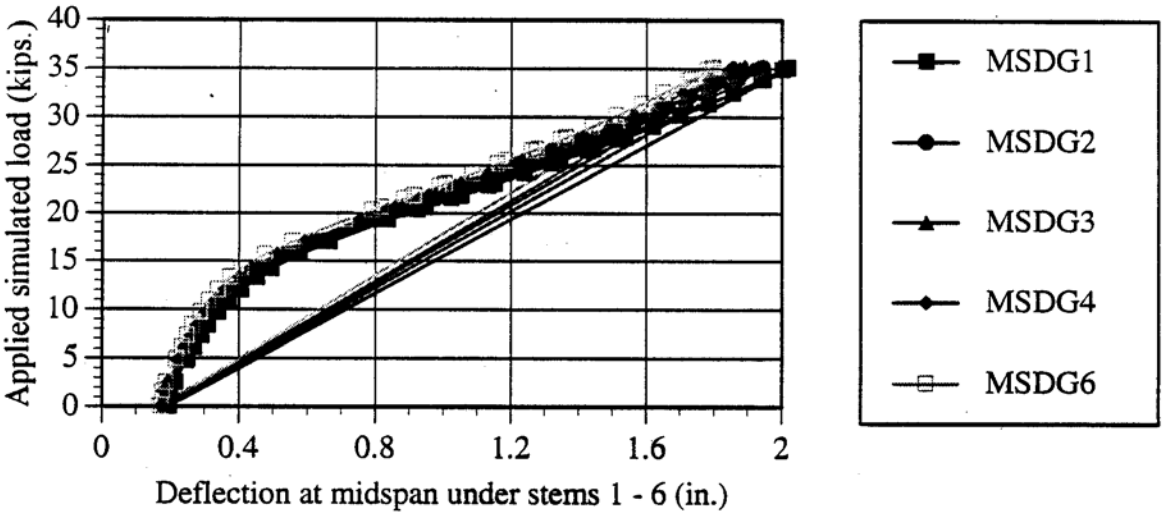

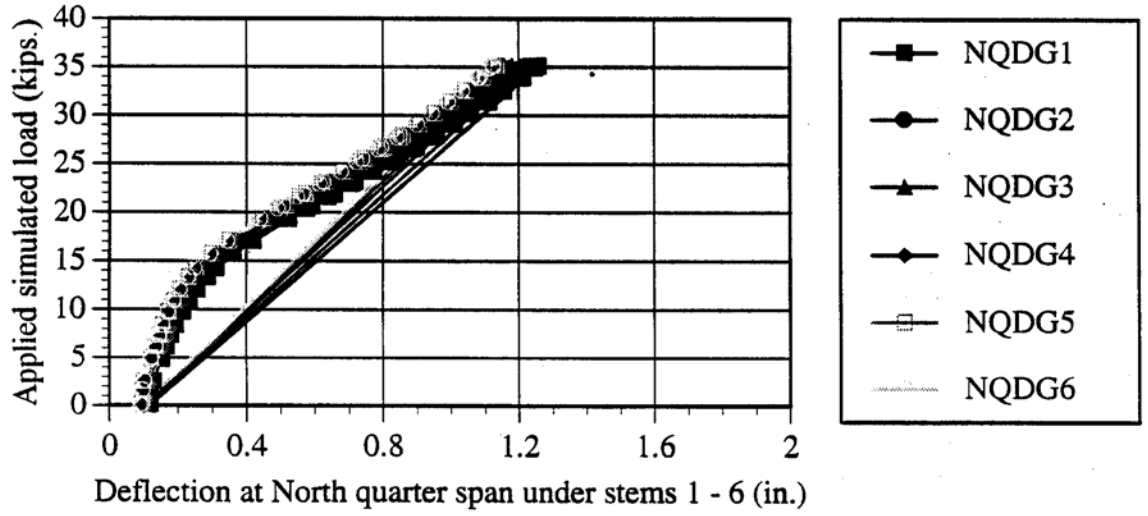

Fig. 7.44 P_{max} = 36 kips; P_{min} = 12 kips
Load deflection of AFRP Double Tee bridge system : 58,000 Cycles

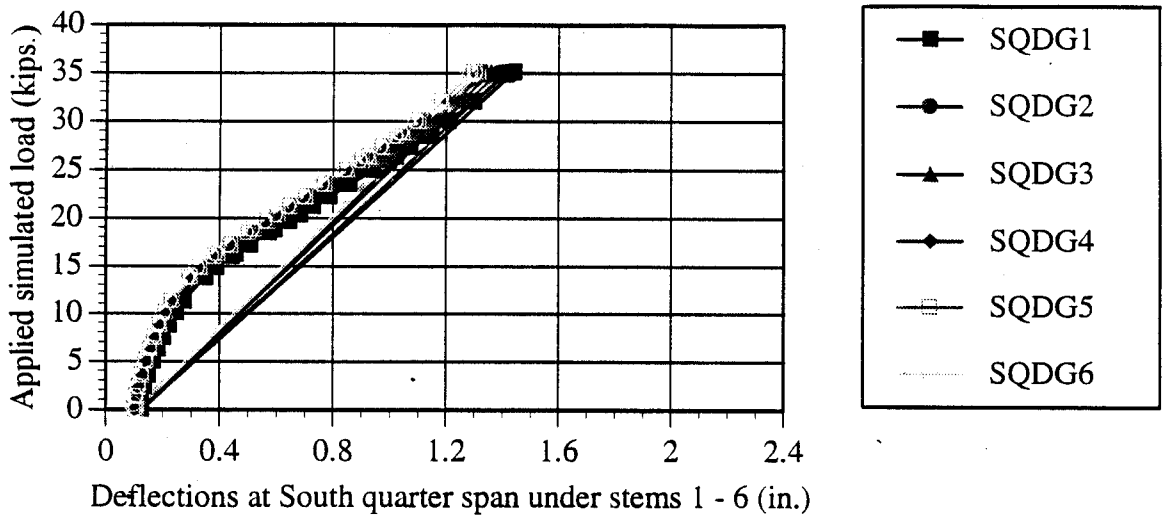

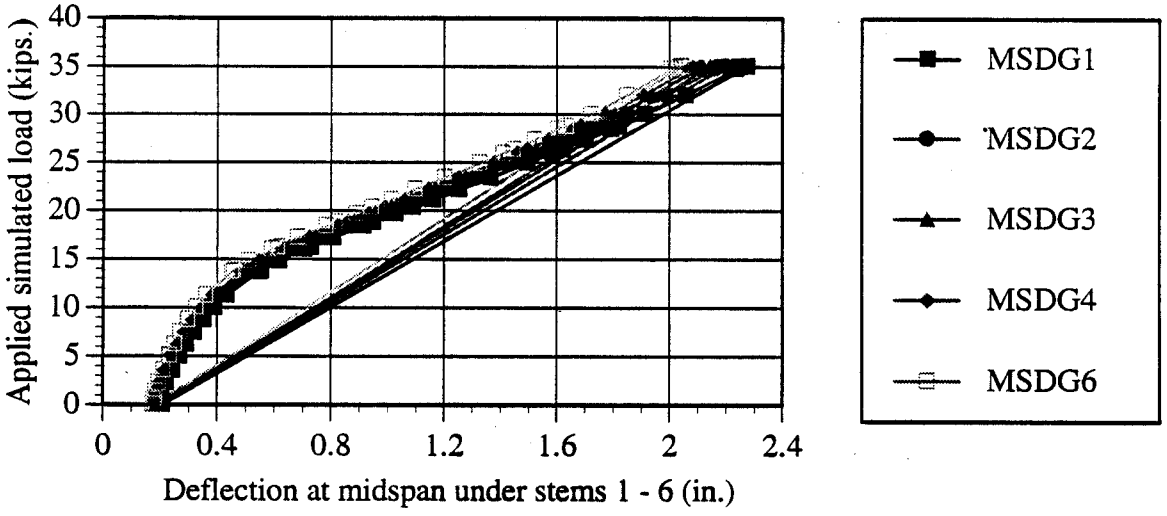

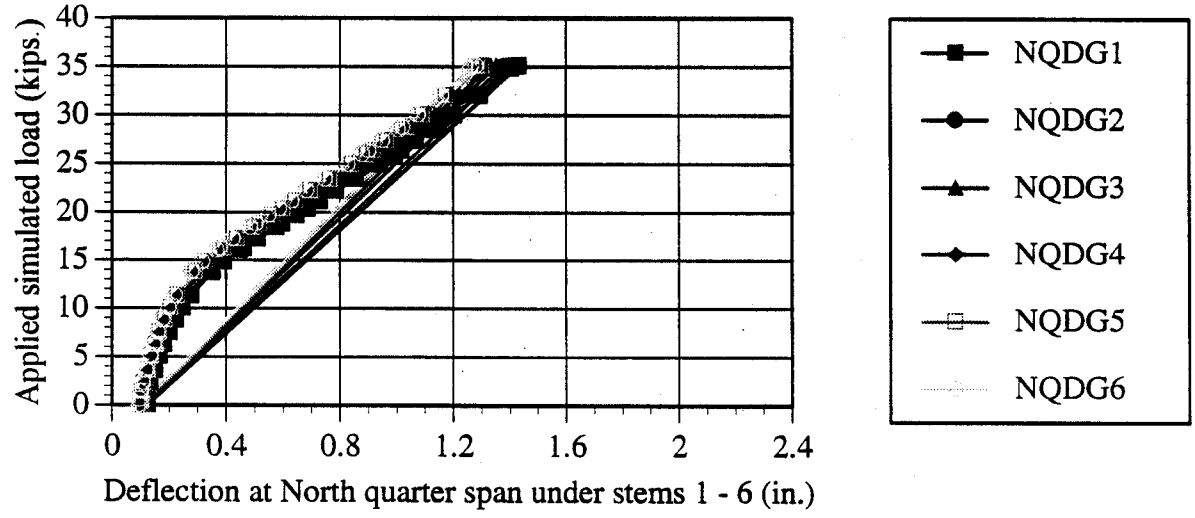

Fig. 7.45 P_{max} = 36 kips; P_{min} = 12 kips
Load deflection of AFRP Double Tee bridge system : 350,000 Cycles

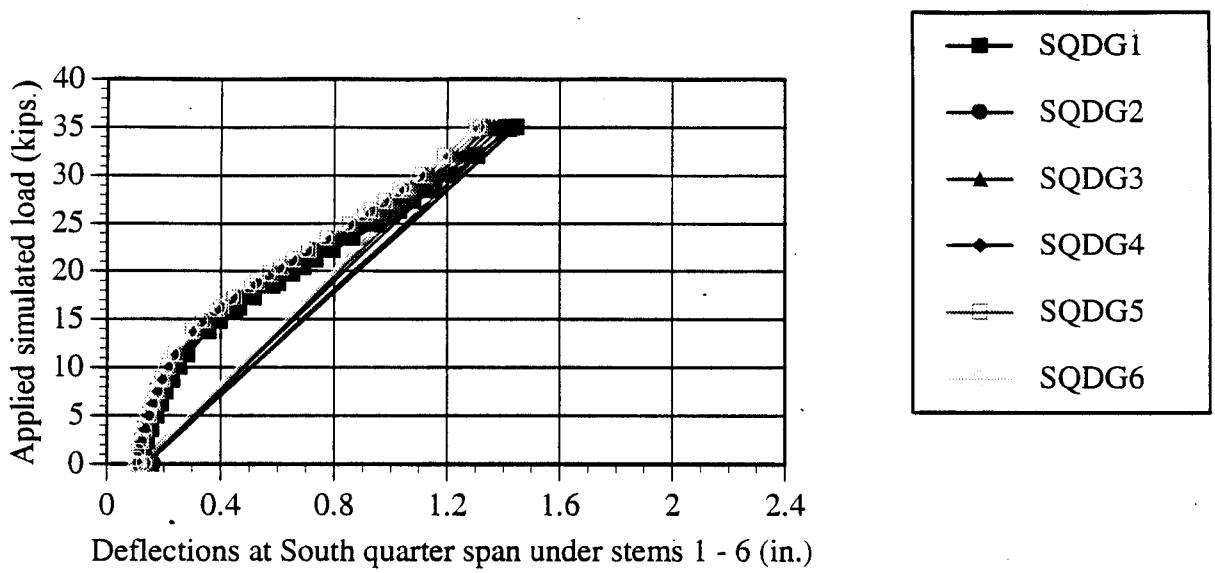

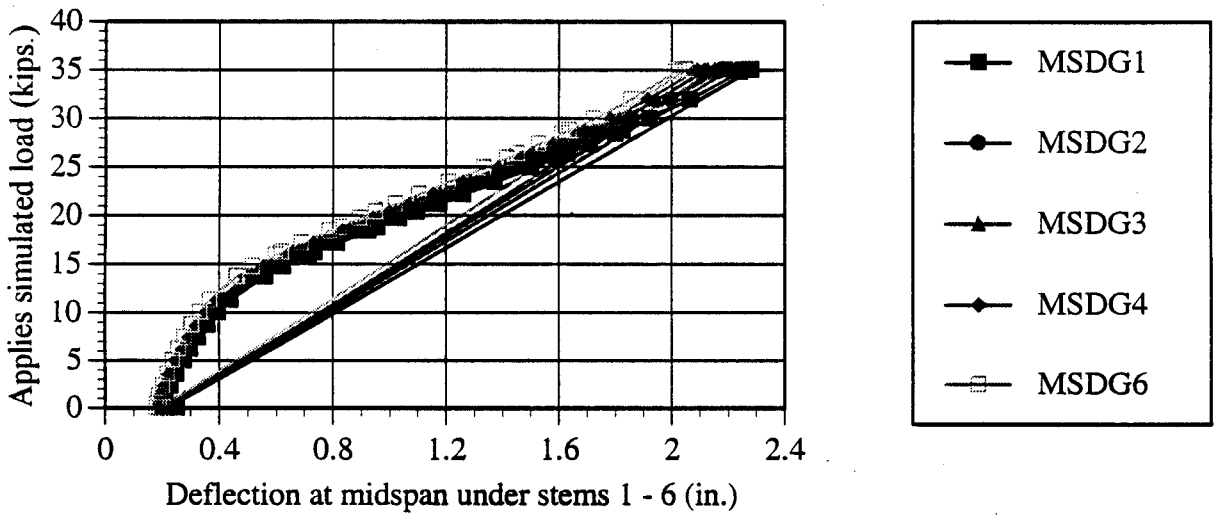

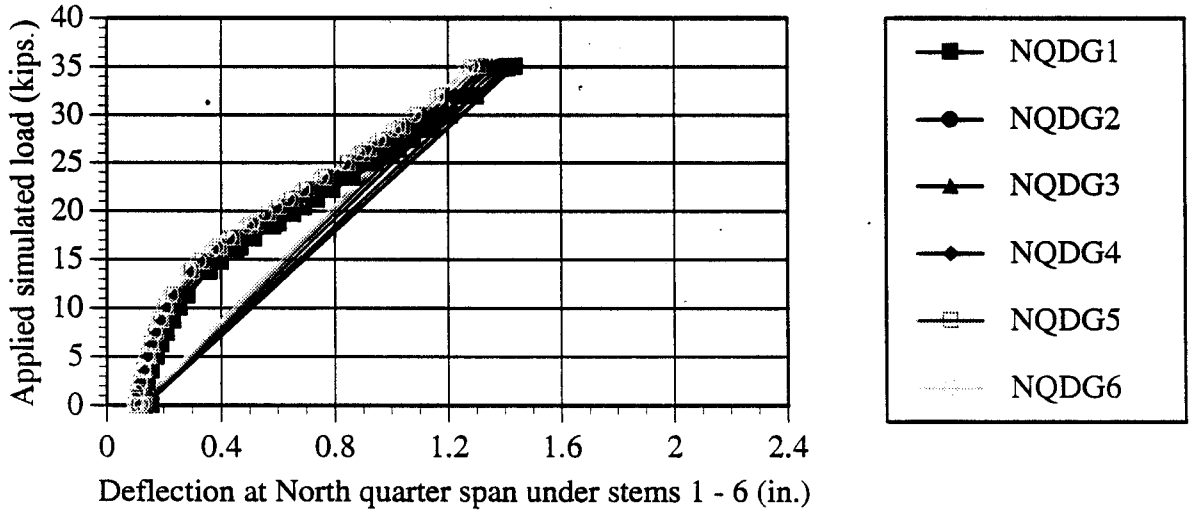

Fig. 7.46 P_{max} = 36 kips; P_{min} = 12 kips

Load deflection of AFRP Double Tee bridge system : 500,000 Cycles

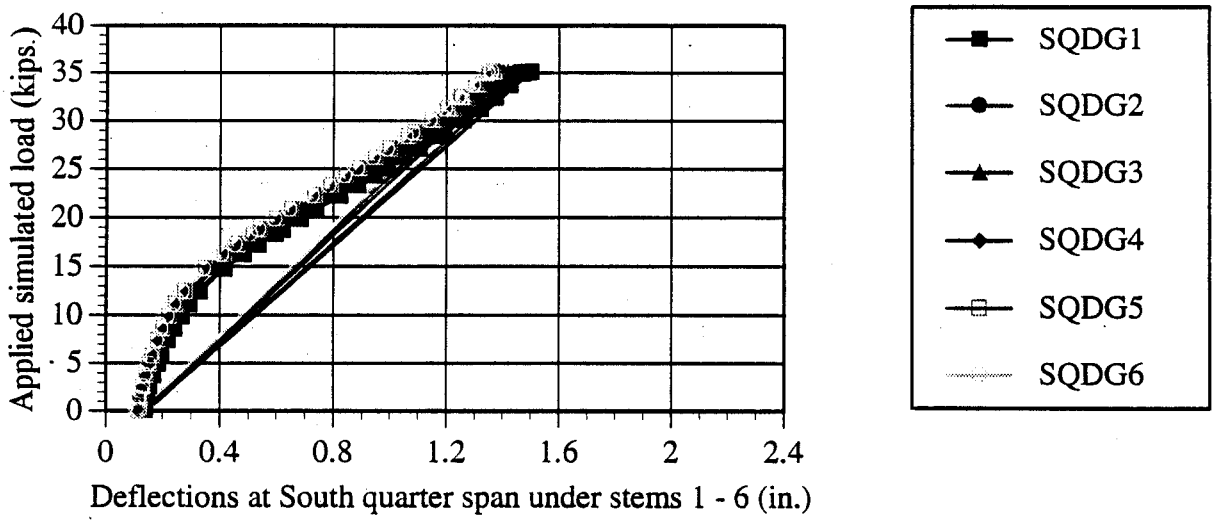

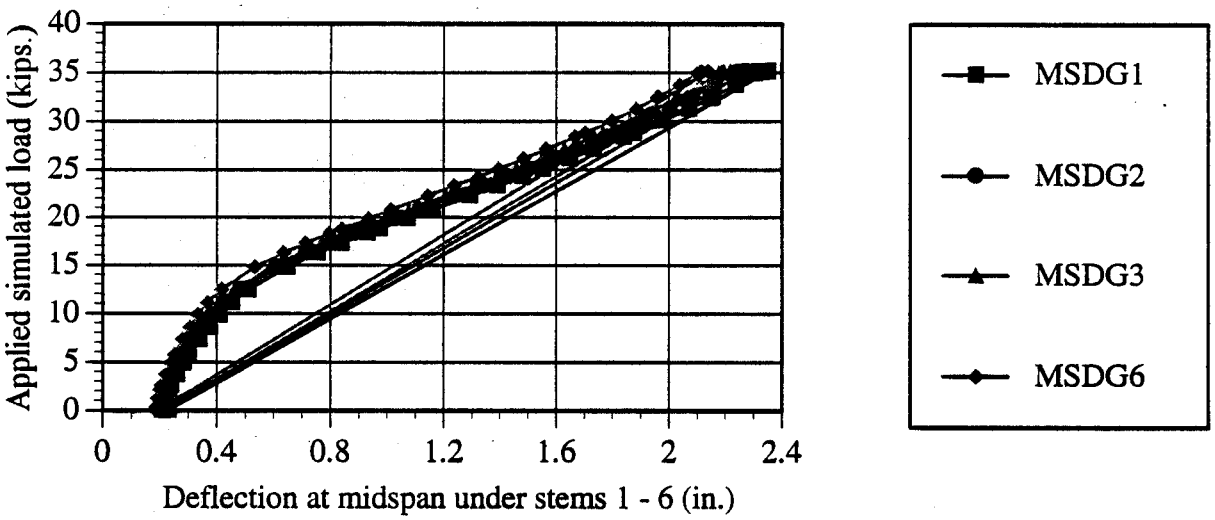

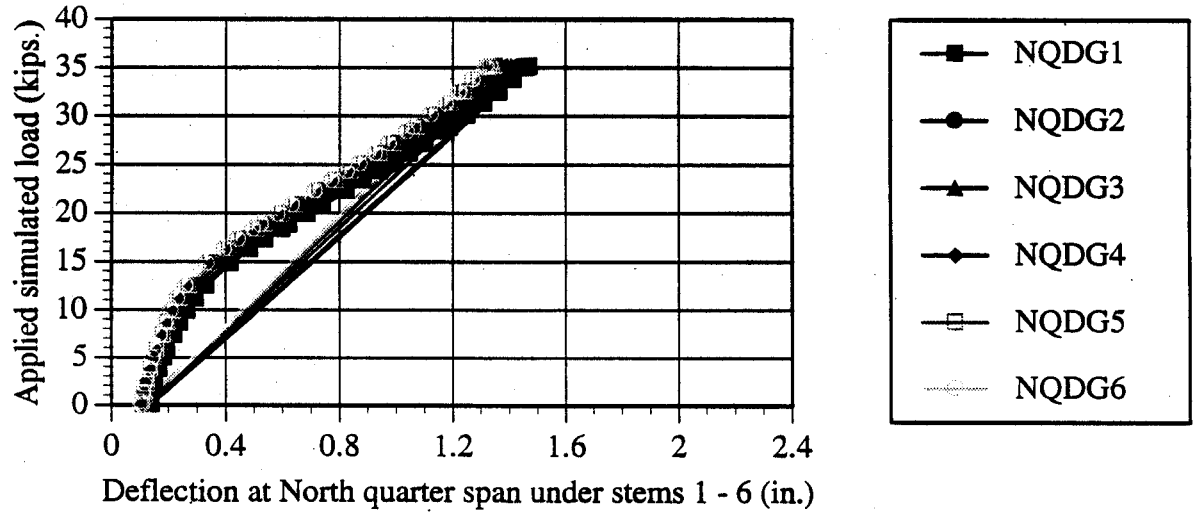

Fig. 7.47 P_{max} = 36 kips; P_{min} = 12 kips
Load deflection of AFRP Double Tee bridge system : 1,000,000 Cycles

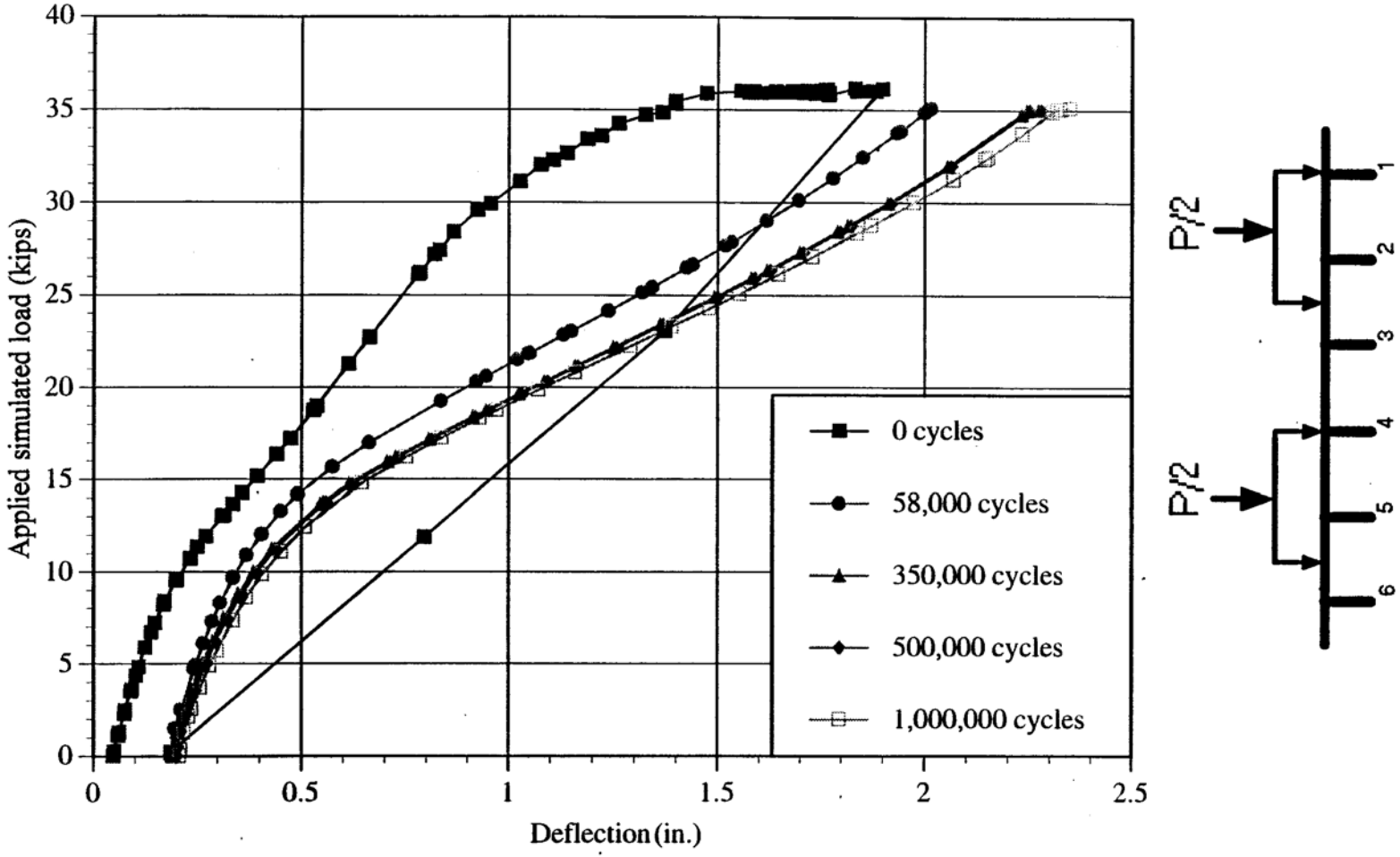

Fig. 7.48 P_{max} = 36 kips; P_{min} = 12 kips
Load deflection at midspan of stem 1 during various stages of fatigue testing

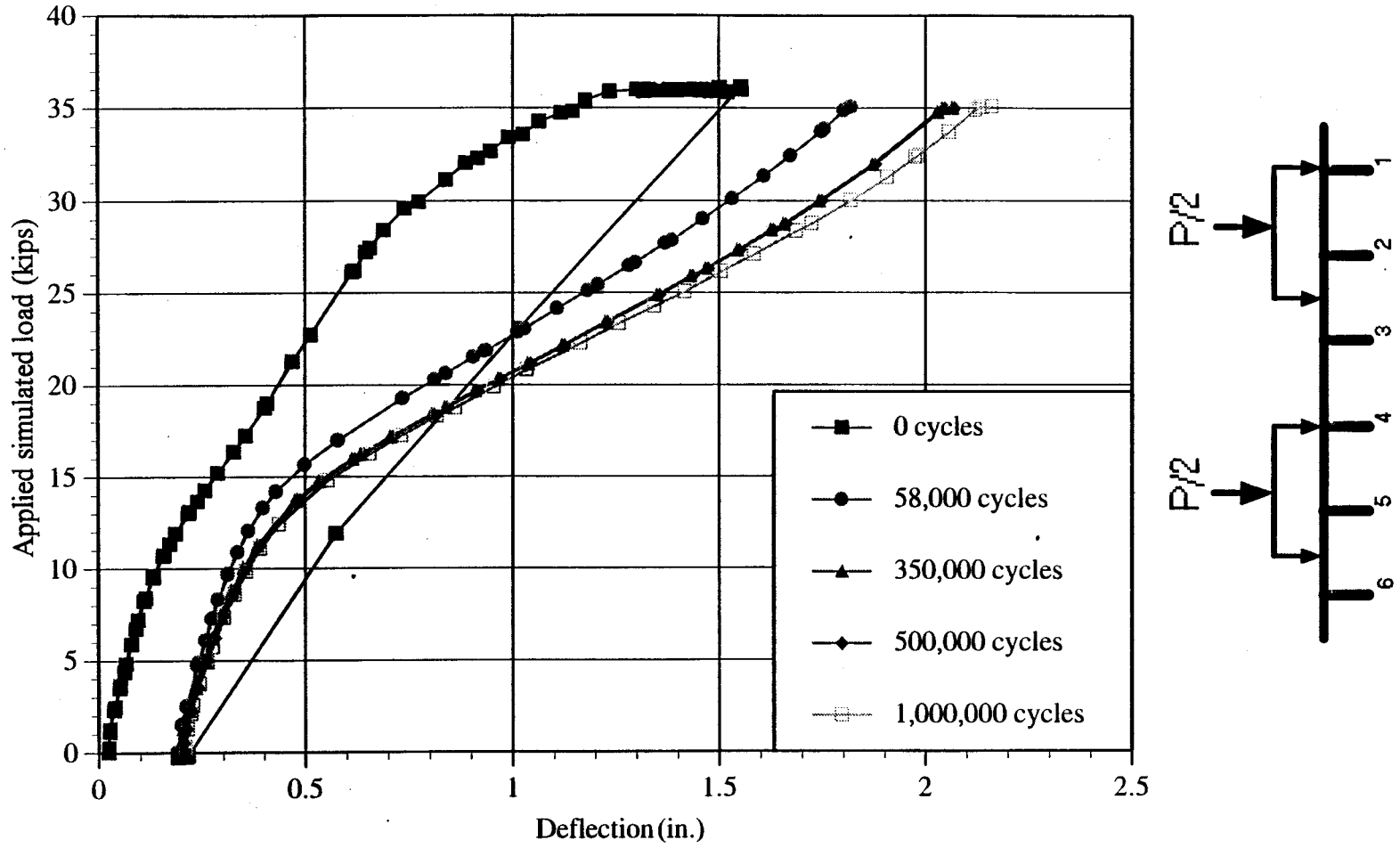

Fig. 7.49 P_{max} = 36 kips; P_{min} = 12 kips
Load deflection at midspan of stem 6 during various stages of fatigue testing

Fig. 7.50 The deflection shape of the bridge deck after 58,000 cycle loading

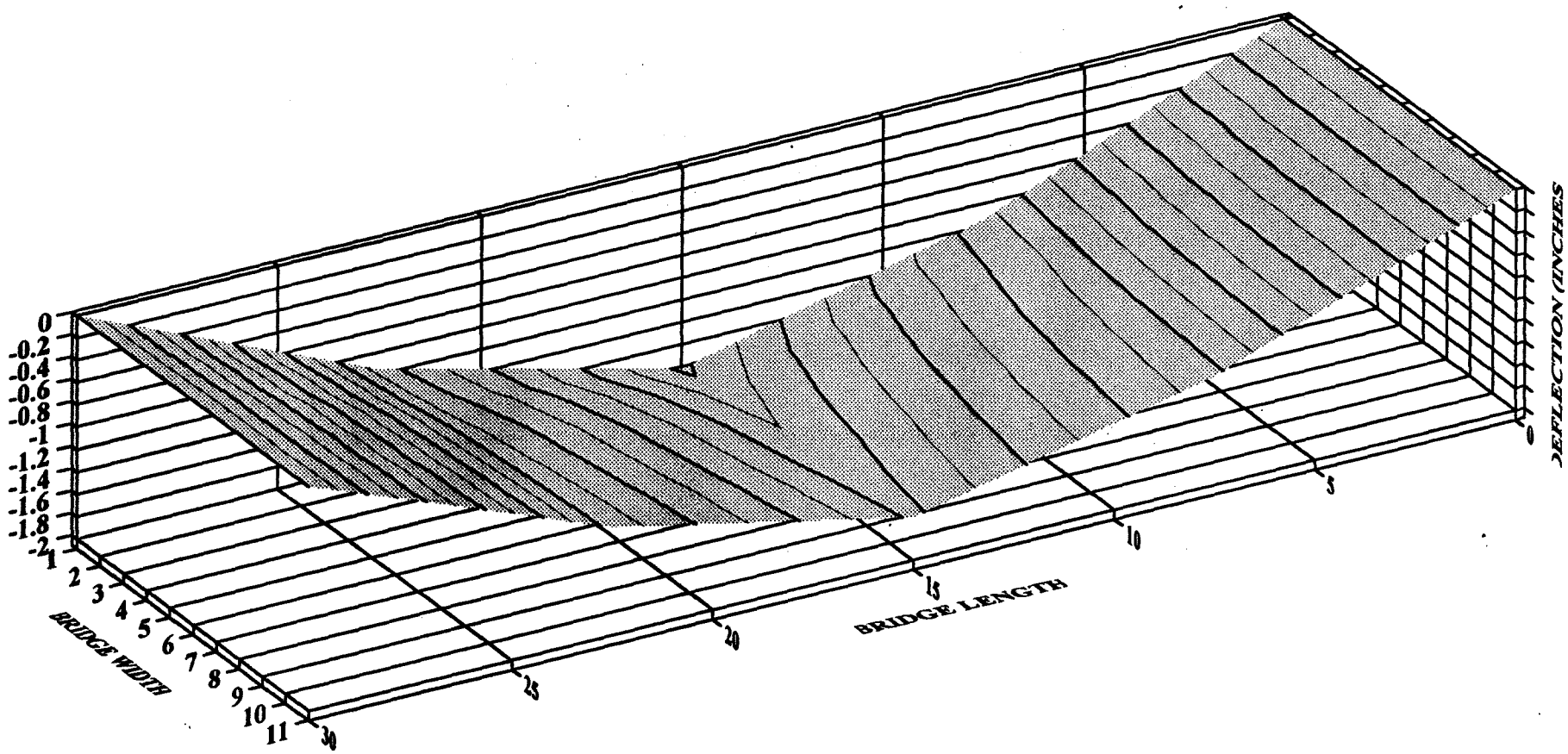

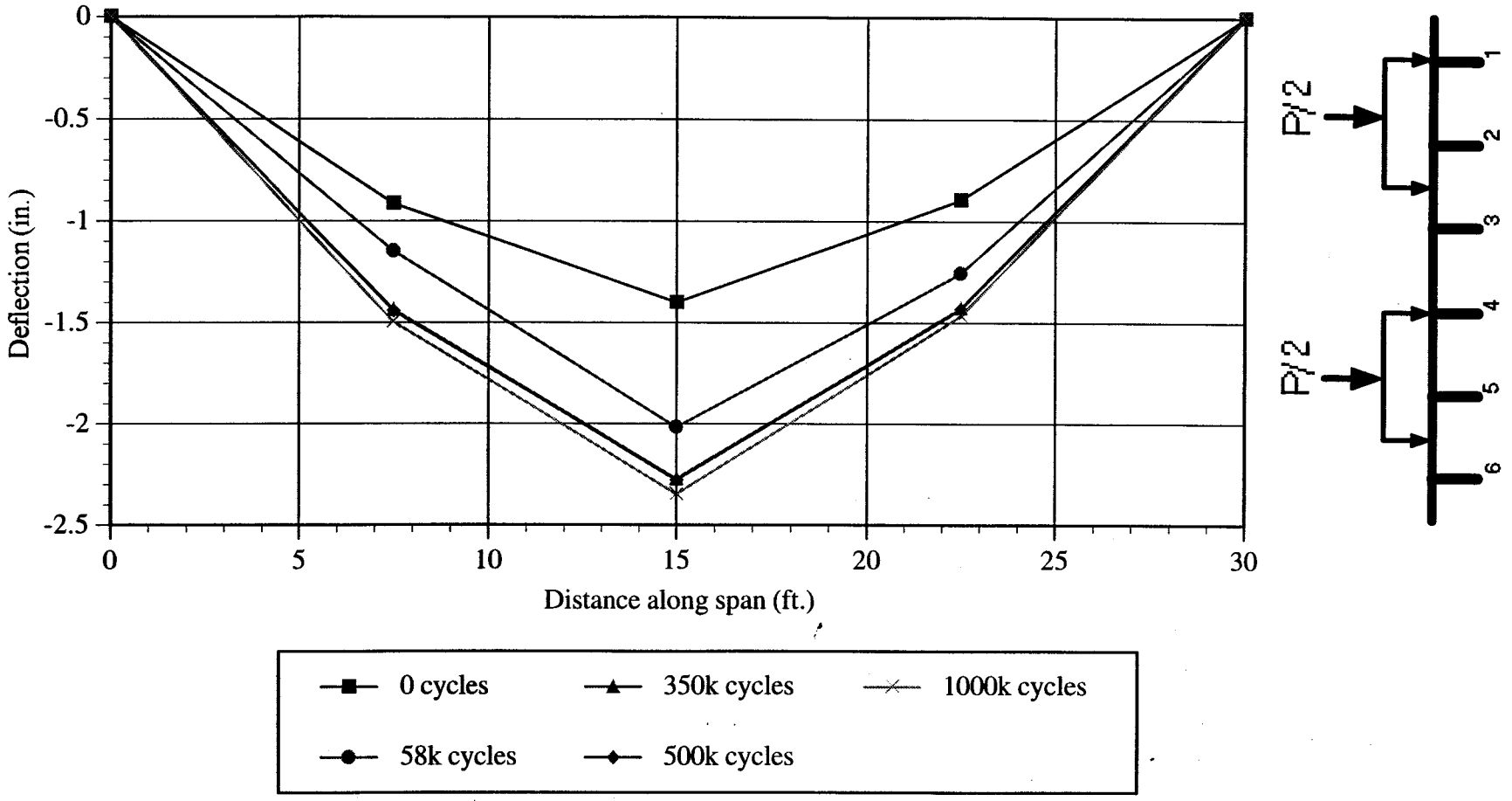

Fig. 7.51 Longitudinal deflection profile of stem 1 after being subjected to fatigue loading (Applied simulated load = 36 kips, fatigue load range : 12 to 36 kips)

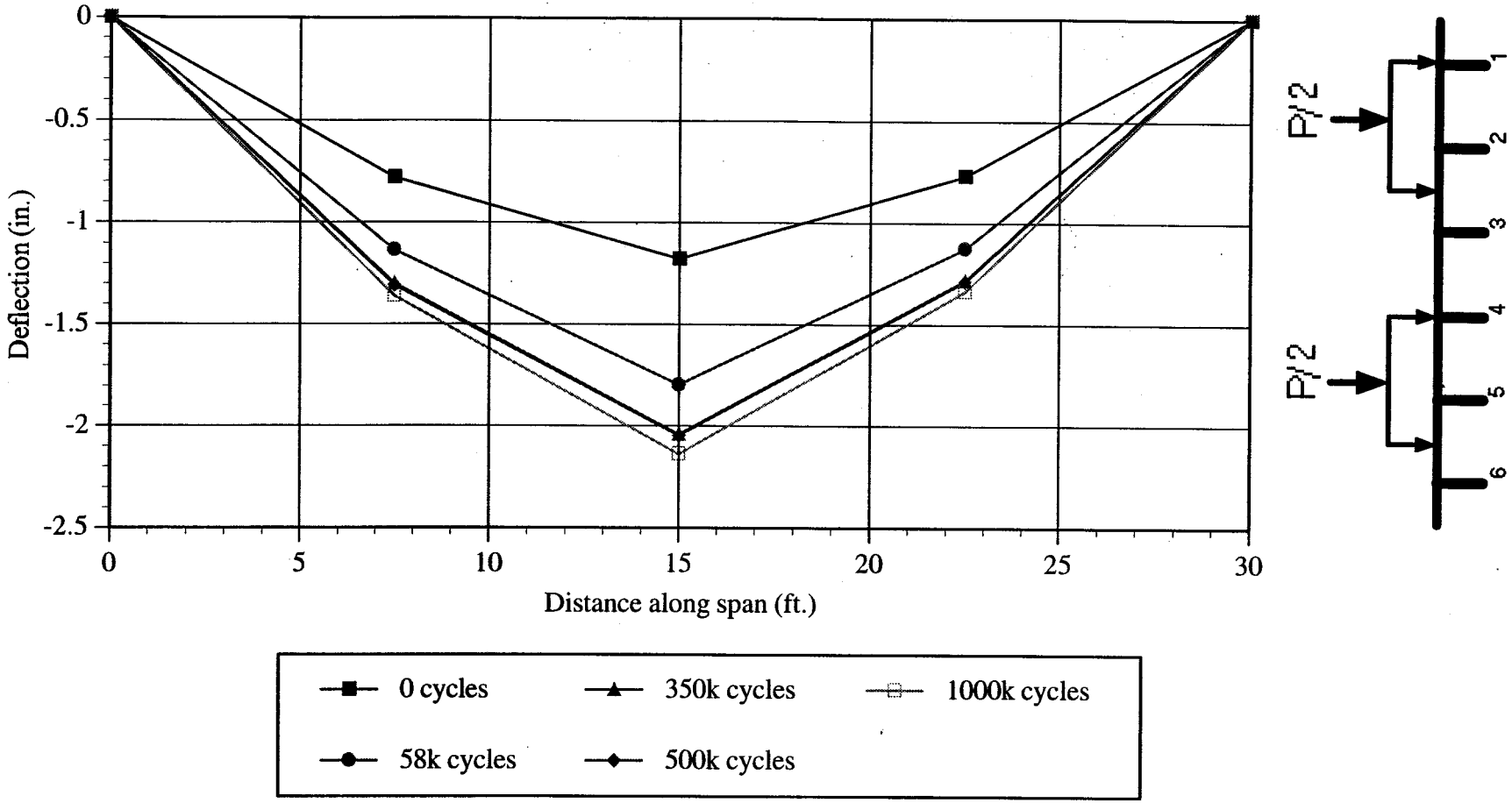

Fig. 7.52 Longitudinal deflection profile of stem 6 after being subjected to fatigue loading (Applied simulated load = 36 kips, fatigue load range : 12 to 36 kips)

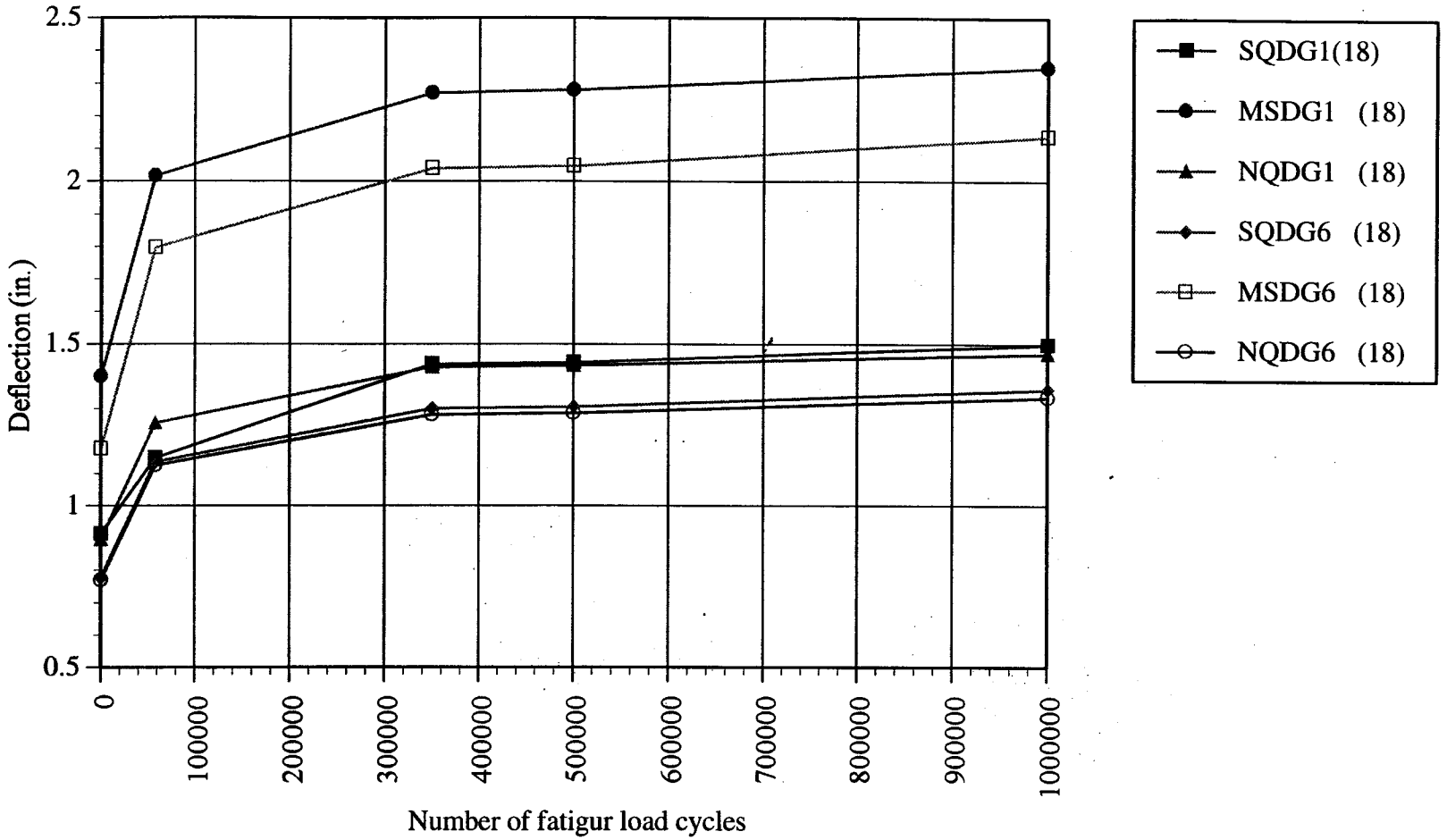

Fig. 7.53 Deflection increase at mid, South and North quarter spans of stems 1 and 6 with number of cycles (Applied simulated load = 36 kips : fatigue load range = 12 to 36 kips)

An isometric view of the deflected shape of the bridge model after 58,000 cycles is shown in Fig. 7.50. The longitudinal deflection profiles of stems 1 and 6 are shown in Figs. 7.51 and 7.52 corresponding to the static tests conducted at typical intervals. The maximum deflections under stems 1 and 6 after one million cycles of fatigue loading were 2.32 and 2.15 in. respectively. Fig. 7.53 shows the increase in deflections at south and north quarter and midspan sections with the number of cycles. Variation of crack width with applied load at a typical location in stem 1 is shown in Fig. 7.54 for selected cycles of loading. It can be seen from Fig. 7.54 that the maximum crack width at a total applied load of 36 kips. was about 0.024 in. Similar to the observation with regard to deflection variations, significant increase in crack width was observed after 58,000 cycles of fatigue loading and very marginal in the subsequent load cycles upto the completion of lmillion cycles of cyclic loading in the second stage fatigue test. The crack distribution in the bridge system at the completion of both first and second stage fatigue tests is shown in Fig. 7.55.

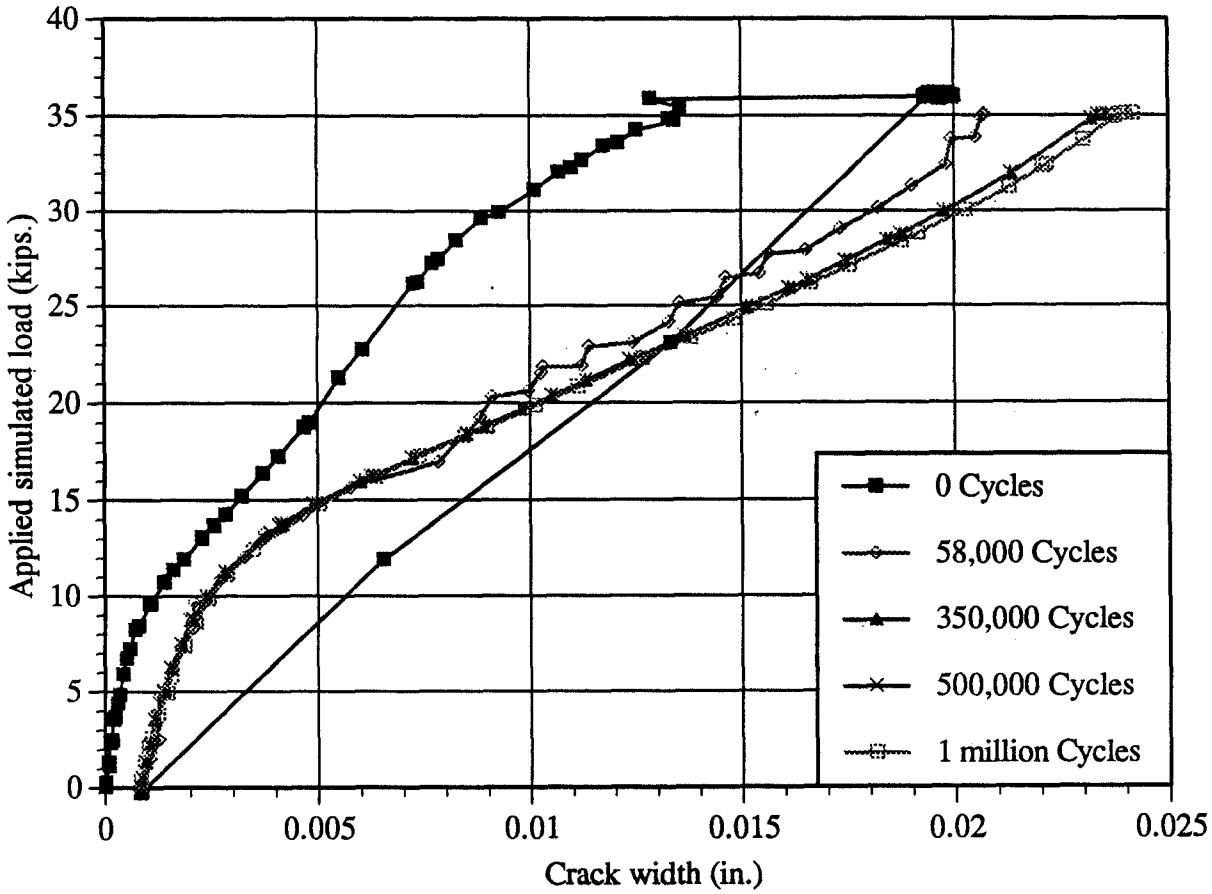

Fig.7.54 Crack width measured in stem 1 at midspan section

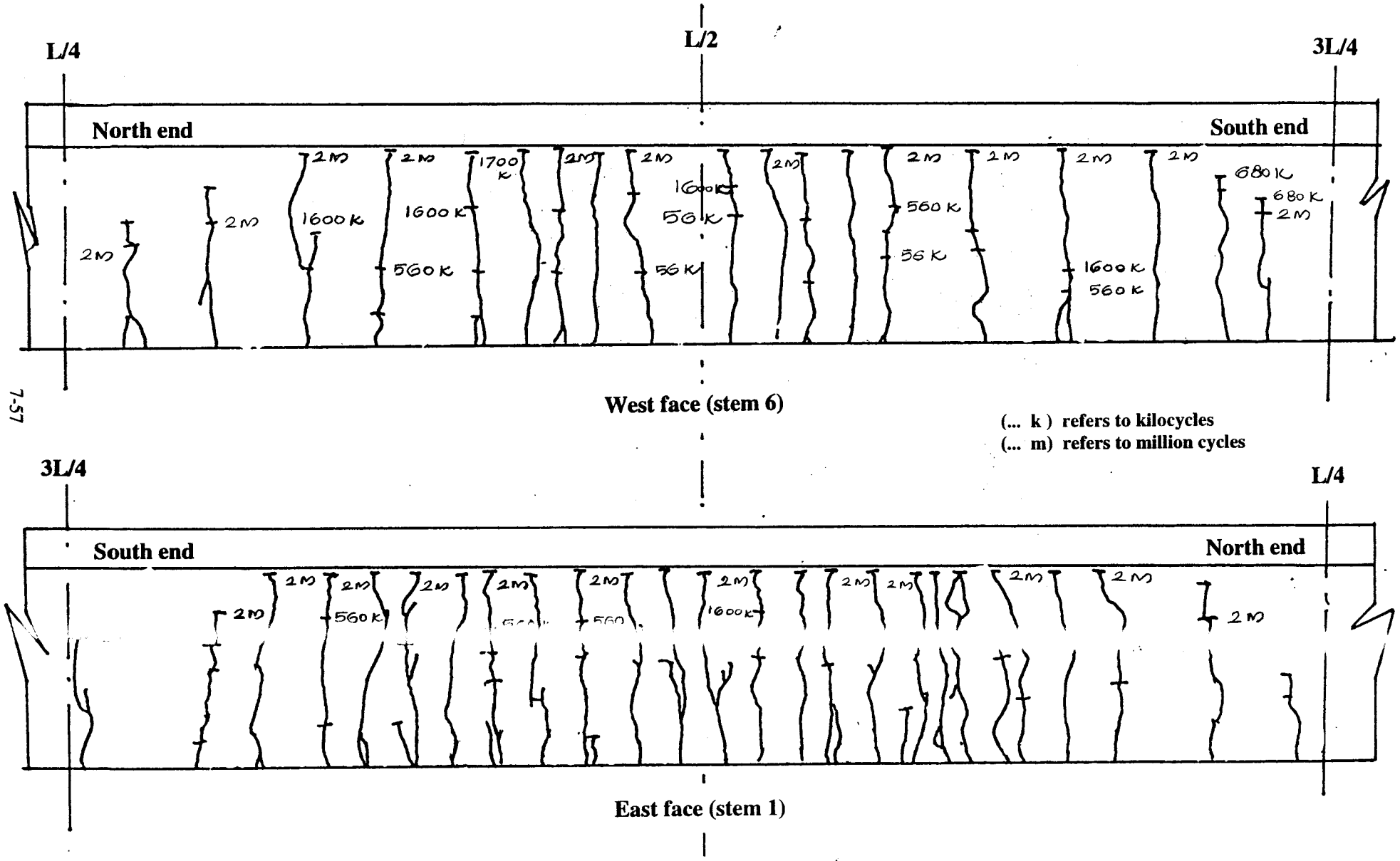

Fig. 7.55 Crack distribution after second stage fatigue test

7.4 ULTIMATE LOAD TEST

After the completion of two stages of fatigue testing, the model bridge system was subjected to static loading upto the ultimate capacity. The load application was similar to that of the fatigue tests simulating the presence of two HS20-44 trucks on the two lanes. The deflections, concrete strains, distribution of cracks and crack widths were monitored in the bridge system. This section presents the experimental setup, instrumentation and results and discussions of the ultimate load test.

7.4.1 Experimental Setup and Instrumentation

The position of the live loads (two HS20-44 trucks) on the model for the ultimate load test was similar to that of the two fatigue tests. The single Double-Tee beam exhibited a large deflection which exceeded the available range of travel of the two Enerpac hydraulic jacks used in the test.This necessitated replacement of the two MTS actuators with a single hydraulic jack with a large travel to apply the load to a wideflange beam which in turn distributes to the two loading frames. Fig. 7.56 shows the stiffening of the wide flange beam corresponding to the jack position to avoid any local buckling. The stiffened wideflange beam was then placed symmetrically on the two loading frames on the bridge system to simulate the HS20-44 AASHTO trucks. Figs. 7.57 and 7.58 show the wide flange beam resting over the load distribution frames arranged on the model bridge system. The load cell attached to the hydraulic jack is shown in Fig. 7.59. Fig. 7.60 shows the complete overview of the Double-Tee bridge system ready for the ultimate load test.

Instrumentation was setup for measuring concrete strains, deflections and crack widths. The instrumentation details of the bridge system are similar to those used in the fatigue tests and shown in Fig. 7.60. One exception was that the LVDTs and strain transducers at midspan

Fig. 7.56 The stiffening of the wide flange beam for distributing load

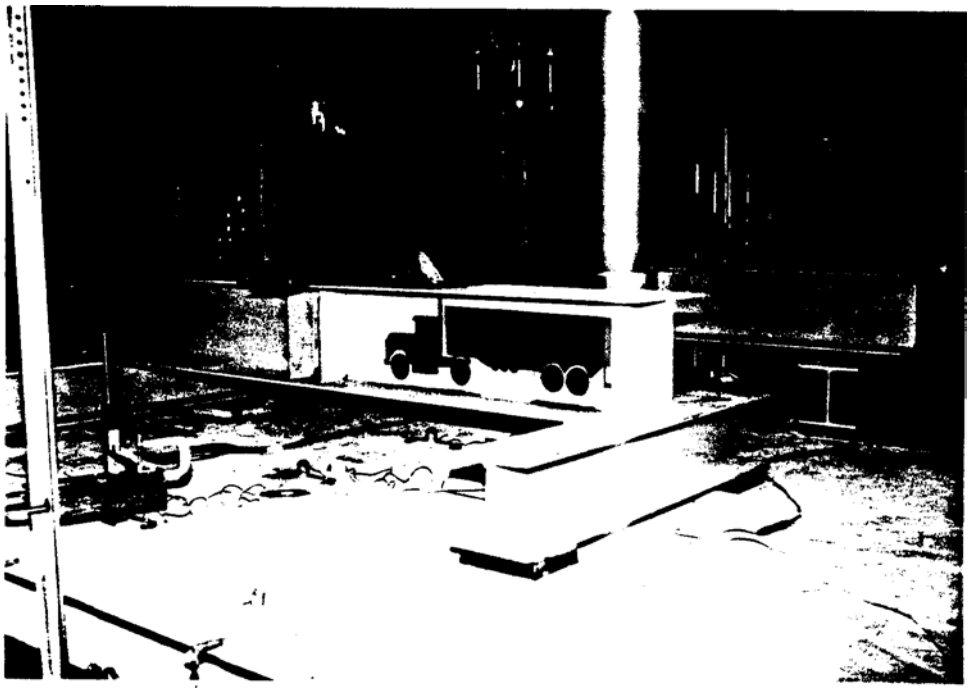

Fig. 7.57 The wide flange beam resting over the load distribution frames

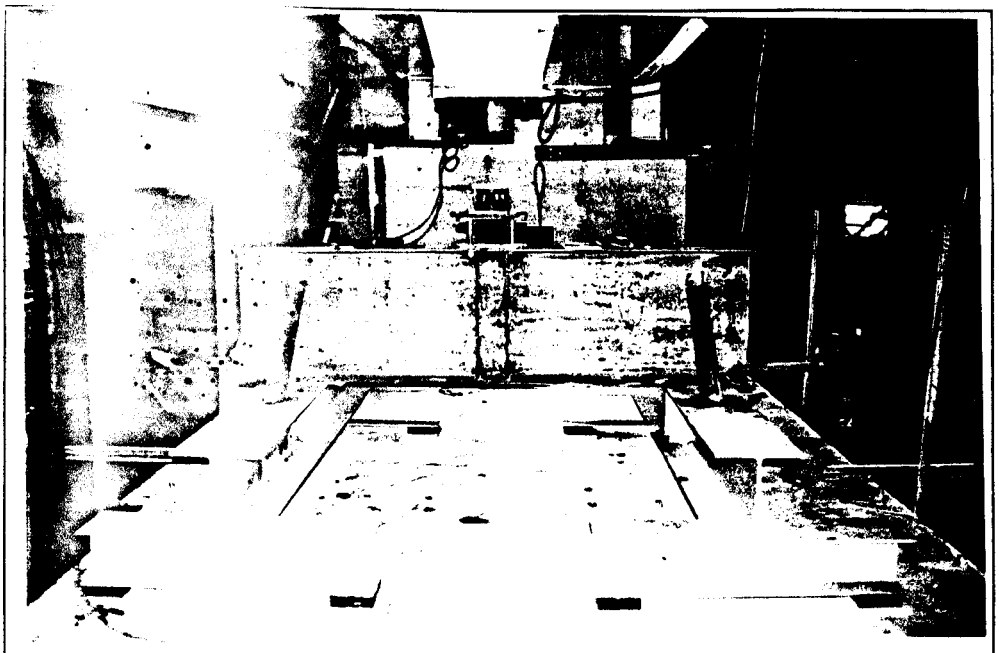

Fig. 7.58 Load distribution frame

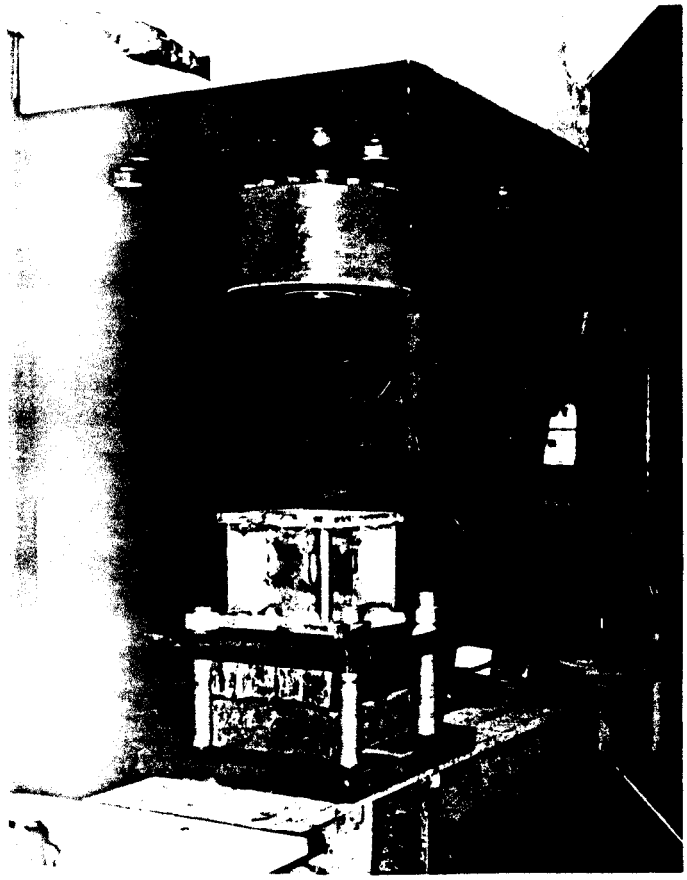

Fig. 7.59 The load cell attached to the hydraulic jack

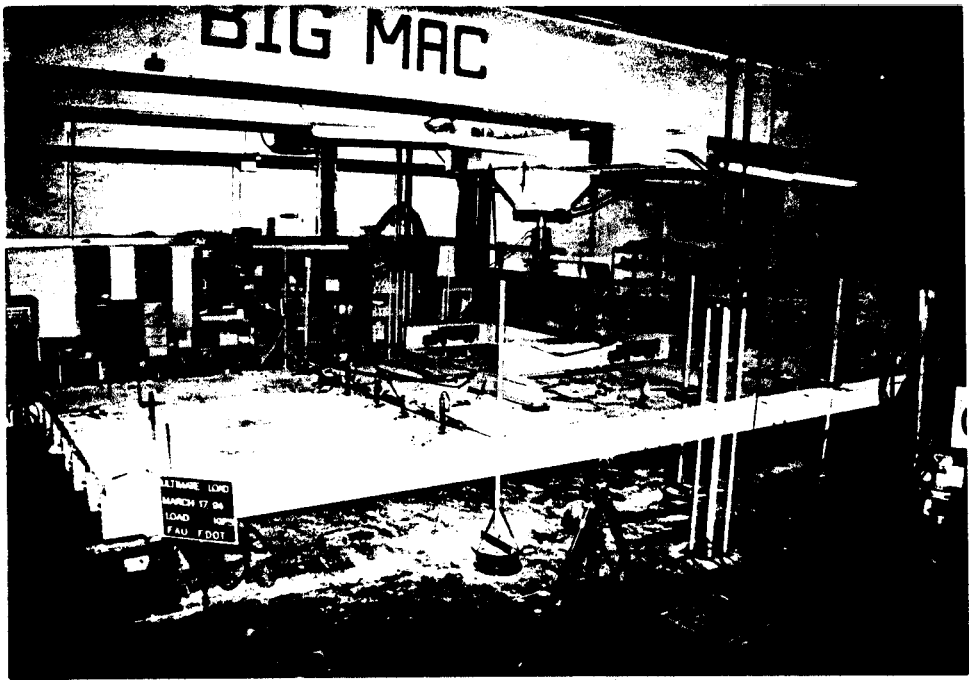

Fig. 7.60 Overview of the Double-Tee bridge system ready for the ultimate load test

sections on the bridge deck corresponding to stems 2 to 5 were removed to avoid interference with the load frames. The instrumentation for measuring the tendon slip was not considered essential for the ultimate load test, since no slip was observed during the ultimate load test of the single Double-Tee beam.

7.4.2 Results and Discussions

Fig. 7.61 shows the ultimate load test of the Double-Tee bridge system in progress. The loads were applied at regular increments and cracks monitored together with deflections. As the applied load was increased new flexural cracks accompanied with loud noise were observed during the test. Fig. 7.62 shows identification of new cracks. The deflected shape of the bridge system close to the ultimate stage is shown in Fig. 7.63. The observed deflections were excessive and hence steel plates were used between the LVDTs and the bridge deck surface to make up for the limited available travel and measure the deflections.

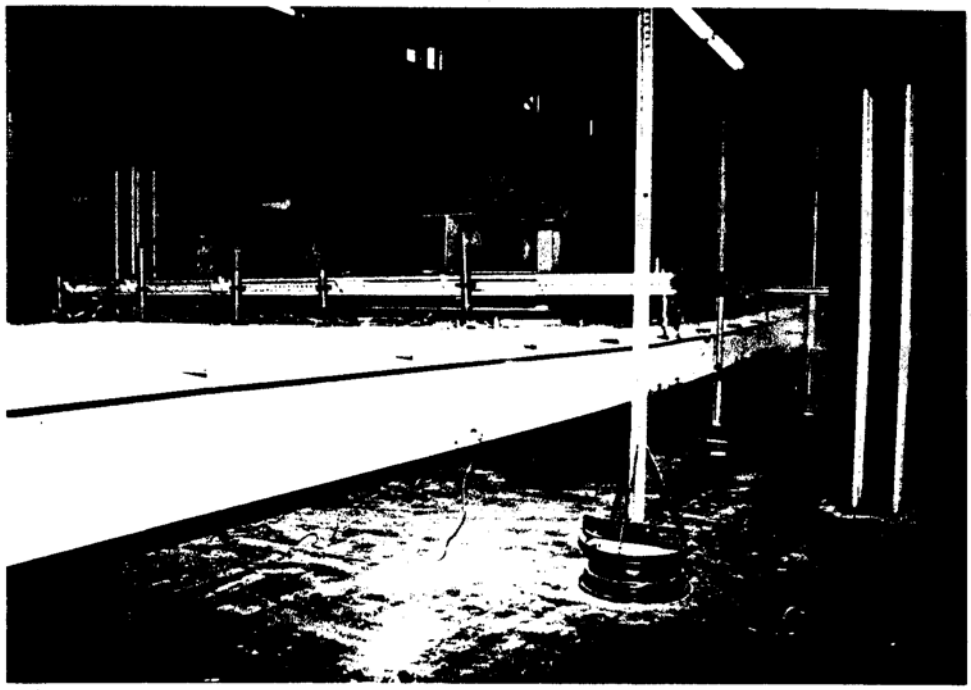

Fig. 7.61 The ultimate load test of the Double-Tee bridge system in progress

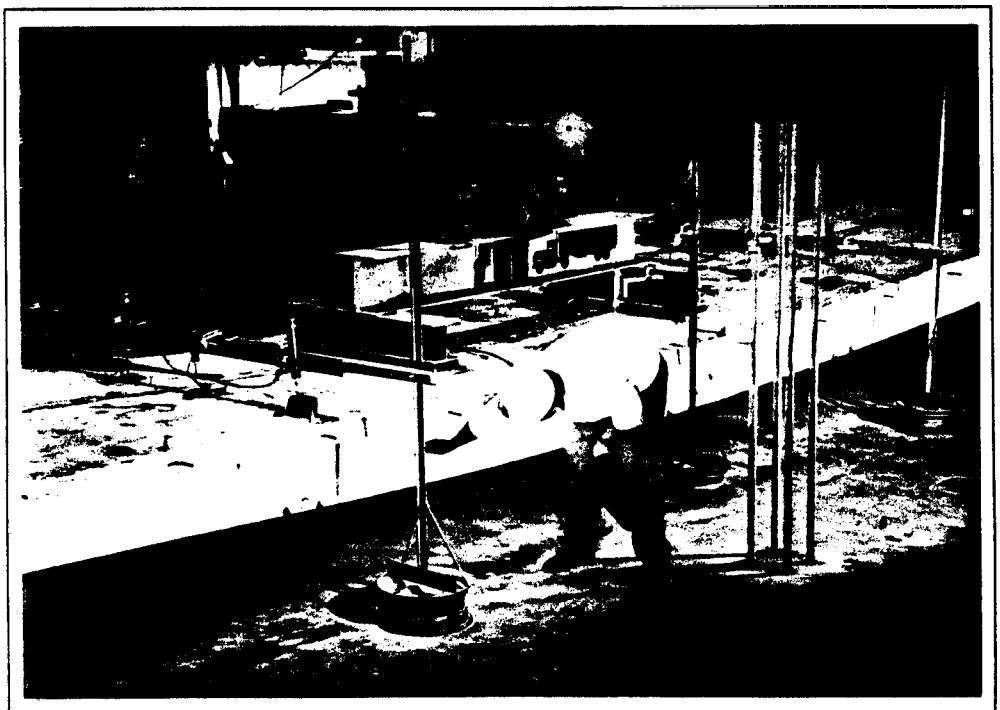

Fig. 7.62 Identification of new cracks

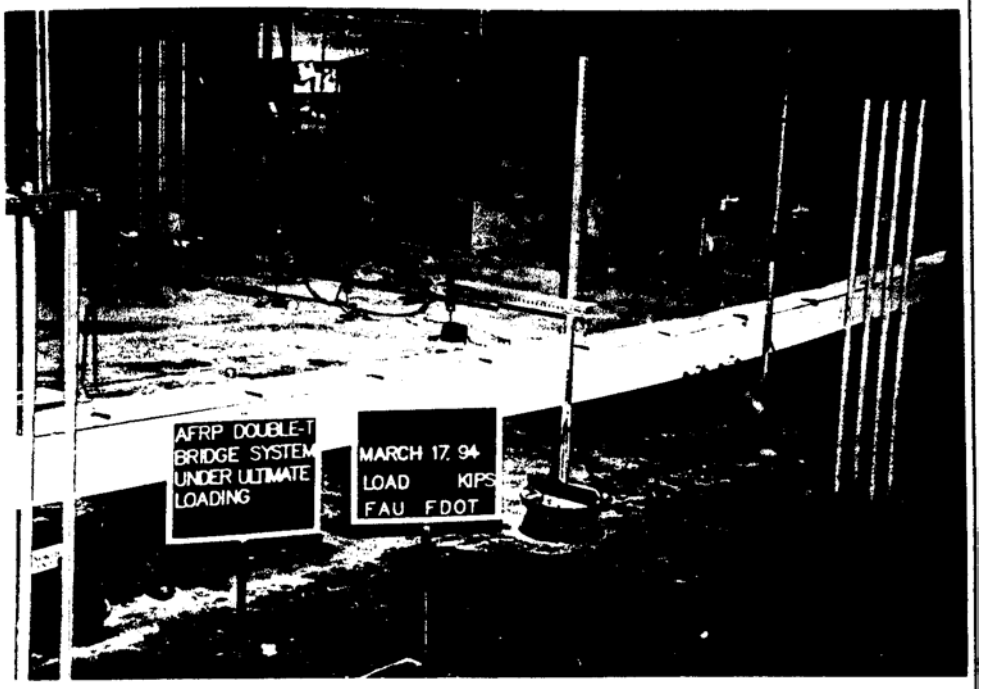

Fig. 7.63 The deflected shape of the bridge system close to the ultimate stage

When the applied load in the bridge system was about 81.0 kips, a loud noise was heard accompanied with a sudden decrease in the hydraulic jack pressure and resulting drop in the applied load by about 25.0 kips. At this stage, stem 1 exhibited a continuous horizontal crack at the level of the bottom most tendon in the midspan region, extending from north quarter to south quarter span sections, indicating loss of bond between the tendon and concrete. The large deflections of the bridge system could be seen from Figs. 7.64 a and 7.64 b. Figs. 7.65 and 7.66 show the end rotations of the Double-Tee bridge system. At this moment, it was decided to unload the bridge system and monitor the deflections, strains and crack widths. After the bridge is completely unloaded, permanent deformations were recorded and the concrete in the midspan region below the horizontal crack in stem 1 was removed to examine the bottom most tendon. Horizontal splitting of the tendon was noticed together with loss of bond with concrete (Fig. 7.67).

Fig. 7.64 a

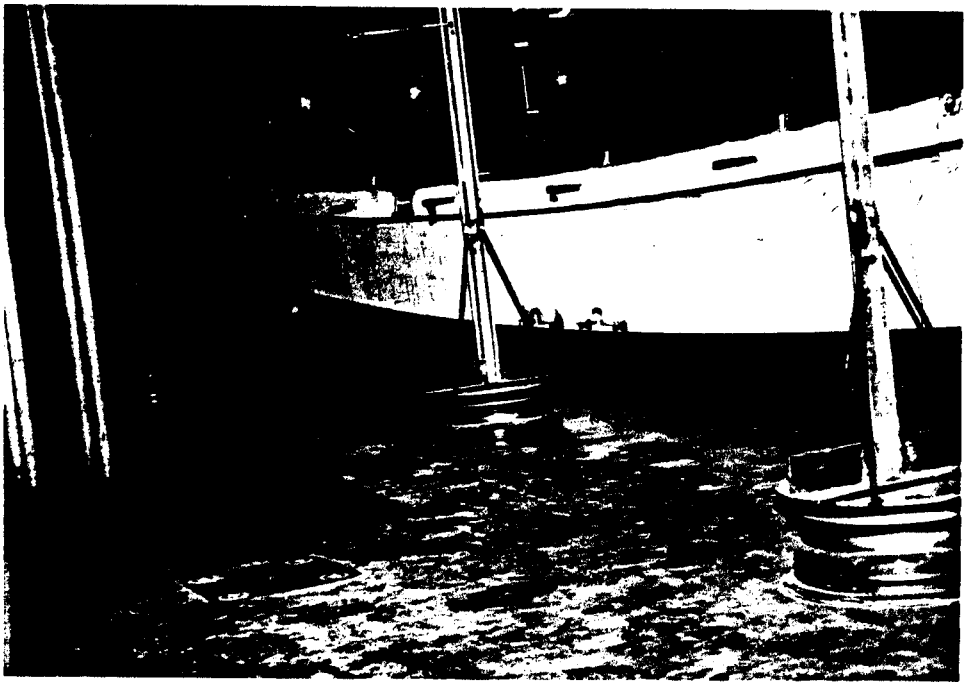

Fig. 7.64 b

The large deflections of the bridge system at the maximum load

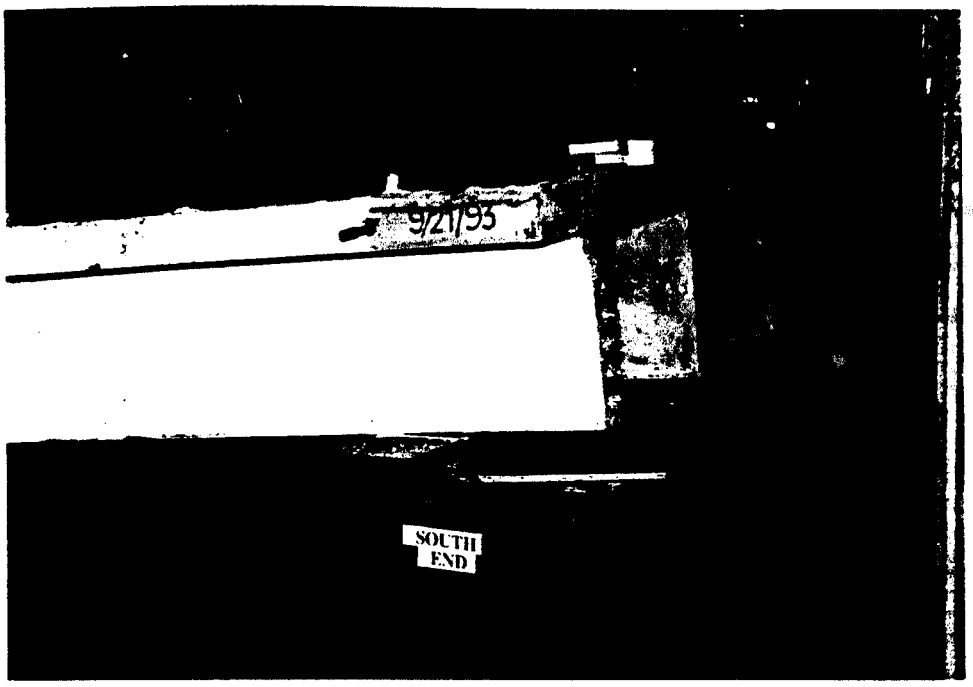

Fig. 7.65 The elevation showing end rotations

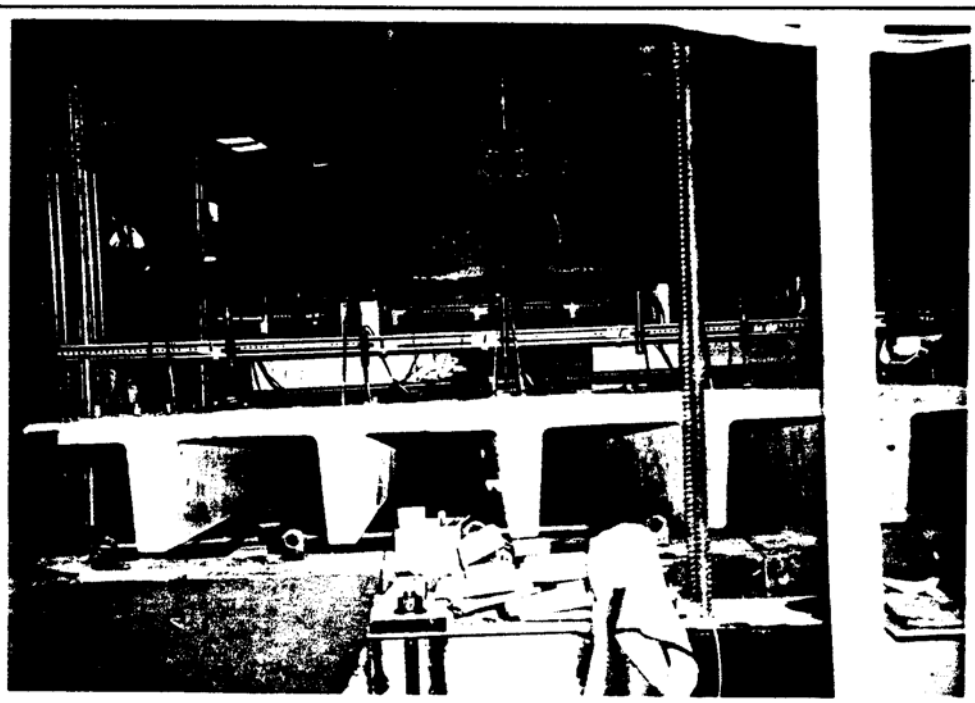

Fig. 7.66 The end view of rotations

Fig. 7.67 Horizontal splitting of the tendon together with loss of bond with concrete

7.4.2.1 Concrete strains

The variations of compressive strains in concrete measured on the top surface of the flange over typical stems at mid, south and north quarter span sections are shown in Figs. 7.68 to 7.70. The recorded compressive strains in the bridge deck over stems 1, 3, 5, and 6 at south quarter span section were not reliable and hence not analyzed; the strains on stem 2 and 4 are shown in Fig. 7.69. The applied load vs. strain graphs distinctly show the bilinear nature; the midspan strains exhibit a smaller initial linear portion than those measured at the south and north quarter spans. This is due to the formation of cracks at midspan at an early stage. The ultimate load as seen from the above figures (Figs. 7.68 to 7.70) is about 81.0 kips. and the corresponding maximum compressive strain over stem 1 at midspan is about 2500 microstrains. The compressive strain over stem 1 is significantly higher than that over stem 6, which is mainly due to the applied eccentric load over stem 1 (Fig. 7.68).

When the load reached the value of 81.0 kips. a sudden drop in the load was observed due to the loss of bond and consequent increase of about 200 microstrains in concrete (Fig. 7.68). This could be observed clearly at midspan and to a certain extent partial loss of bond at south quarter span (Fig. 7.69) indicating the loss of bond of concrete only within the midspan region from north quarter to south quarter span sections. The prestressing force in bottom most tendon in stem 3 was lost immediately after concreting due to anchorage failure; the prestress in all the tendons in stem 4 could more easily initiate the partial loss of bond as evident from the drop in the load in Fig. 7.69..

7.4.2.2 Load deflection characteristics

Figs. 7.71 and 7.72 show the load-deflection relationships of stems 1 and 6 at midspan superimposed with those obtained from the static tests in the first and second stage fatigue testing. The load-deflection curves at the end of the second stage fatigue test perfectly match with those of the ultimate load test upto the load of 36.0 kips. The overall load deflection relationship can be characterized to be trilinear and the linear portion of the second segment extends upto a maximum load of about 44.0 kips. At the maximum applied load of 81.0 kips. the sudden decrease in the load is caused, as explained in the earlier section, by the loss of bond of the tendon. This decrease in the load is not accompanied by an increase in deflection unlike the compressive strains in concrete observed in Fig. 7.68. The small decrease in load values seen in the graphs is caused by formation of new flexural cracks as the applied load is increased on the bridge model. The maximum deflection, at midspan in stem 1, was about 11.1 in. and permanent deflections of stems 1 and 6, immediately after unloading the bridge system, were observed to be 4.5 and 4.8 in. respectively. Based on the maximum deflection of 11.1 in. and the immediate permanent deflection of 4.5 in. the elastic recovery of the system could be estimated to be approximately 60 precent only. This relatively low recovery might be due to the loss of bond in the tendons and extensive closely spaced cracks in the midspan region.

The variations of deflections with applied loads, at mid and south quarter span sections are given in Figs. 7.73 and 7.74. These graphs also exhibit the trilinear characteristics very similar to those for a conventional concrete bridge deck with prestresssing steel. The deflection of stem 1 is greater than that under stem 6 at mid span, since the simulated HS20-44 truck load was positioned with two wheels exactly over the stem 1. The deflection measurements at LVDT positions over stems 2 through 5 were discontinued due to difficulty in access to add steel plates for continuous recording at south quarter span section as the applied load increased beyond approximately 55.0 kips. (Fig. 7.74). The comparison of load-deflection relationships for the mid, south and north quarter span sections is shown in Fig. 7.75. It is seen, as one could expect, that the north and south quarter span sections have the same almost identical load-deflection relationships. The longitudinal deflection profiles of stems 1 and 6 (Figs. 7.76 and 7.77) show a gradual increase in deflections as the load is increased upto the ultimate value.

7.4.2.3 Crack distribution and crack width

The crack distributions in the stems 1 and 6 on the west and east faces respectively are shown in Figs. 7.78. Fig. 7.79 presents a close up view of the cracks on the west face. Extensive horizontal cracks at the level of the bottom most tendon could be seen in stem 1 on the east face; however, only limited horizontal cracks were observed in stem 6 on the west face. The reason for this observation is that stem 1 is subjected to wheel load directly above it and hence the load shared by stem 1 would be greater than that of any other stem, including stem 6, as a result of the applied loading . The variation of crack width measured at midspan of stem 1 is shown in Fig. 7.80. This load vs. **crack width relationship is also seen to exhibit the ideal trilinear characteristics. The maximum crack width observed was about 0.088 in. and a permanent crack width of approximately 0.014 in. This crack closure would amount to approximately 85 % of the crack width recovery in the bridge system. Fig. 7.81 shows a typical crack on the stem at the maximum load of the ultimate load test.**

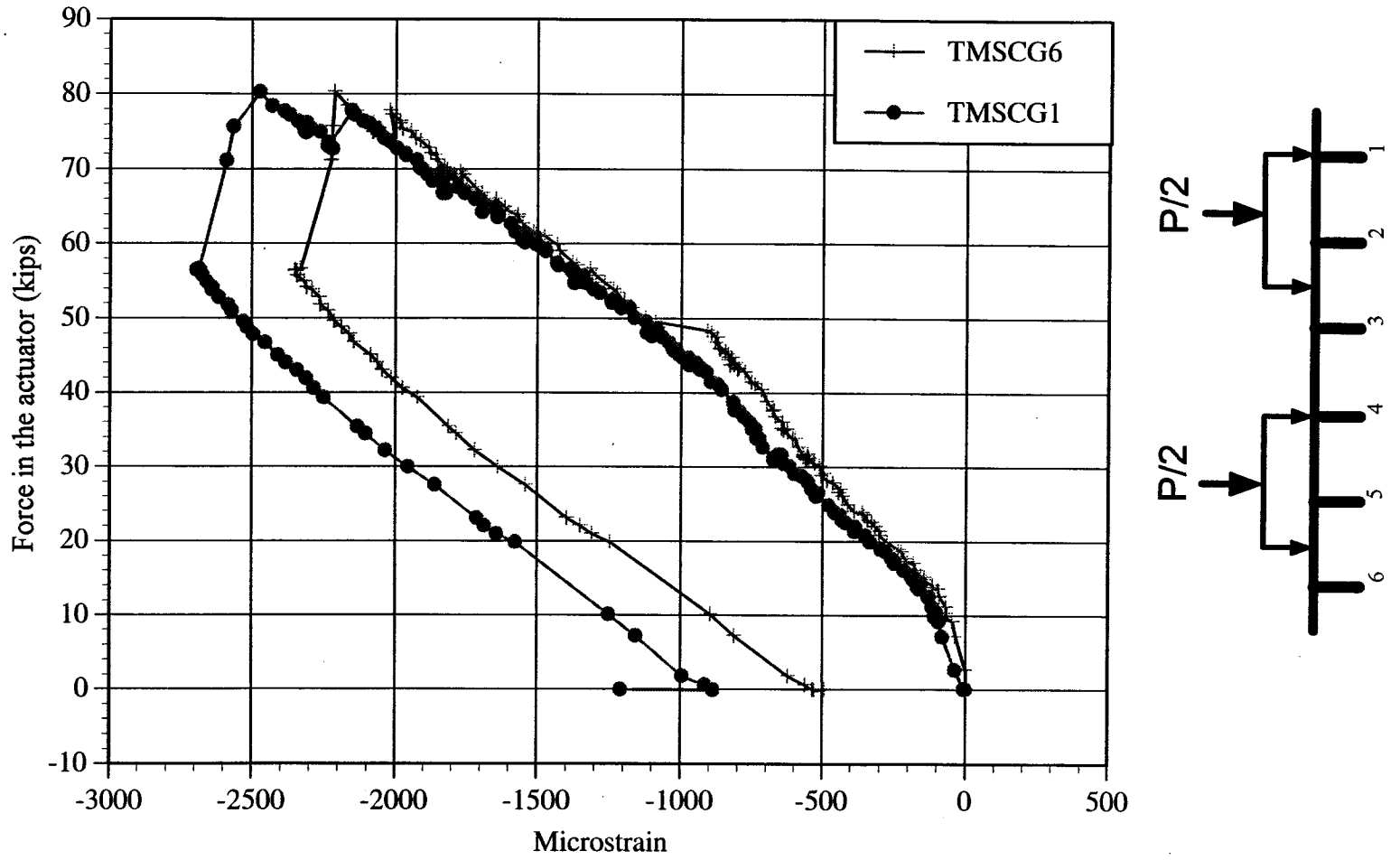

Fig. 7.68 Mid-span strain in top layer in the extreme stems (1 and 6)

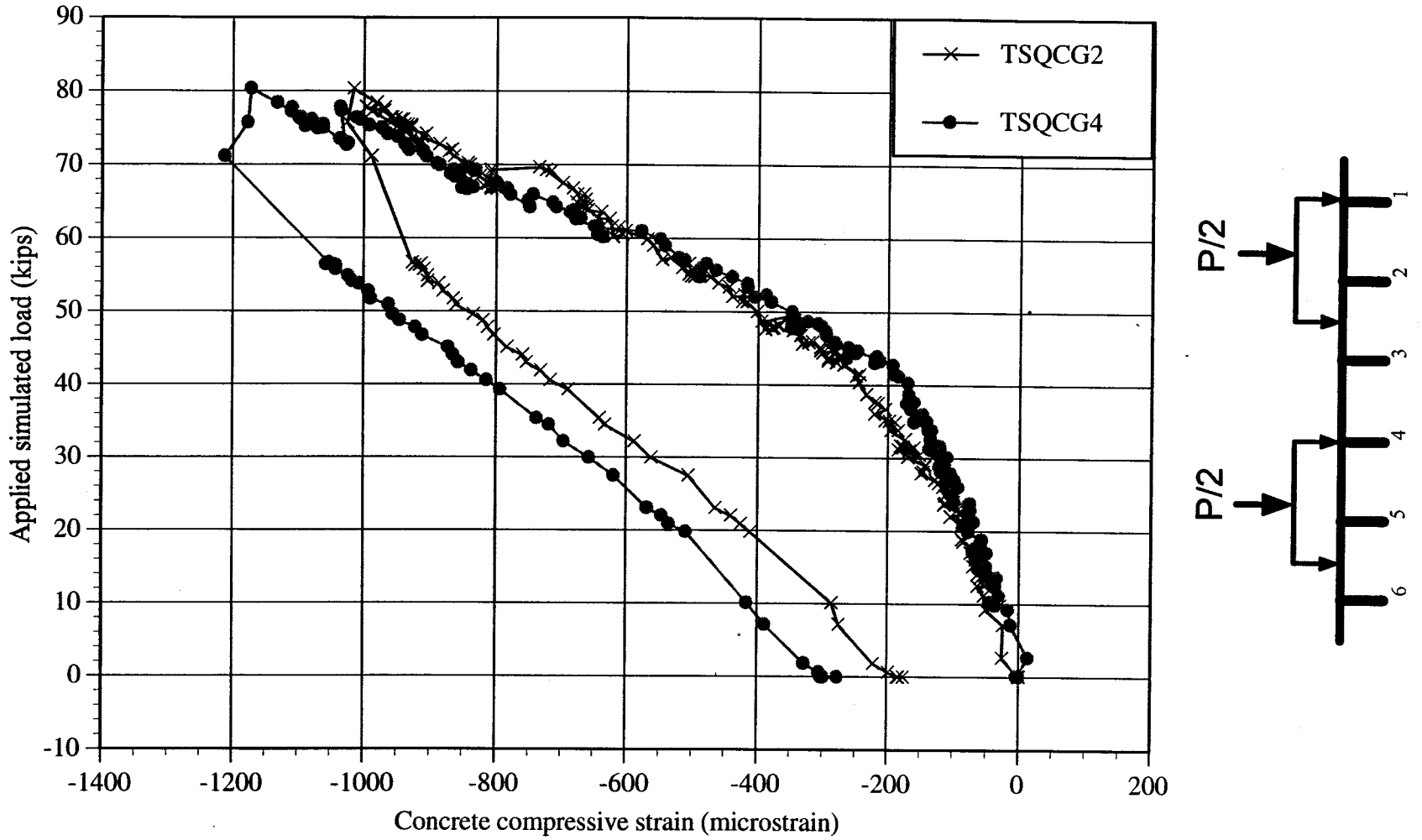

Fig. 7.69 Strain variations in top layers of stems 2 and 4 at South quarter span

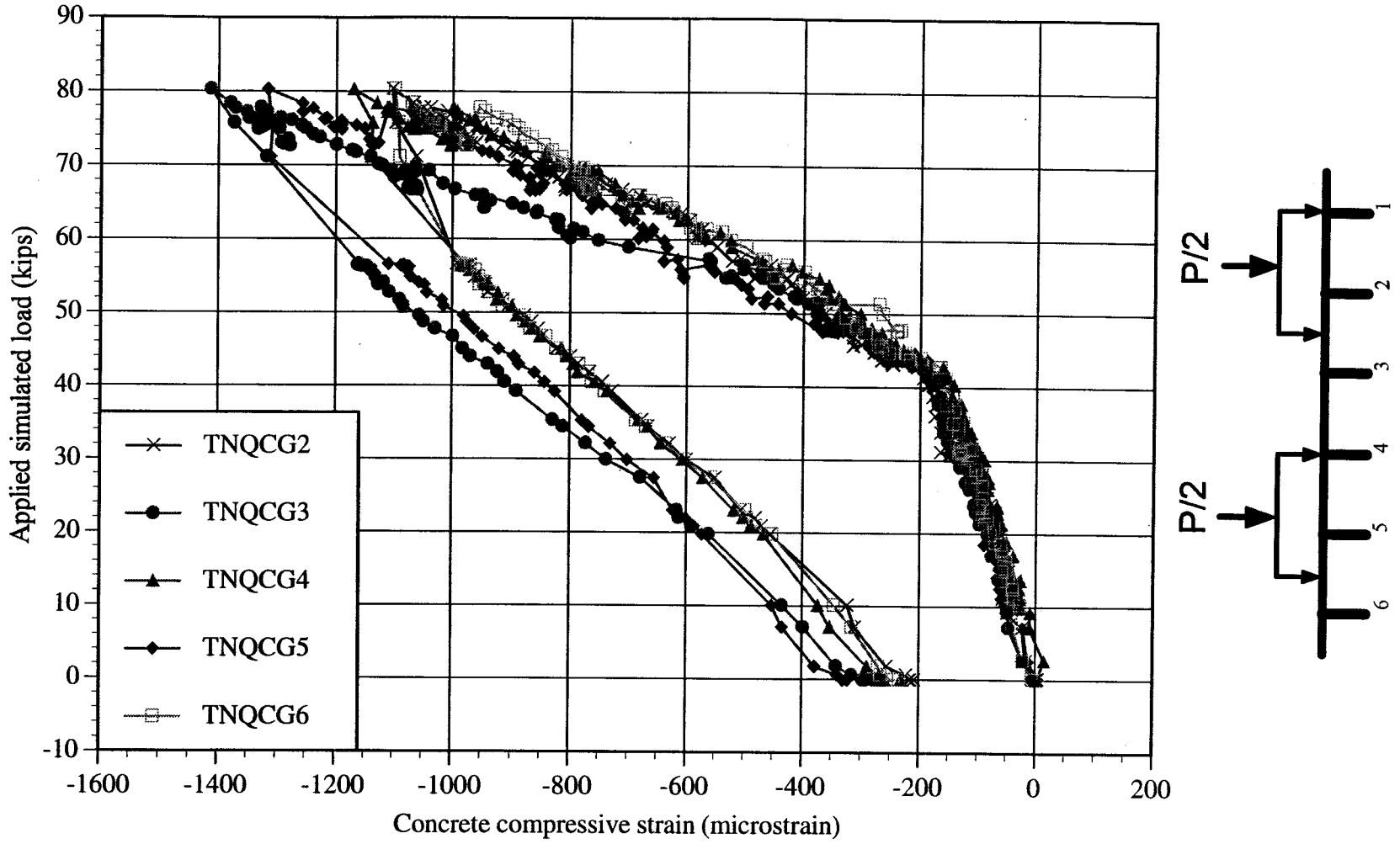

Fig. 7.70 Strain variations in top layers of stems 2 through 6 at North quarter span

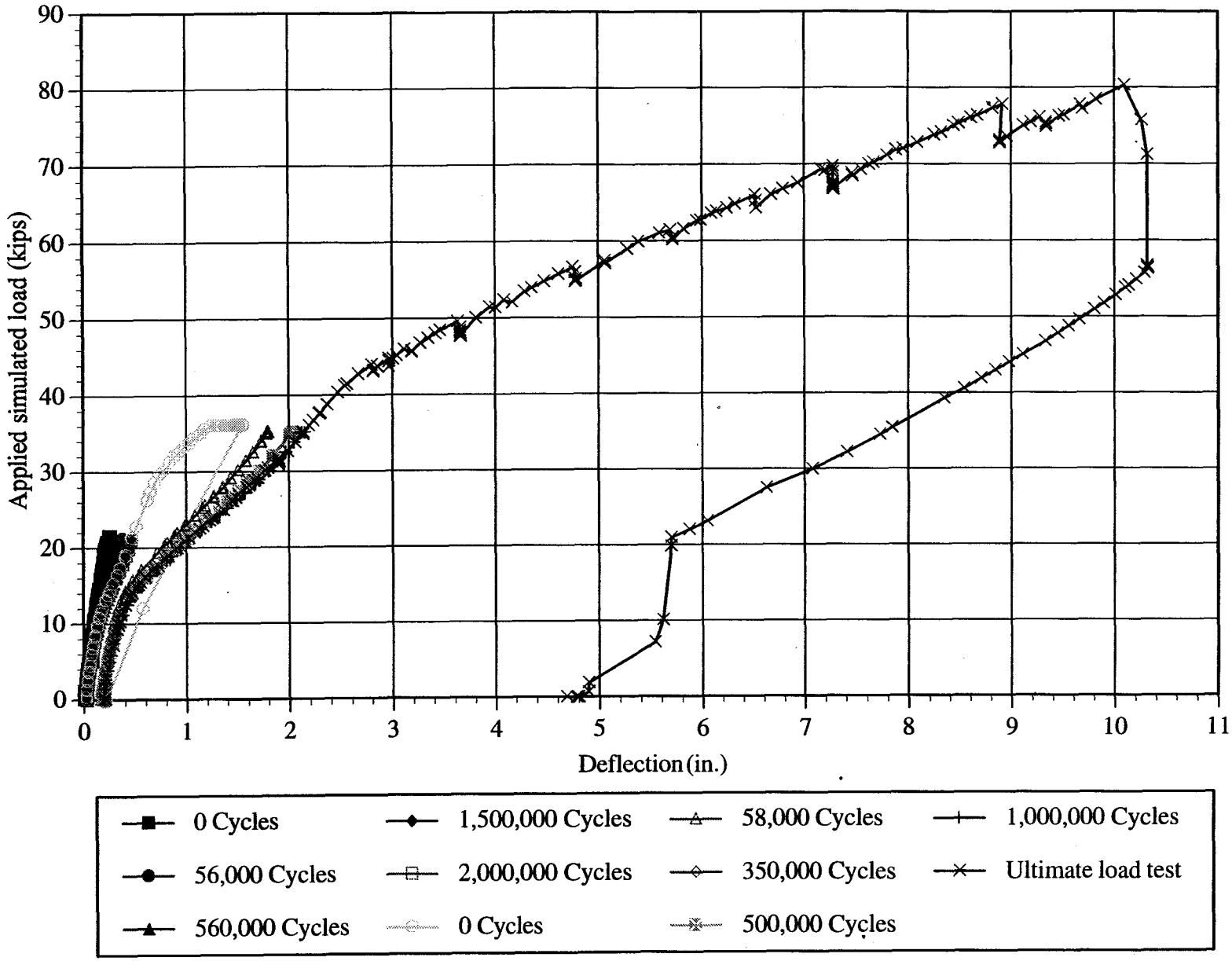

Fig. 7.71 Load deflection history at midspan of stem 6

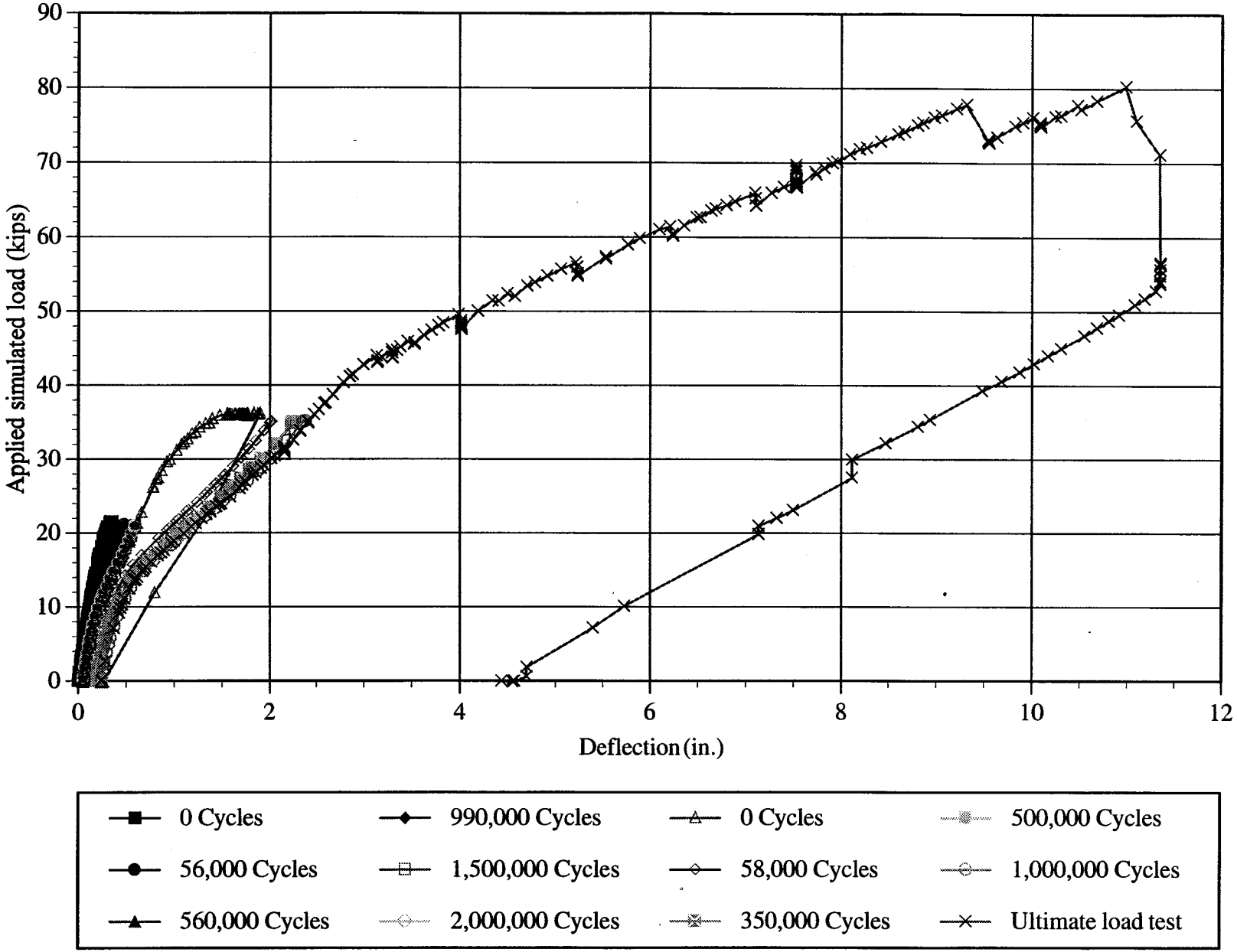

Fig. 7.72 Load deflection history at midspan of stem 1

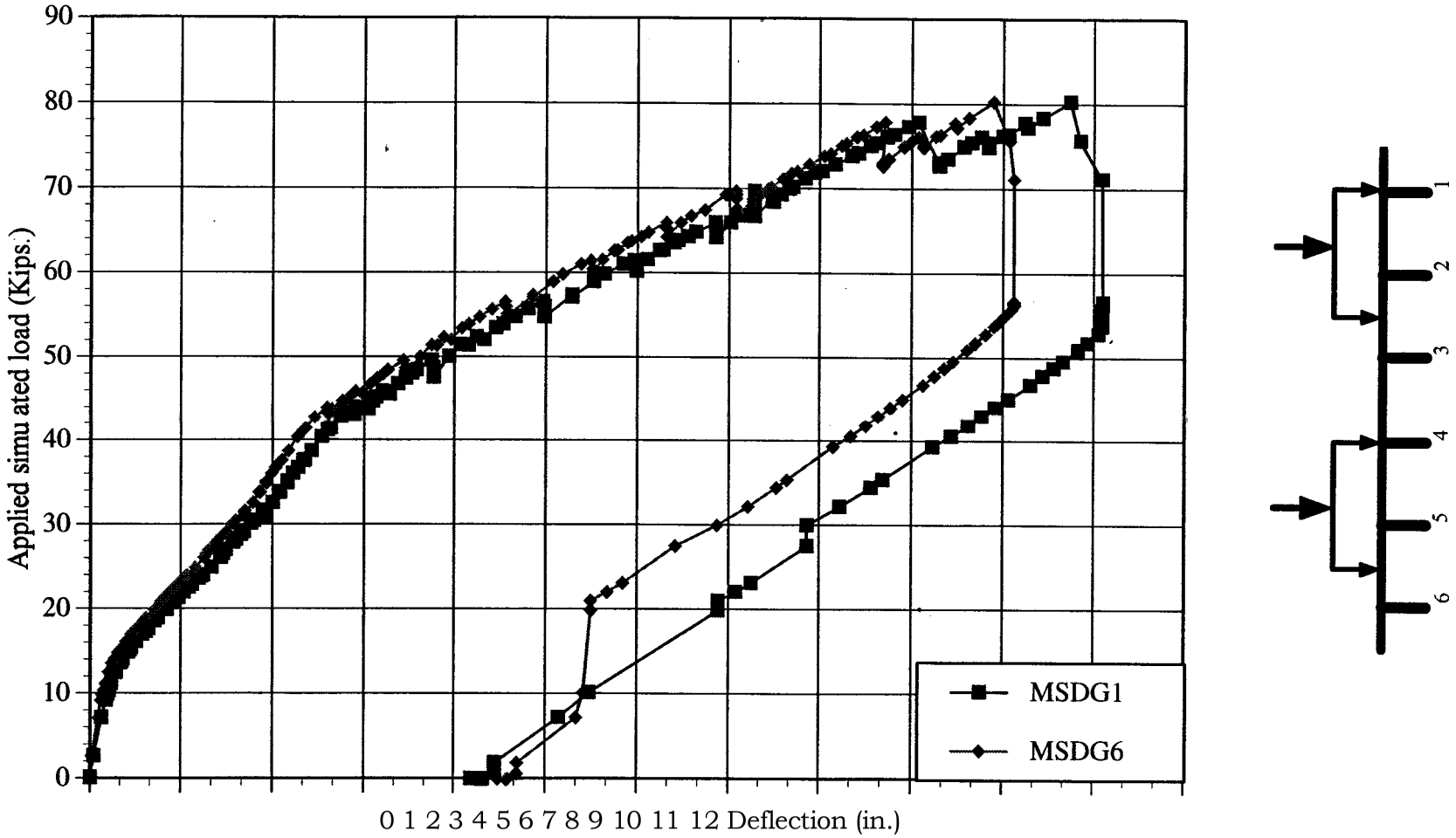

Fig. 7.73 Mid-span deflection variation in stems 1 and 235

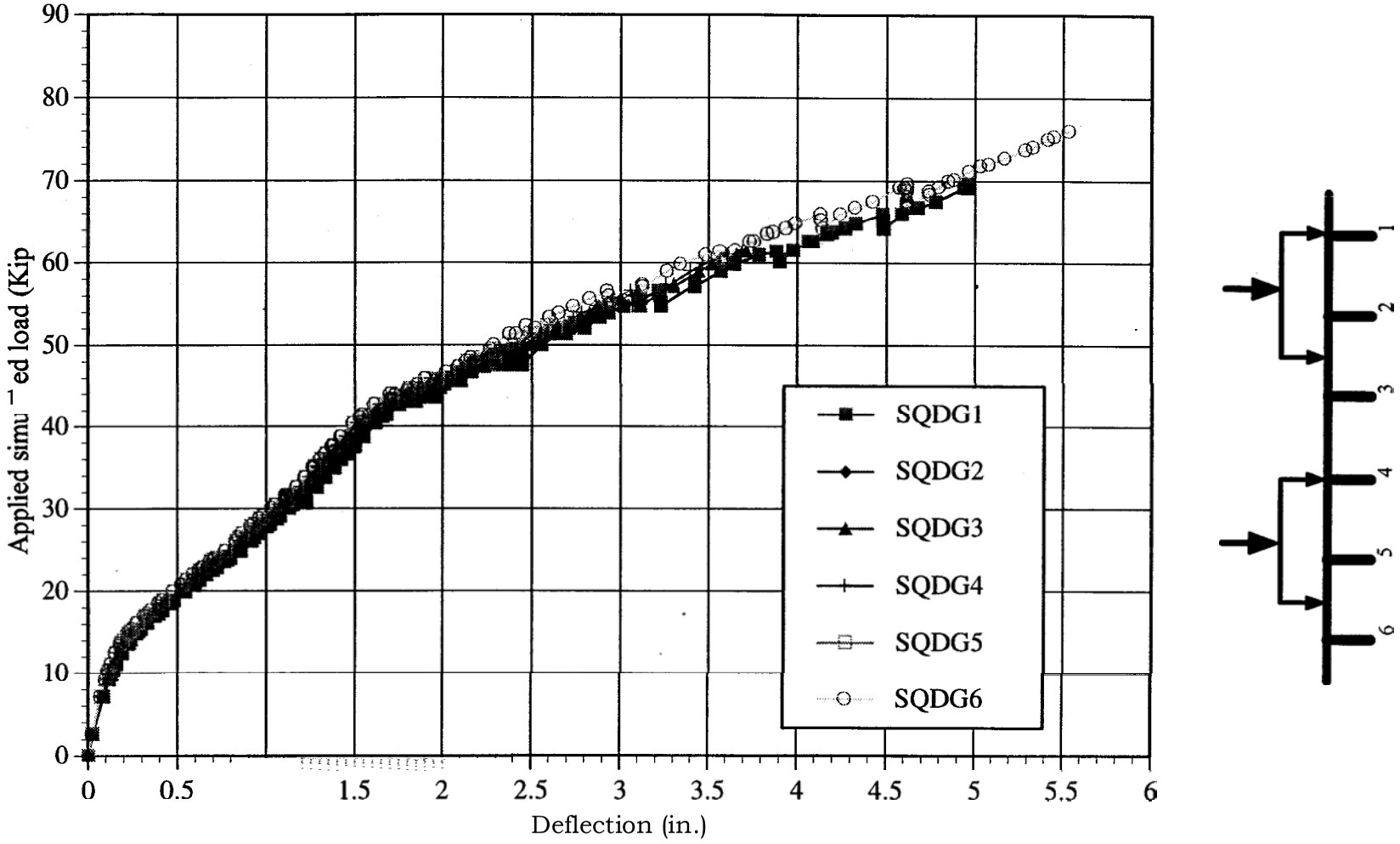

Fig. 7.74 South quarter span deflection variation in stems 1 through 6

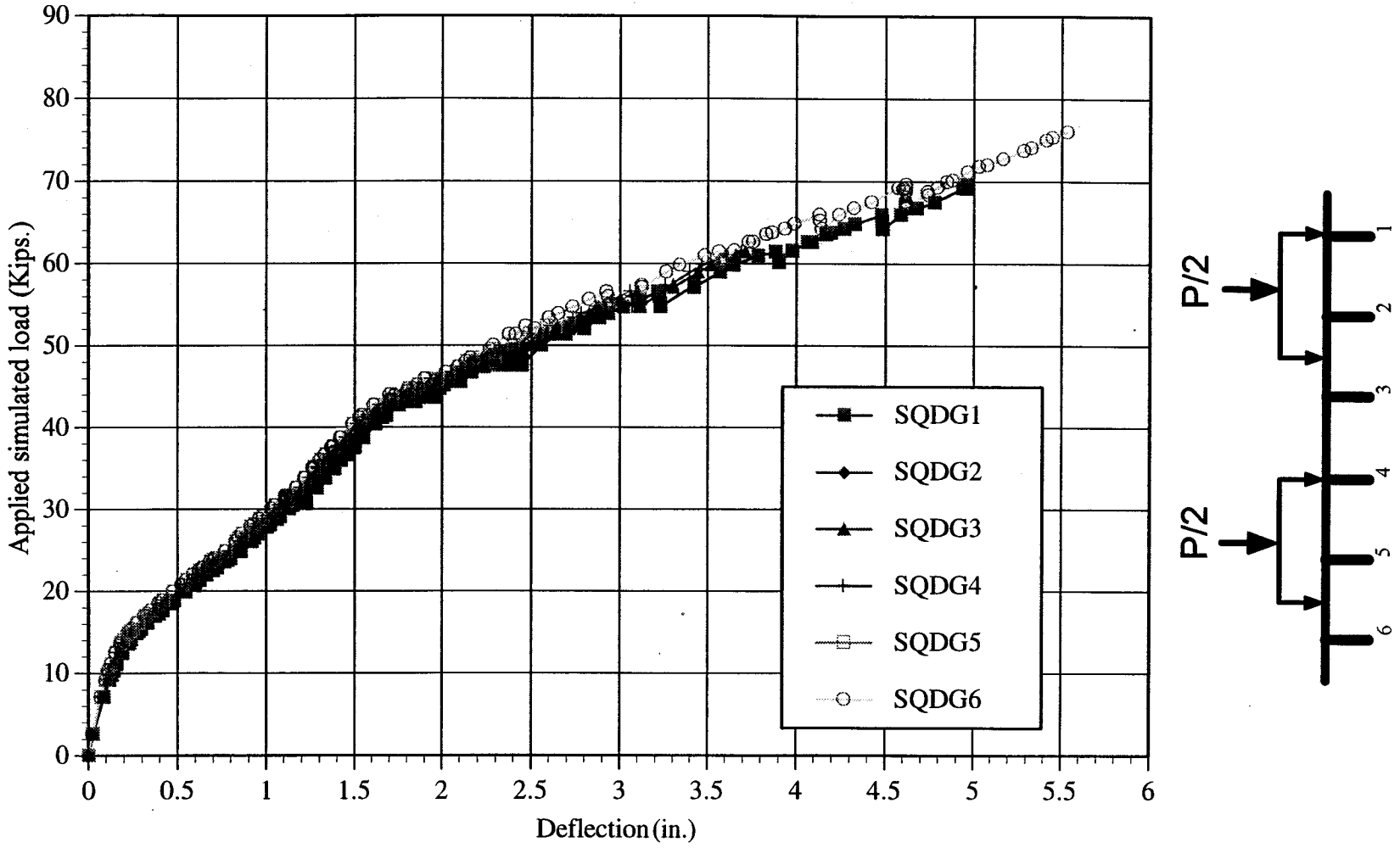

Fig. 7.74 South quarter span deflection variation in stems 1 through 6

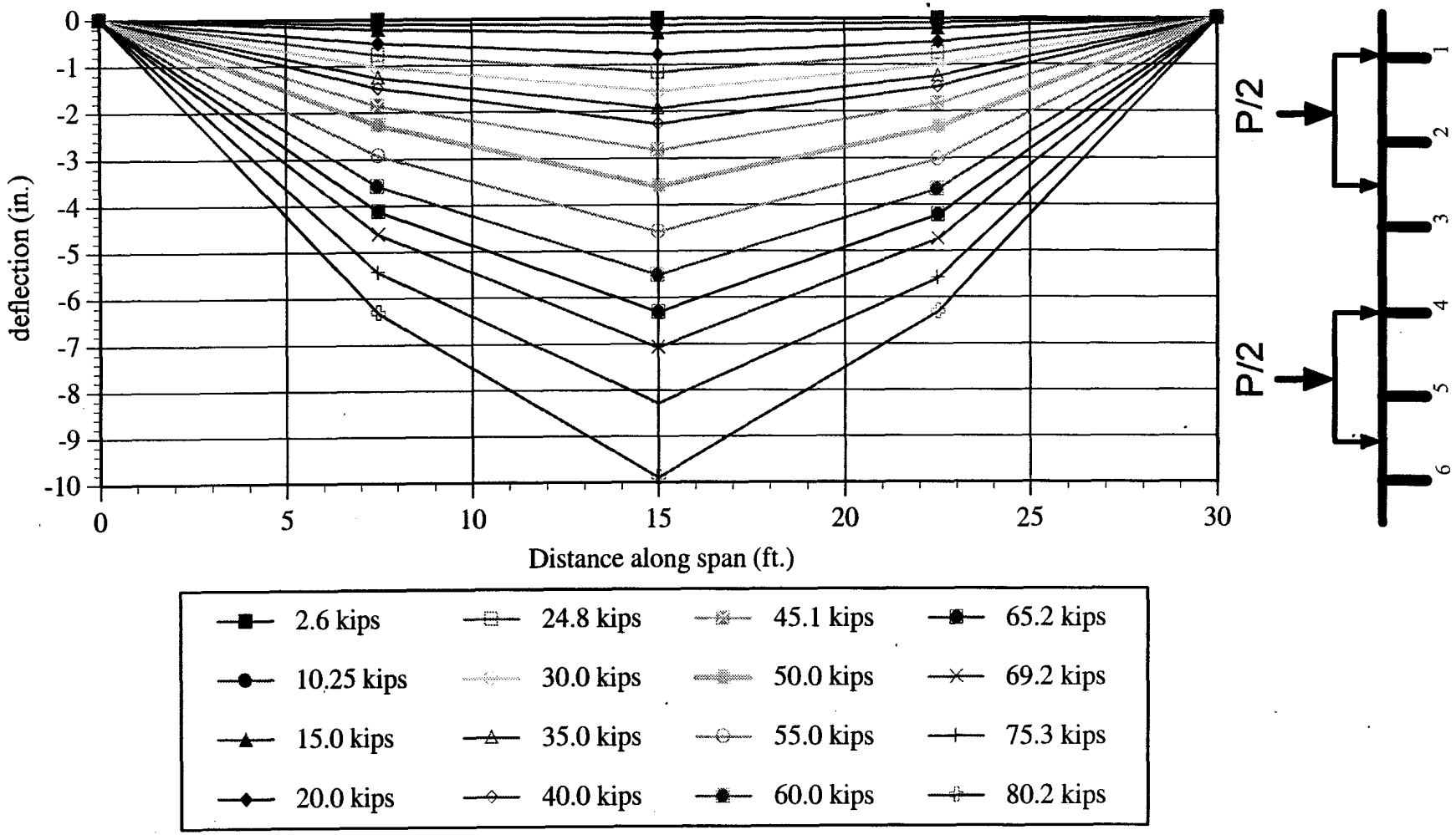

Fig. 7.77 Deflection profile of stem 6 under different load conditions

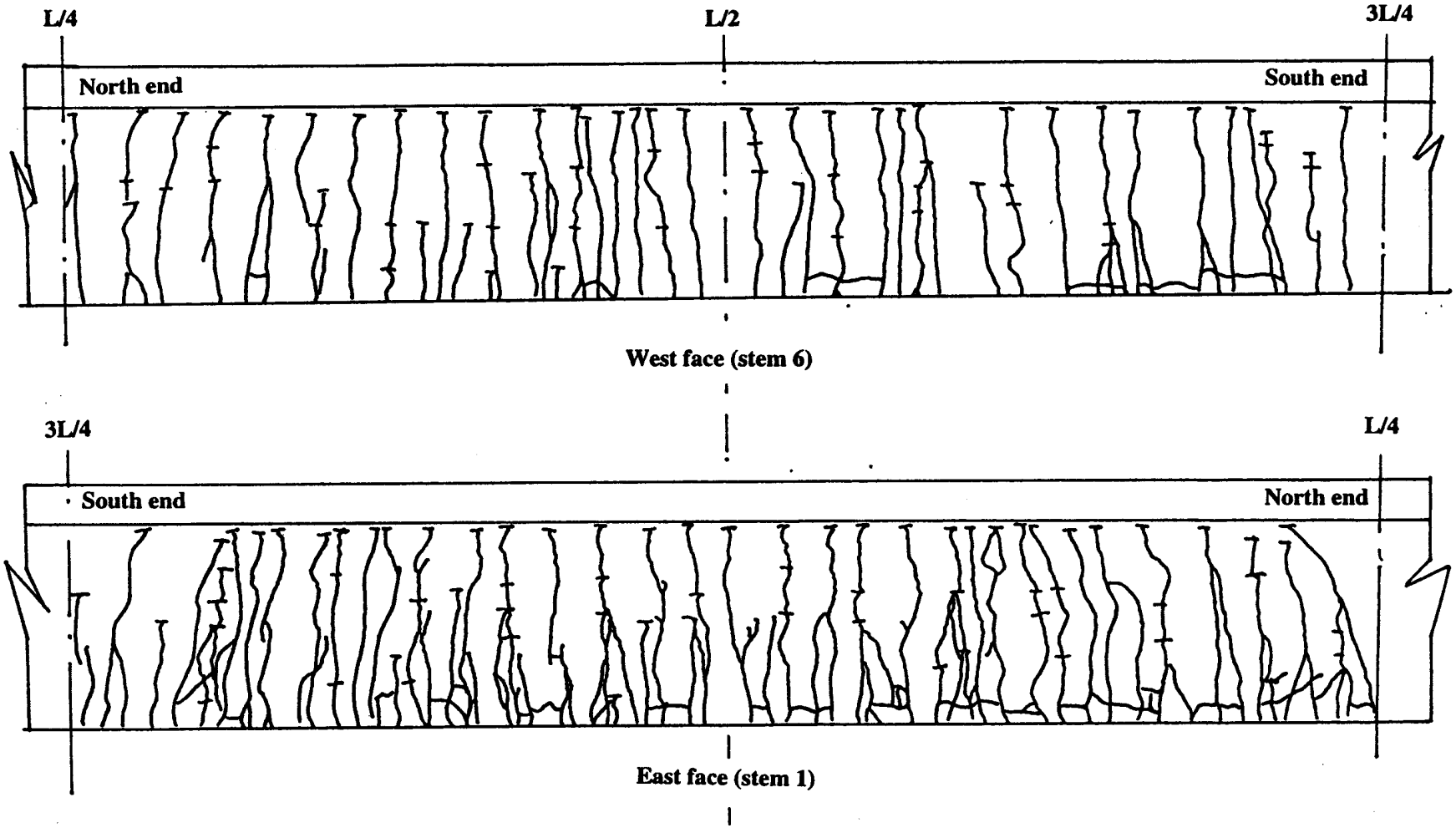

Fig. 7.78 Crack distribution in the stems of the bridge system after ultimate load test

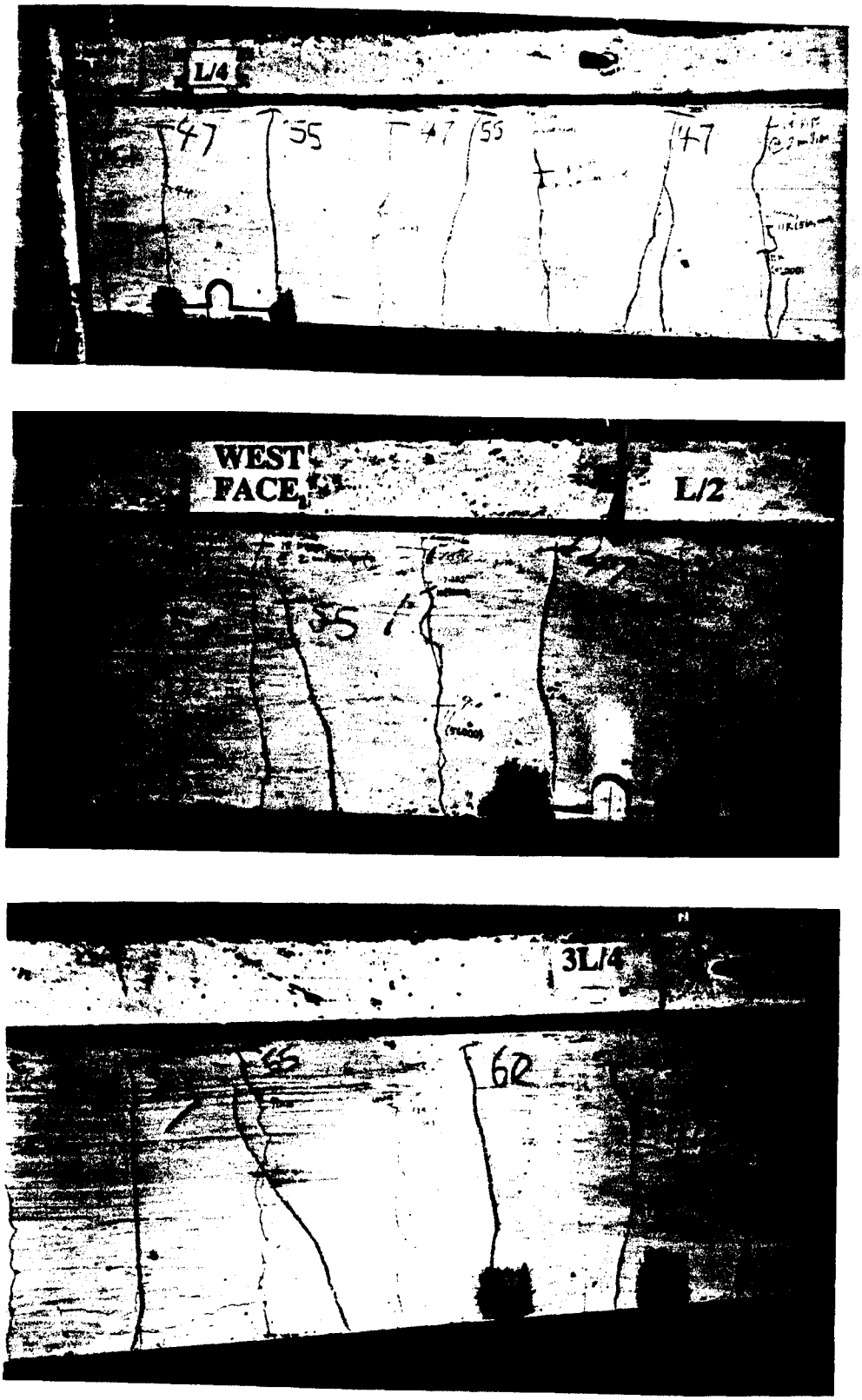

Fig. 7.79 A close up view of the cracks on the west face

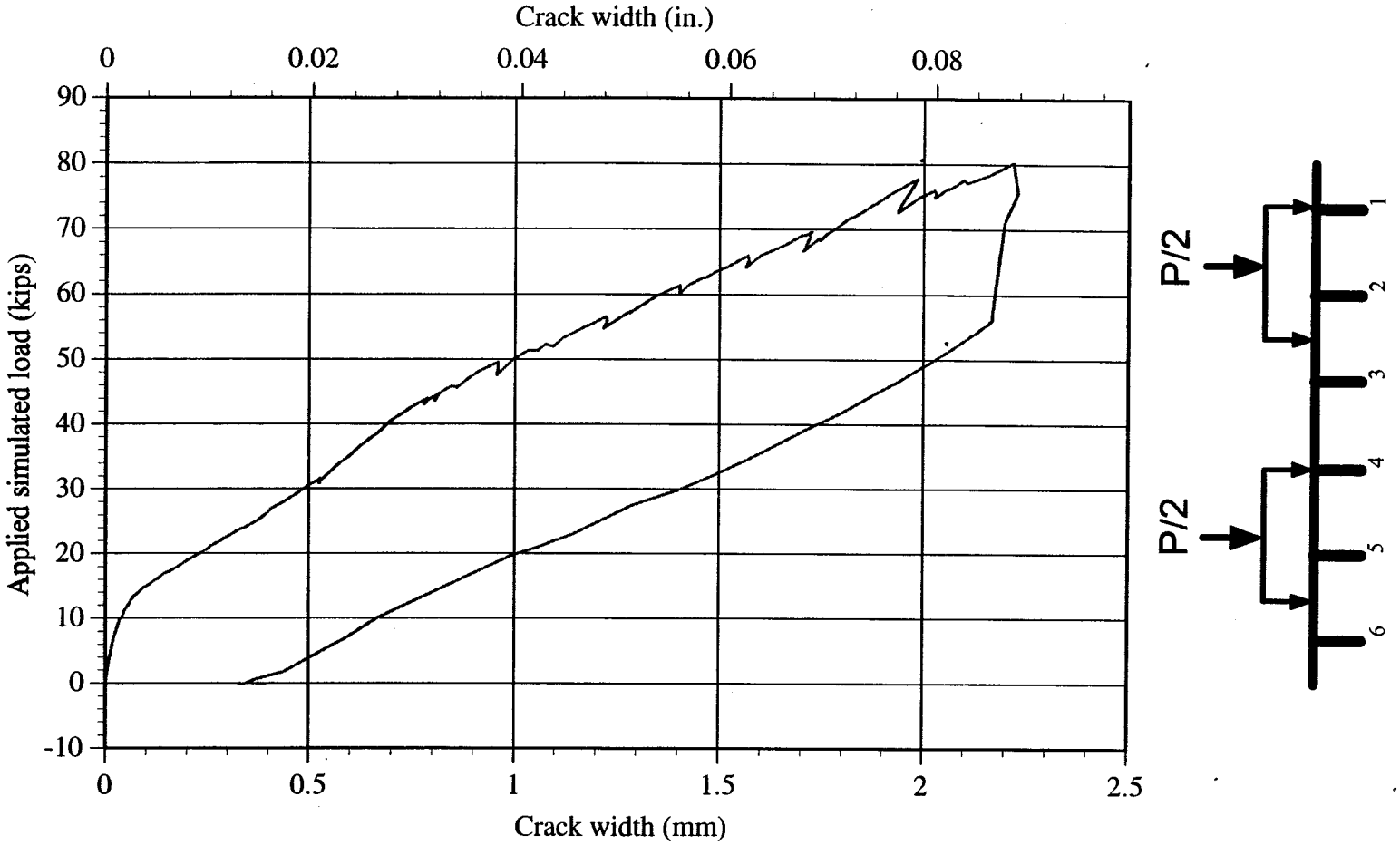

Fig. 7.80 Variation of crack width measured at midspan near the bottom of stem 1

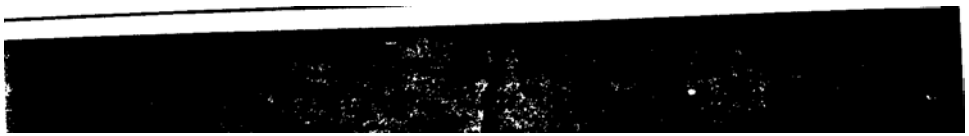

CHAPTER 8

ACTIVE STRUCTURAL CONTROL OF BRIDGES PRESTRESSED WITH FRP

8.1 INTRODUCTION

As part of the inter-disciplinary research effort for solving traditional engineering problems, attention is being focused on the application of Fiber Reinforced Plastics (FRPs) in civil engineering. Although adequate experimental and performance data are not available regarding FRPs and their application in civil engineering, there is considerable interest among designers and researchers for using FRPs as prestressing and reinforcing elements in bridges. Modern technology in civil engineering has led to design and construction of slender, long span and flexible bridge structures. Introduction of Fiber Reinforced Plastics (FRPs) as prestressing and reinforcing elements would result in bridge structures that are lighter in weight, longer in span and more *flexible* **structures. Hence, deflections would play an important role in service and design considerations of these structures.**

The objective of this investigation is to propose a simplified, yet a powerful method of active control of excessive deformations / vibrations in bridge structures. In recent years, significant amount of advancement is achieved in the dynamic modeling of moving loads on bridge structures. This knowledge together with the proposed active control methodology, would prove useful in successful implementation of FRPs as prestressing and reinforcing elements in bridge structures. This chapter presents the proposed active control methodology and an example illustrating controlled and uncontrolled response computations. A dynamic simulation of a moving load on a beam is shown together with a time history analysis of the controlled and uncontrolled responses, with and without the consideration of structural damping. The analysis is performed for two different speeds of the moving

vehicle. The time history analysis performed with an assumed post-tensioning control force variation, illustrates the methodology of the proposed active control method in bridges.

8.2 BACKGROUND

Although structures are designed for the worst expected loading conditions, there is always a possibility for an unexpected loading situation which might exceed the design loads. Also, very little information is available regarding the FRP composites and their application in concrete structures. Active structural control would lead to accurate assessment and continuous monitoring of performance of the FRP as well as the structure which would ensure safety of structure under unexpected loading conditions.

Significant amount of research has been done on active control of vibrations of flexible structures [Soong, 1990, Rohman and Leipholz 1980, Yang and Giannnapolous 1979, Roorda, 1975]. Although the problems are more or less similar to each other, each of them poses a specific challenge to researchers in terms of algorithms and applicability of a particular method of active control. Active control of heavy structures like bridges is usually accompanied by large forces applied at specific points of the structure. Yang [19791 dealt with active control of a cable stayed bridge, subjected to wind loads, by controlling the forces in the cable stays.

Recently significant attention is given towards the concept of employing fiber optic sensors for strain and displacement measurement in the concrete structures. Incorporation of these fiber optic sensors in the concrete structures would lead to accurate, continuous and long term strain / displacement measuring system. Establishment of such a monitoring system is required to implement a real time control mechanism in a bridge structure. FRPs are very friendly towards fiber optic sensor installation due to their non-conducting and non-magnetic property.

8.3 PROPOSED ACTIVE CONTROL FORMULATION

8.3.1 Theory

Pre-tensioning and post-tensioning are well established concepts implemented in civil engineering' structures since 19th century. The concept of prestressing has also contributed significantly to the economy in bridge construction. The recent introduction of FRPs into the bridge construction collaborated with the concept of prestressing is leading to more flexible bridges. The construction industry has always been in search for answers to the new complexities, which arose in the implementation of new concepts and technology. This investigation is an attempt to arrive at an easily implementable solution to problems arising from the flexibility of the bridge structures prestressed / reinforced with FRPs.

The deformations and large vibrations caused in the flexible bridge structures due to heavy and high speed traffic could be controlled by active post-tensioning tendons placed at a predetermined eccentricity. Theoretically, undesirable large deformations or high vibration amplitudes would be controlled actively by introducing tensile force (through actuators) in the active tendons. This active tensile force in the tendons would act as post-tensioning force on the section and hence controls the excessive deformation and / or vibrations in the structure. The methodology is quite feasible and any type of control algorithm could be utilized to achieve the desirable and practical results. Fig. 8.1 shows a schematic representation of the active control system being implemented in an experimental beam Fig. 8.2 shows the flow chart of control methodology presented herein, with all the three types of control systems i.e. closed-loop, open-loop, and closed-open-loop systems.

8.3.2 Equations of Motion

A bridge is modeled by an n-degree-of-freedom mass-dashpot-spring system The equations of motion of the structural system can be represented as

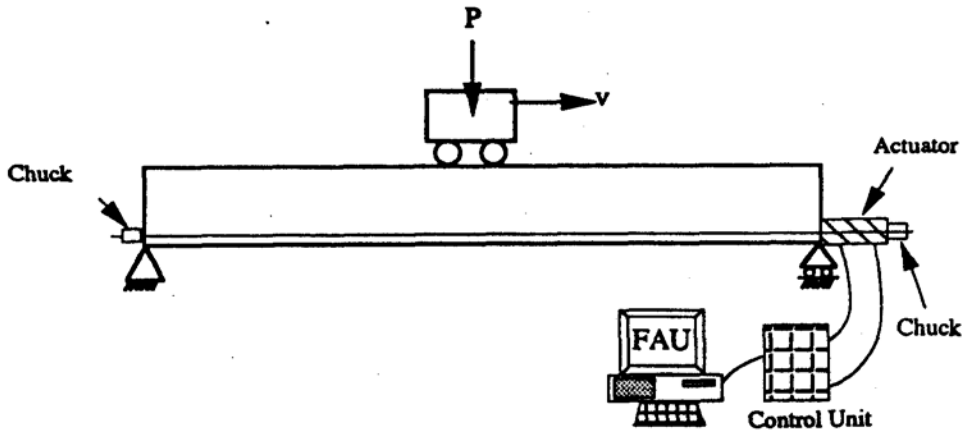

Fig. 8.1 Schematic representation of proposed active control setup

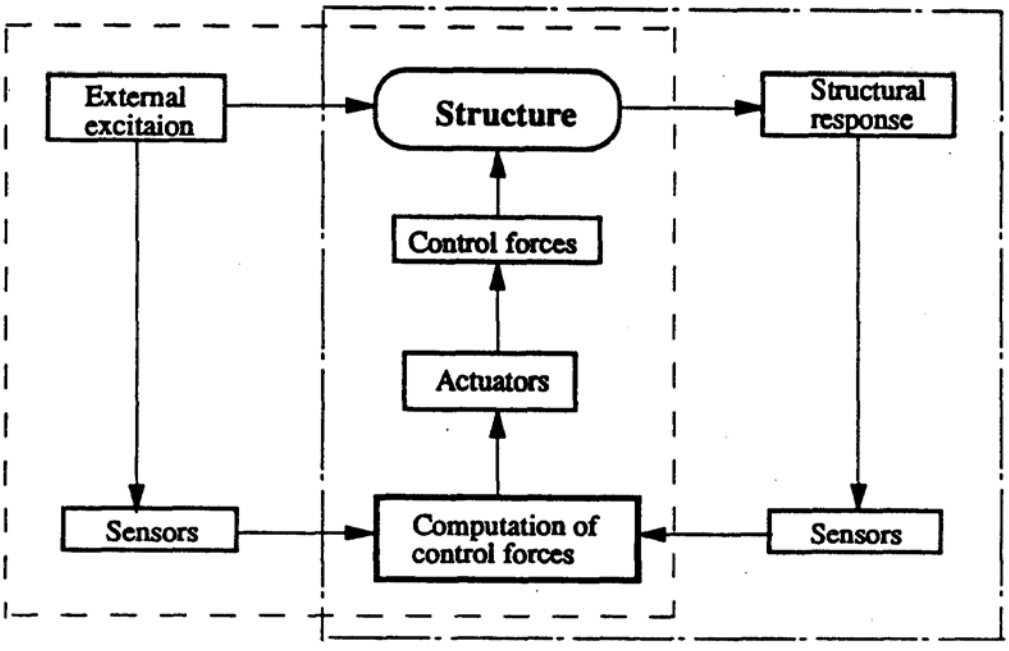

Fig. 8.2 Schematic diagram of active control

$$M\ddot{w} + C\dot{w} + Kw = Df(x, t) + Eu(x, t) \quad \text{... (1)}$$

where M, C and K are mass, damping and stiffness matrices and D and E are position matrices of the excitation, *f(x,t)* and control forces *u(x,t),* acting on the structure respectively. For a given bridge type, the control force could be represented as follows:

$$u(x,t) = K_1 w(x,t) \quad \text{... (2)}$$

where K, represents the change in stiffness of the system due to control forces.

Substitution of Eqn. 2 into Eqn. 1 yields the following:

$$M\ddot{w} + C\dot{w} + (K - EK_1)w = Df(x,t) \quad \text{... (3)}$$

Comparing Eqns. 1 and 3, the change in the structural stiffness would control the response of the structure. Introduction of post-tensioning force would alter the structural stiffness according to a predetemvned algorithm and hence controls the vibration / deformation amplitude of the structure.

8.4 PROBLEM FORMULATION

The bridge structure can be modeled as a simply supported beam whose behavior is described by Euler-Bernoulli's differential equation with a structural damping constant β (Eqn. 4).

$$EI\frac{\partial^4 w}{\partial x^4}(x,t) + \rho A\frac{\partial^2 w}{\partial t^2}(x,t) + \beta\frac{\partial w}{\partial t}(x,t) = f(x,t) \quad \text{... (4)}$$

Without loss of generality, the following assumptions would simplify the **solution:**

i) **The beam is of constant cross sectional area A, uniform mass density p, and a flexural rigidity El.**

ii) **The vehicle is modeled as a moving load of constant magnitude traveling from one end of the beam to the other with a constant speed v.**

iii) If the structural damping is not considered in the modeling, the equation of motion reduces to

$$EI\frac{\partial^4 w}{\partial x^4}(x,t)+\rho A\frac{\partial^2 w}{\partial t^2}(x,t)=f(x,t) \qquad \text{... (5)}$$

A point load moving at a speed v, on a beam of span 1 could be represented in the form of Fourier series as

$$f(x,t)=\sum_{n=1}^{\infty}\frac{2f}{1}\sin\left(\frac{n\pi x}{1}\right)\sin\left(\frac{n\pi vt}{1}\right) \qquad \text{...(6)}$$

The solution of Eqn. S with forcing function as represented in Eqn. 6 would yield the following response function of the beam for a moving load as a function of space and time:

$$w(x, t) = W(x)T(t) \qquad \text{... (7)}$$

Using the response information, closed loop control is possible by continually monitoring the responses, determining the control forces and applying them to the structure. Since the response function is known for given bridge system, and can be expressed in terms of weight and speed of the moving load, it is possible to adapt a predictive open loop control or an open-closed-loop control. Open loop "predictive" control can be established by treasuring the velocity and weight of vehicle entering the bridge structure. Here, open loop control is termed as "predictive" because the control forces are predicted by the control force computing system using the external excitation (measured weight and velocity of the vehicle entering the bridge structure) as input.

8.5 DYNAMIC SIMULATION

A simply supported prestressed concrete beam was analyzed for time history response, subjected to a moving load of 10 kips. The time history analysis is performed for two different

velocities of the moving load, 30 mph. and 65 mph. The forcing function is computed using Eqn. 6. and the analyses performed using. structural analysis software package SAP90. The primary aim of the analyses is to establish the effectiveness and workability of the proposed active control methodology. However, analyses were performed with and without considering structural damping ratio to study its effect on structural control in the presence/ absence of control forces. The following assumptions are made in the analysis:

i) the beam is of constant cross sectional area A and flexural rigidity EI;

ii) the beam is simply supported,

iii) mass contributions of reinforcement and active tendons are neglected,

iv) structural damping is neglected. This assumption is made primarily to establish the individual contribution of the active tendon forces in controlling the deformations / vibration amplitudes. Since the structural damping is unique for a given bridge / beam system, it could only be evaluated experimentally,

v) the vehicle is simulated as a point load moving at a constant velocity, and

vi) the beam is analyzed as a linear system i.e. analyses performed in the linear range of load vs. deflection relationship.

Fig. 8.3 shows the dimensions and finite element discretization of the beam Two node 3-dimensional beam element with six degrees of freedom at each node, is used in the analyses. The beam is divided into 32 elements of 3 in. each.

8.5.1 Structural Control : Effect of Active Tendon Stressing

Figs. 8.4 to 8.6 show the time history response analyses of the beam with a moving load at a velocity of 30 mph. Fig. 8.4 shows the variation of time function (time function portion of Eqn. 6) and Figs. 8.5 and 8.6 show the time history response of the beam without and with control forces respectively. A **tensile control force of 20 kips in the active tendon at an eccentricity of 3 in. is applied to the structure at a shift (t) of the response curve is noticed initially without any significant change in the total amplitude of the response. A reduction in the amplitude is observed after the vehicle exits the**

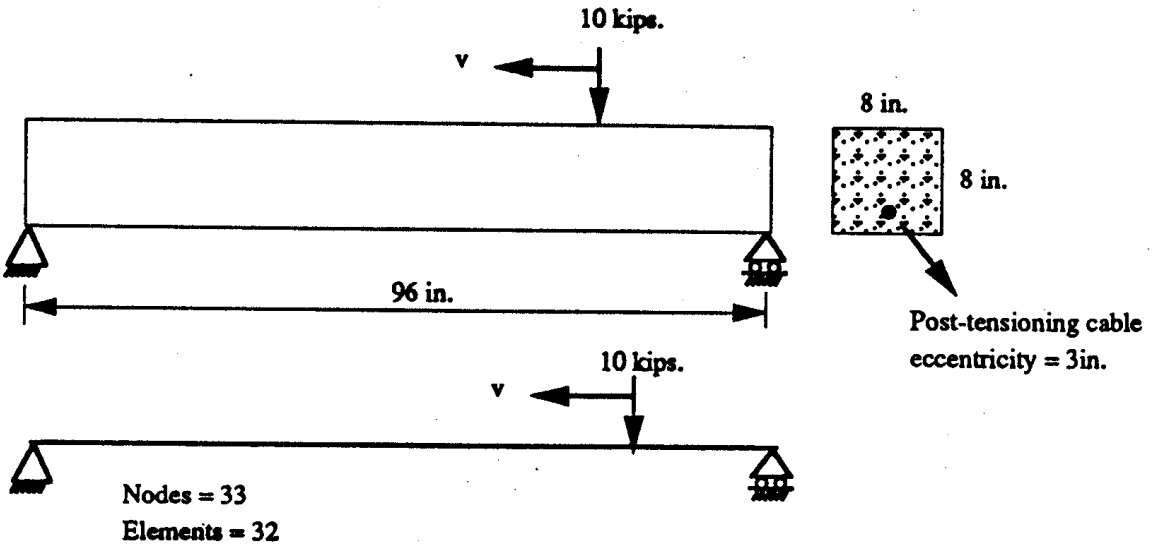

Fig. 8.3 Analytical beam dimensions and discretization

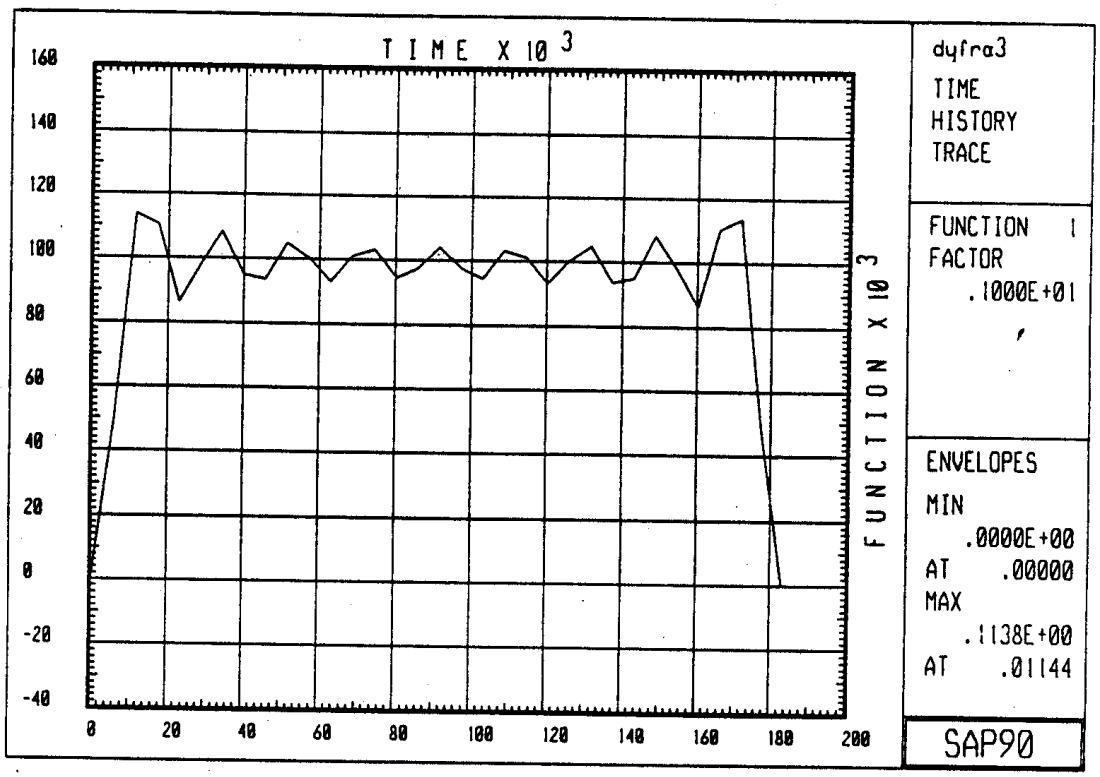

Fig. 8.4 Variation of periodic function with time (v = 30 mph)

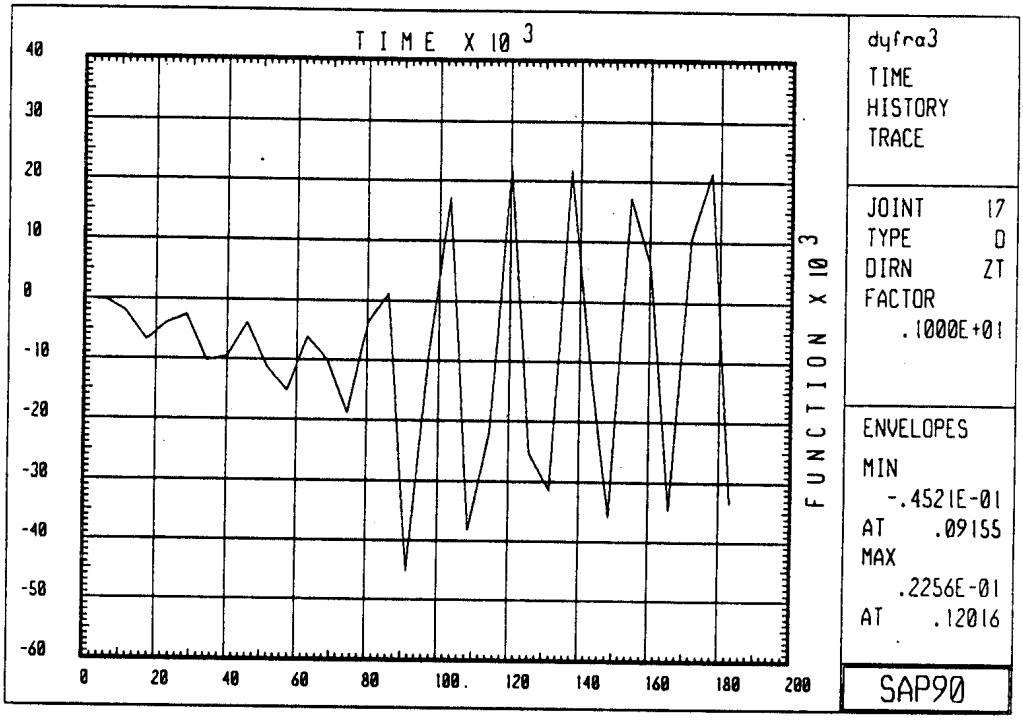

Fig. 8.5 Time history response variation - uncontrolled (v = 30 mph)

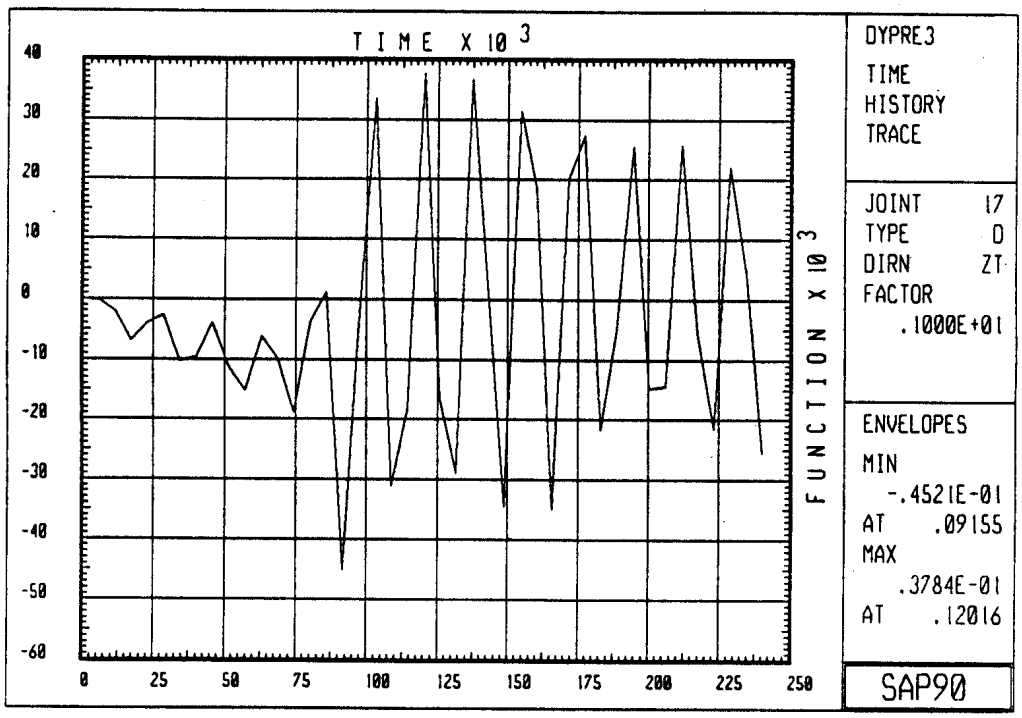

Fig. 8.6 Time history response variation - controlled (v = 30 mph)

beam The reason for this behavior of beam can be attributed to the constant application of a high control force, regardless of the variation in the amplitude. The control forces should be applied at the time they are needed the most and in a way to counter the response due to the external excitation. This is achieved in the following analyses:

Figs. 8.7 to 8.9 show the time history analyses performed on the beam subjected to the load moving at a constant speed of 65 mph. Fig. 8.7 shows the time history response of the beam for the load duration. Figs. 8.8 and 8.9 show the time history variation of control force and the response of the beam respectively. The control force is applied in accordance with the amplitude of the actual response ("predictive" open loop control, since response amplitudes are known prior to the application of control forces, as function of known mass and speed of the vehicle). From Fig. 8.9, it could be seen that the amplitude is controlled to a significant extent even while the load is present and after the load exits the beam

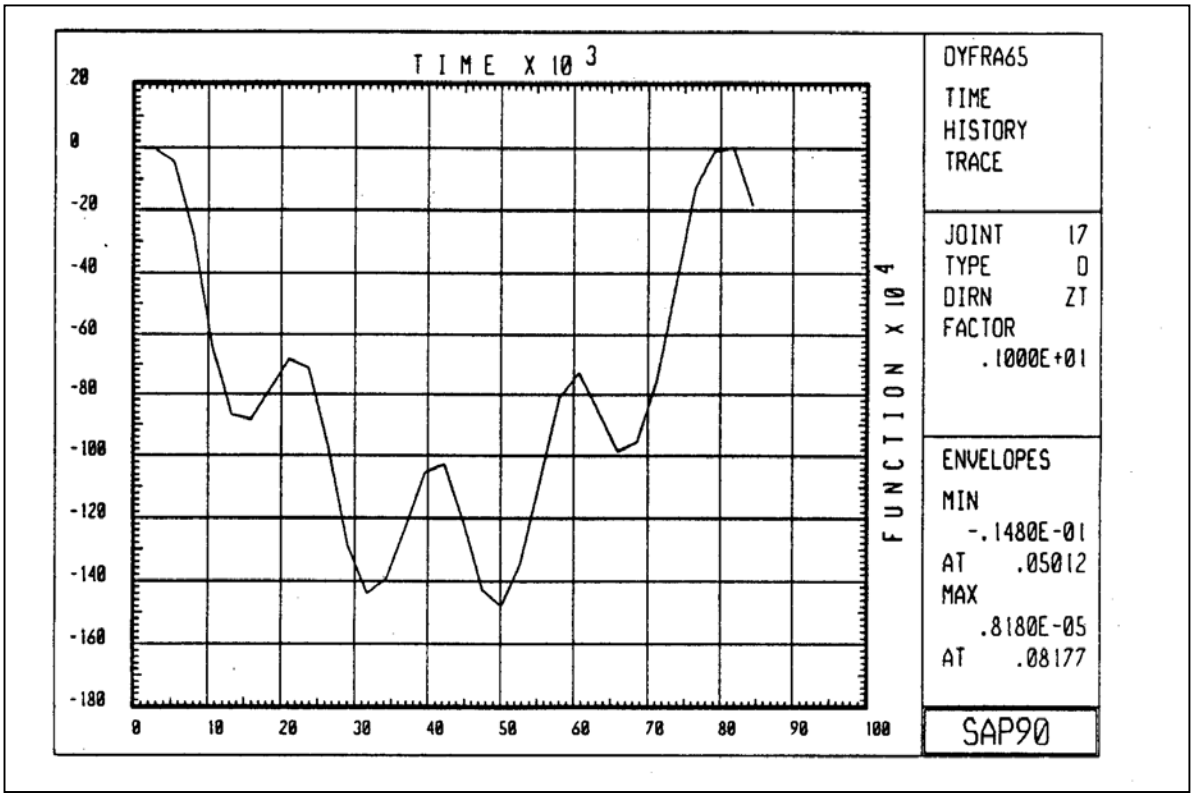

Fig. 8.7 Time history response variation - uncontrolled (v = 65 mph)

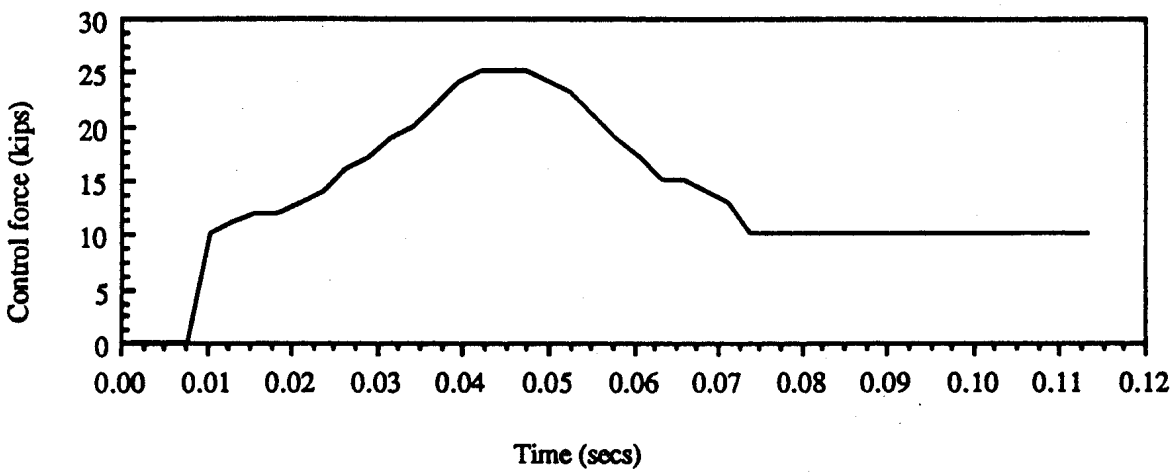

Fig. 8.8 Variation of control force (v = 65 mph)

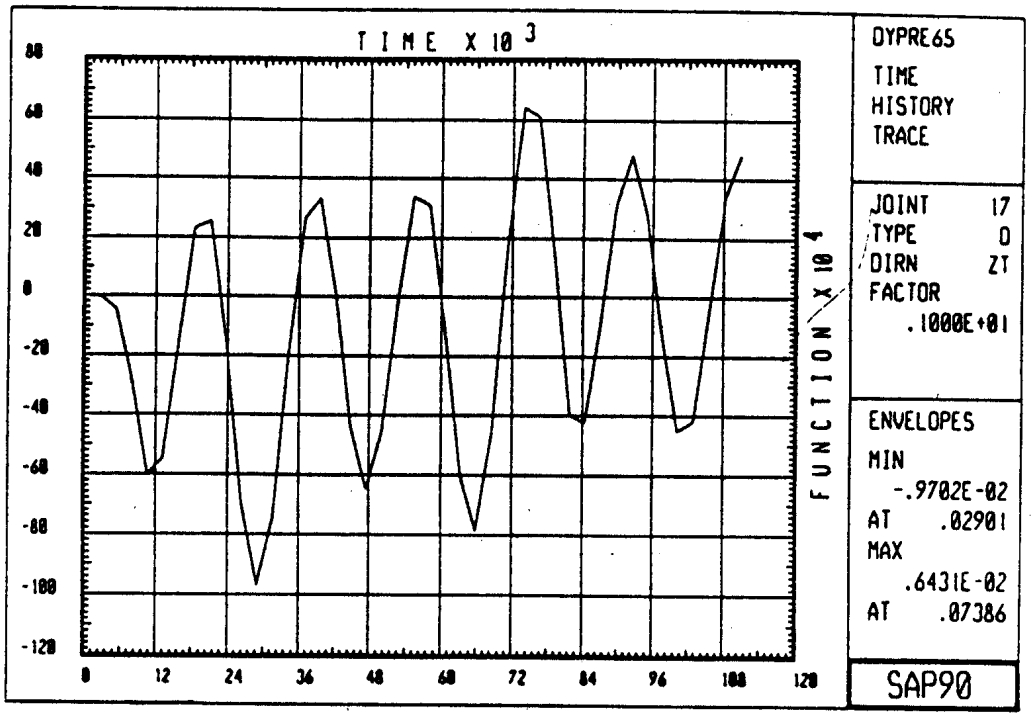

Fig. 8.9 Time history response variation - controlled (v = 65 mph)

8.5.2 Structural Control : Combined Effect of Active Tendon Stressing and Structural Damping

The active control technique and the illustration presented in the above sections do not consider the effect of inherent structural damping of the member. The structural damping is a unique characteristic of a structure, owing to the type of material which is utilized in construction of the structure due to intergranular friction. Structural damping ratio is usually expressed as a non-dimensional term. This damping enables the structure to mitigate the vibrations due to any external perturbation(s). Significant amount of research has been done to estimate and generalize the damping ratios of reinforced / prestressed concrete structures. The following analyses illustrate the effect of (i) structural damping alone and (ii) damping together with active control tendon stressing.

Similar to the second analysis explained in the previous section, the speed of the vehicle is taken as 65 mph, but the analyses were performed for a longer duration (0.136 secs.). This would enable the observation of response after the vehicle exits the beam. Fig. 8.10 shows uncontrolled - undamped response of node # 17 (midspan of the beam) throughout the duration of analysis. It can be seen that the beam experiences large amplitudes until shortly before the vehicle exits the beam and a mode of free vibration is observed after the vehicle exits the beam Amplitude of this variation would remain constant, since the structural damping is not considered in the analysis. The following analyses illustrate changes in the vibration amplitudes shown in Fig. 8.10, wherein structural damping is considered together with control forces.

To study the effect of structural damping alone, analyses were performed using a damping ratio of 0.3. Although this damping ratio of 0.3 is impractical for concrete structures, these analyses were designed to exaggerate and observe the effect of damping with and without the action of control forces. Figs. 8.11 and 8.12 show the damped-uncontrolled and damped-controlled response of the structure respectively. It is observed that the sinusoidal shaped amplitudes shown in Fig. 8.10 are damped and a smooth response with a lower amplitude (about 10% less) was obtained, when a damping ratio of 0.3 was used in the analysis (Fig. 8.11).

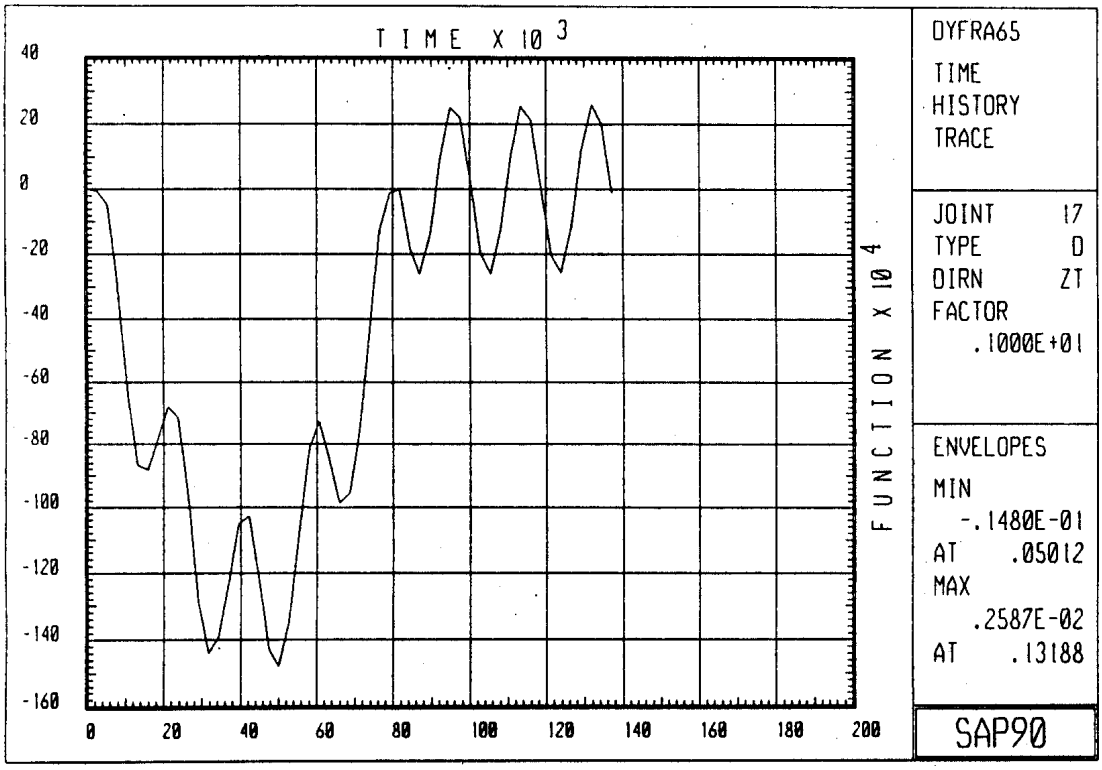

Fig. 8.10 Uncontrolled - undamped time history response variation

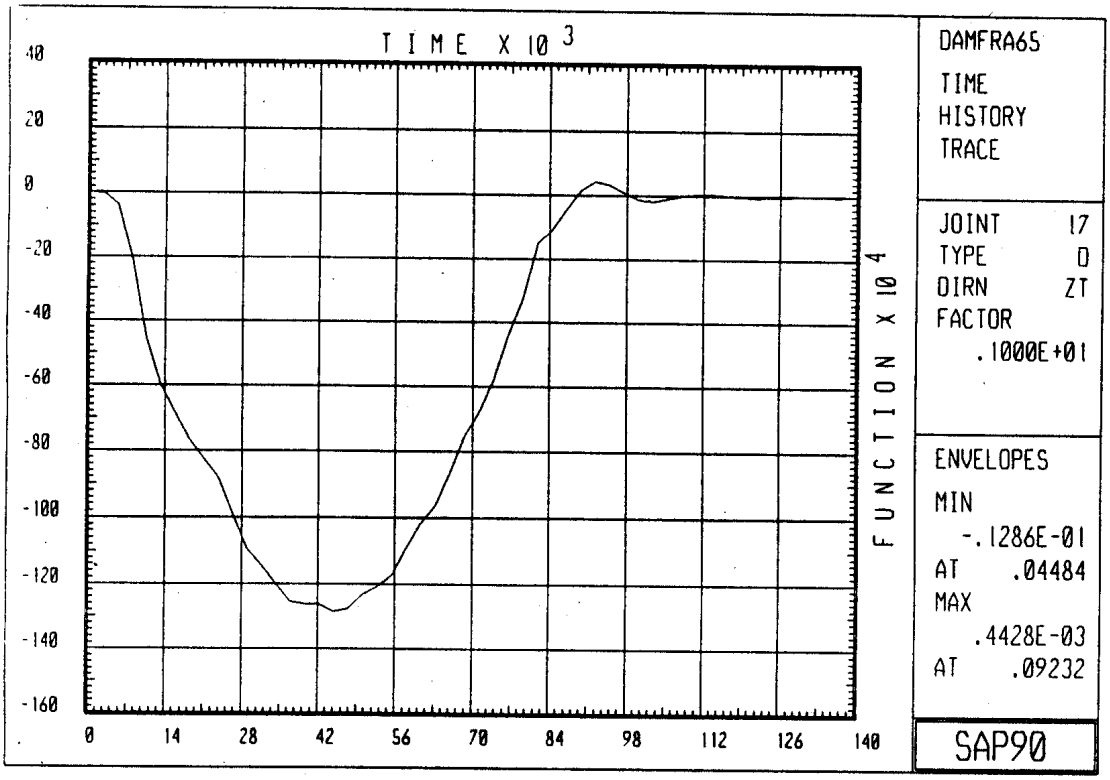

Fig. 8.11 Uncontrolled - damped time history response variation (DR = 0.3)

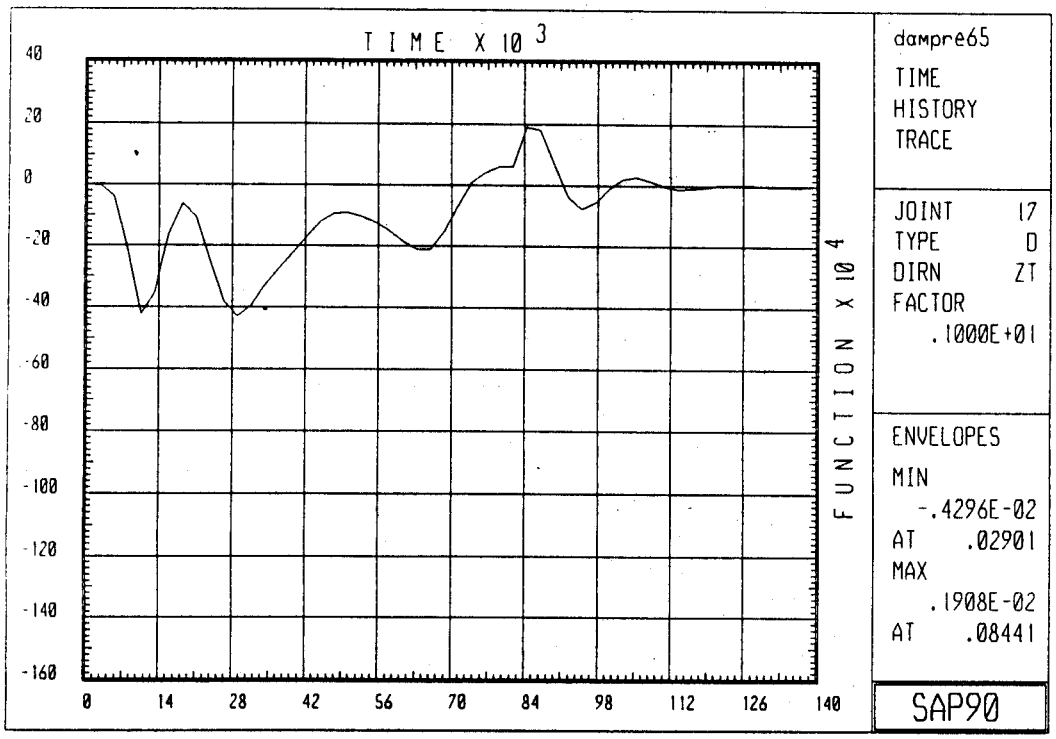

Fig. 8.12 Controlled - damped time history response variation (DR = 0.3)

Fig. 8.12 Controlled - damped time history response variation (DR = 0.3)

The response, after the vehicle exits the beam, is seen to diminish very rapidly indicating the damping ratio has a dominating effect on the response of the structure. Fig. 8.11 shows the controlleddamped time history response of the beam A significant decrease in the response amplitude (about 70% less) due to the applied control force is observed together with a rapid decrement of the response after the vehicle exits the beam due to structural damping. Hence, it can be concluded that the effect of control force is dominating over that of structural damping in diminishing the vibration amplitudes, when the vehicle is present on the beam After the vehicle exits the beam and when the control forces are decreased to zero (assuming that no control is necessary at this point), structural damping plays an important role in diminishing the residual vibrations.

Researchers in the past have estimated a structural damping ratio of approximately 0.07 for concrete structures. Hence analyses were performed using a damping ratio of 0.07 (for all the nine modes used in the analyses) with and without the control force. Figs. 8.13 and 8.14 show the damped - uncontrolled and damped - controlled. response respectively.

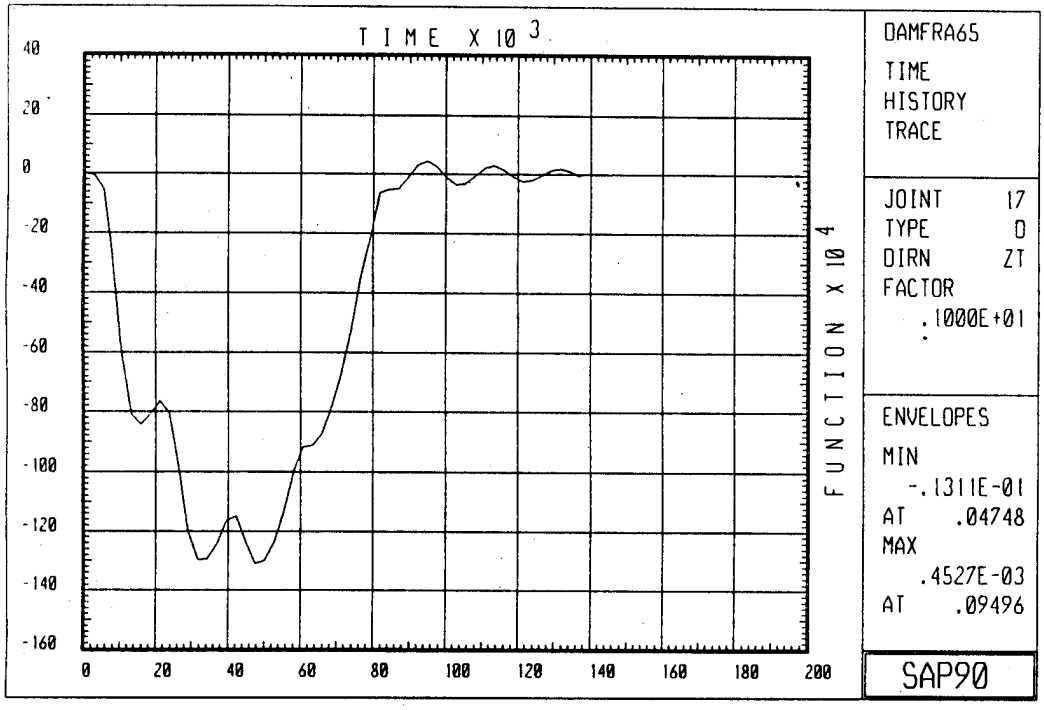

Fig. 8.13 Uncontrolled - damped time history response variation (DR = 0.07)

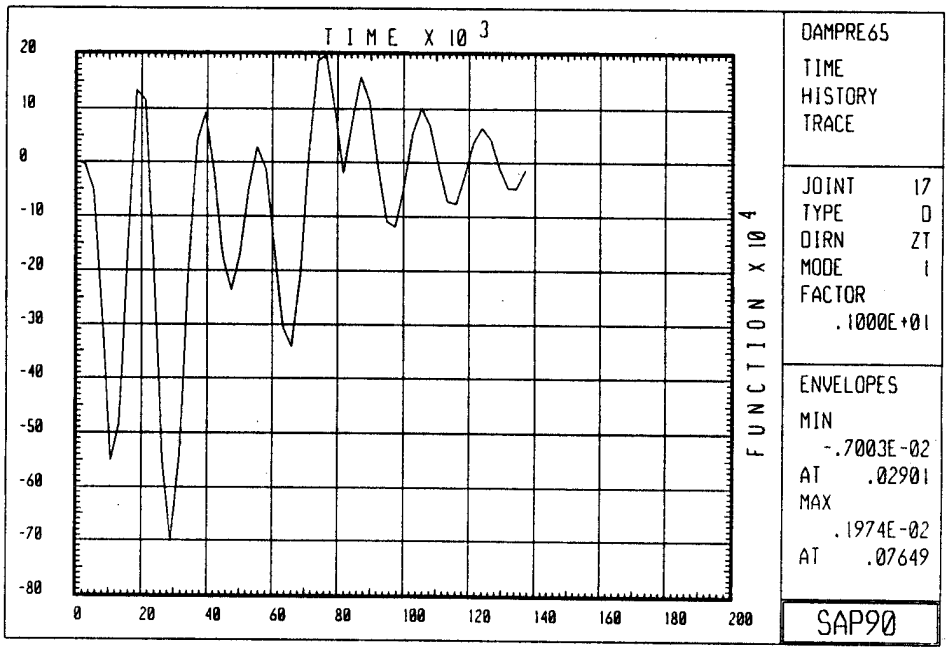

Fig. 8.14 Controlled - damped time history response variation (DR = 0.07)

A close comparison of Figs. 8.11 and 8.13 reveals the decreased effect of structural damping. Fig. 8.15 shows an amplitude reduction of about 55 percent when compared with undamped-uncontrolled response (Fig. 8.10). It was observed that the mitigation of the residual (after vehicle exits the beam) vibration is faster in the case of damped-uncontrolled analysis than that of damped-controlled situation. This could be due to the fact that (as shown in Figs. 8.13 and 8.14) the vibration amplitude at time when vehicle exits the beam, is higher in the case of damped-controlled analysis. This could be avoided, if the control algorithm is designed in such a way to keep amplitude to a minimum level when the vehicle is about to exit the beam.

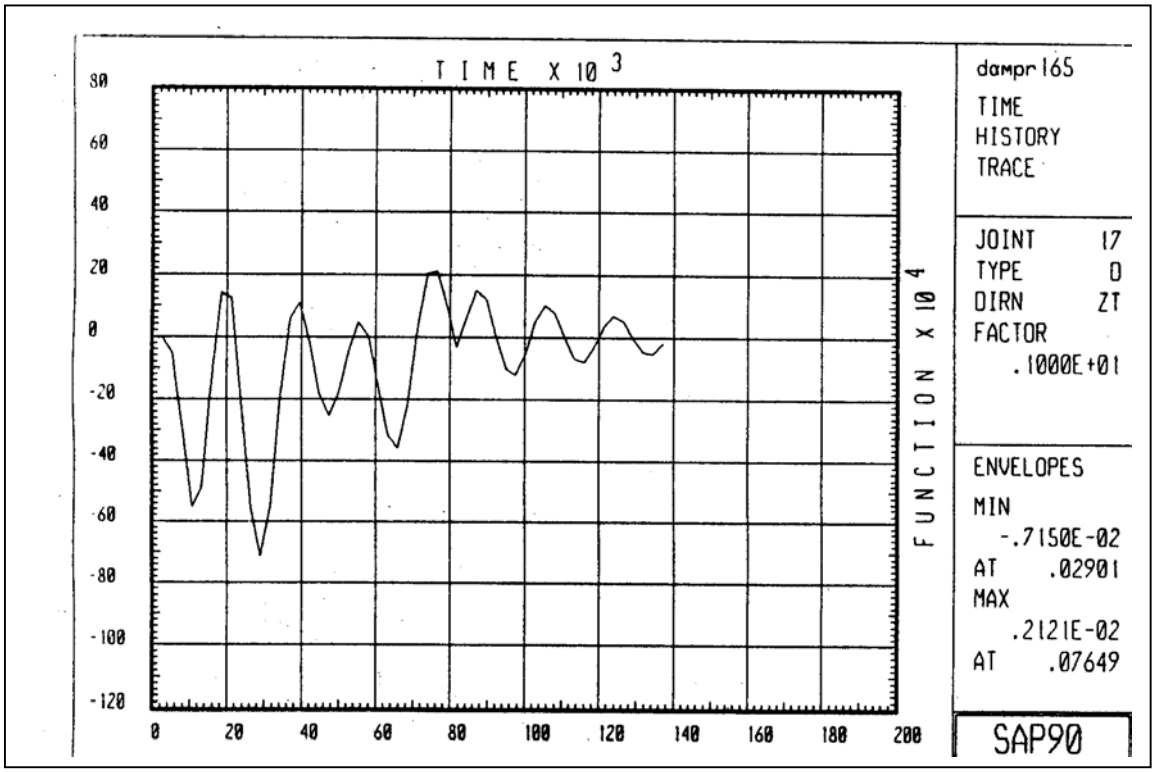

Fig. 8.15 Controlled - damped time history response variation

(DR = 0.0644, 0.1013, and 0.0566 for V, $2^{\circ d}$ and $3^{`d}$ modes)

Yukito Tamura et al., (1992) reported a recent investigation on estimation of structural damping ratios of reinforced concrete structures in Japan. They have formulated empirical formulae (Eqn. 8.8) to compute damping ratios of first, second and third mode shapes for reinforced concrete structures. These equations yield values of 0.0644, 0.1013, and 0.0566 as damping ratios for the first three modes of vibration. Damped-controlled time history analysis was performed using first three

modes with the corresponding damping ratios mentioned above. Fig. 8.15 shows the time history response of the beam for this condition. It can be observed from Fig. 8.15 that the vibration amplitude control is very efficient, while the vehicle is moving on the beam as well as after its exit. Hence, it can be said that it is vital to choose correct damping ratios in the estimation of response of a structure. It would be of great interest, if researchers attempt to estimate damping ratios in the case of structures prestressed / reinforced with FRPs.

8.6 DISCUSSIONS AND NEED FOR FURTHER RESEARCH

The active control methodology presented here is highly efficient and feasible. The analyses performed on a beam subjected to moving loads establish the effectiveness of the proposed active control technique. It could also be inferred from the analyses that choosing the appropriate damping ratios is vital for the estimation of correct response. Since the methodology is very flexible and could be used in conjunction with any type of control mechanism, it forms a powerful tool in estimation and control of the undesired deformations and/or vibrations in bridge structures. Further analytical and experimental studies are needed in this field to arrive at a most suitable algorithm. A robust control system requires an efficient continuous monitoring system FRPs are very ideal for integration of optic fiber sensors, which would make the control system very efficient and reliable.

Further investigation for estimation of optimum sensor locations and active tendon eccentricity could be made through parametric studies. A predictive control model could be addressed to avoid solving Riccati equation together with consideration of possible nonlinear structure behavior. Development of a more realistic dynamic model of bridges and the vehicle, formulation of control algorithm(s) would aid a great deal for practical implementation of the proposed methodology.

CHAPTER 9

SUMMARY AND CONCLUSIONS

9.1 INTRODUCTION

Experimental and theoretical investigations have been made on the feasibility of using aramid FRP (AFRP) tendons as prestressing elements in concrete bridges. This study included experimental work on durability of AFRP tendons, bond and flexural behavior of Double-Tee beam prestressed with AFRP, and fatigue and ultimate load behavior of Double-Tee bridge system prestressed with AFRP tendons. Analytical modeling of the behavior of flexural members prestressed and / or reinforced with FRP tendons and active structural control of bridges are also included in the present study. The analytical model developed in the study can also be applied to estimate the flexural response of members strengthened with FRP composites. The following sections present the summary and conclusions of the studies based on the ARAPREE tendons as prestressing elements in concrete members.

9.2 DURABILITY OF AFRP TENDONS

Pilot experimental studies were conducted on rectangular AFRP coupon specimens to determine the mechanical properties and assess the durability characteristics in sea water and alkali solution heated to about 45° C in laboratory environment.

i) A test. procedure has been developed for determining the mechanical properties of rectangular AFRP specimens.

ii) The width of the specimens was dictated by the size of the ARAPREE tendons rather than the specifications recommended by ASTM. The total length of the coupons as recommended by the Japanese Society of Civil Engineers (JSCE) seems to be adequate to determine the tensile strength of the tendons.

iii) Tensile tests were conducted by gripping the specimens with the end tabs which ensure proper stress transfer from the end fixtures to the specimen without any local failure of the specimen. The ends of the specimens should be prepared for attachment of end tabs by sanding and cleaning with water followed by acid solution and neutralizer.

iv) Premature failure of coupon specimens could be avoided by having sufficient length of the end tabs, good surface preparation, epoxy with high shear strength, and adequate curing time.

v) Coupon specimens exposed to sea water and alkali solution for 900 hours, were tested and found to fail prematurely. Although great care was taken during these coupon tests (as described in item iii.), the premature failure could be due to the changes in the matrix due to exposure which affected the bond between the end tabs and the specimen resulting in end tab slip.

vi) Detailed scanning electron microscope (SEM) analysis indicate abnormalities of the matrix in the specimen exposed to alkali solution.

9.3 PRETENSIONING OF DOUBLE-TEE BEAMS WITH AFRP TENDONS

Four pretensioned Double-Tee beams were cast for the study with the present state-of-the-art ARAPREE tendons in concrete. _ A number of shortcomings were encountered during the pretensioning operation and hence full design prestress levels could not be achieved in the ARAPREE tendons. The premature slip of the anchorage system could be avoided by improving the bond between the polyamide wedges and the epoxy used for adhering sand particles.

i) The pretensioning of the ARAPREE tendons is quite different from the present technology associated with prestressing steel. The technique used in pretensioning is applicable only to specialized situations in the laboratory; this has to be extensively modified before transferring the technology to the industry.

ii) Two jacks in series were used in pretensioning ARAPREE tendons to accommodate the large elongation together with the initial slack of the tendons over the form length of about 72.0 ft. This type of operation could be avoided and the technique adapted to the field conditions with long pretensioning beds, if only the wedge system were to be easily reusable.

iii) The anchorage system needs significant modifications so that higher prestress levels in the tendons could be achieved during pretensioning. In the present study, the initial jacking force was severely restricted to only 35 to 40 % of the tendon capacity.

iv) The prestress loss based on the measured strains in the tendons immediately after release was estimated to be approximately 11 %.

v) The mechanical properties of the ARAPREE tendons could be defined in terms of either effective fiber cross sectional area or gross sectional area; the final results of the analysis and design would be the same as long as consistency is maintained in the computations.

vi) Based on the effective fiber cross sectional area, the ARAPREE tendons have a higher ultimate tensile strength and lower Young's modulus than the conventional prestressing steel.

vii) The transfer length for the f 400 000 rectangular ARAPREE specimens was determined to be in the range of 12.0 - 18.0 in. based on measured strains in the Double-Tee beams. The comparison of the measured transfer length with the ACI formula for 0.5 in. diameter prestressing steel is given in Table 4.2. Although the estimated transfer length for prestressing steel is within the range of that measured for the ARAPREE tendon, a generalization for calculating transfer length could only be made, if more data are generated using varying tendon sizes and concrete strengths.

viii) The design computations of nominal moment of resistance of the Double-Tee beam were based on (a) the bottom most tendon rupture and (b) concrete crushing in the compression zone with Ecu = 0.003. The moment of resistance based on the bottom most tendon rupture is higher than that corresponding to crushing of concrete. However, the assumptions made in the values of stress block factors could only be confirmed based on more experimental data.

9.4 FLEXURAL BEHAVIOR OF DOUBLE-TEE BEAMS PRESTRESSED WITH AFRP TENDONS

The flexural behavior of the Double-Tee beam prestressed . with AFRP tendons was investigated in the linear and non-linear ranges. The experimental data obtained from the investigation included concrete and tendon strains, crack pattern and bond behavior, and deflections.

i) The Double-Tee beam exhibited excessively large deflections in the post-cracking stage, since the ARAPREE tendons are purely elastic in nature upto rupture and have a relatively lower Young's modulus than prestressing steel. Due to the limitations in the application of load as well as measurement of deflection, the test was conducted in three load stages.

ii) The strain variation based upon the measured concrete and tendon strains was almost linear in all the three load stages.

iii) The variation in compressive strains in concrete and typical tendon strains show an initial elastic and linear behavior with changes into the post-cracking stage with a transition zone between the linear and the non-linear regime.

iv) An average permanent compressive strain in concrete was observed to be about 175 microstrains and the corresponding tensile strain value in the tendon as 400 microstrains after the third load stage.

v) The load-deflection relationship exhibits typical bilinear characteristics with a short transition zone between the two linear portions with the first crack at a load of 5.5 kips.

vi) The maximum central deflection in the Double-Tee beam was 8.5 in. corresponding to the maximum load in the third load stage and the deflection recovery after unloading was quite significant with the final permanent deflection of only 0.4 in.

vii) The flexural cracks in the Double-Tee beam were almost vertical and uniformly spaced within the constant bending moment region and somewhat inclined in the region outside the points of load application.

viii) Uniformly spaced flexural cracks in the beam would indicate no bond failure between ARAPREE tendons and concrete.

ix) No tendon slip was observed from the LVDT measurements at the beam ends.

9.5 FATIGUE AND ULTIMATE LOAD BEHAVIOR OF DOUBLE-TEE BRIDGE SYSTEM

The Double-Tee bridge system was subjected to two stages of fatigue testing followed by the ultimate load test. The bridge system was loaded both in fatigue and ultimate tests simulating two HS20-44 AASHTO trucks on the two lanes. The deflections, concrete strains, distribution of cracks and crack widths were monitored in the bridge system

9.5.1 Fatigue Behavior

i) The effect of cyclic loading on the bridge system stiffness was evaluated in terms of load-deflection behavior and distribution and width of cracks.

ii) **A maximum load of 22.0 kips. was applied in the initial static test when the first crack was observed at a load of 17.0 kips on the model bridge system. The pre-cracked model bridge system was then subjected to first stage fatigue test with a load range of 8.0 to 22.0 kips. upto two million cycles, the lower load limit corresponding to the partial dead load compensation.**

iii) **The model bridge system showed significant reduction in stiffness after the first 56,000 cycles. However, the increase in deflections resulting from the change in stiffness was small thereafter upto the end of the first stage fatigue testing.**

iv) **No significant increase in permanent deflection was observed in the bridge system after the completion of the first stage fatigue test.**

v) **The second stage fatigue test was conducted with a load range of 12.0 to 36.0 kips., the upper limit corresponding to two HS20-44 trucks on the two lane bridge model.**

vi) **The stiffness degradation of the bridge model system in the second stage fatigue test was significant at 58,000 cycles and the change in stiffness thereafter was very marginal with no increase in permanent deformation upto one million cycles.**

vii) **Crack width variation with number of cycles of fatigue loading was quite similar to that of the deflections.**

9.5.2 Ultimate Load Behavior

Maximum load in the ultimate load test was recorded as 81.0 kips. when a loud noise was heard resulting from the extensive loss of bond in the bottom most tendon in the most heavily loaded stem (stem 1).

ix) **The bottom most tendon in stem 1 exhibited horizontal splitting with loss of bond with concrete.**

x) The ratio of the maximum load to the first crack load in the bridge system was 4.77 which is significantly higher than the minimum AASHTO recommended value of 1.20.

xi) The maximum compressive strains in concrete at the ultimate load of 81.0 kips. was measured to be 2500 microstrains. The variation of concrete strains with applied load show the bilinear nature with a more limited initial linear range at midspan than that at the south and north quarter span sections.

xii) A maximum permanent compressive strain of 900 microstrains was recorded after the bridge model system was unloaded from the maximum applied load.

xiii) The overall load-deflection relationship can be characterized to be trilinear resembling that for members prestressed with prestressing steel.

xiv) The maximum deflection observed at midspan was about 11.1 in. and with the unloading of the bridge system, the deflection reduced to about 4.5 in., which amounts to 60 % of deflection recovery.

xv) Formation of extensive horizontal cracks at the level of the bottom most tendon in stem 1 confirmed the bond loss with concrete.

xvi) The crack width variation with load exhibit the ideal trilinear characteristics.

The middle region of the bridge system had uniformly spaced crack pattern with a maximum crack width of 0.088 in., which decreased to 0.014 in. upon unloading.

9.6 FLEXURAL ANALYSIS OF SECTIONS PRESTRESSED WITH FRP

A detailed theoretical analysis is presented for members prestressed/reinforced with FRP to determine the moment-curvature and load-deflection relationships. A special purpose computer code was developed to analyze the members with rectangular and Tee sections having glass fiber reinforced plastic (GFRP), carbon fiber reinforced plastic (CFRP) or AFRP rods/tendons. The members could have multiple layers of reinforcing bars/ prestressing strands.

i) The theoretical analysis is applicable to members with concrete strengths upto 6000 psi.

ii) The moment deflection relationships predicted by the analytical procedure compare well with those obtained from the experiments in which GFRP [Sen, 1992] and CFCC [Arockiasamy, 1994] tendons have been used as prestressing elements in concrete.

iii) Typical example of a beam with multi-layered prestressing tendons illustrates (Section 5.3.2) the rupture of the bottom most tendon at the ultimate load stage; this is followed by the beam offering additional resistance to the applied load with increase of strains in the upper layers of tendons. Thus an additional reserve of energy in the beam is predicted by the analysis.

iv) The theoretical prediction of the load-deflection relationship for the single Double-Tee beam prestressed with AFRP tendons, agrees closely with the experimental data.

v) The predicted moment-curvature and load-deflection relationships are used to compute the energy absorbtion of Double-Tee beam prestressed with AFRP tendons.

vi) The ductility factor defined as the ratio of the ultimate deflection to the deflection corresponding to the rupture of the bottom most tendon is computed for the Double-Tee beam to be about 1.3.

vii) The large deformations observed in the ultimate load tests of both single Double-Tee beam and bridge system, give ample warning and hence the overall behavior could be taken to satisfy the ductility considerations.

viii) The predicted energy in the single Double-Tee beam after the bottom most tendon rupture is about 45 % of energy before rupture, which also indicates satisfactory ductility requirements.

9.7 ACTIVE STRUCTURAL CONTROL APPLICABLE TO BRIDGES PRESTRESSED WITH FRP

The active control methodology would prove useful in successfully utilizing FRPs as prestressing and reinforcing elements in bridges. A dynamic simulation is made of a moving load on a beam and time history analyses carried out for controlled and uncontrolled responses with and without considering structural damping.

i) The active control methodology proposed in this study is highly efficient and feasible for application in structures.

ii) Appropriate damping ratio for the type of structure need to be chosen for estimation of realistic response.

iii) The analyses carried out on a beam subjected to moving load establish the effectiveness of the proposed active control technique.

iv) Further analytical and experimental studies are needed in the field before implementing this concept to bridges.

REFERENCES

l. Abdel-Rohman M., and Leipholz"H H E "Structural Control by Poleassignment Method" Journal of Engineering Mechanics, ASCE Vol. 104, pp 1157-75, 1978.

2. Arockiasamy M., Neelakanta P.S., Sreenivasan G., "Vibration Control of Beams with Embeded Smart Composite Material", ASCE Journal of Aerospace Engineering, Vo1.5, No.4, October 1992.

3. Arockiasamy M., A. P. Badve, B.V. Rao, D.V. Reddy, " Fatigue Strength of Joints in a Precast Prestressed Concrete Double-Tee Bridges", PCI Journal, Jan.-Feb. 1991.

4. Arockiasamy M., "Experimental Studies on the Behavior-of Concrete Bridges Prestressed with Carbon Fiber Composite Cables" Progress Report I, May 1993.

5. Arockiasamy M., "Experimental Studies on the Behavior of Concrete Bridges Prestressed with Carbon Fiber Composite Cable" Progress Report II, Aug. 1993.

6. Arockiasamy M., "Experimental Studies on the Behavior of Concrete Bridges Prestressed with Carbon Fiber Composite Cable" Progress Report III, Nov. 1993.

7. Arockiasamy M., "Experimental Studies on the Behavior of Concrete Bridges Prestressed with Carbon Fiber Commosite Cable" Progress Report IV, May 1993.

8. Arockiasamy M., M. A. Shahawy, K S. Sandepudi et al., "Performance of Fiber Reinforced Plastics in Prestressed Concrete Bridges" Proceedings, XII FIP congress, May 29 - June 2, 1994, Washington D.C., pp B49-B55.

9. Arockiasamy M., M. A. Shahawy, K S. Sandepudi, "Performance Double-Tee Bridge Prestressed with ARAPREE" presented in, ACI Spring convention March 20 - 25, 1994, San Francisco, California.

10. Arockiasamy M., M. A. Shahawy, K. S. Sandepudi, "Studies on Bond Behaviorof Concrete Double-Tee Beams Prestressed with Aramid FRP Cables" presented in, ACI Spring convention March 20 - 25, 1994, San Francisco, California.

11. Arockiasamy M., M. Zhuang, K S. Sandepudi,. S. Kanneganti, "Flexural Behavior of Concrete Beams Prestressed with CFRP Tendons" to be presented in, IABSE symposium on Extending Life Span of Structures, August 1995, San Francisco, California.

12. **Austin S., R Goodall, J Nolan, "Towards a methodology for designing active elements into civil structures", pp 251-254, Proc. 1st European Conf.** on **Smart Structures and Materials, Glasgow, 1992.**

13. **Ballinger C. et al "Development of Fiber Reinforcement Plastic Products for the Construction Market", Advanced Composite Materials in Bridges and Structures, CSCE, P3, 1992.**

14. **Ballinger C.. "Development of Composites for Civil Engineering" Advanced Composites Materials in Civil Engineering Structures, ASCE, P288, Jan. 1991.**

15. **Charles W. Dolan "Developments in Non-metallic Prestressing Tendons", PCI Structure Journal, Sept.-Oct. 1990.**

16. **Chong KP., Liu S.C. and Li J.C., Intelligent Structures, --Proceedings of the International Workshop on Intelligent Structures held in Taipei, Taiwan, July, 1990.**

17. **Dehghanyer T. J., Masri S F, Miller R. Kand Caughey T K "On-line Parameter Control of Nonlinear Flexible Structures" in Leipholz "Structural Control" ppl41-159, 1987.**

18. **Dhillon S. S., and W. C. Lennox, "Time delay effect on dynamic response of actively controlled structures", ASCE, Jr. of Aerospace Eng., Vol. 5, No. 4, pp 450-464, October 1992.**

19. **Escobar P., et al, "Fiber-optic interferometric sinsors for concrete structures", pp 215-218, Proc. 1st European Conf. on Smart Structures and Materials, Glasgow, 1992.**

20. **Faza and H. V. S. Cangakao "Theoretical and Experimental Correlation of Behavior of Concrete Beams Reinforced with FRP rebars", International Symposium, FRP for RC structures, P599, March 1993.**

21. **Gerritse A., "Durability Criteria for Non-Metallic Tendons in an Alkaline Environment" Advanced Composite Materials in Bridges and Structures, CSCE, P129, 1992.**

22. **Handerek V. A., and A. J. Rogers, " Sensor system architechtures for spatially-resolved dynamic strain measurement using optical fibers ", pp 31-34, Proc. 1st European Conf.** on **Smart Structures and Materials, Glasgow, 1992.**

23. **Hankers and F. S. Rostasy "FRP Tendons for Post-tensioned Concrete Structures Acceptance Testing, Requirements and Mechanical Behaviors", Advanced Composite Materials in Bridges and Structures, CSCE, P191, 1992.**

24. Housner G. W., S. F. Masri, T. T. Soong, "Recent developments in active structural control research in the USA", pp 201-206, Proc. 1st European Conf, on Smart Structures and Materials, Glasgow, 1992.
25. Iwamoto et al "Flexural Fatigue Behavior of Prestressed Concrete Beams Using Aramid-Fiber Tendon", International Symposium, FRP for RC structures, P509, March 1993.
26. Iyer S., "Evaluation of Graphite Composite Cables for Prestressing Concrete", Advanced Composite Materials in Bridges and Structures, CSCE, P73, 1992.
27. Iyer S., and C. Kumaraswamy "Performance Evaluation of Glass Fiber Composite Cable for Prestressing Concrete Units" 33rd International SAMPE Symposium 33, Anaheim, CA. March 7-10,1988.
28. Iyer S., and Mahantesh Anigol, "Testing and Evaluating Fiberglass, Graphite, and Steel Prestressing Cables for Pretensioned Beams", Advanced Composites Materials in Civil Engineering Structures, ASCE, P44, Jan. 1991.
29. Iyer S., et al "Fiberglass and Graphite Cables for Bridge Decks", Advanced Composites Materials in Civil Engineering Structures, ASCE, P371, Jan. 1991.
30. Kakizawa, et al "Flexural Behavior and Energy Absorption of Carbon FRP Reinforced Concrete Beams", International Symposium, FRP for RC structures, P585, March 1993.
31. Kanakubo et al "Bond Performance of Concrete Members Reinforced with FRP Bars", International Symposium, FRP for RC structures, P767, March 1993.
32. Katawaki, I. Nishizaki and I. Sasaki "Evaluation of the Durability of Advanced Composites for Applications to Prestressing Concrete Bridges" Advanced Composite Materials in Bridges and Structures, CSCE, P119, 1992.
33. Katebi Reza, "Control design for smart flexible structures", pp 305-308, Proc. 1st European Conf. on Smart Structures and Materials, Glasgow, 1992.
34. Kato and N. Hayashida "Flexural Characteristics of Prestressed Concrete Beams with CFRP Tendons", International Symposium, FRP for RC structures, P419, March 1993.
35. Kobayashi and Y. Tanaka "Impact Tensile Strength of Carbon Fiber Composite Cable" Advanced Composite Materials in Bridges and Structures, CSCE, P83, 1992.

36. **Kruschwitz B., et al, "Optical fiber sensors for the quantitative measurement of strain in concrete structures", pp 241-244, Proc. 1st European Conf.** on **Smart Structures and Materials, Glasgow, 1992.**

37. **Lee S. K, and Kozin F "Bounded State Control of Linear Structures" in Leipholz "Structural Control" pp 387-407, 1987.**

38. **Leipholz H.H.E. and Abdel-Rohman M. , Control of Structures, 1986.**

39. **Lin, F. L. Lewis and T. Huang "Dynamic modeling for bridge vibration control" TRB Annual meeting, August 1993.**

40. **Makitani et al "Investigation of Bond in Concrete Member with Fiber. Reinforced Plastic Bars", International Symposium, FRP for RC structures, P315, March 1993.**

41. **Martin C. R., and Soong T. T., "Modal Control of Multistorey Structures" Journal of Engineering Mechanics, ASCE Vol. 102, pp613-623, 1976.**

42. **Mason B., D. Hogg and M. Measures, " Fiber optic strain sensing for smart adaptive structures ", pp 135-138, Proc. 1st European Conf.** on **Smart Structures and Materials, Glasgow, 1992.** 43. **Masri S. F., Bekey G. A. and Caughey T. K "On-line Control of Nonlinear Flexible Structures" Journal of Applied Mechanics, ASME Vo1.49 pp 877-884, Dec.' 1982.**

44. **Masri S. F., Bekey G. A. and Caughey T. K "Optimum Pulse Control of Flexible Structures" Journal of Applied Mechanics, ASME Vo1.48 pp 619-626, Sept. 1981.**

45. **Mckay and M. A. Erki "Aramid Tendons in Pretensioned Concrete Applications" Advanced Composite Materials in Bridges and Structures, CSCE, P221, 1992.**

46. **Miller R. K, Masri S F, Dehghanyar T J and Caughey T K, "Active Vibration Control of Large Civil Structures", Journal of Engineering Mechanics, ASCE Vol. 114 pp 1542-70, 1988.**

47. **Mochizuki & Y. Matsuzaki & M. Sugita, "Evaluation Items and Methods of FRP Reinforcement as Structural Elements", International Symposium, FRP for RC structures, P117, March 1993.**

48. **Morse A. and T. F. "Overview of optical fiber sensors embedded in concrete", , SPIE proceedings, Vol. 1798, No. 22, Fiber Optic Smart Structures and Skins, 1992.**

49. **Morse** T. F., **A. Morse and F. Mendez "Applications of embedded optical fiber sensors in reinforced concrete buildings and structures",. SPIE Vol. 1170, Fiber Optic Smart Structures and Skins, 1989.**

50. Mukae et al. " Characteristics of Aramid FRP Rods", SP 138-3, Proceedings, ACI Simposium on FRP Reinforcement for Concrete Structures, Vancoover, Canada, 1993.

51. Naaman A., and K H. Tan et al "Partially Prestressecd Beams with Carbon Fiber Composite Strands: Preliminary Tests Evaluation", International Symposium, FRP for RC structures, P441, March 1993.

52. Nagasaka, H.Fukuyama and Tanigaki "Shear Performance of Concrete Beams Reinforced with FRP Stirrups", International Symposium, FRP for RC structures, P789, March 1993.

53. Nakano and Y. Matsuzaki "Flexural Performance of the Concrete Beams Reinforced with Continuous Fiber bars", International Symposium, FRP for RC structures, P743, March 1993.

54. Nanni A., et al., "Fiber Optic Sensors for concrete strain/stress measurement", ACI Materials Journal, Vol. 8, No. 3, May - June 1991.

55. National Science Foundation, "Structural Control Research for Performance, Safety and Hazard Mitigation" announcement of program initiative.

56. Rao, Mechanical Vibrations, second edition, Addison-Wesley Pub. Company, 1990.

57. Reinhorn A.M. and Soong T.T., et al "Full-Scale Implementation of Active Control I: Design and Simulation", ASCE Journal of Structural Engineering. Vol. 119, June 1991.

58. Rodellar Jose "Predictive control of structures", et al, ASCE, Jr. of Eng. Mech., Vol. 113, No. , pp 797-812, June 1987.

59. Rohman and H. H. Leipholz, "Automatic Active Control of Structures", ASCE, Structural Journal, March 1980, pp 663-677.

60. Roorda, "Tendon Control in Tall Structures", ASCE, Structural Journal, March 1975, pp 505-521.

61. Rostasy and H. Budelmann, "FRP Tendons for the Post-tensioning of Concrete Structures" Advanced Composites Materials in Civil Engineering Structures, ASCE, P155, Jan. 1991.

62. Rostasy, "FRP Tensile Elements for Prestressed Concrete --- State of the Art, Potentials and Limits", International Symposium, FRP for RC structures, P347, March 1993.

63. Sandepudi K S., M. Arockiasamy, "Active Structural Control of Bridges Prestressed with FRPs" Proceedings, 2nd International Conference on Intelligent Materials, June 5 - 8, 1994, Williamsburg, Virginia, pp B49-B55.

64. Sandepudi K. S., M. Arockiasamy, "Thermal Stresses in Bridges Prestressed with FRPs" to be presented in, IABSE symposium on Extending Life Span of Structures, August 1995, San Francisco, California.

65. Sen R, S. Iyer, M. Issa and M. Shahawy "Fiberglass Pretensioned Piles for Marine Environment", Advanced Composite Materials in Civil Engineering Structures, ASCE, P348, Jan. 1991.

66. Sen R., Danial Mariscal, Mohsen Shahawy, "Durability of Fiberglass Pretensioned Beams"ACI Structural Journal, Sept.-Oct. 1993.

67. Sen R., M. Issa, Danial Mariscal "Fiberglass Pretensioned Piles for Marine Environment", Final report submitted to U.S. and Florida Department of Transportation, August, 1992.

68. Shahawy M., " Feasibility Study of Transversely Prestressed Double-Tee Bridges", PCI Journal, Sept.- Oct. 1990.

69. Sirkis J. S., and A. Dasgupta, " What do embedded optical fibers really measure? ", pp 69-72, Proc. 1st European Conf. on Smart Structures and Materials, Glasgow, 1992.

70. Soong T. T. , Active Structural Control, NY Aug. 1989.

71. Soong T.T., Reinhorn A.M. et al "Full-Scale Implementation of Active Control. I: Design and Simulation", ASCE Journal of Structural Engineering. Vol. 117, Nov. 1991.

72. Sueoka, K Yasuoka et al "Mechanical Properties of Composite Beams -by FRP", International Symposium, FRP for RC structures, P133; March 1993 structures, P133, March 1993.

73. Tanigachi and H. Mutsuyoshi et al "Ductile Behavior of Beams Using FRP as Tendons and Transverse Reinforcement", International Symposium, FRP for RC structures, P651, March 1993.

74. Tokyo Rope MFG. Co. Ltd. "CFCC Technical Data" Oct 1989.

75. Tottori and H. Wakui "Shear Capacity of RC and PC beams Using FRP Reinforcement" International Symposium, FRP for RC structures, P615, March 1993.

76. Uomoto T., and H. Hodhod, "Properties of Fiber Reinforced Plastic Rods for Prestressing Tendons" International Symposium, FRP for RC structures, P101, March 1993.

77. Wolff R., and H-J. Miesseler " Monitoring of prestressed concrete structures with optical fiber sensors", , pp 23-29, Proc. 1st European Conf. on Smart Structures and Materials, Glasgow, 1992.

78. Yang IN., Akbarpour A and Ghaemmaghami P "Optimal Control Algorithms for EarthquakeExcited Building Structures", in Leipholz "Structural Control" pp 748-761, 1987.

79. Yang IN., Long F.X. and Wong D, "Optimal Control of Nonlinear Structures", Journal of Applied Mechanics, ASME Vo1.55 pp931-939, 1988.

80. Yang, F. Giannopolous, "Active Control and Stability of Cable Stayed Bridge", ASCE, Structural Journal, August 1979, pp 677-695.

81. Yao J.T.P., "Concept of Structural Control", Journal of Structural Division., Vo1.98 pp1567-74, ASCE, 1972.

82. Yonekura et al "Flexural and Shear Behavior of Prestressed Concrete Beams Using FRP Rods as Prestrssing Tendons", International Symposium, FRP for RC structures, P525, March 1993.

83. Zuk W., "Kinetic Structures", Civil Engineering, ASCE 33, PP62-64, 1968.